Physik-Department E13
Technische Universität München
&
Laboratoire des Verres,
Université Montpellier II

Structure and Dynamics of Hydrous Silica(tes) as seen by Molecular Dynamics Computer Simulations and Neutron Scattering

Markus Pöhlmann

Vollständiger Abdruck der von der Fakultät für Physik der Technischen Universität München und dem Laboratoire des Verres der Université Montpellier II zur Erlangung des akademischen Grades eines

Doktors der Naturwissenschaften (Dr. rer. nat.)

genehmigten Dissertation

Vorsitzender: Univ.-Prof. Dr. M. Kleber

Prüfer der Dissertation:

1. Univ.-Prof. (komm. L.) Dr. A. Meyer
2. Prof. Dr. W. Kob, Univ. Montpellier II / Frankreich
3. Univ.-Prof. Dr. M. Stutzmann
4. Prof. Dr. B. Hehlen, Univ. Montpellier II / Frankreich

Die Dissertation wurde am 9.12.2004 bei der Technischen Universität München eingereicht und durch die Fakultät für Physik am 27.1.2005 angenommen.

The reader should note that important background information for the lecture of the present manuscript can be found in the appendices. In particular, a list of all used abbreviations and symbols can be found in appendix B, information on the composition of natural rocks can be found in appendix C, appendix D provides information on the scattering experiments at the Institut Laue-Langevin, and appendix E shows the input file for the CPMD code (version 3.4.3) for the molecular dynamics computer simulations

Contents

English Summary

In recent years the influence of water on the structure and viscosity of silica (SiO_2) and silicate melts has attracted the interest of many experimental groups due to its importance in geology (e.g., magmatic flow in the earth crust and explosive volcanism) as well as technology (e.g., glassy optical fibers and semiconductor devices).
These, mostly spectroscopic, measurements suggest that the mechanism of dissolution of water in silica(te) melts varies strongly with the total amount of water. In addition to dissolved water, molecular water may be present. In chemical terms it represents a balance of the form

$$\mathrm{Si-O-Si} + \mathrm{H_2O} \longleftrightarrow 2(\mathrm{SiOH})$$

that follows the Chatelier principle and which can be shifted to either side by the variation of external conditions like temperature or concentration of one species.
This project is an attempt to perform a quantum-chemical verification of the existing and new experimental data (for reviews see [Bu79, Mi94, Ko00]) and hence to obtain a deeper understanding of the dissolution mechanisms of water. Neutron scattering experiments that give experimental access to statistical quantities extracted from the simulation (such as vibrational densities of states and structure factors) are performed in parallel.
The equilibration of hydrous silica systems has been successfully set up with the CPMD code at temperatures of 3000 K and 3500 K. The results for the system $30SiO_2$-$4H_2O$ are chemically and physically reasonable and all water is dissolved to SiOH groups. It is for the first time possible to investigate the diffusion mechanisms for hydrogen in real space and to reveal important intermediate states.
Quenches to ambient temperature allow comparisons to the experiments. Concerning the neutron scattering structure factor, the agreement between the simulation and the experiment is rather good. The structure factor of the hydrous SiO_2 is (in both approaches) very close to the one of the pure material. Nevertheless the simulation shows that the silica tetrahedral network is partially broken. Also the vibrational density of states was extracted from the simulation and a neutron scattering experiment. In this case, the agreement is not as good since the statistics is dominated by the 8 hydrogen atoms in the simulation. In the experiment the silicate composition was varied from silica over sodium silicates to albite (sodium alumino silicate). It is found that the densities of states depend considerably on the silicate matrix but they do not show a dependence on the total water content. This is a very surprising result since Raman and Infrared spectroscopy suggest that the ratio of SiOH to H_2O changes significantly with the total water content. Therefore one concludes that the dynamics of the matrix is not affected by the $SiOH/H_2O$ ratio, and neither are all associated mechanisms like the viscosity of the silicate.
Quenches of selected configurations in the simulation allow also the electronic structure to be studied. In particular states in the electronic band gap of pure silica were found. The correlation of these electronic states with the structural intermediate states for hydrogen diffusion has been discussed for a long time due to their importance in semiconductor technology.

Deutsche Zusammenfassung

In den letzten Jahren bestand von experimenteller Seite ein reges Interesse an wasserhaltigen Schmelzen von Siliziumdioxyd und Silikaten aufgrund der hohen Bedeutung dieser Materialien in der Geologie (z.B. dem Magmafluss in der Erdkruste und explosivem Vulkanismus) und bei technologischen Fragestellungen (z.B. in Lichtleitern und Halbleiterbausteinen).
Diese meist spektroskopischen Untersuchungen legen nahe, dass die Lösung von Wasser in Silikaten stark von der Gesamtwasserkonzentration abhängt. Zusätzlich zu gelöstem Wasser kann auch molekulares Wasser vorhanden sein. In chemischer Terminologie stellt das ein Gleichgewicht der Form

$$\mathrm{Si-O-Si} + \mathrm{H_2O} \longleftrightarrow 2(\mathrm{SiOH})$$

dar, das dem Prinzip von Chatelier unterliegt und das auf jede Seite verschoben werden kann, ensprechend den äußeren Bedingungen wie Temperatur oder Konzentration einer Komponente.
Dieses Projekt ist ein Versuch einer quantenchemischen Verifikation existierender und neuer Daten (Übersichtsartikel [Bu79, Mi94, Ko00]), um damit ein tieferes Verständnis der Lösungsmechanismen von Wasser zu erhalten. Neutronenstreuexperimente die experimentellen Zugang zu statistischen Größen (wie der Schwingungszustandsdichte oder Strukturfaktoren) geben, werden parallel durchgeführt.
Die Äquilibration von wasserhaltigem Siliziumdioxyd bei Temperaturen von 3000 K und 3500 K wurde erfolgreich mit dem CPMD Code bewerkstelligt. Die Ergebnisse für das System $30SiO_2$-$4H_2O$ sind chemisch und physikalisch sinnvoll und das ganze Wasser ist in Form von SiOH Gruppen gelöst. Es ist zum ersten Mal möglich, die Diffusionsmechanismen von Wasserstoff im reellen Raum zu untersuchen und wichtige Übergangszustände zu ermitteln. Abkühlung auf Raumtemperatur ermöglicht Vergleiche mit Experimenten. Bezüglich des Neutronenstrukturfaktors ist die Übereinstimmung von Experiment und Simulation ziemlich gut. Der Strukturfaktor des wasserhaltigen Materials ist dem des trockenen Materials sehr ähnlich (in beiden Ansätzen). Nichtsdestotrotz zeigt die Simulation, dass das Tetraedernetzwerk des Silikates gebrochen ist. Die Schwingungszustandsdichte wurde ebenfalls aus dem Experiment und der Simulation extrahiert. In diesem Fall ist die Übereinstimmung nicht so gut, da die Statistik von den nur 8 Wasserstoffatomen der Simulation bestimmt wird. Im Experiment wurde die Silikatzusammensetzung von Siliziumdioxyd über Natriumsilikat zu Albit (Natriumaluminiumsilikat) hin variiert. Es konnte herausgefunden werden, dass die Zustandsdichten beträchtlich von der Silikatmatrix abhängen, jedoch nicht vom Wassergehalt. Das ist ein sehr überraschendes Ergebnis, da Infrarot- und Ramanspektroskopie nahe legen, dass sich das $SiOH/H_2O$ Verhältnis signifikant mit dem Gesamtwassergehalt ändert. Man schließt daraus, dass die Dynamik der Matrix vom $SiOH/H_2O$ Verhältnis ebensowenig beeinflusst ist, wie alle von ihr abhängenden Mechanismen wie z.B. die Viskosität der Silikate.
Kühlen von ausgesuchten Konfigurationen in der Simulation erlaubt es auch die elektronische Struktur zu untersuchen. Insbesondere wurden Zustände in der elektronischen Bandlücke von Siliziumdioxyd gefunden. Die Korrelation dieser elektronischen Zustände mit den strukturellen Übergangszuständen für die Wasserstoffdiffusion wird schon lange wegen ihrer Bedeutung in der Halbleitertechnologie diskutiert.

Resumé Français

L'influence de l'eau sur la structure et la viscosité de la silice et des silicates a fait l'objet de nombreuses études dans les années précédentes grâce à son importance géologique (par exemple le flux magmatique dans la croûte du globe terrestre et le volcanisme explosif) ansi que technique (par exemple dans les fibres optiques et les semiconducteurs).
Ces mesures spectroscopiques proposent que le mécanisme de dissolution de l'eau dans la silice et les silicates est bien une fonction de la concentration totale de l'eau. De l'eau dissociée ainsi que de l'eau moléculaire peuvent être présentes. En termes chimiques, le problème représente une balance de la forme

$$\mathrm{Si-O-Si + H_2O \longleftrightarrow 2(SiOH)}$$

suivant le principe de Chatelier, qui peut être déplacé des deux côtés en fonction des conditions externes comme la température ou la concentration d'une espèce.
Ce travail de thèse constitue une tentative de vérification des données existantes et nouvelles (voir les références [Bu79, Mi94, Ko00]) en utilisant des méthodes de la chimie quantique pour mieux comprendre le mécanisme de dissolution de l'eau. Des expériences neutroniques ont été parallèlement poursuivies, donnant accès aux mêmes quantités statistiques que celles extraites de la simulation numérique (par exemple le facteur de structure et la densité d'états vibrationnels).
La simulation de la silice hydratée a été mise en œuvre avec le code CPMD à des températures de 3000 K et 3500 K. Les résultats pour le système $30SiO_2$-$4H_2O$ sont chimiquement et physiquement raisonnables et l'eau est entièrement dissociée en groupes SiOH. Il est pour la première fois possible d'étudier les mécanismes de diffusion de l'hydrogène dans l'espace reél et de révéler ainsi des états intermédiaires importants.
Les trempes à des températures ambientes permettent la comparaison à l'expérience. Concernant le facteur de structure neutronique, la correspondance entre la simulation et l'expérience est remarquablement bonne. Le facteur de structure du matériau hydraté est (dans les deux approches) très proche de celui de la silice pure. Les simulations montrent cependant que le réseau tetrahédrique du silicate est partiellement brisé. La densité d'états vibrationnels a été également extraite de la simulation et de l'expérience neutronique. Dans ce cas-là, la correspondance n'est pas aussi bonne car la statistique est dominée par les 8 atomes d'hydrogène de la simulation. Dans l'expérience la composition du silicate a été variée de la silice aux silicates du sodium et à l'albite (silicate du sodium aluminium). Il a été trouvé que les densités d'états dépendent considérablement de la matrice silicatée mais qu'elles ne montrent pas de dépendance en fonction de la concentration en eau. C'est un résultat très surprenant car les spectroscpies infrarouge et Raman suggèrent que la relation $SiOH/H_2O$ change considérablement avec la concentration en eau. On conclue ansi que ni la dynamique de la matrice est affectée par la relation $SiOH/H_2O$, ni les mécanismes associés comme la viscosité des silicates.
Des trempes réalisées à partir de configurations selectionnées dans la simulation permettent également d'étudier la structure électronique du verre. En particulier, des états dans la bande interdite électronique de la silice hydratée ont été trouvés. La corrélation de ces états électroniques avec les états structuraux intermédiaires pour la diffusion de l'hydrogène a été discutée depuis longtemps étant donnée leur importance pour la technologie des semiconducteurs.

Chapter 1

Introduction and Motivation

1.1 Introduction

The structure of silica and silicate glasses has long been considered to be a disordered network of SiO_4 tetrahedrons and optional alkali and earth-alkali atoms as displayed in figure 1.1 [Wa38]. That this picture is *not* completely true has recently been confirmed [Ho01, Me02]. However, it was early recognized that an even more important question is if and how a water molecule can attack a silicon oxygen bond in such a silicate [Bo28]. How and to what extent

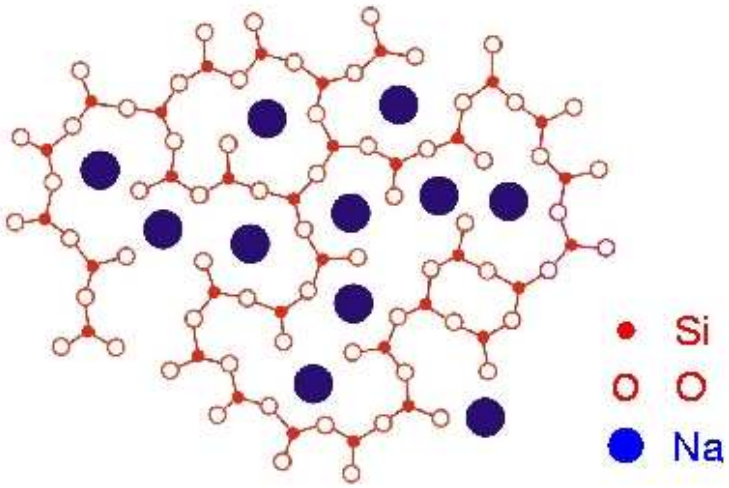

Figure 1.1: *Two dimensional projection of a silicate structure as proposed by Warren and Biscoe in the 1930s [Wa38]. A perfect randomly disordered network of silica and metal units is realized.*

this dissolution is actually performed is still under debate and it is one of the main goals of this work to analyze this process. The current idea of the underlying process is displayed in figure 1.2. Many questions have been and are still associated with this reaction: On which

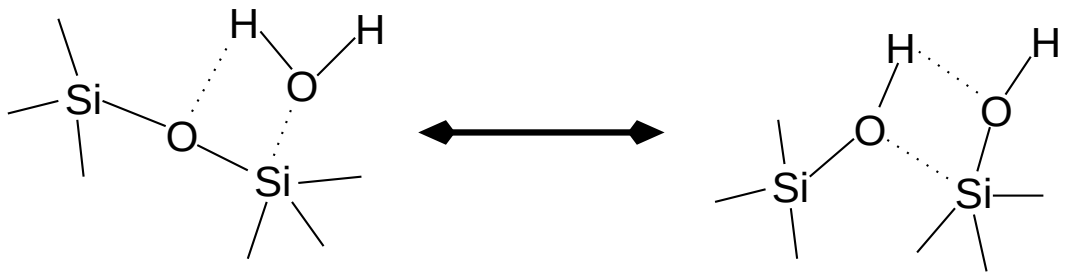

Figure 1.2: *Reaction of water with a silica bond of the network.*

side is the chemical equilibrium as a function of pressure and temperature? What is the

influence of the composition of the silicate? What are the macroscopic consequences of this dissolution, especially for the viscosity and optical properties. Is there an increase of the electrical conductivity due to proton injection?
In fact, it has already been found that the effect of water on the above mentioned quantities is very strong. The viscosity of silicate melts seems to decrease by up to 6 (six!) orders of magnitude by the addition of only one percent weight of water [Di96b] and even the addition of water in the ppm regime affects the viscosity of silica [Ba86] in the percent range. In silica water reduces the refraction index, the sound velocity and the density, while it increases the thermal expansion coefficient [He62, Br64, Sc59]. Effects on the crystallization rate [Wa64] and on the irradiation resistance [Ar59, We64] have also been reported.

1.2 Applications and Motivations

The release of water and hydrogen from the silica structure is the main danger associated to hydrous silicates in nature and technology.

1.2.1 Geology

Explosive volcanic eruptions are one of the most spectacular and also most dangerous events on earth. Fortunately not all eruptions are explosive. In fact, the eruption style of a volcano depends on the composition of the magma (molten silicate rock [1]) in the magma chamber and the way it breaks into small particles, a process that is called fragmentation [Di96a, Sa99]. If and how such fragmentation occurs is correlated with the viscosity of the magma and hence its ability to react on external strains imposed by temperature or pressure changes. If such deformations are slow enough relative to the material's viscosity, the melt can relax as a viscous liquid. On the other hand, if the stress is imposed fast enough relative to the material's viscosity, relaxation is suppressed and brittle failure and fragmentation are the logic consequence. According to this picture, it is the viscosity of the melt that is decisive for the fragmentation process. However, it is very well known that volatiles like carbon dioxide and especially water govern the viscosity of a silicate melt.
Figure 1.3 shows the viscosity of the haplogranitic melt HPG8[2] as a function of the water content. It can be seen that the viscosity drops by four orders of magnitude with the addition of the first wt.% of water. More viscous magmas have slower diffusivities for volatiles [Sa99]. The process of fragmentation is supposed to be strongly related to the separation of volatile (in particular water) bubbles from the melt [Sa99, Pr98]. The equations that control the evolution of the bubbles will be presented in section 2.3. In the column of a volcano their growth is governed by the inward diffusion of gas and expansion due to relaxed pressure. Smaller pressure reduces also the gas solubility in the melt and accelerates further the bubble growth. When the foam can no longer support the stress induced by bubble growth, brittle failure and fragmentation occur in the remaining glass. The key for fragmentation is that the remaining melt has a considerably lower volatile content and therefore a higher viscosity than the foam (see figure 1.3). Hence the magma has no more time to relax like a viscous liquid if the volatiles are released sufficiently fast.

[1] For the composition of natural rocks see appendix C

[2] HPG8 corresponds to the composition (in mol%) of 83.8%SiO_2, 8.1%Al_2O_3, 4.7%Na_2O, and 3.4%K_2O

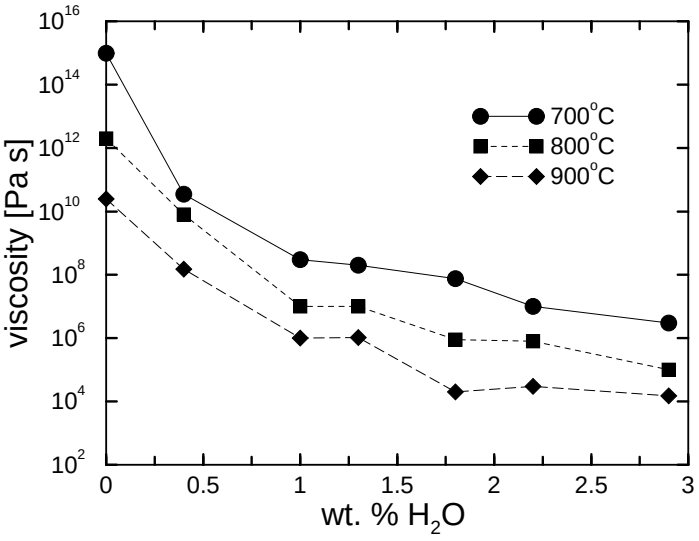

Figure 1.3: *Dependence of the viscosity of the haplogranitic melt HPG8 on the water content. Within the addition of the first wt.% of water the viscosity drops by more than four orders of magnitude (after [Di96b]).*

To conclude the section on explosive volcanic eruption, it should be briefly mentioned how water comes into the magma. Current models propose that water is already physically adsorbed in minerals at the sea floor. With continental plate drifting the water saturated minerals can get into the earth mantle. At typical mantle temperatures of several thousands of Kelvin and several kbars of pressure, the water dissolves chemically to the silicates [Za02].

1.2.2 Semiconductor Devices

A major concern in silicon technology is the reliability of metal-oxide field-effect transistors (MOSFETs). The MOSFETs consist in principle of a three layered structure, a metal (mostly aluminum), the dielectric (mostly silicon dioxide), and silicon. The performance of every day computers scales with the number of such transistors in the central processing unit and in storage devices. The impressive progress of the semiconductor industry in the fabrication of integrated circuits accommodating more and more transistors is commonly described by the so called *Moore's Law*. This law summarizes the history of the last 40 years of integrated circuit fabrication by the statement that *the power (measured in the number of transistors) of CPUs increase by a factor of ten each ten years*. This was indeed the case from the year 1970 to the year 2000. The main challenge in the forthcoming years will be to prevent Moore's law from becoming more and more flat. This will impose a further miniaturization on the structures in microchips. However, a natural limit of the miniaturization is certainly given by the atomic length scale. The requirements for the next 15 years on device processing are summarized and regularly updated by the "road map" of the Semiconductor Industry Association [SIA01]. The main features of this road map were recently summarized by Arden [Ar03].

Regarding the MOSFET, mainly problems related to the gate-oxide interfere with the road map requirements. Among the problems encountered are an increased leakage current, a reduced threshold for dielectric breakdown, and gate-oxide charging. These problems have been attributed to various defect states in the oxide and on the silicon - silicon oxide interface. This was reviewed by Helms *et al* in 1994 [He94]. These defects are separated in ones that cause a positive oxide charge Q_{ox} and others leading to charged interface traps Q_{it} [Po95]. The most prominent candidate for a Q_{it} is the so called P_b center on the silicon side of the

Si-SiO_2 interface: $\cdot Si = Si_3$. Dangling Si bonds in the oxide, an example for Q_{ox} are the so called E' centers: $O_3 = Si\cdot$ .... $^{+}Si = O_3$. Water and / or hydrogen is now introduced in order to compensate such oxide charges. This can either happen directly at the oxide growth process ("wet oxidation") as it was described by Deal and Grove [De65] or later. The passivation of a P_b center by a water molecule is demonstrated in Figure 1.4. During the diffusion and the passivation process, water molecules can of course dissolve to SiOH groups as it was indicated in Figure 1.2. This opens, in principle, the possibility of an

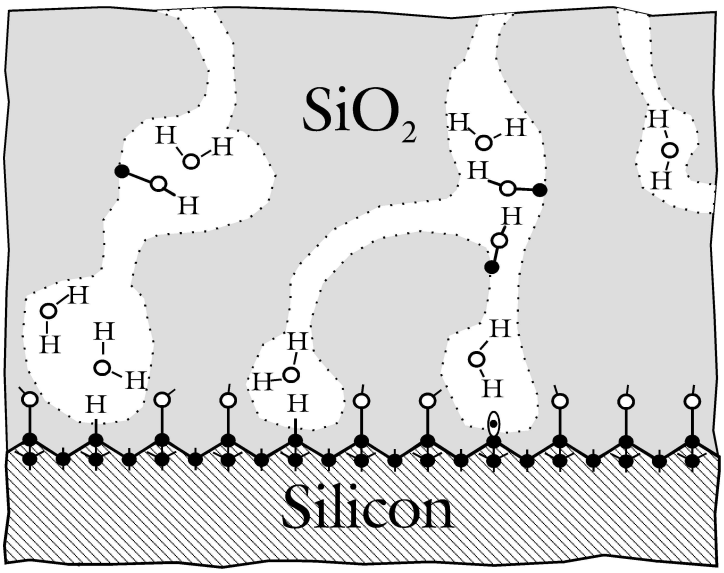

Figure 1.4: *Passivation of Si dangling orbitals (P_b centers) at the Si-SiO_2 interface by water molecules. On the other hand water can dissolve to SiOH groups in the oxide. After [Po95].*

oxygen exchange between water molecules and the silica matrix. In fact it was found using isotope studies that such oxygen exchange takes place [Pf81]. The process of water molecule diffusion, water molecule dissolution and defect center passivation was reviewed by Helms *et al* 1994 and Poindexter 1995 [He94, Po95]. It is pointed out by Poindexter that despite the outstanding importance of the subject, systematic research on the complex interplay of the mentioned processes has never been done and only fragmental knowledge has been obtained. This has certainly to do with the complexity of the processes on the one hand and absence of appropriate investigation tools on the other. It should be mentioned that the application of high electric fields in the device or the irradiation during the fabrication process introduce many more effects that are not mentioned here. Finally, the SiOH site can now themselves degrade the oxide gate if hydrogen is released by a thermal process or by irradiation. According to the reaction

$$\text{SiO - H} \quad \longrightarrow \quad \text{SiO}\cdot + \cdot\,\text{H} \tag{1.1}$$

SiO dangling bonds with an unpaired electron that may serve as electron capturers can be formed. In section 3.1.1 it will be shown that the electronic states of such structural anomalies are situated in the electronic band gap of amorphous silica. Hence, if the half-occupied SiO dangling state captures an electron, it operates like an acceptor level in a semiconductor. The electronic properties of the insulator SiO_2 are lost and device failures will occur. Nishikawa *et al* [Ni93] found with ESR spectroscopy that the SiO$\cdot$ defect density in fused SiO_2 is $5{\cdot}10^{16}$ cm^{-3} at a SiOH density of $4{\cdot}10^{19}$ cm^{-3}. An overview on the hydrogen release of SiOH sites in silica is given in [Gr03].

1.2.3 Fuel Cells

It is generally considered that water bearing silicates can serve as proton conductors for example in fuel cells [No99, Sh96]. This is also indicated in figure 2.9. However, the detailed nature of the diffusion process (i.e if the protons are transported by water molecules or diffuse independently) is less important in this context than a high diffusion constant. Indeed it could be shown by Nogami *et al* [No97] that the activation energy for proton conductivity decreases linearly with the logarithm of proton concentration and if molecular water was added the activation energy decreased with the logarithm of the product of proton and water concentration. Starting from this work, efforts are currently undertaken to functionalize silicates in order to achieve faster proton conduction [Mi02].

1.2.4 Optical Wave Guides

Silica glasses are often used as under water waveguides for information transmission. The inward diffusion of sea water and/or hydrogen becomes a concern when hydrogen related defects weaken the intensity of the transmitted signal. Indeed it is known that hydrogen gives rise to rotational absorption bands in the cable [Fr86].

1.3 The Comparison to Sodium Silicates

A class of silicates that has been investigated with success in the past years was sodium silicates of the composition $xNa_2O+(1-x)SiO_2$ [Ho02, Me04]. The mobility of sodium atoms in sodium silicates exceeds the one of the Si-O network by orders of magnitude [Jo51]. It has been assumed in the 1980's by Greaves and Angell *et al* that sodium silicates contain a channel structure in which the sodium atoms diffuse [An82, Gr85] to assure the high mobility. Note that also the addition of sodium oxide to silica causes a viscosity drop similar to the one presented for hydrous silicate in figure 1.3 [Kn94]. Due to the equivalent valence shell configuration of the sodium atom and the hydrogen atom, compositions of the type $xH_2O+(1-x)SiO_2$ ("hydrous silica"), may show equivalent chemical and physical properties to sodium silicates. In particular it is interesting if pathways for diffusion exist also in hydrous silica and if the formation of bubbles could be related to such phenomenon.
Recently, on the experimental side it was predominantly neutron scattering that was able to give new insights into the structure and dynamics of sodium silicate systems, also at elevated temperature [Me02]. Here it is a prepeak in the neutron scattering structure factor at roughly 0.9 $Å^{-1}$ that emerges with the addition of more and more sodium to the silica network. Whereas at room temperature this prepeak is almost invisible it becomes very pronounced at elevated temperatures. This behavior is shown in Figure 1.5 for sodium trisilicate. With the invention of the effective interatomic potential for silica by van Beest *et al* [Be90] and its generalization by Kramer *et al.* [Kr91] the basis for a computational description was set up. The problem regarding sodium silicates remained that with the originally assigned charges of $q_{Si} = 2.4$, $q_O = -1.2$ and $q_{Na} = 1.0$ charge neutrality could not be achieved for sodium silicates. Finally it was Horbach, Kob, and Binder [Ho01] who overcame this problem by introducing distance dependent charges $q_{Na}(r)$ for the sodium atom. It became possible to perform computer simulations for sodium disilicate and sodium trisilicate with 8064 and 8016 atoms, respectively. These simulations could completely confirm the idea of Angell

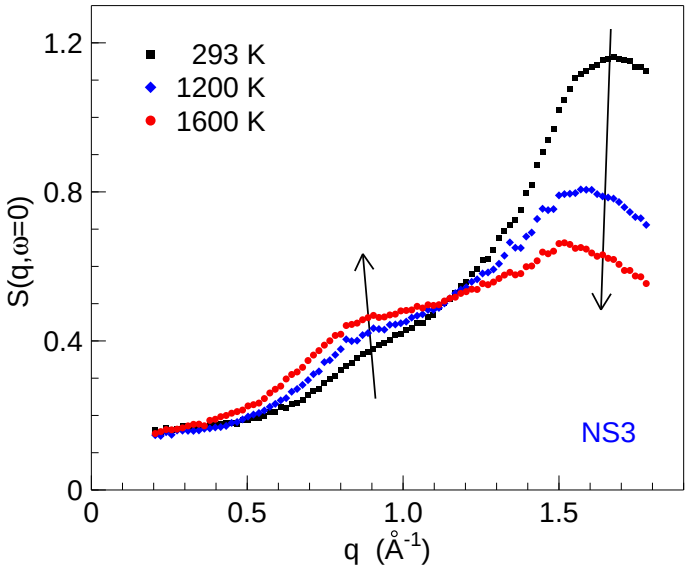

Figure 1.5: *Elastic neutron scattering structure factor for sodium trisilicate dependent on temperature. At high temperatures a prepeak at 0.9 Å $^{-1}$ becomes visible and the first sharp diffraction peak at 1.7 Å $^{-1}$ is suppressed by the Debye-Waller factor.*

et al [An82] for the preferential ion conducting pathways for sodium atoms in the silica matrix. It turned out that that these channels have a characteristic distance of 6-8 Å . The simulations were able to show that this 6-8 Å length scale leads exactly to the the prepeak at 0.9 Å^{-1} in the neutron scattering structure factor and that therefore the prepeak is assigned to the channel network [Me04]. An idea of such channel structure can be obtained from Figure 1.6. Recalling the chemical similarity of sodium and hydrogen regarding the single

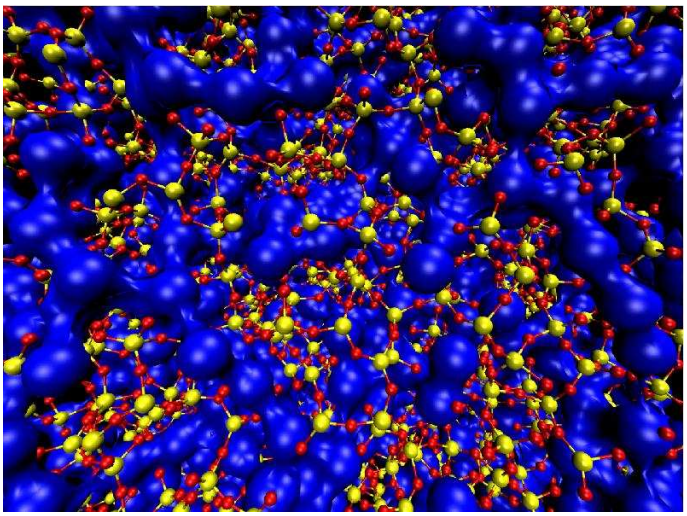

Figure 1.6: *Snapshot of the computer simulation of Horbach et al [Me04]. Sodium atoms (enlarged blue) diffuse in channels in the matrix formed by Si atoms (yellow) and oxygen atoms (red).*

valence shell electron, the question emerges whether water and hydrogen have equivalent relaxation mechanisms compared to sodium. Unfortunately, the research on hydrous silica is confronted with two dramatic restrictions: An appropriate classical potential for silica and water is not known and on the experimental side, it was found that the amount of water dissolved to the silica matrix goes with the square root of pressure [Go31]. Hence, in order to generate samples of hydrous silica that contain as much water as e.g. sodium trisilicate contains sodium, it is necessary to apply pressures in the kbar range. This condition is of course naturally fulfilled in the inner of the earth where magmatic activity takes place, but in the laboratory pressure in these magnitudes, at high temperature, remains an experimental challenge. Table 1.1 summarizes the differences regarding the experimental and theoretical approach to hydrous silica compared to sodium silicates.

	sodium silicate	hydrous silica
suitable interatomic potential	known	not known ($\longrightarrow$ *ab initio*)
experimentally	relatively easy	difficult (pressure)

Table 1.1: *Comparison of sodium silicates and hydrous silica on the experimental and theoretical side.*

The organization of the present manuscript is the following: In chapter 2 the problem of hydrous silicates is reviewed from a classical thermodynamic point of view. The following chapter 3 summarizes briefly the successes and the lacks of previously employed methods of investigation and draws a picture of the current state of the art. The methods for the present work are presented in chapter 4. The setup of the simulation and the experiments is described in chapter 5, results from the computer simulation are shown in chapter 6 and results from the experiments are shown in chapter 7. First comparisons of both are made in the concluding chapter 8.

Chapter 2

The Thermodynamic Problem

2.1 Water Dissolution

If water is added to silica (at any temperature) it is generally not obvious if and how water molecules will dissolve. The silicon atom, as the carbon atom, is four fold coordinated and has in principle affinities to any of silicon, oxygen and hydrogen. Hence the formation of Si-Si, O-O, H-H and Si-H bonds has a priori to be considered as likely as the formation of SiOH groups according to reaction 1.2. However, if a certain analogy to sodium silicates is existing, SiOH groups should be among the dissolution products. Figure 2.1 gives an overview over SiOH gas phase units and their chemistry. The arrows in the figure indicate

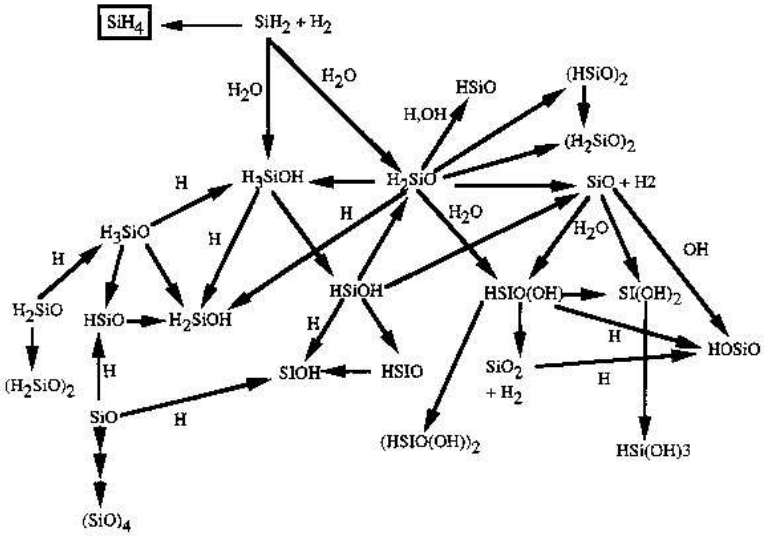

Figure 2.1: *Known gas phase molecules involving silicon, oxygen and hydrogen; after [Za95]. The arrows indicate the direction of an exothermal reaction.*

the directions of the exothermal reactions. Indeed, it can be seen that oxygen-rich and hydrogen-poor species seem to be the energetically preferable states. A brief look at the formation (or bond) enthalpies of several possible units will confirm this picture. Figure 2.2 shows the formation enthalpies of possible structural units in a hydrous silica liquid. The line at 0 kJ/mol separates exothermal ($H^o < 0$) and endothermal ($H^o > 0$) species. Note that endothermal behavior does not necessarily rule out the existence of a structural unit since counterbalancing of coexisting exothermal structural units has to be taken into account. It can be seen from figure 2.2 that a silica tetrahedral network is, at any temperature, an energetically extremely preferable state with formation enthalpies of less than -500 kJ/mol. Also the formation of water is exothermal with a value of -250 kJ/mol at 300 K, but, with

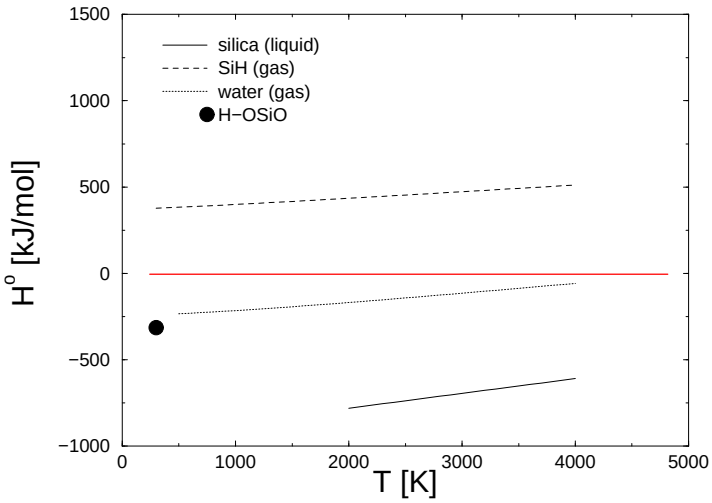

Figure 2.2: *Bond enthalpies of possible dissolution species. After [Ni03, Za95].*

increasing temperature, the formation enthalpy gets close to zero kJ/mol at 4500 K. HOSiO units have a formation enthalpy of -315 kJ/mol [Za95] a value that is located between that of water molecules and the one of a silica tetrahedral network. In fact this shows that it is questionable if a lower energy balance is obtained for coexisting silica and water liquids (summing up a very low and a rather high formation energy), or the dissolution of water to OSiOH units as indicated in Figure 1.2.

The formation of SiH units would also require the rupture of the silica tetrahedral network at a very high energy cost. Since the SiH formation to counterbalance is then higher than the SiOH formation enthalpy, the formation of SiH instead of SiOH is not very likely.

Silicate-water systems are often described as *mixtures between two liquids* [Bu71, Bu94, Oc97, Ri96, Sc96, Ze96, Tu48, Wa57]. On the other hand it is known that over large temperature scales neither of the two compounds is a liquid. Under ambient pressure conditions the fluid range of water (0^oC to 100^oC) is far away from that of any silicate having liquidus temperatures of usually more than 1000^oC. From this point of view it becomes quickly evident that the *mixture of liquids* concept will have its strict limitations by the inventions of vapor and solid phases and that temperature and especially pressure will govern the miscibility.

However, basic thermodynamic features of the system will be revealed by a *mixture of liquids* model as presented in the following section.

2.1.1 Silicate-Water Systems as Regular Solutions

[1] Within the fundamental work of Wasserburg [Wa57] it became evident that classical thermodynamics is able to predict the impact of pressure and temperature on the composition of these melts.

This theory represents in principle the application of the Flory-Meyer theory for polymer solutions [Fl42, Me35] on the wet silicate problem. The basic idea of this theory is that a certain volume element can be either occupied by a water molecule or a SiO_2 unit. Like atoms in real gases, solvent (water) molecules cannot occupy sites that are already occupied by SiO_2. In the Flory-Meyer approach for polymer solutions, this matter of fact is usually

[1] The expression "regular" was formed by Hildebrand [Hi16].

referred to as "excluded volume". The main idea of Wasserburg is that each of the SiO_2 units can share a fraction $\overline{r}$ ($0 \leq \overline{r} \leq 2$) of its two oxygens with a water molecule. Each of the total volume sites N can carry one of the N_2 SiO_2 units or, $N_1 = N - \overline{r}N_2$ water molecules. Hence there are

$$\begin{aligned} N = &\quad N_1 + \overline{r}N_2 &&\text{ways of placing the first water molecule} \\ N-1 = &\quad N_1 + \overline{r}N_2 - 1 &&\text{ways of placing the second water molecule} \\ N-2 = &\quad N_1 + \overline{r}N_2 - 2 &&\text{....the third ...} \end{aligned}$$

the total number of possible choices Ω is given by the binomial coefficient

$$\Omega = \begin{pmatrix} N_1 + \overline{r}N_2 \\ \overline{r}N_2 \end{pmatrix} = \frac{(N_1 + \overline{r}N_2)(N_1 + \overline{r}N_2 - 1)....(\overline{r}N_2 + 1)}{N_1!} \tag{2.1}$$

Using Stirling's approximation, the (mixing) entropy $S_m = R \ln \Omega$ of the system can be

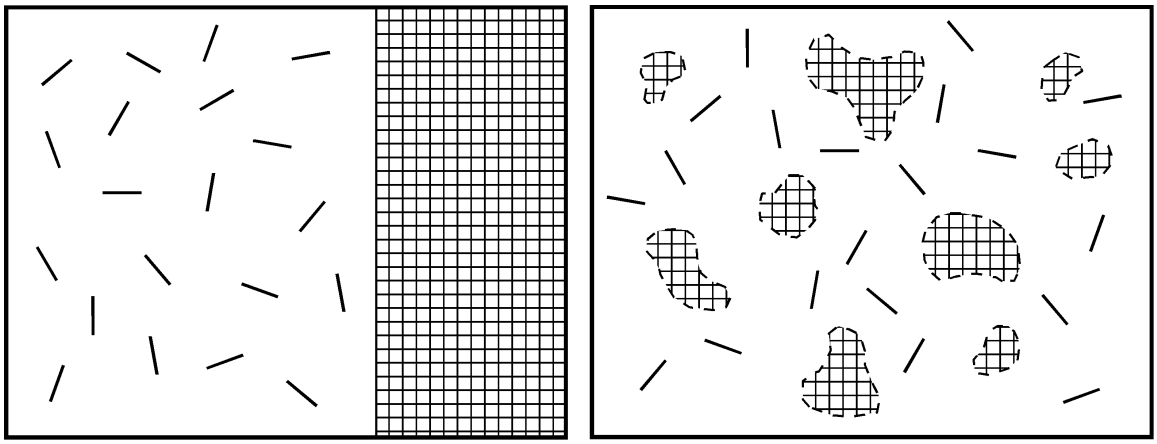

Figure 2.3: *Two dimensional model of water speciation in a silicate; $Si-O-Si$ bridge positions (dashes) and water positions (squares);* **left***: before water dissolution, water positions are collected on the right hand side;* **right***: after water attack some bridge bonds are broken and water positions are distributed in a random array. No Further assumptions are made in this model [Wa57].*

written as

$$s_m = -RN_1 \ln \frac{N_1}{N_1 + \overline{r}N_2} - R\overline{r}N_2 \ln \frac{\overline{r}N_2}{N_1 + \overline{r}N_2} \tag{2.2}$$

or, for the mixing entropy per unit cell S_m in terms of molar fractions

$$\overline{x} = \frac{N_1}{N_1 + \overline{r}N_2} \qquad \text{and} \qquad 1 - \overline{x} = \frac{\overline{r}N_2}{N_1 + \overline{r}N_2} \tag{2.3}$$

the simple expression

$$S_m = -R\overline{x} \ln \overline{x} + R(1 - \overline{x}) \ln (1 - \overline{x}) \tag{2.4}$$

remains. Inspection of equations 2.2 and 2.4 shows that S_m is the entropy of an ideal mixture of N_1 water molecules and $\overline{r}N_2$ molecular segments, or, in other words the perfect solution of the oxygen atoms of H_2O and the bridging oxygens in the silicate.
Taking into account interactions between particles in the melt (i.e. dealing with non-ideal mixtures), activity coefficients γ_i replace the activities a_i of a melt component i in the ideal solution

$$\gamma_i = \frac{a_i}{\overline{x}_i} \tag{2.5}$$

where $\overline{x}_i$ is the molar fraction of the component. In these terms the Gibbs free energy of mixing is [St89] for a n-component system

$$\Delta G_m = \overline{x}_1 RT \ln \gamma_1 + \overline{x}_2 RT \ln \gamma_2 + ... + \overline{x}_n RT \ln \gamma_n \tag{2.6}$$

Using the *regular solution equation* for binary mixtures $RT \ln \gamma_i = B\overline{x}_j^2$ [Hi16], the Gibbs free energy of mixing can be rewritten as

$$\begin{aligned} \Delta G_m &= B(\overline{x}_1\overline{x}_2^2 + \overline{x}_1^2\overline{x}_2) + RT(\overline{x}_1 \ln \overline{x}_1 + \overline{x}_2 \ln x_2) \\ &= B\overline{x}(1-\overline{x}) + RT(\overline{x} \ln \overline{x} + (1-\overline{x}) \ln (1-\overline{x})) \end{aligned} \tag{2.7}$$

again making use of $\overline{x}_1 = \overline{x}$ and $\overline{x}_2 = 1 - \overline{x}$ since the mixture is binary. From of the basic equation for chemical thermodynamics

$$\Delta G = \Delta H - T\,\Delta S \tag{2.8}$$

related to 2.7 and 2.4, the first term in 2.7 can be revealed as the enthalpy contribution to the Gibbs free energy:

$$\Delta H_m = B\overline{x}(1-\overline{x}) \tag{2.9}$$

It can be shown that for some value of x the Gibbs free energy of mixing ΔG_m is negative for any value of B. This can be interpreted in the way that each pair of two liquids A and B is mixable to some extent, which might be tiny as will be shown for the silica water case, or, unlimited like in the sodium chloride water case. However, equation 2.7 demonstrates that the miscibility is governed by the *temperature dependent* interplay between the enthalpy and the entropy. The actual value of the constant B has to be deduced by fits to experimental data. At this point it becomes decisive whether B is positive or negative:

1. Positive B's

For high temperatures only one minimum of the Gibbs free energy exists. The two liquids

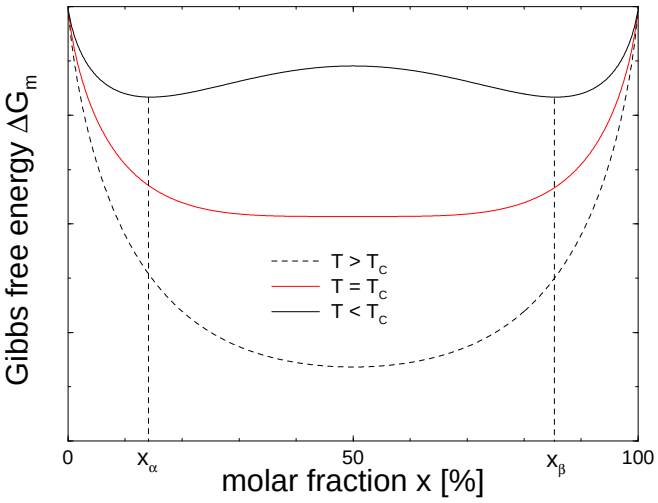

Figure 2.4: *Temperature dependence of the Gibbs free energy after equation 2.7 for $B \geq 0$. For high temperatures only one minimum with an equilibrium composition exists, whereas for temperatures below a critical temperature T_c two minima occur.*

are mixable to any extent. For temperatures below a critical temperature T_c, the energy of the system can be decreased most if the two compositions x_α and x_β (and hence two phases) corresponding to the two minima of G_m are realized. For any imposed composition $x_\alpha \leq x \leq x_\beta$ the system will aim for a more preferable state and return to the equilibrium

concentrations x_α and x_β. A *miscibility gap* emerges.
Figure 2.5 shows the resulting solubility curve. For any temperature below T_c the system will separate if the composition of the mixture is such that $x_\alpha \leq x \leq x_\beta$. Two equilibrium phases, one rich of A and one B rich will form.

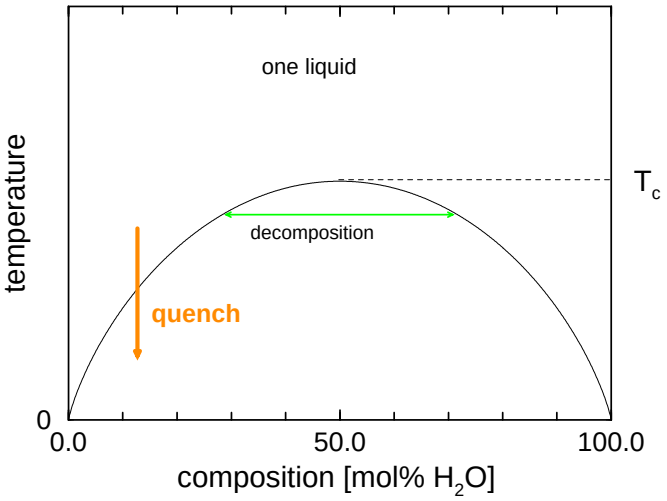

Figure 2.5: *Solubility curve corresponding to the Gibbs free energy after equation 2.7. For temperatures and compositions below the curve, the system will decompose in two phases. Rapid quenches freeze the mixture and suppress the separation.*

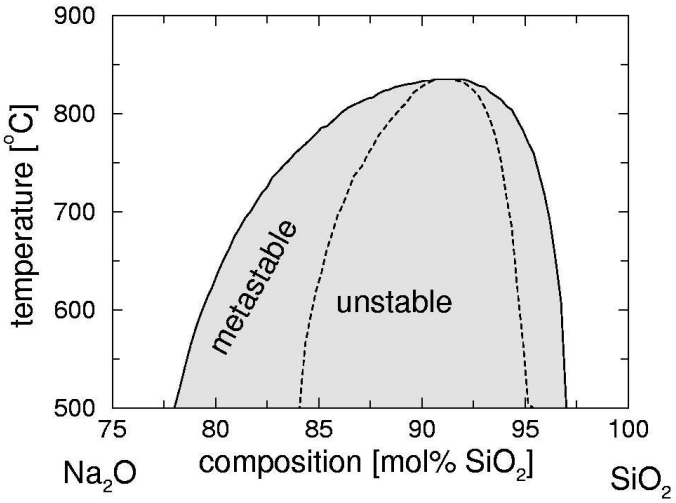

Figure 2.6: *Solubility gap in sodium silicate after [Re68].*

2. Negative B's
For $B \leq 0$ for any temperature only one minimum is present. Liquid immiscibility does not occur and the two compounds are mixable to any extent at any temperature.

The thermodynamic behavior of various silicate-water compositions seems to be quite different. In particular the systems silica-water and sodium-silicate-water seem to show a $B \geq 0$ behavior and hence a liquid miscibility gap [Tu48, Ke62, Sh64], whereas sodium aluminosilicate systems show a $B \leq 0$ behavior with continuous miscibility [Ze96, We94, Wa57].
Due to the high pressures and temperature ranges involved, the exploration of the entire curves for SiO_2-H_2O is very difficult. For the system SiO_2-Na_2O the exploration is much easier. The curve is shown in figure 2.6. Though having started the above derivation of the

solubility thermodynamics from a model of silica and water, it turned out to be equivalent to that of any pair of liquids with a miscibility gap. To conclude, it should be mentioned that the physics of the miscibility gap is the one of a spontaneously broken symmetry, a phenomenon that this widely known in several disciplines of physics. The most prominent examples are the broken O(3) symmetry of ferromagnetism or the broken chiral $SU(2)_L \times SU(2)_R$ in quantum chromo dynamics. The analogy to such general phenomena leads necessarily to the question if and how the results -especially the formation of two phases and the existence of a critical temperature- hold for silicate water systems?

2.1.2 Deviations from the Regular Solution Concept

As already mentioned, complications plug in at this point since the solution does not behave regularly in any pressure and temperature range. Crystallization and/or the formation of dry amorphous phases will occur at low temperatures and the question of the existence of the above described two liquid or one liquid phases arises. As will be seen below, usually water is kept fluid (or at least as a dense gas) under high pressures in the kilobar range and is pressed into the dry silicate (crystal) causing a depression of its freezing point. Therefore at least a phase with two liquids is experimentally accessible. This two liquid phase will have a lower boundary to the dry crystalline/amorphous phase and an upper boundary to the one liquid phase. The position of the lower boundary (in the dry case the silicate's liquidus temperature) will be governed by the freezing point depression under water addition. This behavior was investigated by Wasserburg [Wa57].

2.1.3 Phase Diagrams

Due to the numerous phases (fluid, crystalline, amorphous,..) and phase transitions, the phase diagrams of the silicate water systems are usually rather complicated. The limitation to two dimensions enforces projections to either the pressure-temperature plane, the pressure-composition or the temperature-composition plane. To provide systematic access, the diagram of silica-water (which is presented in Figure 2.7) is discussed first.
The main feature of the diagram in the pressure-temperature representation is the melting relation. The first two kbar pressure shift the liquidus temperature of silica from 1720^{o}C to 1120^{o}C. Further pressure decreases the liquidus point just slightly. On the right side of this melting line a water rich and a silica rich liquid (according to section 2.1.1) can coexist with a crystalline phase. Due to these three phases, the area is usually denoted as the *three phase region* and the melting (liquidus) curve as the *three phase boundary*. At the left side, of the melting relation quartz is in equilibrium with only one fluid phase, a water rich liquid. This region is denoted as the *two phase region*. As indicated in figure 2.7, only samples from the three phase region can be quenched to glass containing ambient mixtures. At 9.7 kbar and 1100^{o}C a critical end point is found, corresponding to the critical temperature of figures 2.4 and 2.5. The two immiscible liquids of the three phase region merge to one as described in section 2.1.1. The critical temperature T_c of this dissolution gap is strongly pressure dependent. It is 1100^{o}C at 9.7 kbar and should increase as pressure is decreased. Unfortunately no data is available on this pressure dependence of T_c. The temperature-composition and pressure-composition projections have so far only been investigated along the three phase boundary.

The measured pressure composition diagram along the three phase boundary is similar to a diagram such as proposed in figure 2.5 if the critical temperature is replaced by a critical pressure. For a given volume, the easiest and worst way to do this is to use the ideal gas law. The thermodynamics of these systems has been experimentally intensively investigated in the 1950's and 1960's. How many phases are actually in equilibrium with each other depends on the composition of the silicate. For silica three crystalline phases are known.

The phase diagrams for sodium silicate - water and albite - water systems are naturally

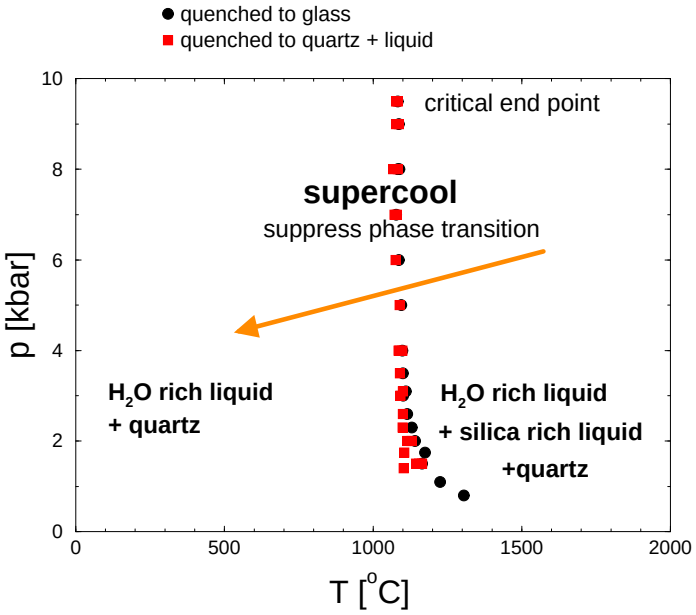

Figure 2.7: *p-T projection of the phase diagram for the system SiO_2-H_2O. Circles correspond to samples quenches with variable contents of hydrous glass, dots correspond to quenches to quartz and a water-rich liquid. In order to obtain hydrous glasses, it is necessary to supercool from points right of the p-T limit for hydrous glasses, the so called three phase boundary. After [Ke62].*

much more complicated. They can be found in references [Tu48] and [We94], respectively.

2.2 Water Diffusion

Two different kinds of diffusion play a role in hydrous silicates: diffusion due to an entropy gradient (also known as *self*-diffusion) and diffusion due to chemical bond energy gradients (also known as *uphill*-diffusion).

Self diffusion processes occur also in chemically homogeneous solids. It will be demonstrated in section 2.3 that in particular the second type of diffusion is responsible for water release in magmas and associated phenomena.

2.2.1 Fundamentals of Diffusion Processes

The mathematical theory of diffusion in isotropic substances is based on the hypothesis that the particle flux J through a unit area of a cross section is proportional to the concentration gradient C measured orthogonal to this cross section. Hence:

$$J = -D\frac{\partial C}{\partial x} \tag{2.10}$$

D is called the diffusion coefficient. The fundamental differential equation of diffusion in an isotropic medium can be obtained considering the flux through the faces $dxdy$, $dydz$, and

$dxdz$ of a volume element. The differential equation obtained this way is given by

$$\frac{\partial C}{\partial t} = D\,\nabla^2 C \tag{2.11}$$

The three dimensional generalization of equations 2.10 and 2.11 are usually referred to as Fick's first and second law of diffusion [Cr75].
The diffusion of atoms in an isotropic liquid or solid results from a random movement. This motion is usually called a random walk process. Each diffusional jump is independent of all others. The analysis of such random walk processes leads to a flux in one dimension that can be expressed as follows:

$$J(x,t) = C\frac{\langle x\rangle}{t} - \frac{\langle x^2\rangle}{2t}\frac{\partial C}{\partial x} + \mathcal{O}(\langle x^3\rangle) \tag{2.12}$$

Here x is the displacement of one atom and $\langle x\rangle$ and $\langle x^2\rangle$ are averaged and the squared averaged displacement (or mean square displacement) of all atoms, respectively. For the case of an isotropic three-dimensional liquid $\langle x\rangle = \langle y\rangle = \langle z\rangle = 0$ and $\langle r^2\rangle = \langle x^2\rangle + \langle y^2\rangle + \langle z^2\rangle = 3\langle x^2\rangle$ equation 2.12 reduces to Fick's first law with the self diffusion coefficient

$$D = \lim_{t\to\infty}\frac{\langle x^2\rangle}{2t} = \lim_{t\to\infty}\frac{\langle r^2\rangle}{6t} \tag{2.13}$$

Equation 2.13 is called the *Einstein* diffusion equation. The average distance that an atom diffuses in time t is approximately given by $L = \sqrt{\langle x^2\rangle} \sim \sqrt{Dt}$.

2.2.2 Self-Diffusion

Figure 2.8 visualizes the self-diffusion as a thermally activated process. At a finite temperature an atom can jump to a neighboring site at distance a with a reaction rate $R(T)$. In order to perform such jump the energy barrier E_a has to be overcome.

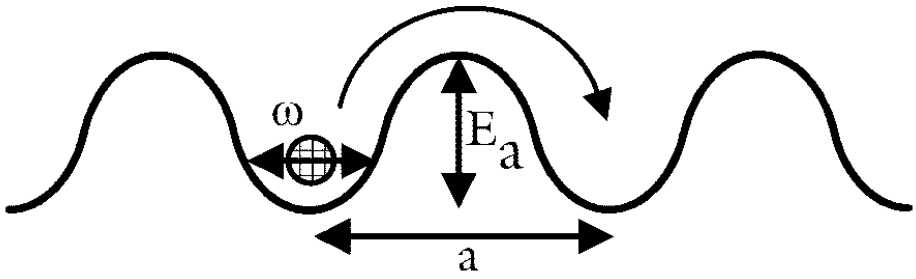

Figure 2.8: *Potential barrier and activation energy E_a for an atom jump to a suitable neighbor site. The atom vibrates with the frequency ω.*

The rate $R(T)$ is proportional to the vibrational frequency of the atom ω and a Boltzmann factor

$$R(T) \approx \frac{\omega}{2\pi}\exp\left(-\frac{E_a}{k_B T}\right) \tag{2.14}$$

where T is the absolute temperature. Equation 2.14 has the general form of a thermally activated process which is usually described with an Arrhenius law.
If in this simple one dimensional model $R/2$ of the jumps are to the right and $R/2$ are to

the left, the net flux between two potential minima in Figure 2.8 in positive x-direction is given by

$$J = -\frac{aR}{2}\frac{dN}{dx} = -\frac{a^2R}{2}\frac{dC}{dx} = -D\frac{dC}{dx} \tag{2.15}$$

where the one dimensional concentration $C(x)$ is given by $C(x) = N(x)/a$. D is the so called diffusion constant or diffusivity which is usually given in units of $[\mathsf{m}^2/\mathsf{s}]$. From 2.14 and 2.15 one reads off

$$D(T) = \frac{a^2R(T)}{2} \approx \frac{a^2\omega}{4\pi}\exp\left(-\frac{E_a}{k_BT}\right) \tag{2.16}$$

In the liquid state, the above described hopping like diffusion is accompanied by uncorrelated collisions of atoms. The atoms are confined in nearest neighbor cages and by collisions cages are ruptured, allowing a displacement motion. The transition from the liquid like diffusion to the hopping processes in the solid is usually referred to as the glass transition. The behavior of the cage rupture in viscous liquids and its relation to the glass transition is theoretically well described by the so called mode coupling theory [Go92]. Liquid like diffusion leads to deviations from the Arrhenius law (Eq. 2.16) for the diffusion constant.

2.2.3 *Uphill*-Diffusion in Hydrous Silicates

If water is not randomly distributed in a silicate, or external conditions like pressure and temperature are changed, diffusion processes other than self-diffusion will govern the the behavior of the mixture.

In order to quantify the water speciation, it is useful to define a chemical standard equilibrium constant K (see for example [St89]) for the reaction indicated in Fig. 1.2:

$$\mathsf{Si\text{-}O\text{-}Si} + \mathsf{H_2O} \longleftrightarrow 2\ \mathsf{Si\text{-}O\text{-}H} \quad \text{with} \quad K = \frac{C^2(\mathsf{OH})}{C(\mathsf{H_2O})} \tag{2.17}$$

where C(OH) is the concentration of SiOH groups in the glass and C($\mathsf{H_2O}$) is the concentration of molecular water. Since the concentration of lattice groups Si-O-Si remains nearly constant in the range of 0-10 mol.% water, it is omitted from the equilibrium constant K.

Since a chemical reaction is involved, the *uphill*-diffusion of water molecules in a silicate network cannot be considered to obey the above given standard Fick's diffusion laws. Due to the reaction of 2.17, water molecules become immobilized. At this point it becomes evident that at least two diffusion constants are necessary to describe water diffusion in silicates, one for water molecules and one for OH groups. It is also clear that, the one for water molecules will be higher.

Extensions of Fick's second law to the case of partial immobilization of the diffusing species are known [Cr75]. In the simplest case, the concentration of immobilized substance $C(\mathsf{OH})$ is directly proportional to the concentration of molecular water $C(\mathsf{H_2O})$, i.e. $C(\mathsf{OH}) = R\,C(\mathsf{H_2O})$. The extended diffusion law is then given after Crank [Cr75]

$$\frac{\partial C(\mathsf{H_2O})}{\partial t} = D_{\mathsf{H_2O}}\,\nabla^2 C(\mathsf{H_2O}) - \frac{\partial C(\mathsf{OH})}{\partial t} \tag{2.18}$$

The equilibrium constant K (Eq. 2.17) can be introduced into the extended diffusion equation 2.18. The gradient of the water concentration ∇C can be calculated for Eq. 2.17 as

$$\nabla C(\mathsf{H_2O}) = \frac{2C(\mathsf{OH})}{K}\nabla C(\mathsf{OH}) \tag{2.19}$$

In non-equilibrium (water dissolution process) it is appropriate to assume that $\partial C(\mathsf{OH})/\partial t > \partial C(\mathsf{H_2O})/\partial t$ [Do95], and equation 2.18 becomes therefore

$$\frac{\partial C(\mathsf{OH})}{\partial t} = \nabla \left[\frac{2C(\mathsf{OH}) D_{\mathsf{H_2O}}}{K} \nabla C(\mathsf{OH}) \right] \tag{2.20}$$

Equation 2.20 has the form of Fick's second law (2.11) with the concentration-dependent effective diffusion coefficient

$$D_{\text{eff}} = D_{\mathsf{H_2O}} \frac{2C(\mathsf{OH})}{K} \tag{2.21}$$

As predicted above, it turns out that the real (or effective) diffusion constant for OH groups D_{eff} is different from the one for water molecules $D_{\mathsf{H_2O}}$. The shape of the diffusion profile $C(\mathsf{OH}, \mathbf{r}, t)$ was investigated by Doremus [Do69]. It was found that the shape is quite different from the one for a regular Gaussian diffusion profile, but fits much better to experimental data [Do69].

The diffusion constants of water diffusion and release in the silicate melt are mostly deduced from the associated relaxation times. Relaxation times for water release in liquids are experimentally accessible by the measurement of the relaxed Newtonian shear viscosity η_N and the un-relaxed elastic shear modulus G_∞[2] with the Maxwell relationship [Di95, Go92]:

$$\tau = \frac{\eta_N}{G_\infty} \tag{2.22}$$

The shear viscosity is hence proportional to the relaxation time τ. The proportionality G_∞ is usually approximated as a constant [Di90]. Relaxation times of hydrous species in silicate melts were reviewed by Dingwell in 1995 [Di95]. Figure 2.9 shows relaxation times in water bearing rhyolite [3]. According to the above theory, relaxation times for the silicate matrix

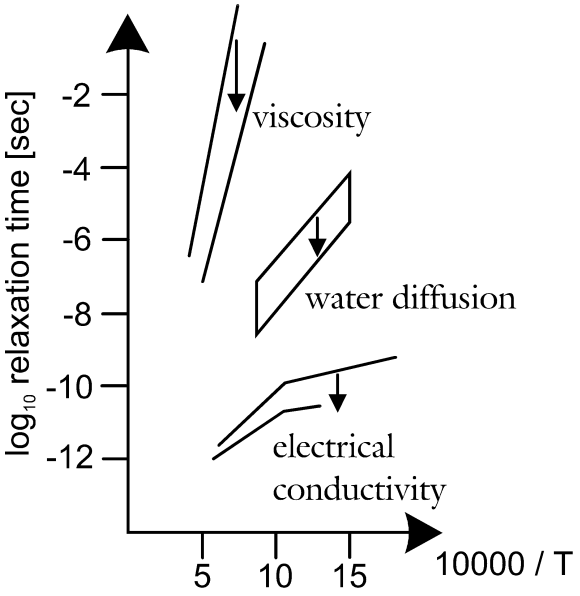

Figure 2.9: *Relaxation map of water bearing rhyolite. Three regions are distinguished: viscous relaxation, molecular water mobility and proton mobility (electrical conductivity). The arrows indicate increasing water content. After [Di95].*

and water molecules are situated in two different domains. A third domain with much smaller relaxation times is ascribed to proton transport in the liquid that leads to electrical conductivity.

[2] The index ∞ refers to the modulus above α resonance [Go92].

[3] For the composition of natural rocks see appendix C.

2.3 Water Release

It seems plausible that a re-exsolution of the successfully dissolved water (and hence phenomena like bubble formation and explosive volcanism) is possible if temperature and pressure conditions of the system are changed after the dissolution process. It is clear that such a release can only take place if the dynamics of the hydrogen atoms decouples from the dynamics of the silicate matrix. This can happen in the solid state (below the glass transition temperature T_g) if the sample is exposed to stresses such as radiation as well as in the melt above T_g. Whereas the exsolution in the solid was important in section 1.2.2, the exsolution in the liquid state is discussed in the following:
Most of the established models for water release in melts suffer from certain number of parameters that have not been measured yet due to the difficulty of in-situ measurements at elevated pressures and temperatures. In addition the microscopic origin of the bubbles is not yet understood and the models are limited to the growth and the stability of the bubbles [Sa99]. Therefore it will be an essential point of this thesis to understand the initialization of the water release on an atomic level.
Figure 2.10 shows the approach suggested by Proussevitch *et al* [Pr98]. The main idea is to model an isolated spherical bubble surrounded by a viscous liquid. This model reduces the number of parameters considerably since only one (the radial) direction is taken into account. Once the bubble is initialized its life is determined by several physical conservation laws and the bubble radius $R(t)$ of the growing (or shrinking) bubble and its velocity $v(t)$ are the parameters of interest. The underlying conservation laws shall be presented here:

Continuity equation and momentum conservation
The "first principles" for any kind of flow are the continuity equation

$$\mathsf{div}\mathbf{J} + \dot{\rho} = 0 \tag{2.23}$$

(with the density ρ and the mass flux $\mathbf{J}$) and the momentum conservation

$$\rho\frac{dv}{dt} = -\nabla p + \partial_k \tau_{ik} \tag{2.24}$$

with the radial velocity v, the pressure p and the stress tensor τ_{ik}. For Newtonian liquids, the stress tensor can be related to the liquid's viscosity and the integration of 2.24 with appropriate boundary conditions for a spherical bubble yields the pressure equilibrium

$$p_b = p_a + \frac{2\sigma}{R} - 4vR^2\int_{z(R)}^{z(\infty)}\eta(z)dz \tag{2.25}$$

with the bubbles gas pressure p_b, the external (ambient) pressure p_a, the pressure due to the surface tension $p_\sigma = 2\sigma/R$ and the dynamic pressure caused by the work performed on a viscous liquid. The abbreviation z stands for r^{-3} and r is the usual radial coordinate.

Mass balance and diffusion
At the bubble interface the volatile diffusion must be balanced against the volatile mass flux in the melt. Hence

$$\frac{dm}{dt} = 4\pi R^2\mathbf{J} \tag{2.26}$$

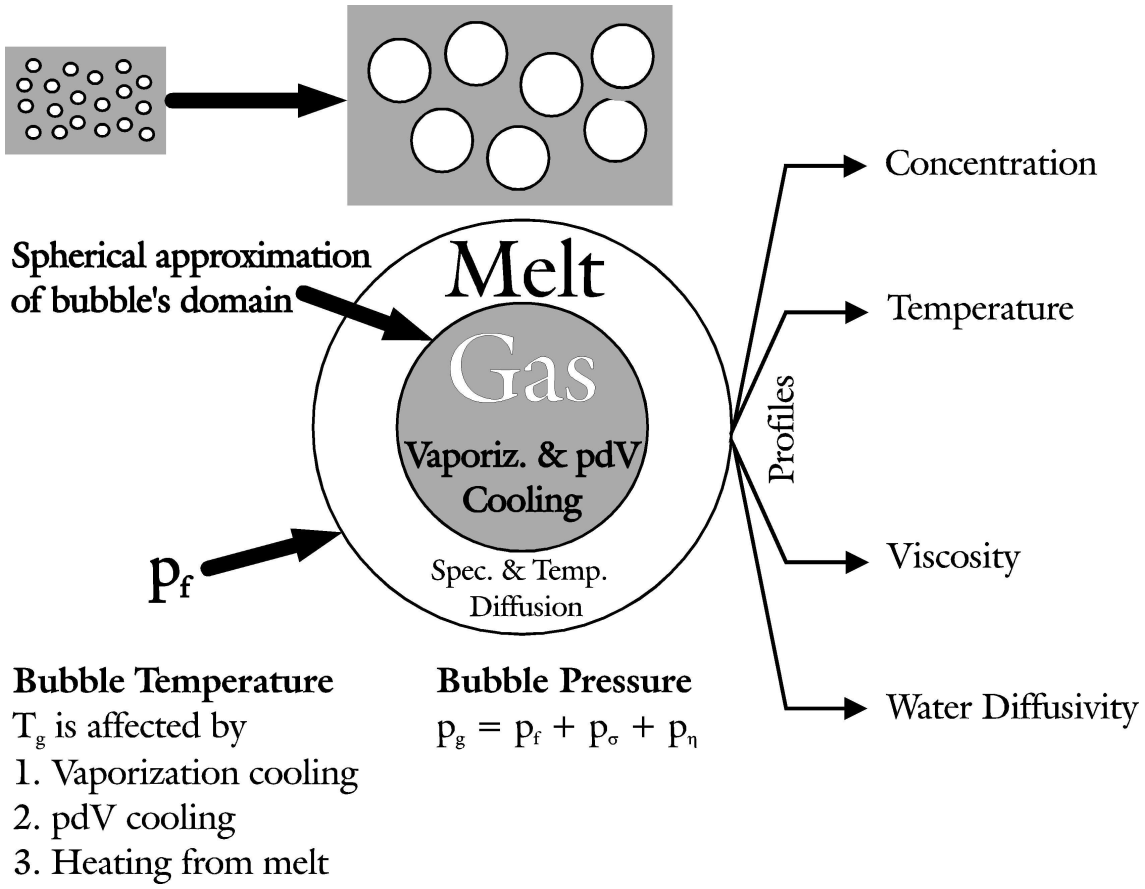

Figure 2.10: *Bubble Growth Model (BGM) after Proussevitch [Pr98]. The time evolution of bubbles depending on temperature, pressure, melt composition is modeled. These decisive variables are driven by numerous processes. The bubble temperature is affected by vaporization cooling, work of isobaric expansion (pdV) and heating from the melt heat reservoir. The total pressure of the gas in the bubble is the sum of the ambient pressure p_f, the contribution of the bubble's surface tension p_σ and the resistance of the melt upon gas diffusion p_η. Aiming for mass and heat balance at the bubble interface, and a volatile diffusion obeying a diffusion equation, equilibrium profiles for the volatile concentration C, the temperature T, viscosity η and water diffusivity D_{H_2O} as well as the bubble radius can be obtained from the model [Pr98].*

Modeling water as an ideal gas (which is considered to be an appropriate approximation in the melt [We76]) the bubble radius can be directly related to the diffusion constant D of the volatile in the melt. The diffusion equation itself becomes in spherical coordinates for spatially variable water concentration

$$\frac{\partial C}{\partial t} + v\frac{\partial C}{\partial r} = \frac{1}{r^2}\frac{\partial}{\partial r}\left(Dr^2\frac{\partial C}{\partial r}\right) \tag{2.27}$$

Heat balance
The total enthalpy H^o of the system is composed of several contributions (1) the enthalpy $m_b c_p dT$ of the bubble gas (2) cooling due to gas volume expansion at bubble growth (3) cooling due to latent heat of the volatile exsolution and (4) heating due to heat flux from the melt. Heat balance in the bubble requires

$$dH^o = 0 \tag{2.28}$$

Again, expressing the contributions (1)-(4) in terms of an ideal gas and spherical coordinates, the heat conservation can be written in terms of calculable variables and measurable constants. Problems show up at this point since experimental data such as heat capacities of the volatile in the melt have not been measured yet.

Thermal conductivity
The equation for heat transport can be modeled with a Fourier-Kirchhoff equation for incompressible fluids

$$\rho c_p \frac{dT}{dt} = \mathsf{div}(\kappa\ \mathsf{grad}\ T) + \frac{1}{2\eta}(\tau_{ik})^2 + dQ_{vt} \tag{2.29}$$

The first term of the right of equation 2.29 is the normal expression for the thermal conductivity. The second term on the right takes into account dissipative heating processes due to the viscous resistance of the liquid. The third term, Q_{vt} is the latent heat of a optional phase transition (crystallization or vitrification) of the liquid. The dissipative term can be expressed in spherical coordinates and hence be related to r and v. The only unknown parameters entering this expression remain therefore the heat capacity c_p and the latent heat Q_{vt}.

These conservation laws govern in principle the bubble life. The temperature dependent viscosity can be modeled with an Arrhenius behavior. The diffusion constant is found with the equilibrium constant of the water speciation reaction and a reference value. The following table shows what such a model is really able to perform: It gives an overview over the required input parameters and the obtained quantities

required input	output parameters
ρ density	T temperature
η viscosity reference	p pressure of the gas
σ surface tension	C volatile concentration in the melt
c_m heat capacity of the melt	η viscosity of the melt
c_p heat capacity of the gas	D volatile diffusion constant
Q_{vt} heat of vitrification	R bubble radius
T_g vitrification temperature	v expansion velocity
K_H Henry's constant (relates the volatile concentration at the bubble surface to the bubble pressure)	
χ heat diffusion constant	

It was shown by Proussevitch *et al* [Pr98] that the above mentioned equations can be integrated numerically and solutions for stable bubbles can be obtained. Figure 2.11 shows for example the dependence on the final bubble radius on the initial temperature of the rhyolite[4] melt. It can be seen clearly that bubbles can grow faster at higher temperature since

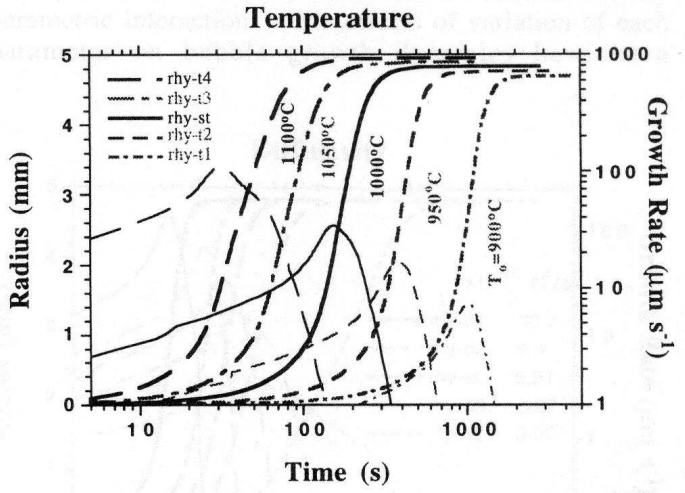

Figure 2.11: *The effect of initial temperature on the bubble radius dependent on time for a magma. Higher temperatures lead to lower viscosities and therefore higher water diffusivities. Thin lines indicate corresponding growth rates. After [Pr98].*

the resistance caused by viscosity is significantly smaller (equation 2.25). The final bubble radius depends slightly on the temperature due to thermal expansion of the gas (equation 2.28). A nice microscope image of a bubble in a natural silicate rock is shown by Navon *et al* [Na98].

[4]For the composition of natural rocks see appendix C

Chapter 3

Methods of Investigation

The aim of this chapter is to give an overview of theoretical end experimental methods for the investigation of hydrous silicates. The history of the application of the particular method and its suitability are briefly discussed.

3.1 Theoretical Methods

3.1.1 *Ab Initio* Approaches

Despite of the demanding computational effort, *ab initio* methods started to be applied very early to hydrous silicate systems. Interestingly, many *ab initio* studies have an industrial rather than an academic origin. The early investigations were mainly driven by the interest of the semiconductor industry as demonstrated in section 1.2.2. The first *ab initio* study is the one of Bennett and Roth which goes back to the year 1971 [Be71]. The investigations were based on an extended Hückel approach [Hu31]. Despite the rudimentary electronic structure method at fixed atomic positions, Bennett and Roth were able to explain basic features of defect states in amorphous silica. Studies based on tight binding methods [As76] which seemed to confirm the ideas of Bennett and Roth followed in the 1980's [Re83, Ro88]. At that time one had already a detailed picture of the electronic structure of amorphous SiO_2 and how defects, also defects related to water, influence the electronic structure. It became indeed evident that the structural defects mentioned in section 1.2.2 produce electronic states in the band gap of amorphous silica and hence degrade the electronic insulating properties. The situation of several defect states in the electronic band gap of silica is illustrated in figure 3.1. Note that in particular the -O^o dangling bond defect is related to the presence of water. It was also in the 1980's when the first investigations based on Hartree and Hartree Fock frameworks appeared. With the development of *ab initio* packages as GAUSSIAN in the 1990's [Ga90], much more systematic studies became feasible. In addition, the computational power allowed equilibrium geometries of molecular fragments to be computed directly from the electronic structure. It was Pelmenschikov *et al* [Pe97] who first compared the results of Hartree Fock based calculations to structures of the same clusters obtained using a density functional framework (DFT) [Ko65]. The predominant accuracy of (DFT) with respect to Hartee Fock based approaches was commonly recognized in the 1990's. Hence it is understandable that DFT is the basis of nearly all modern work on the subject. The current understanding of hydrous silica from the *ab initio* point of view is presented by Bakos *et al* [Ba02, Ba03, Ba04].

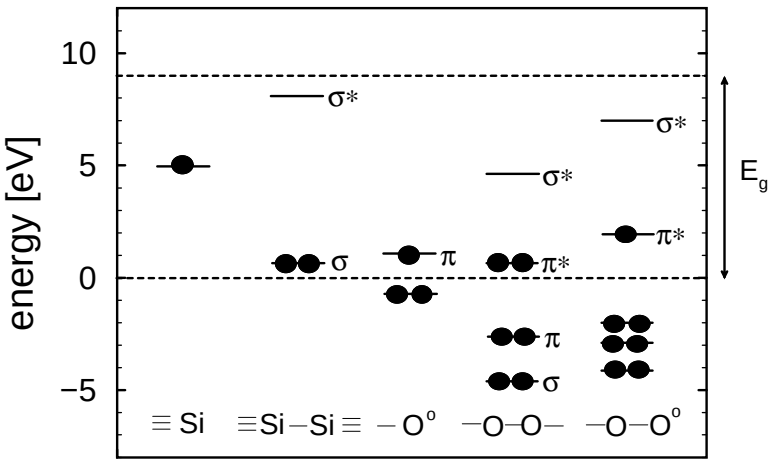

Figure 3.1: *Electronic states in the electronic band gap of amorphous SiO_2 associated to several structural defects. The band gap is situated between the two dotted lines. The black dots refer to electrons. Fully occupied orbitals are filled with two dots (after [Ro88]).*

The latter studies place water and oxygen molecules at several positions of a silica network and determine the dissolution of the molecules to the matrix with geometry optimizations by means of energy minimization. The authors were able to obtain activation energies for diffusion of a water molecule dependent on the ring sizes. It was found that water molecules exhibit an energy barrier for diffusion of 0.8-0.9 eV in six and seven membered rings of the silica network. As soon as the water molecules encounter a smaller ring, the activation energy for diffusion increases rapidly to more than 2 eV. Hence it becomes more likely for a water molecule to react with the silicate matrix by the formation of two SiOH groups as demonstrated in figure 1.2. The ratio between SiOH groups and water molecules in the structure is accordingly determined by the fact if all water molecules had enough time to diffuse to a less than six membered ring. Such an idea leads finally to the question of an equilibration time. The studies of Bakos *et al* refine also the picture of defect creation and annihilation [Ba04] and the associated consequences for the electronic states (figure 3.1) [Ba03].

3.1.2 Classical Molecular Dynamics

An instructive review on classical molecular dynamics computer simulations and its application to silicate melts was given by Poole *et al* [Po99]. The motion of the nuclei in a solid is determined by the properties of the electronic structure as will be extensively discussed in section 4.3. However, the most important features of the vibrations in a solid can be obtained without detailed knowledge of the electronic properties. The only thing that is required in order to deduce vibrational properties is an (approximate) idea of the shape of the electrostatic energy surface throughout the solid (usually referred to as a "potential"). In this section the effort made in order to find suitable potentials for water bearing silicates is briefly reviewed.

The discussion should be started by the consideration of pure silica. Several interatomic potentials for silica have been proposed among which the one proposed by van Beest *et al* [Be90] turned out to be one of the best [Ko99]. In this potential the interactions Φ_{IJ} between the ions I and J at a distance r are given by

$$\Phi_{IJ} = \frac{q_I q_J e^2}{r} + A_{IJ}\exp(-B_{IJ}r) - \frac{C_{IJ}}{r^6} \tag{3.1}$$

where e is the electronic charge. The constants are given by $A_{SiSi} = 0.0$ eV, $A_{SiO} = 18003.7572$ eV, $A_{OO} = 1.388.7730$ eV, $B_{SiSi} = 0.0$ Å^{-1}, $B_{SiO} = 4.87318$ Å^{-1}, $B_{OO} = 2.76000$ Å^{-1}, $C_{SiSi} = 0.0$ eVÅ^{-1}, $C_{SiO} = 133.5381$ eVÅ^{-1}, $C_{OO} = 133.5381$ eVÅ^{-1} [Be90]. The partial charges are $q_{Si} = 2.4$, $q_O = -1.2$, and e^2 is given by $1602.19/(4\pi 8.8542)$ eVÅ. The remarkable property of the van Beest's potential (BKS potential) is that it contains only two-body terms and it is nevertheless able to describe a disordered tetrahedral network. Indeed it could be shown that the competition between the different two body terms mimic the three body forces [Vo96]. From the computational point of view the lack of three body contributions is well appreciated since three-body interactions are costly to evaluate.
It was already mentioned in the introduction that the BKS potential has been extended to alumino-silicates by Kramer, de Man, and van Santen [Kr91] and it was Horbach and Kob [Ho01] who found an appropriate modification of Kramer's potential in order to describe sodium silicate systems. According to the already mentioned analogy between sodium silicates and hydrous silica systems, a similar adaption of Kramer's potential to hydrous silica could be envisaged. Unfortunately this idea is rather bad, since the O-H interaction -in contrast to the O-Na interaction - was approximated by an effective oxygen O_H in the approach of Kramer *et al.* A rupture of an OH bond or a formation of a water molecule is hence naturally not accessible with the potential of Kramer *et al.* Clearly this means that despite the chemical similarity of sodium and hydrogen, the two atoms are completely differently implemented in the BKS potential, making an adaption possible for sodium silicates only.
The remaining way to go would now be to try an adaption of a three body potential to hydrous silica. Two kinds of three-body potentials have been adapted to hydrous silicates.

Hill and Sauer Hill used the method illustrated in figure 3.2 to adjust appropriate molecular dynamics potentials for zeolites [Hi94]. Hill's method consists of an iteration of results obtained from *ab initio* calculations. These results are fitted to a molecular potential expression of the consistent force field (CFF) type [Ma90]. The so generated potential is used to perform a molecular dynamics whose structural results are compared to the original *ab initio* results. The parameters for the potential are refined until the desired accuracy is reached. The quality of the obtained potential was not tested within the present work.

Garofalini Garofalini and coworkers tried to merge a Born-Meyer-Huggins (BMH) ionic potential [Fe89] for the silica part with a Rahman-Stillinger-Lemberg (RSL2) water potential [St78]. The potential seems to work satisfactorily for the description of polymerization reactions of silica sols [Fe90], but seems to perform badly for basic structural features of silica [Be04].

Summarizing the simulation work on the subject, it should be pointed out that it can be considered to be relatively hard to construct a suitable potential. The reason for this are the many different forms in which water can exist in the silicate network (SiOH groups, free water molecules, dissolved water molecules...). On the other hand no *ab initio* molecular-dynamics simulation has been applied yet. Note that an *ab initio* simulation and its structural and dynamical results would also be a highly appreciated basis in order to construct a potential.

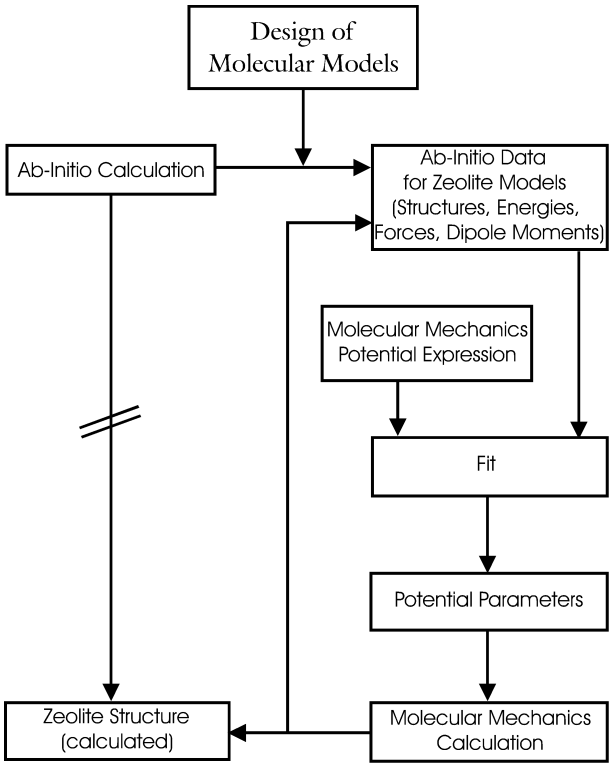

Figure 3.2: *Method used by Hill et al to predict zeolite structures. After [Hi94].*

3.2 Experimental Tools

3.2.1 Light Scattering

If an incident monochromatic light beam hits an isolated molecule J with a polarizability tensor α^J, the electric field $\mathbf{E}$ of the incident light induces a dipole moment

$$\mathbf{m}(t) = \alpha^J \cdot \mathbf{E}(t) \tag{3.2}$$

which varies with time. The spectral density of scattered light can be expressed as [BP76]

$$I_{if}(\mathbf{q},\omega) = \left[\frac{I_o k_f^4}{16\pi^2 r^2 \epsilon_o^2}\right] \frac{1}{2\pi} \int_{-\infty}^{\infty} dt\, e^{-i\omega t} \langle \delta\alpha_{if}^*(\mathbf{q},0)\, \delta\alpha_{if}(\mathbf{q},t)\rangle \tag{3.3}$$

where

$$\delta\alpha_{if}(\mathbf{q},t) = \sum_{J=1}^{N} \alpha_{if}^J\, e^{i\mathbf{q}\cdot\mathbf{R}_J(t)} \tag{3.4}$$

is the component of the polarization fluctuation tensor α_{if} along the initial i and the final f polarization directions of the light. The intensity 3.3 has the characteristic λ^{-4} dependence and the attenuation in space which goes as r^{-2}, where r is the distance from the sample. I_o is the incident intensity and ϵ_o the vacuum dielectric constant.
The polarizability component α_{if}^j is regarded as the sum of two contributions: (i) the polarizability of the molecule in its equilibrium position with a displacement $u = 0$, and (ii) the term linear in vibrational displacements $u \sim \exp(i\Omega t)$ [BP76]. Therefore equation 3.3, will consist of four terms. One term contains only the rigid molecule polarizability, two cross terms containing both, polarizability and displacements, and a quadratic term with the vibrational displacements. The contributions from the polarizability changes involve

changes of molecular orientation and translations. This type of scattering is usually called *Rayleigh-Brillouin* scattering. The scattering arising from the vibrational contributions (ii) is usually referred to as the *Raman* spectrum. A mode is Raman allowed if

$$\left(\frac{\partial \alpha_{if}}{\partial u}\right)_{t=0} \neq 0 \tag{3.5}$$

The Raman terms give rise to frequency shifts to $\omega + \Omega$ and $\omega - \Omega$ which are called the Stokes and anti-Stokes band. The frequency displacements of Raman shifts are usually in the range of 100 to 4000 cm^{-1}. These frequencies are much higher than those related to the equilibrium position polarizabilities arising from (i).
From the above presentation it is already clear that light scattering is not able to scan all vibrational modes in the solid and certain selection rules will apply. A review of infrared and Raman modes in hydrous silicates is given in [Da96b]. In the following the main ideas and problems of the two types of light scattering applied to hydrous silicates are discussed.

Infra Red Spectroscopy The main idea of infrared spectroscopy is to determine the absorption of infrared light. This absorption is measured in terms of an imaginary refraction index $\hat{n}$ where $\hat{n} = n' + in''$ with the ordinary refraction index n' and the extinction coefficient n''. Since the complex refraction index is the square root of the (complex) dielectric constant, $\hat{n} = \sqrt{\epsilon}$ where $\epsilon = \epsilon' + i\epsilon''$ the following relations emerge:

$$\begin{aligned} \epsilon' &= n'^2 - n''^2 \\ \epsilon'' &= 2n'n'' \end{aligned} \tag{3.6}$$

The complex dielectric constant is then proportional to $I_{if}(\mathbf{q}, \omega)$ as given in equation 3.3. Several ways exist to determine ϵ''. The most common are the measurement of n'' by direct absorption of infrared light and the so called Fourier Transform Infra Red Spectroscopy (FTIR).
Once the spectrum is obtained, the peaks have to be related to the concentration of SiOH and H_2O units. That this is a rather arbitrary task has already been discussed by Kohn [Ko00]. Indeed several groups seem to have different ways of processing data. For example it is controversial if the peak heights or the area under the peak is the quantity of interest for the concentration. If the area is chosen as a criterion, the subtraction of a baseline becomes crucial. Here Stolper [St82] and Zhang [Zh97] used a baseline fit by the eye, whereas Behrens *et al* [Be96] used a linear extrapolation from different parts of the spectrum. To conclude, it should be pointed out that infrared spectroscopy is nevertheless a suitable method for the investigation of hydrous silicates and in the literature there exists a broad agreement that different hydrous species such as hydroxyl groups and water molecules can be clearly distinguished with this tool [Da96a].
A particular problem regarding a possible speciation change with temperature arises from the temperature dependence of the dielectric constants itself. Clearly this means that a change in the recorded spectrum does not necessarily need to be due to a speciation change of the dissolved water. This behavior was first recognized and systematically investigated by Behrens *et al* in 2003 [Be03].

Raman Spectroscopy In contrast to IR spectroscopy, Raman spectroscopy provides mainly information on the silicate matrix of a hydrous silicate. Although the OH stretch

vibrations can be clearly identified at roughly 3500 cm^{-1} they do not really provide structural information about the speciation of the OH groups. A review on Raman spectra of dry glasses was provided by McMillan [Mi84], stimulated by the early work of Stolen and Walrafen [St76]. A very detailed analysis of the spectra of water containing silicate glasses is given by Mysen and Virgo [My86]. Raman spectroscopy was able to identify the vibrations of silicate and aluminosilicate tetrahedron with varying numbers of non-bridging oxygen sites. However, some Raman bands are still not assigned to vibrations. A severe problem of Raman spectroscopy is the overlap of numerous bands of a spectrum. Such overlapping requires under-determined deconvolutions of a spectrum, a process that leads to disagreements and over-interpretations of studies between different groups [Ko00]. Nevertheless it should be pointed out that Raman spectroscopy is a suitable tool for high temperature and high pressure studies since the laser can be focused on the small cell geometries that are used in high temperature and pressure apparatus.

3.2.2 Nuclear Magnetic Resonance

Nuclear Magnetic Resonance (NMR) is one of the most powerful tools to analyze molecular structures. It measures the chemical shift on the energy spectrum of a nucleus that is due to its chemical environment. The chemical shift is then recorded with respect to a reference. The most common reference is tetra methyl silane (TMS). In contrast to any light scattering technique (where the scattering arises from the total electronic density), NMR is element specific. Most of the nuclei involved in hydrous silicates have suitable NMR isotopes. A further plus of NMR spectroscopy is that it is quantitative to a much higher accuracy than light scattering where the exact determination of the peak heights causes problems. In addition NMR is capable of probing a variety of dynamic processes in a sample. Nevertheless NMR can only hardly be applied at elevated temperatures and pressures.
Mainly three types of NMR spectroscopy are applicable and have already been applied to hydrous silicates: ^{29}Si NMR [Fa87, Ku92], ^{1}H NMR [Ko89, Ku92] and ^{17}O NMR [Ma98]. It was in particular the study of Farnan *et al* [Fa87] performed with ^{29}Si (magic angle spinning) MAS NMR that gave a very clear picture of water speciation in hydrous silica. It could be clearly demonstrated that four coordinated silicon atoms Q^4 are converted to Q^3-OH and at high water concentrations to Q^2-$(OH)_2$. Relating the data to the highest theoretical possible value of OH groups, it was possible to extract a ratio between dissolved and molecular water. The data could be roughly confirmed by the ^{1}H NMR studies of Kohn *et al* [Ko89]. According to the study of Kümmerlen *et al* [Ku92] the same ratios are present in hydrous sodium silicates.

3.2.3 X-Ray and Neutrons

The application of X-Ray diffraction on hydrous glasses is rather limited by the small scattering factor of hydrogen (due to the low electronic density of the hydrogen atom). Nevertheless impacts of water on the position of the first sharp diffraction peak (FSDP) of silica were revealed with X-Ray diffraction [Zo92, Hi85]. It has already been pointed out by Kohn [Ko00] that it is very difficult to extract reliable structural information from the radial pair distribution functions obtained from X-Ray diffraction, since they contain contributions from all

atoms in the glass. The analytical power of such studies is therefore limited.
Neutron diffraction provides similar correlation functions. The absolute values of the coherent neutron scattering length of hydrogen ($b_{coh} = -3.741 \cdot 10^{-15}$ m) and its isotope deuterium ($b_{coh} = 6.674 \cdot 10^{-15}$ m) are close to the ones of silicon ($b_{coh} = 4.149 \cdot 10^{-15}$ m) and oxygen ($b_{coh} = 5.805 \cdot 10^{-15}$ m). Therefore the structure factor for neutron scattering is more sensitive to hydrogen than that of X-rays. Even if concrete structural information is hard to obtain, comparisons of the pure and hydrous materials can be made. Zotov *at al* compared neutron scattering structure factors for dry and deuterated sodium tetra-silicate [Zo96]. It could be confirmed in this study that the structure factor of the silicate is only slightly influenced by the presence of water. Note that nevertheless the viscosity drops rapidly upon water addition (see figure 1.3).

3.3 Vibrations

Once a potential energy function for a structure is theoretically found (by means of *ab initio* calculations or by classical molecular dynamics), the vibrational properties can be determined in the so called harmonic approximation as presented in the following. The vibrational properties can therefore be considered as the intersection point between experiment and theory.
For sufficiently small displacements $s_{I,\alpha}$ from the equilibrium position $R^o_{I,\alpha}$the total potential energy of the system $\Phi(R_{I,\alpha})$ can be expanded in a Taylor series

$$\Phi(R_{I\alpha}) = \Phi(R^o_{I\alpha}) + \sum_{\alpha,I}^{3,N} \underbrace{\frac{\partial \Phi(R^o_{I\alpha})}{\partial R_{I\alpha}}}_{=0} s_{\alpha I} + \frac{1}{2} \sum_{\alpha,I}^{3,N} \sum_{\beta,J}^{3,N} \underbrace{\frac{\partial^2 \Phi(R^o_{I\alpha})}{\partial R_{\alpha I} \partial R_{\beta J}}}_{\Phi_{\alpha\beta}(R^o_I, R^o_J)} s_{\alpha I} s_{\beta J} + O(3) \tag{3.7}$$

The first term in 3.7 is the potential at the equilibrium position, the second term is zero per definition. The derivatives $\Phi_{\alpha\beta}(R^o_I, R^o_J)$ are usually referred to as coupling or force constants. Since third and higher order effects are neglected in 3.7 it is called the *harmonic approximation*. Vibrational effects that need to be described by higher terms are usually called *anharmonic effects*.
The equations of motion read then in harmonic approximation

$$M_I \ddot{s}_{\alpha I} = -\frac{\partial \Phi(R_{I\alpha})}{\partial s_{I\alpha}} = -\sum_{\beta,J}^{3,N} \Phi_{\alpha\beta}(R^o_I, R^o_J) s_{\beta J} \tag{3.8}$$

This is a set of $3N$ coupled differential equations. The plane wave ansatz

$$s_{\alpha I} = \frac{1}{\sqrt{M_I}} u_{\alpha I}(\mathbf{q}) e^{i(\mathbf{q}\mathbf{R}_I - \omega t)} \tag{3.9}$$

leads to the eigenvalue problem

$$-\omega^2 u_{\alpha_I}(\mathbf{q}) + \sum_{\beta J} \underbrace{\frac{1}{\sqrt{M_I M_J}} \Phi_{\alpha\beta}(R^o_I, R^o_J) e^{i\mathbf{q}(\mathbf{R}_I - \mathbf{R}_I)}}_{D^{\alpha\beta}_{IJ}(\mathbf{q})} u_{\beta J}(\mathbf{q}) = 0 \tag{3.10}$$

which has a solution if the secular determinant vanishes:

$$det\left\{D_{IJ}^{\alpha\beta}(\mathbf{q}) - \omega^2\, 1\right\} = 0 \tag{3.11}$$

The matrix $D_{IJ}^{\alpha\beta}(\mathbf{q})$ is the so called dynamical matrix. The $3N$ eigenvectors and 3N eigenfrequencies of the system are hence obtained by the diagonalization of the dynamical matrix. In this formalism the eigenvectors $\{\mathbf{e}^k\}$ are $3N$ component vectors ($k = 1, ..., 3N$). The real space vectors $\mathbf{e}_I^k$ ($I = 1, ..., N$) are proportional to the displacement $\mathbf{u}_I^k$ of atom I. The $3N$ space eigenvectors satisfy the ortho-normality and closure conditions:

$$\sum_I \mathbf{e}_I^k \mathbf{e}_I^{k'} = \delta_{kk'} \tag{3.12}$$

$$\sum_k \mathbf{e}_{\alpha I}^k \mathbf{e}_{\beta I'}^k = \delta_{\alpha\beta}\delta_{II'} \tag{3.13}$$

Having obtained the eigenvalues ω_k and the eigenvectors $\mathbf{e}_I^k$ it becomes possible to define widely used quantities in order to describe the vibrational properties of a solid: The vibrational density density of states (vdos)

$$g(\omega) = \frac{1}{3N}\sum_{k=1}^{3N}\delta(\omega - \omega_k) \tag{3.14}$$

and the partial vibrational density of states (pvdos) with respect to atom type a

$$g_a(\omega) = \frac{1}{3N}\sum_k \sum_{I\epsilon a} |\mathbf{e}_I^k|^2 \delta(\omega - \omega_k) \tag{3.15}$$

Definitions 3.14 and 3.15 imply the relation

$$g(\omega) = \sum_a g_a(\omega) \tag{3.16}$$

The *vibrational spectrum* is composed by the well explored one of the silicate matrix (1meV to 160meV) [Be02, Mi84, Zo01a] and the additional modes of OH and H_2O [Ho96, Mi86, My86, Si89, St82]. The vibrational spectrum of amorphous SiO_2 is shown in Figure 3.3 as obtained from classical and *ab initio* molecular dynamics simulations and a neutron scattering experiment. The composition of the vibrational spectrum of amorphous SiO_2 of bend and stretch vibrations has been analyzed by Taraskin *et al* [Ta97a]. According to this study it is the SiO bending and rocking components that principally form the vdos curve in the range between 0 meV and 100 meV, whereas the stretch vibrations are responsible for the broad asymmetric peaks at 120 meV and 140 meV. Ispas *et al* studied the effect of the addition of sodium oxide on the vibrational spectrum of amorphous SiO_2 [Is03]. They find a vibrational spectrum also in the range of 1-150 meV for sodium tetra-silicate but with a dramatically altered shape.

The vibrational spectrum of the silicate matrix has now to be accomplished by the vibrational excitations of water. Vibrations of water are preferably characterized in crystalline or amorphous solid phases. Figure 3.4 shows the vibrational excitations as obtained from a neutron scattering experiment in two forms of crystalline ice. It should be generally recognized that vibrational excitations differ only little between the many forms of ice that are

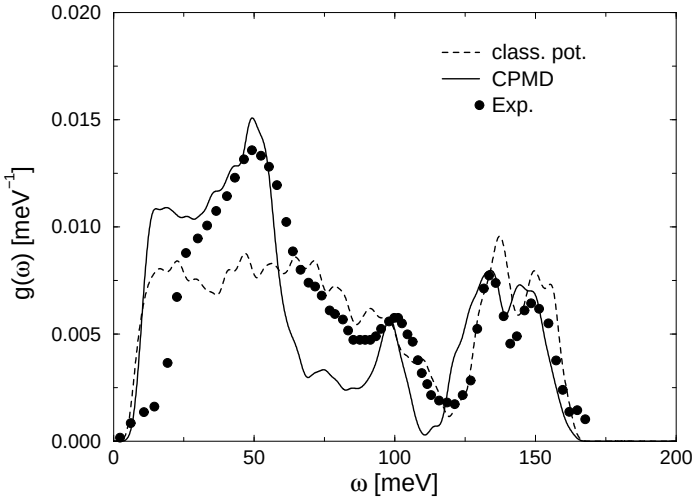

Figure 3.3: *Vibrational density of states of amorphous SiO_2 as obtained from a classical MD simulation, an ab initio simulation using the Car-Parrinello method and a neutron scattering experiment. After [Be02].*

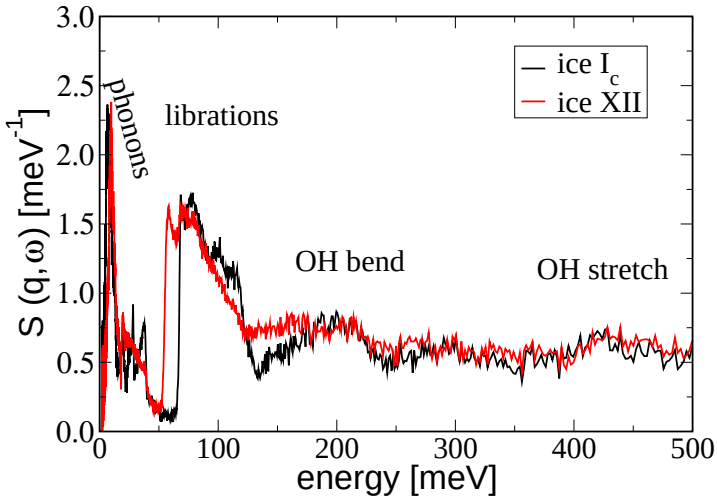

Figure 3.4: *Neutron scattering structure factor of two different types of crystalline ice as obtained from neutron scattering. From [Ko01].*

known today. However, in liquid water the characteristic excitations are smeared out. In figure 3.4 one can clearly distinguish several regions of vibrational excitations of ice. The crystalline phonons are located in a range between 0 and 40 meV. Internal vibrations of the water molecules are represented by the OH bend vibrations (140 meV -240 meV) and the OH stretch vibrations (380 meV - 460 meV). It is clear that vibrational excitations are for molecules accompanied by rotational bands. A precursor for rotational excitations in a dense crystalline or amorphous structure are the so called librations. These librations are situated between 50 meV and 130 meV as can be seen from figure 3.4.

3.4 Conclusion and Synthesis

3.4.1 Summary of the Previous Work

Driven by the recognition of the fundamental importance of water for the viscosities of silicates melts, the above tools have been extensively applied to the subject. As demonstrated above, many experimental techniques have already been employed to get insight into dissolution mechanisms and structural features of water in silicates. Considerable progress was made over the years with these methods but nevertheless almost all seem to lack at one or

the other point and "unresolved peaks" remain.
On the simulation side, dynamical approaches are absent. Thus, comparisons to experimentally recorded vibrational spectra do neither exist. In literature it is generally accepted that

- according to figure 1.2, water is found in at least two chemical different forms in silicate melts, namely water molecules and SiOH groups
- the equilibrium 1.2 is strongly influenced by the total amount of water (see [Di90] for data of albite)

In particular Raman and infrared spectroscopy suggest that for total water concentrations smaller than 3wt.% SiOH groups are the dominating dissolution species and for concentration greater than 3wt.%, H_2O molecules become more numerous than SiOH units.
On the other hand, neither a clear picture of the diffusion reactions of water and hydrogen nor an idea of diffusion constants do exist. Questions of the position of the balance 1.2, dependent on temperature, pressure and silicate composition as well as the initialization of the bubble formation are not understood and are still debated.
The aim of the present work is to provide explanations for these questions with molecular dynamics computer simulations and neutron scattering techniques.

3.4.2 The "hydrous silicate area"

Before employing any further experimental or theoretical method to the subject of hydrous silicates it is necessary to have an idea where typical vibrational excitations and typical space correlations are found in such system.
The "hydrous silicate area" has to be such that the complete *vibrational spectrum* and *diffusional motions* are covered. The vibrational spectrum of pure SiO_2 and water were discussed in section 3.3. It became evident that the principle excitations of silica and water are situated between 0 and 160 meV. Stretch vibrations of OH bonds have energies of more than 350 meV. Between 240 meV and 350 meV no significant vibrations can be expected.
Figure 2.9 proposes relaxation times for an extended temperature scale between 10^{-8}s and 10^{-5}s. The assumption of an equivalent channel relaxation behavior as was observed for sodium atoms (see section 1.3) gives rise to a range of typical space correlations of roughly 6 Å . Taking into account the different size of the hydrogen atom and also a different affinity to certain atoms, it seems realistic to assume a relaxation structure for hydrogen atoms between 2 Å and some 10 Å.
Figure 3.5 gives an overview over accessible time and space ranges by each method and relates these to problem specific frequencies and interatomic distances of hydrous silicates as discussed above.

3.4.3 New Approaches

Figure 3.5 indicates that space and time correlations of interest for hydrous silicates should be accessible with molecular dynamics simulations.
The section for water relaxation dynamics is naturally more challenging from the simulation point of view since relatively large space correlations have to be covered, a fact that imposes

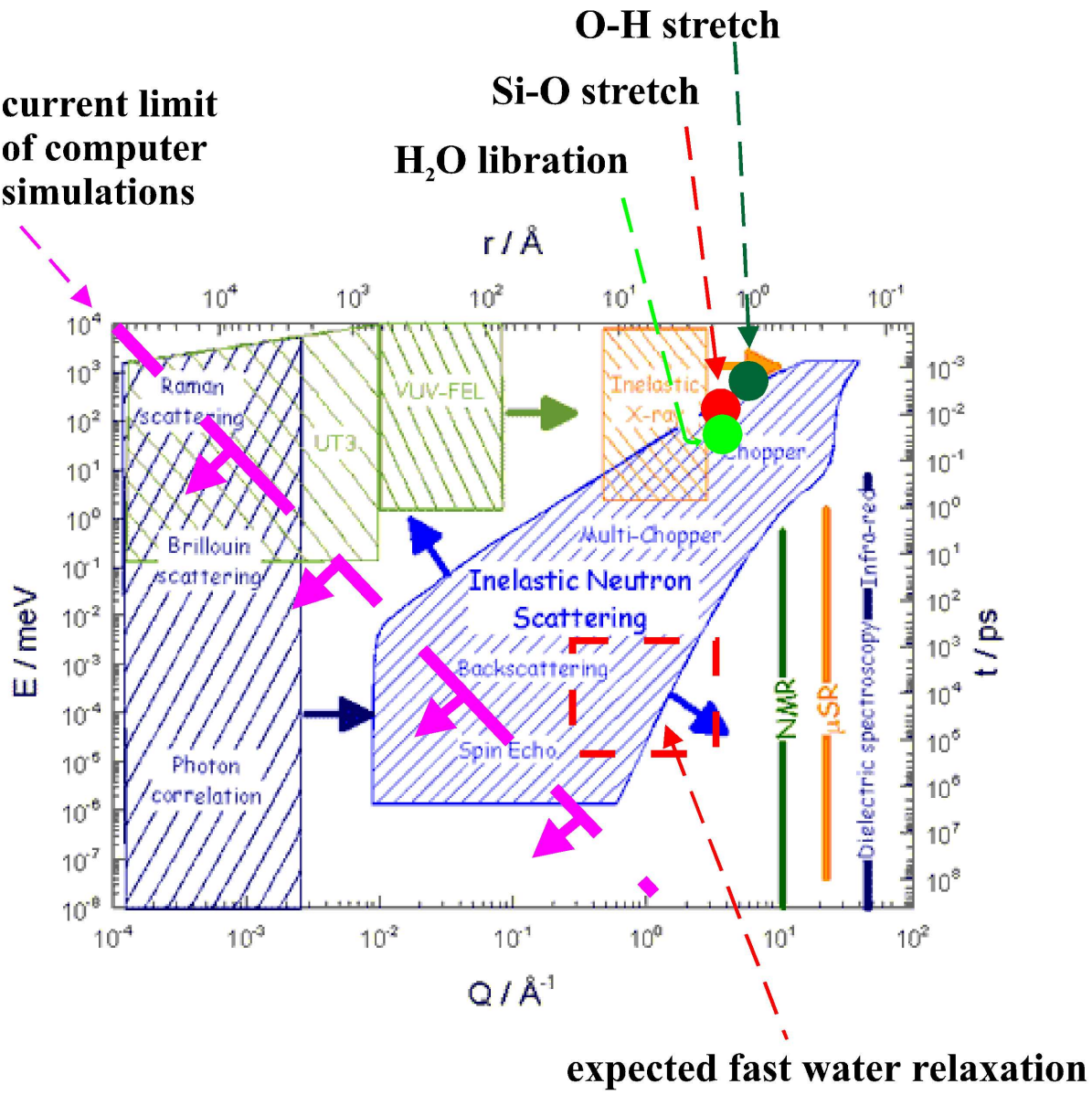

Figure 3.5: *Overview of time and space ranges covered by several experimental tools and computer simulations. Techniques that do not directly provide distance information are indicated only as bars parallel to the time axis. Arrows show zones to which techniques are aimed to be extended. All correlations situated right of the purple line are accessible with present day's computers. Both, the position of typical vibrational frequencies as well as the area where one expects water diffusion are accessible with neutrons and molecular dynamics techniques. After [ESS02].*

a large simulation box. The interesting space correlations are nevertheless at least one order of magnitude within the current limit. The situation for time correlations is even better. This opens in principle the use of "luxury" methods such as *ab initio* approaches.
On the experimental side the instruments of a neutron scattering center like the Institute Laue-Langevin (ILL) are able to cover the interesting regions. An exception may be the OH stretch vibrations at several hundred meV that are hardly accessible with neutrons. Since Raman scattering turned out to be capable of resolving these vibrations the lack of a neutron scattering description is acceptable. Apart from a relatively good coverage of the interesting time and space correlations, neutrons have further well appreciated advantages for the investigation of hydrous silicates:

- Neutrons are sensitive to the complete vibrational spectrum from 0 to roughly 150 meV. Selection rules for specific modes that govern the Raman spectra do not apply for neutrons. Furthermore, as it will be shown in section 4.2, quantities that can be easily related to a true vibrational density of states can be extracted from neutron signals. Note that this quantity is directly comparable to results extracted from molecular dynamics simulations.

- Neutrons are not sensitive to the electronic density in the solid, which would be very low for the case of hydrogen. Neutrons have, on the opposite a very high sensitivity to hydrogen atoms, a fact that is reflected by the very high neutron scattering cross section of hydrogen ($\sigma_s = 81.67$ barn) compared to those of silicon ($\sigma_s = 2.173$ barn) and oxygen ($\sigma_s = 4.234$ barn). In addition, the hydrogen isotope deuterium has a rather low scattering length. This opens in principle the possibility of extracting the contributions of the protons to the vibrational spectrum. The higher nuclear mass of deuterium can give interesting insights into the speciation of hydrogen since the mass difference between hydrogen and deuterium has different consequences for vibrational and rotational motions.

What remains to be summarized in this section is that despite the immense body of previous work, molecular dynamics simulations and neutron scattering techniques have not yet been applied with their full potential to the subject. It should again be pointed out that it was exactly this combination which lead to fundamental new ideas in the case of sodium silicates. This is the starting point of the present work. The aim of this work is to build up a basis from which it will be possible to merge the two approaches for hydrous silicates as was done for sodium silicates [Me04]. That this is a rather demanding task due to the elevated pressures on the one hand side and the lack of a potential for molecular dynamics simulation on the other was already pointed out in table 1.1. The lack of a suitable potential should be overcome with the use of *ab initio* Car-Parrinello molecular dynamics, a method that was already successfully applied to many silicate systems [Pa01]. Details for silica and sodium silicate systems are given in references [Sa95a, Sa95b, Pa97, Be02, Is01, Is03]. The compromise of a small simulation cell and the loss of the access to dynamical properties is unavoidable. Note that also the development and the testing of a potential would require the comparison to an *ab initio* study. On the experimental side the access to dynamical properties with neutrons can be supposed to give some new insight into the system, even if currently *in situ* measurements in the neutron beam at high temperature *and* high pressure are not feasible.

Chapter 4

Methods for this Approach

4.1 Neutron Scattering - the Experiment

Neutrons coming from a reactor beam tube have usually a broad distribution of energies. Neutron guides lead the neutrons to the scattering instrument. So called single crystal monochromators select a beam of neutrons in a narrow energy band by means of Bragg reflection. The monochromated beam penetrates the sample which is usually mounted on a sample table. The neutrons are scattered by the sample into all directions. In the sample the neutrons can conserve their energy -elastic scattering- or they gain or lose energy -inelastic scattering. At a finite temperature the neutrons can interact with phonons in the sample, leading to inelastic contributions. Accordingly behind the sample the neutron beam has again a broad distribution of energies.

4.1.1 Neutron Diffraction

Neutron diffraction measurements are usually carried out at so called two-axis spectrometers. Two-axis spectrometers can be understood best by starting from the more complex three-axis spectrometers. These three-axis spectrometers are used to selectively measure the scattering function $S(\mathbf{q}, \omega)$ at chosen values of $\mathbf{q}$ and ω. The $\mathbf{q}$-ω selection is performed using a second type of monochromator, the so called analyzer crystal. The name three-axis spectrometer refers to the axis of the monochromator, sample and analyzer crystals.
In contrast to three-axis spectrometers, the analyzer crystal is now missing in two-axis spectrometers. At a given value of $\mathbf{q}$ the integration over all neutron energies is the logic consequence. If the scattered intensity is recorded in a detector, the signal is proportional to the static structure factor defined in Eq. 4.12.
For the present work, the ILL diffractometers D20 and D4 were used. The diffractometer D20 has a very high flux and is equipped with a very large position sensitive detector. Figure 4.1 gives an overview over the instrument. The diffraction pattern is recorded at 1600 positions covering the 160^o angle.

4.1.2 Time-of-Flight Spectrometry

An additional time-of-flight measurement is the only principal difference between diffraction and time-of-flight spectroscopy. In time of flight spectrometry the energy of the scattered

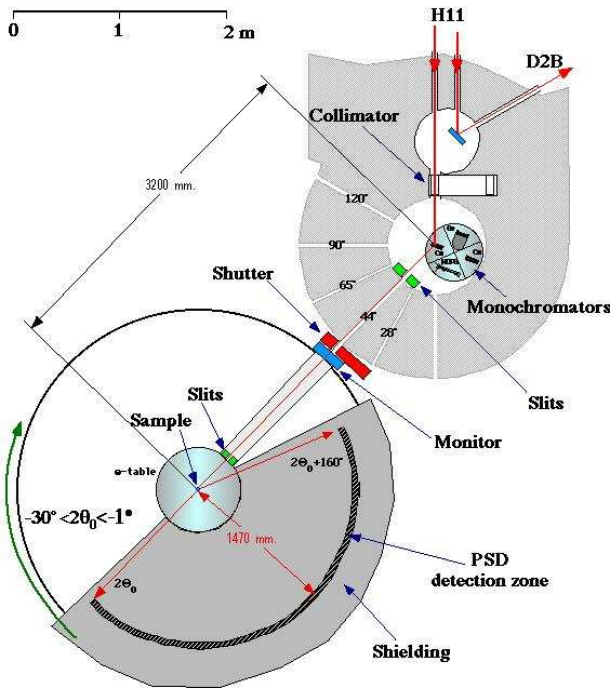

Figure 4.1: *Layout of the ILL diffractometer D20.*

neutrons is analyzed by measuring their time of arrival at the detectors which cover a wide angular distribution, too. Such a flight time scan can be obtained if the monochromated beam is pulsed by a chopper. Neutrons that lost energy in the sample will then have a longer flight time and hence a later arrival at the detectors than elastically scattered neutrons, whereas neutrons that gained energy will arrive earlier than elastically scattered neutrons at the detectors. Figure 4.2 shows the setup of the time of flight spectrometer IN6 at the ILL. The triple monochromator with slightly different angles of the monochromator

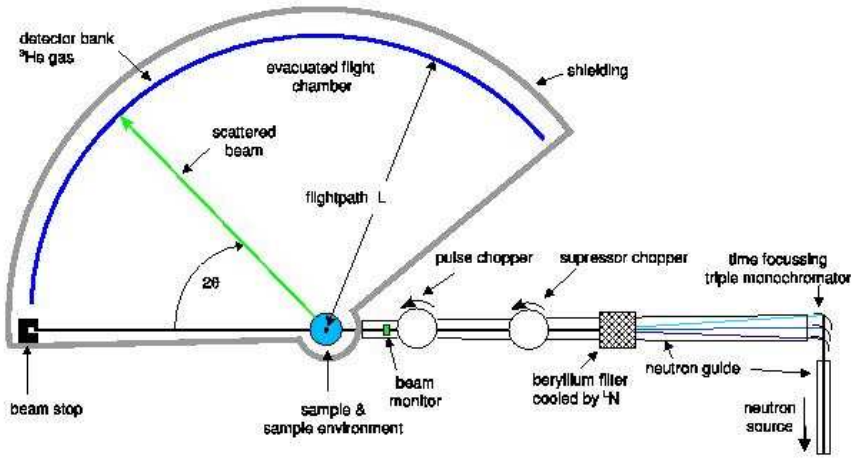

Figure 4.2: *Layout of the ILL time-of-flight spectrometer IN6.*

assures a flux increase at the cost of an energy band broadening. Second order Bragg reflexes are suppressed with a Beryllium filter. The chopper system consists of two choppers, the suppressor chopper and the pulse chopper itself. Both have so called Fermi geometry which means that the slit(s) are rotating around a vertical rotation axis. Appropriate tuning of

the angular velocity of the two choppers assures the suppression of neutrons of the $n+1$ and $n-1$ acceptance cycle at the detection interval for neutrons of the nth chopper acceptance cycle. The relation between the two angular velocities of the chopper is usually called the ratio. The detectors count then the neutrons arriving in a certain detection time $\Delta\tau$ in the time channel n. Identifying $\Delta\tau$ with an energy width ΔE, the count rate in the detector is the one given in Eq. 4.4. The absolute flight time is given as

$$t = n\,\Delta\tau \tag{4.1}$$

The energy transfer in the sample is then given as

$$\hbar\omega = E_i - \frac{1}{2}m_n\left(\frac{L}{L\sqrt{m_n/2E_i} + \Delta n\Delta\tau}\right)^2 \tag{4.2}$$

with the incident neutron energy E_i, the neutron mass m_n and the flightpath L from the sample to the detectors which is 2.43 m in the case of IN6. Δn is the difference between the flight path number n and the flight path number n_{el} of the elastic channel.

4.2 Neutron Scattering - the Theory

The principle goal of neutron scattering experiments is to measure the number of scattered neutrons depending on the momentum $\hbar\mathbf{q}$ and energy E exchanged with a sample. In terms of the neutrons' incident and scattered wave vector, $\mathbf{k}_i$ and $\mathbf{k}_f$, the wave vector transfer $\mathbf{q}$ is given as $\mathbf{q} = \mathbf{k}_f - \mathbf{k}_i$ and the magnitudes of the momentum and energy transfers read as follows:

$$\begin{aligned} q^2 &= k_i^2 + k_f^2 - 2k_ik_f cos\,2\theta \\ \hbar\omega &= \hbar^2/2m_n(k_f^2 - k_i^2) \end{aligned} \tag{4.3}$$

where $k_i = \sqrt{2m_nE_i/\hbar^2}$ and $k_f = \sqrt{2m_n(E_i + \hbar\omega)\hbar^2}$. In neutron scattering experiments the scattering intensity is described by a double differential cross section per atom $d^2\sigma/d\Omega dE$ and 2θ is the angle between k_i and k_f (scattering angle). This cross section is related to experimental quantities as follows: The number of counts in a detector I is proportional to the time averaged neutron flux at the sample Φ, the number of atoms in the beam N, the detector solid angle $\Delta\Omega$ and the detector efficiency f, and finally the width of an energy channel ΔE. Hence

$$I = \Phi N\Delta\Omega f\Delta E\left(\frac{d^2\sigma}{d\Omega dE}\right) \tag{4.4}$$

In order to obtain a quantity that is completely independent of the details of the scattering experiment and hence being exclusively a property of the sample under investigation, the average scattering function $S(\mathbf{q},\omega)$ is introduced:

$$\frac{d^2\sigma}{d\omega dE} = \langle\overline{b^2}\rangle\frac{k_f}{k_i}\,S(\mathbf{q},\omega) \tag{4.5}$$

Since the interaction of a neutron with a nucleus happens on a much smaller distance than a distance constituted by the neutron's wave length, the scattering is isotropic. It becomes

possible to describe the scattering process with the amplitude of the scattered wave, the so called scattering length b_I. In Eq. 4.5 the scattering lengths are averaged over all atoms $\langle\overline{b^2}\rangle = 1/N \sum_I \overline{b_I^2}$ and the spin and isotope distributions of each element (indicated by the bar). The average scattering function is given by

$$S(\mathbf{q},\omega) = \frac{1}{2\pi\hbar N\langle\overline{b^2}\rangle}\int_{-\infty}^{+\infty}\sum_{IJ}\overline{b_I b_J}\langle e^{-i\mathbf{q}\mathbf{R}_I(0)}e^{i\mathbf{q}\mathbf{R}_J(t)}\rangle\, e^{i\omega t}dt \tag{4.6}$$

It contains a double indexed sum. The spins of the nuclei are generally not correlated, hence, $\overline{b_I b_J} = \overline{b_I}\,\overline{b_J}$ for $I \neq J$. Therefore it becomes possible to separate the sum into two contributions that are called *coherent* and *incoherent*:

$$S_{coh}(\mathbf{q},\omega) = \frac{1}{2\pi\hbar N\langle\overline{b^2}\rangle}\int_{-\infty}^{+\infty}\sum_{IJ}\overline{b_I}\,\overline{b_J}\langle e^{-i\mathbf{q}\mathbf{R}_I(0)}e^{i\mathbf{q}\mathbf{R}_J(t)}\rangle\, e^{i\omega t}dt \tag{4.7}$$

$$S_{inc}(\mathbf{q},\omega) = \frac{1}{2\pi\hbar N\langle\overline{b^2}\rangle}\int_{-\infty}^{+\infty}\sum_{IJ}(\overline{b_I^2}-\overline{b_J^2})\langle e^{-i\mathbf{q}\mathbf{R}_I(0)}e^{i\mathbf{q}\mathbf{R}_I(t)}\rangle\, e^{i\omega t}dt \tag{4.8}$$

If solids at ambient temperature are investigated, the atoms move around well defined equilibrium positions $\mathbf{R}_I$. If the corresponding wave vector is small compared to typical vibrational frequencies ω_k ($\omega_k > \hbar q^2/2M_I$), it is appropriate to expand the scattering function (eq. 4.6) in terms of orders of the phonon scattering [Pr86]:

$$S(\mathbf{q},\omega) = S_{elastic}(\mathbf{q},\omega) + S_{1\,phonon}(\mathbf{q},\omega) + S_{2\,phonon}(\mathbf{q},\omega) + \ldots. \tag{4.9}$$

In the harmonic approximation (see section 3.3) the first terms may be given in a closed form. In the following the various terms will be discussed regarding their physical information on the sample.

The 0-th order:
The first term in Eq. 4.9 contains information on the elastically scattered neutrons. Its *coherent* part reads

$$\begin{aligned} S_{coh,elastic}(\mathbf{q},\omega) &= S_{el}(\mathbf{q})\delta(\omega) \\ &= \delta(\omega)\underbrace{\frac{1}{N\langle\overline{b^2}\rangle}\sum_{IJ}\overline{b_I b_J}\, e^{-(W_I+W_J)}\, e^{i\mathbf{q}(\mathbf{R}_J-\mathbf{R}_I)}}_{S_{el}(\mathbf{q})} \end{aligned} \tag{4.10}$$

$S_{el}(\mathbf{q})$ is the so called *elastic structure factor*. For an isotropic system the exponent terms in the Debye-Waller factors are

$$W_I(\mathbf{q}) = \frac{1}{6}q^2\langle u_I^2\rangle \tag{4.11}$$

where $\langle u_I^2\rangle$ is the time averaged mean-square displacement of atom I averaged over time (see section 2.2.1).
The integration over the energy of Eq. 4.7 gives the *static structure factor*

$$S(\mathbf{q}) = \int_{-\infty}^{+\infty} S_{coh}(\mathbf{q},\omega)\, d\omega = \frac{1}{N\langle\overline{b^2}\rangle}\sum_{IJ}\overline{b_I}\,\overline{b_J}\langle e^{-i\mathbf{q}\mathbf{R}_I(0)}e^{i\mathbf{q}\mathbf{R}_J(0)}\rangle \tag{4.12}$$

It is important to note the difference between $S(\mathbf{q})$ in Eq. 4.12 where $S(\mathbf{q})$ depends on the instantaneous relative positions of the particles, and $S_{el}(\mathbf{q})$ in Eq. 4.10 which depends on

relative positions of equilibrium sites.

The first order:
For phonon orders higher than zero, the scattering is naturally inelastic and two possibilities for a neutron arise: Scattering with energy gain ("up-scattering") and scattering with energy loss ("down scattering"). According to these two possibilities, the higher order terms have always two contributions. The first order can be written as follows:

$$S_{1\,phonon}(\mathbf{q},\omega) = \frac{1}{2N\langle\overline{b^2}\rangle}\sum_k \frac{|F_k(\mathbf{q})|^2}{\omega_k}[\underbrace{\langle n_k+1\rangle\delta(\omega-\omega_k)}_{\text{energy loss}} + \underbrace{\langle n_k\rangle\delta(\omega+\omega_k)}_{\text{energy gain}}] \tag{4.13}$$

with the *dynamic structure factor*

$$|F_k(\mathbf{q})|^2 = \sum_{IJ}\frac{\overline{b_I b_J}}{\sqrt{M_I M_J}}\, e^{-W_I(\mathbf{q})-W_J(\mathbf{q})}\,\left(\mathbf{q}\mathbf{e}_I^k\right)\left(\mathbf{q}\mathbf{e}_J^k\right)\, e^{i\mathbf{q}(\mathbf{R}_I-\mathbf{R}_J)} \tag{4.14}$$

where $\mathbf{e}_I^K$ is the displacement vector of atom I belonging to the normal mode k with eigen frequency ω_k and the population factor $\langle n_k\rangle = [exp\{\hbar\omega_k/k_BT\}-1]^{-1}$. A common approximation in order to further simplify the expression for the first order phonons (Eq. 4.13) is the so called *incoherent approximation*. The main idea of this approximation is that if Eq. 4.13 is averaged over a certain range of q, the interference effects of the phase factors cancel out. It can be shown that indeed this is the case if the scattering arose completely from the incoherent part of 4.13. For the case of neutron energy loss (phonon creation +1) the incoherent part is given as

$$S_{inc,+1}(q,\omega) = \frac{1}{N\langle\overline{b^2}\rangle}3\sum_I \overline{b_I^2}\, e^{-2W_I}\frac{\overline{|\mathbf{q}\mathbf{e}_I|^2}}{2M_I\omega}\langle n_k+1\rangle g(\omega) \tag{4.15}$$

with the one phonon density of states $g(\omega) = 1/3N\ \sum_k^{3N}\delta(\omega-\omega_k)$. If the average over Eq. 4.15 could be performed over each term separately, the result would be the following:

$$S_{inc,+1}(q,\omega) = e^{-2\overline{W}}\frac{q^2}{2\overline{M}\omega}\langle n_k+1\rangle g(\omega) \tag{4.16}$$

where $\overline{M}^{-1} = \sum_I M_I^{-1}/N$ and the Debye Waller factor is calculated using a mean square displacement taken over all atoms in the sample: $\overline{W} = q^2\langle\overline{u^2}\rangle/6$. Equation 4.16 is strictly valid only for incoherent scatterers if only one atom type is involved. For all other systems, the approximation works more or less well if sufficiently high q-ranges are taken into account. Usually computer simulations help to estimate the magnitude of the error. In general it is recognized that even in the worst cases the error does not exceed 20 % [Sc02].

Second and higher orders:
The third term $S_{2\,phonon}(\mathbf{q},\omega)$ and higher orders in Eq. 4.9 represent scattering processes to which two or more phonons contribute simultaneously. In the case of an isotropic system the the n-phonon scattering function can be written in incoherent approximation as [Re84] [1]:

$$S_{inc}(q,\omega) = e^{-\frac{\hbar\omega}{k_BT}}\, e^{-\gamma q^2}\sum_{n=1}^{\infty}\left(\frac{\hbar^2q^2}{2\overline{M}}\right)^n\frac{T_n(\hbar\omega)}{n!} \tag{4.17}$$

[1] Strictly $\overline{M}$ would be here $\overline{M} = \sum_I M_I/N$ which goes over to the above given definition for M^{-1} if the atomic masses are not too different. Note that the actual form of the normalized spectrum is indeed very insensitive to the value of the mass.

The mean square displacement γ can be expressed as

$$\gamma = \overline{u^2} = \frac{\hbar^2}{2\overline{M}} \int_0^\infty \frac{g(\hbar\omega)}{\hbar\omega} cosh\left(\frac{\hbar\omega}{2k_BT}\right) d(\hbar\omega) \tag{4.18}$$

and the functions $T_n(\hbar\omega)$ are recursively defined via the expression

$$T_n(\hbar\omega) = \int_{-\infty}^{+\infty} T_1(\hbar\omega - \hbar\omega')T_{n-1}(\hbar\omega')\, d(\hbar\omega') \tag{4.19}$$

starting at

$$T_1(\hbar\omega) = \frac{g(\hbar\omega)}{2\hbar\omega\ sinh\left(\frac{\hbar\omega}{2k_BT}\right)} \tag{4.20}$$

In an iterative process it becomes then possible to determine the whole inelastic scattering. The first step is to calculate the density of states as if higher orders would not exist. The result is taken into Eq. 4.18 and Eq. 4.20 in order to calculate the next higher order with Eq. 4.19 and Eq. 4.17. The deviation of the measured scattering function and the iterated one (after Eq. 4.17) is then used to refine the guess for the vibrational density of states $g(\omega)$. This process is repeated until the $g(\omega)$ converges in a self consistent way. The order of phonon terms is freely chosen under the limits of a good and rapid convergence.
Equation 4.17 shows that the n-th phonon term varies as $(\hbar q^2/2\overline{M}\omega)^n$. Hence the terms become decreasingly significant as n increases (note that $(\hbar q^2/2\overline{M}\omega) < 1$ was the condition for the multi phonon expansion 4.9). The higher order phonon terms constitute normally a relatively smooth and low background under the one-phonon vibrational spectrum.
The equations 4.17 to 4.20 are valid for one particular wave vector transfer $\mathbf{q}$. If the incoherent approximation has to be applied or, in order to have a better statistics, it is often desirable to sum over all wave vector transfers $\mathbf{q}$. This summation leads to [Re84]:

$$\frac{1}{k_ik_f}S(\mathbf{q},\omega) = \frac{1}{2k_i^2}e^{-\frac{\hbar\omega}{2k_BT}} \sum_{n=1}^{\infty} \left(\frac{\hbar^2}{2\overline{M}}\right)^n \frac{1}{\gamma^{n+1}} \left(I_n(\gamma q_{max}^2) - I_n(\gamma q_{min}^2)\right) \frac{T_n(\hbar\omega)}{n!} \tag{4.21}$$

where

$$I_n(x) = \int_0^\infty y^n e^{-y} dy \tag{4.22}$$

It it obvious that the averages over the masses and the scattering vectors taken in 4.16 can only lead to an effective density of states $g_{eff}(\mathbf{q},\omega)$ if several atom types, in particular coherent scatterers are involved. Such an effective density of states $g_{eff}(\mathbf{q},\omega)$ can be defined via the relation

$$g_{eff}(\mathbf{q},\omega) = B(\mathbf{q},\omega)S(\mathbf{q},\omega) \tag{4.23}$$

with

$$B(\mathbf{q},\omega) = \frac{2\overline{M}}{q^2}\langle n+1\rangle^{-1} \tag{4.24}$$

The effective density of states 4.23 is experimentally accessible. The structure factor can be extracted from inelastic neutron scattering data while the averaged Debye-Waller factor in 4.16 and 4.24 is obtained from a comparison of the q dependence between the elastic structure factor 4.10 (extracted from the q dependence of the elastic line) and the static structure factor 4.12 (extracted form a neutron diffraction experiment). The remaining task is now to relate the effective vibrational density of states $g_{eff}(\mathbf{q},\omega)$ to the true vibrational

density of states $g(\omega) = 1/3N \sum_k^{3N} \delta(\omega - \omega_k)$ 3.14. A suitable way to do this was proposed by Taraskin and Elliott [Ta97b]. Taraskin and Elliott introduced a correction function $C(\mathbf{q}, \omega)$ defined by

$$g_{eff}(\mathbf{q}, \omega) = C(\mathbf{q}, \omega) g(\omega) = \frac{1}{3N} \sum_{k}^{3N} C(\mathbf{q}, \omega_k) \delta(\omega - \omega_k) \tag{4.25}$$

where $C(\mathbf{q}, \omega)$ becomes unity for the already considered totally incoherent scatterer of a single atom type.
For all other scatterers the mass and $\mathbf{q}$ averages have to be taken into account. Using equations 4.25, 4.23, 4.24, and 4.15 it can be shown that $C(\mathbf{q}, \omega_k)$ has in the incoherent approximation the general form [Ta97b]

$$C(q, \omega_k) = \frac{\overline{M}}{\langle \overline{b^2} e^{-2\overline{W}} \rangle} \sum_a \frac{\overline{b_a^2}}{M_a} e^{-2\overline{W}_a(q)} \rho_a(\omega_k) \tag{4.26}$$

where a runs over all species of atoms in the system. The quantity is related to the partial vibrational density of states 3.15

$$\rho_a(\omega_k) = \frac{g_a(\omega_k)}{g(\omega_k)} = \sum_{I \epsilon a} |\mathbf{e}_I^k|^2 \tag{4.27}$$

and constitutes relative partial vibrational density of states. The index i refers to all atoms of type a. A further simplification of 4.26 can be obtained setting the Debye-Waller factors to unity. This approximation works rather well for ambient temperature and of course below. The correction factor $C(q, \omega)$ can then be written as

$$C(\omega) = \frac{\overline{M}}{\langle \overline{b^2} \rangle} \sum_a \frac{\overline{b_a^2}}{M_a} \rho_a(\omega_k) \tag{4.28}$$

and depends therefore in the simplified form only on the masses and scattering lengths of the involved atoms. Substituting 4.28 into 4.25 leads to the final relations between the true and the neutron vibrational density of states

$$g_{eff}(\omega) = \left[\frac{\overline{M}}{\langle \overline{b^2} \rangle} \sum_a \frac{\overline{b_a^2}}{M_a} \rho_a(\omega) \right] g(\omega) = \frac{\overline{M}}{\langle \overline{b^2} \rangle} \sum_a \frac{\overline{b_a^2}}{M_a} g_a(\omega) \tag{4.29}$$

It should be pointed out that the small mass of the hydrogen atom and its huge incoherent scattering length make the correction particularly important for hydrous silicates. For further use, according to commonly used abbreviations, $g(\omega)$, $g_a(\omega)$, and $g_{eff}(\omega)$ will, will be referred to as vdos, pvdos, and ndos, respectively.

4.3 Ab-Initio Molecular Dynamics - the Principles

The goal of molecular dynamics simulation is to solve the time-dependent Schrödinger equation

$$i\hbar \frac{\partial}{\partial t} \Phi\left(\{\mathbf{r}_i\}, \{\mathbf{R}_I\}, t\right) = \mathcal{H} \Phi\left(\{\mathbf{r}_i\}, \{\mathbf{R}_I\}, t\right) \tag{4.30}$$

for the electronic $\{\mathbf{r}_i\}$ and nuclear $\{\mathbf{R}_I\}$ degrees of freedom of a material. The Hamiltonian for such an atomic many-body system is composed of the kinetic contribution of each particle

(T_I and T_i), electron-electron interactions V_{ij}, nucleus-nucleus interaction V_{IJ} and electron-nucleus interactions V_{iI}:

$$\mathcal{H} = -\underbrace{\sum_I \frac{\hbar^2}{2M_I}\nabla_I^2}_{T_I} - \underbrace{\sum_i \frac{\hbar^2}{2m_e}\nabla_i^2}_{T_i} + \underbrace{\sum_{i\leq j} \frac{e^2}{|\mathbf{r}_i - \mathbf{r}_j|}}_{V_{ij}} - \underbrace{\sum_{I,i} \frac{Z_I e^2}{|\mathbf{R}_I - \mathbf{r}_i|}}_{V_{iI}} + \underbrace{\sum_{I\leq J} \frac{Z_I Z_J e^2}{|\mathbf{R}_I - \mathbf{R}_J|}}_{V_{IJ}} \tag{4.31}$$

The study of the dynamics of a polyatomic system according to equations 4.30 and 4.31 is according to [Bo98] far beyond computational possibilities - now and for decades to come. Note that the equations to solve do not even contain relativistic properties!
In order to facilitate the complex equations, one switches commonly to dimensionless units where $\hbar = e = 1$.

4.3.1 The Born-Oppenheimer Approximation

The most prominent approach to come to a computationally feasible molecular dynamics is the so called *quantum adiabatic* or *Born-Oppenheimer* approximation [Bo27]. This approximation allows to split, at a fixed time, the time independent Schrödinger equation

$$\mathcal{H}\Phi\left(\{\mathbf{r}_i\},\{\mathbf{R}_I\}\right) = E\Phi\left(\{\mathbf{r}_i\},\{\mathbf{R}_I\}\right) \tag{4.32}$$

into an electronic and a nuclear subsystem and to establish separate Schrödinger equations for the two subsystems. Since the Hamiltonian $\mathcal{H}$ is additive, the Ansatz

$$\Phi\left(\{\mathbf{r}_i\},\{\mathbf{R}_I\}\right) = \Psi(\{\mathbf{r}_i\},\{\mathbf{R}_I\})\chi(\{\mathbf{R}_I\}) \tag{4.33}$$

is used yielding

$$\underbrace{\{T_i + V_{ij} + V_{Ii}\}}_{\mathcal{H}_{el}}\Psi(\{\mathbf{r}_i\},\{\mathbf{R}_I\}) = E_{el}\Psi(\{\mathbf{r}_i\},\{\mathbf{R}_I\}) \tag{4.34}$$

$$\underbrace{\{T_I + E_e + V_{IJ}\}}_{\mathcal{H}_I}\chi(\{\mathbf{R}_I\}) = E_{tot}\chi(\{\mathbf{R}_I\}) \tag{4.35}$$

It is clear that Eq. 4.35 is not exact since the nuclear kinetic energy operator T_I acts according to the Ansatz 4.33 also on the electronic wavefunctions $\Psi(\{\mathbf{r}_i\},\{\mathbf{R}_I\})$. The neglected terms are of the form $1/(2M_I)\nabla_I\Psi$ and $1/(2M_I)\nabla_I^2\Psi$. Note that these terms represent the electron-phonon coupling and therefore the separation in Eq. 4.34 and Eq. 4.35 will break down completely for the case of superconductors. For other cases, the contributions of such a typical term can be approximated. Since $|\nabla_I\Psi| \leq |\nabla_i\Psi|$ (in the worst case the electrons follow the nuclei instantaneously) one finds with the momentum of an electron $p_e = 1/(2m_e)\nabla_i$:

$$\frac{1}{2M_I}\nabla_I^2\Psi(\{\mathbf{r}_i\},\{\mathbf{R}_I\}) \approx \left(\frac{m_e}{M_I}\right)T_i \tag{4.36}$$

Due to the mass ratio m_e/M_I of roughly 1/10000, the terms are neglected and 4.34 and 4.35 are justified.
A first type of molecular dynamics can be obtained applying the time dependent Schrödinger equation $i\hbar\partial/\partial t\chi(\{\mathbf{R}_I\}) = \mathcal{H}_I\chi(\{\mathbf{R}_I\})$ on Eq. 4.35. Further simplification of such dynamics is achieved if the time dependent ionic Schrödinger equation is replaced by a classical Newtonian equation of motion. In the limit $\hbar \longrightarrow 0$ the time dependent Schrödinger equation

reduces to the energy conservation $\mathcal{H}_I = const$ and the equations of motions are obtained from 4.35 within in the Hamilton-Jacobi formalism:

$$M_I \ddot{\mathbf{R}}_I(t) = -\nabla_I E_e(\mathbf{R}_I) \qquad \text{where} \qquad E_e = min_\Psi \{\langle\Psi| \underbrace{\mathcal{H}_{el} + V_{IJ}}_{\mathcal{H}_e} |\Psi\rangle\} \tag{4.37}$$

A molecular dynamics algorithm consists then of solving the static electronic structure problem according to

$$\mathcal{H}_e \Psi = E_e \Psi \tag{4.38}$$

at fixed atomic positions at a molecular dynamics time step and a consecutive ionic displacement according to a classical molecular dynamics. The time dependence of the electronic structure is only a consequence of the nuclear motion. The molecular dynamics described by 4.37 and 4.38 is usually referred to as *Born-Oppenheimer Molecular Dynamics.*

4.3.2 Car-Parrinello Molecular Dynamics

Typical classical molecular dynamics simulation trajectories are of the order of 10^4-10^5 time steps. A straight forward computation of the adiabatic approach as presented above would require the solution of a self-consistent electronic structure problem at each time step. Pastore, Smargiassi and Buda [Pa91] noted in 1991 in their paper on the *Theory of ab-initio molecular dynamics calculations* that the adiabatic approach is not feasible for larger systems since even modern minimization algorithms need in the order of ten iterations to converge. However, Car and Parrinello invented a method to circumvent the explicit minimization by partly undoing the adiabatic approach [Ca85]. Note that the quantum-adiabatic approximation reduced the computationally, extremely demanding, oscillatory behavior of the electronic wave functions to the averaged motion around the minimum of the potential energy surface (still expensive to compute). In 1985 Car and Parrinello proposed to replace the adiabatic dynamics of the electrons by a fictious classical Newtonian motion which oscillates around the energy minimum again. The logic of this idea is shown in figure 4.3.

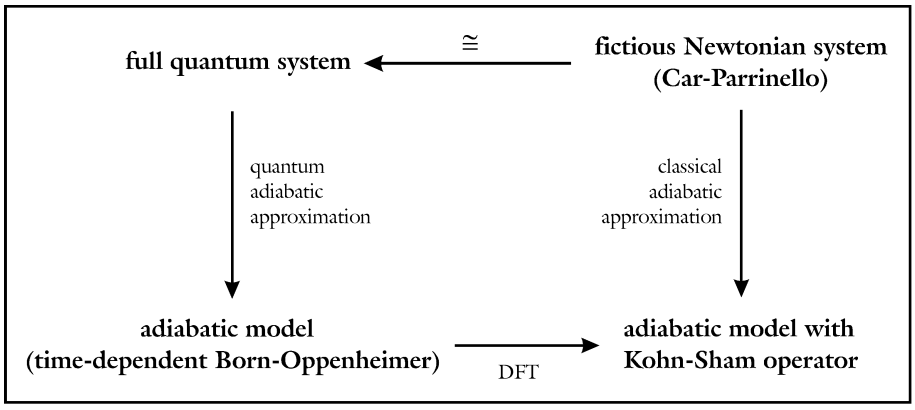

Figure 4.3: *Logic of the Car-Parrinello method (after [Bo98]). The aim of a molecular dynamics computer simulation is to model the quantum mechanical system. This can happen in the Born-Oppenheimer framework (see section 4.3.1) or, preferably by the invention of a fictious classical Newtonian system, the Car-Parrinello approach.*

The idea of the replacement Newtonian dynamics is developed in the Lagrangian formalism.

The following class of Lagrangians with a nuclear and an electronic kinetic energy and the electronic potential was invented

$$\mathcal{L}_{CP} = \underbrace{\sum_I \frac{1}{2} M_I \dot{\mathbf{R}}_I^2 + \sum_i \frac{1}{2}\mu\langle\dot{\psi}_i|\dot{\psi}_i\rangle}_{\text{kinetic energy}} - \underbrace{\langle\Psi_o|\mathcal{H}_e|\Psi_o\rangle}_{\text{potential energy}} + \underbrace{\text{constraints}}_{\text{orthonormality}} \tag{4.39}$$

$\mathcal{L}$ is a function of the ionic positions $\mathbf{R}_I$ and a functional of the ground state electronic wave function Ψ_o. This wavefunction is usually built up by the one particle wave functions ψ_i (which are treated as *classical* scalar fields) in terms of a Slater determinant $\Psi_o = det\{\psi_i\}$. The parameter μ is a *fictive* electronic mass of the unit *energy* $\times$ *time*^{2}. If the electronic wave-functions are treated as classical particles, the corresponding equations of motion are obtained from the associated Euler-Lagrange equations:

$$M_I \ddot{\mathbf{R}}_I(t) = -\nabla_I \langle\Psi_o|\mathcal{H}_e|\Psi_o\rangle + \nabla_I\{\text{constraints}\} \tag{4.40}$$

$$\mu\ddot{\psi}_i(t) = -\frac{\delta}{\delta\psi_i^*}\langle\Psi_o|\mathcal{H}_e|\Psi_o\rangle + \frac{\delta}{\delta\psi_i^*}\{\text{constraints}\} \tag{4.41}$$

According to these equations of motion, a temperature $\sum_I M_I\dot{\mathbf{R}}_I^2$ can be assigned to the ions and a *fictive* temperature $\sum_i \mu\langle\dot{\psi}_i|\dot{\psi}_i\rangle$ is associated to the electronic degrees of freedom. In these terms *zero electronic temperature* means the electronic subsystem is on the Born-Oppenheimer surface (follows the nuclei instantaneously). The electronic mass μ constitutes a kind of control parameter for the deviation from the Born-Oppenheimer surface [Pa91, Bo99]. For the time evolution of the system it is important to note that an electronic subsystem close to the Born-Oppenheimer surface will stay close if its temperature can be kept low. In fact it turns out that one of the main tasks in Car-Parrinello molecular dynamics is to achieve a separation of the electronic and nuclear motion such that the electrons stay cold for the considered trajectories. This is possible if the energy spectra of the nuclear and electronic vibrations do not overlap.

4.3.3 The better method?

Both methods, Born-Oppenheimer and Car-Parrinello dynamics require the efficient calculation of the forces on the nuclei (Eq. 4.37 and Eq. 4.40). A straightforward numerical determination of

$$\begin{aligned}\mathbf{F}_I &= -\nabla_I\langle\Psi_o|\mathcal{H}_e|\Psi_o\rangle \\ &= -\langle\nabla_I\Psi_o|\mathcal{H}_e|\Psi_o\rangle - \langle\Psi_o|\nabla_I\mathcal{H}_e|\Psi_o\rangle - \langle\Psi_o|\mathcal{H}_e|\nabla_I\Psi_o\rangle\end{aligned} \tag{4.42}$$

is too costly for molecular dynamics. Fortunately, if Ψ_o are eigenfunctions, two of the terms in Eq. 4.42 vanish. Hence

$$\mathbf{F}_I = -\langle\Psi_o|\nabla_I\mathcal{H}_e|\Psi_o\rangle \tag{4.43}$$

Equation 4.43 is known as the Hellmann-Feynman Theorem [He33, Fe39]. In practice $\nabla_I\Psi_o = 0$ will never be fulfilled due to a numerical error. Two different types of errors occur. Errors arising from

- the *incompleteness of the basis set and localization of basis functions*

- the *non self-consistency of the effective one particle Hamiltonian (e.g. Eq. 4.51)*

It is obvious that with the employment of non-localized complete basis sets (such as plane waves) the first type of error can be suppressed. For all other types of basis sets the incompleteness forces (also known as Pulay forces [Pu69]) have to be properly included in the calculation. Unfortunately things are more delicate concerning the errors emerging from non self-consistency. These contributions vanish only if the wavefunction Ψ_o is an exact eigenfunction of the Hamiltonian $\mathcal{H}_e$ in the subspace spanned by the finite basis set used. Due to numerical errors, complete self-consistency is never reachable in a numerical approach.
It is now crucial that the impact of these errors on the accuracy of Car-Parrinello simulations is irrelevant. Since the Car-Parrinello method does **not** make use of the minimized expectation value of the electronic Hamiltonian, $min_{\Psi_o}\{\langle\Psi_o|\mathcal{H}_e|\Psi_o\rangle\}$ as the Born-Oppenheimer method does (Eq. 4.37), full self-consistency is not even required in Car-Parrinello dynamics. Furthermore, the finite deviation from the Born-Oppenheimer surface (the deviation from full self-consistency), $\mu_i\ddot{\psi}_i(t) \neq 0$, counterbalances the non self-consistency force. In this picture, a vanishing mass-time-acceleration $\mu_i\ddot{\psi}_i(t) = 0$ would correspond to the tight minimization $min_{\Psi_o}\{\langle\Psi_o|\mathcal{H}_e|\Psi_o\rangle\}$. The conservation of the Car-Parrinello energy is the logic consequence:

$$\frac{dE^{CP}}{dt} = \frac{d}{dt}\left\{\frac{1}{2}\sum_i \mu_i\langle\dot{\psi}_i|\dot{\psi}_i\rangle + \frac{1}{2}\sum_I M_I\dot{\mathbf{R}}_I^2 + \langle\Psi_o|\mathcal{H}_e|\Psi_o\rangle\right\} = 0 \tag{4.44}$$

This motivates the formulation of the "Car-Parrinello credo":

> Whereas deviations from the Born-Oppenheimer surface degrade the accuracy of the forces in Born-Oppenheimer dynamics, Car-Parrinello dynamics is stabilized by the conservation of the so called extended Car-Parrinello energy 4.44

The actual choice of the molecular dynamics method between Born-Oppenheimer and Car-Parrinello depends on the system to be investigated. As it was already pointed out in section 4.3.2, it is essential for Car-Parrinello molecular dynamics that the electronic temperature is kept stable (within oscillations), i.e. electrons stay close to the Born-Oppenheimer surface. In practice this works for systems where electronic and nuclear vibrations are energetically well separated, in particular for materials with high electronic band gap. A further limitation in the application of the Car-Parrinello method is the smallness of the allowed time steps which is for comparable accuracy up to ten times smaller than the one for Born-Oppenheimer dynamics. Since Born-Oppenheimer dynamics on the other hand requires a much higher accuracy for the convergence of the electronic optimization (see the Car-Parrinello credo), the choice is a compromise between greater time step in Born-Oppenheimer dynamics or more steps (the execution time for each being much smaller than in BO MD) in Car-Parrinello dynamics.

4.3.4 Density Functional Theory

The verification and classification of commonly used electronic structure methods (Hartree, Hartree-Fock and their various extensions, Thomas-Fermi approximations and density functional approaches....) is *not* the aim of this thesis. Since the density functional theory (DFT)

is used in combination with the Car-Parrinello technique in the CPMD code [Hu99], the main ideas shall be briefly recalled here.
DFT is mainly based on the Hohenberg-Kohn theorem: It says that the ground state energy of an interacting electronic system can be obtained by a minimization of the Kohn-Sham energy $E^{KS} = min_{\Psi_o}\langle\Psi_o|\mathcal{H}_e|\Psi_o\rangle$ with respect to the electronic density

$$n(\mathbf{r}) = \sum_{i}^{occ} f_i|\psi_i(\mathbf{r})|^2 \tag{4.45}$$

where the sum is over the occupied orbitals and f_i is the integer occupation number. The one particle orbitals $\psi_i(\mathbf{r})$, which are called the Kohn-Sham orbitals are required to be orthogonal:

$$\int d\mathbf{r}\ \psi_i^*(\mathbf{r})\psi_j(\mathbf{r}) = \delta_{ij} \tag{4.46}$$

The electronic Hamiltonian $\mathcal{H}_e$ (equation 4.34) can be expressed as a functional of the electronic density 4.45. With the density 4.45 the functional reads

$$E^{KS}[n] = T_s[n] + \int d\mathbf{r}\ V_{ext}(\mathbf{r})n(\mathbf{r}) + \frac{1}{2}\int d\mathbf{r}\ V_H(\mathbf{r})n(\mathbf{r}) + E_{xc}[n] \tag{4.47}$$

The first term $T_s[n]$ is the kinetic energy of the electrons expressed as a functional of the electronic density. The second term represents the fixed external potentials V_{IJ} and V_{iI} (see equation 4.31):

$$V_{ext}(\mathbf{r}) = -\sum_I \frac{Z_I}{|\mathbf{R}_I - \mathbf{r}|} + \sum_{I\leq J}\frac{Z_I Z_J}{|\mathbf{R}_I - \mathbf{R}_J|} \tag{4.48}$$

The third term comes in analogy to V_{ij} from the electrostatic repulsion energy of two electronic charge clouds. In DFT approaches it is usually called the *Hartree* potential:

$$V_H(\mathbf{r}) = \int d\mathbf{r}'\ \frac{n(\mathbf{r}')}{|\mathbf{r} - \mathbf{r}'|} \tag{4.49}$$

So far the electronic Hamiltonian of equation 4.34 is only rewritten in terms of the electronic density. The main point of the new approach is now to take into account the (unknown) exchange correlation interactions due to the spins of the electrons. These interactions are lumped together in the functional $E_{xc}[n]$ which builds (loosely speaking) the bridge between the exact energy $E^{KS}[n]$ and the decomposition of this energy presented above. Its exact form is unknown and approximations have to be found.
The minimization of the energy functional 4.47 under the constraint 4.46 is performed using Euler-Lagrange techniques. The associated Euler-Lagrange equations are

$$\mathcal{H}^{KS}\psi_i(\mathbf{r}) = \epsilon_i\psi_i(\mathbf{r}) \tag{4.50}$$

with the Lagrange multiplicators ϵ_i and the Hamiltonian

$$\mathcal{H}^{KS} = -\frac{\hbar^2}{2m_e}\nabla^2 + V_{ext}(\mathbf{r}) + V_H(\mathbf{r}) + \mu_{xc}(\mathbf{r}) \tag{4.51}$$

where $\mu_{xc}(\mathbf{r}) = \frac{\delta E_{xc}[n]}{\delta n(\mathbf{r})}$ is the exchange correlation potential. The equations 4.50 are called the Kohn-Sham equations [Ko65]. They are the theoretical basis of modern electronic structure calculations.

4.3.5 Exchange Correlation Functionals

The application of density functional formalism as presented above is subject to the availability of an exchange and correlation functional. Since its exact form is unknown, Ansatzes of the form

$$E_{xc}^{GGA}[n] = \int d\mathbf{r}\, n(\mathbf{r})\epsilon_{xc}^{GGA}(n(\mathbf{r}), \nabla n(\mathbf{r})) \tag{4.52}$$

commonly denoted as *Generalized Gradient Approximation* (GGA) are employed. The function is normally split into additive terms of exchange and correlation contributions. The simplest of the approximation is the so called *Local Density Approximation* (LDA) [Ko65] where the exchange and correlation electron density of an interacting but uniform electron gas at the local density $n(\mathbf{r})$ of the simulated system is used. It should be pointed out that LDA performs remarkably well for many systems. However, significant improvement is obtained with the inclusion of the gradient of the electronic density. The most prominent candidates of GGAs are the exchange functional of Becke [Be88] combined with the correlation functional of Lee, Yang and Parr [Le88] (=BLYP), the ones of Perdew, Burke, and Ernzerhof (=PBE and RPBE) [Pe96, Ha99], Hamprecht, Cohen, Tozer, and Handy (=HCTH) [Ha98]. In so called meta GGAs, ∇^2 terms are considered which bring some improvement for slowly varying densities. Examples are the ones of Perdew, Kurth, Zupan, and Blaha (=PKBZ) [Pe99] and Filatov and Thiel (=FT98) [Fi98]. Figure 4.4 demonstrates how LDA and several GGAs perform for small molecules.

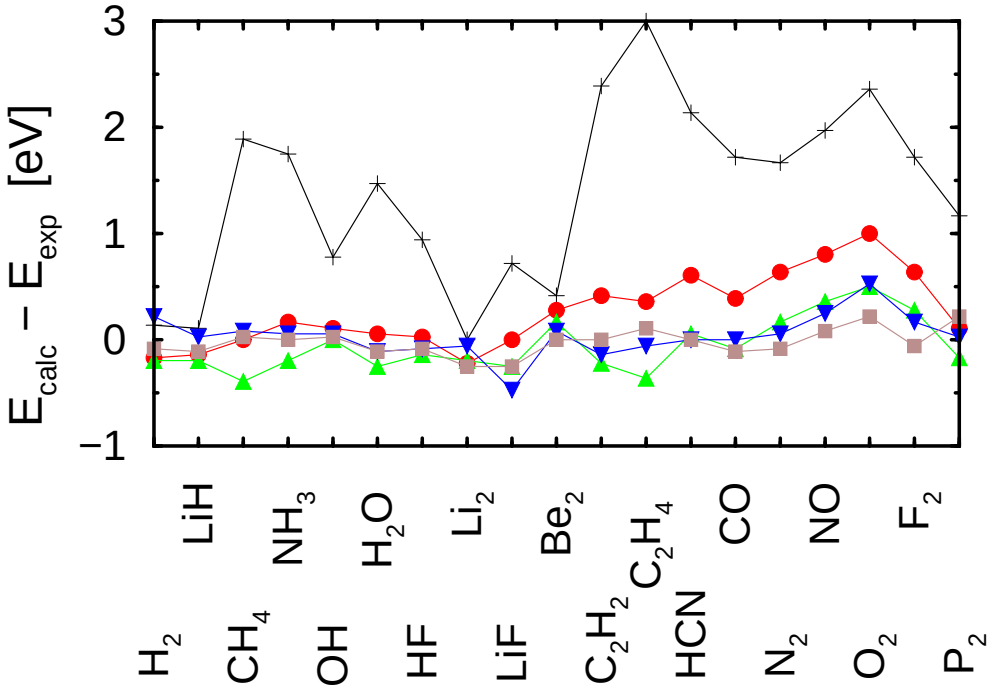

Figure 4.4: *Atomization energy errors ($E_{calc} - E_{exp}$) of small molecules (after [Be93, Ku99]). LSDA black [Ko65], GGAs: PBE red, RPBE [Ha99] green, FT98 [Fi98] blue and B3LYP [Be88, Le88] gray. All GGA functionals work well for water whereas LSDA is rather poor.*

4.3.6 Minimization Techniques

Various techniques are established in order to optimize the Kohn orbitals in Eq. 4.50. Traditional techniques follow the way of numerical diagonalization of the Kohn-Sham matrix 4.50 in an appropriate basis, for example one formed by atomic orbitals. On the other hand, modern methods aim for a direct minimization of the Kohn-Sham energy functional using the gradient of the Car-Parrinello Lagrangian $\partial\mathcal{L}^{CP}/\partial\psi_i$. Commonly used minimization techniques like steepest descent and conjugate gradient methods [Pr89] are then applicable this problem. The most successful of these optimization algorithms is the one of *direct inversion in iterative subspace* (DIIS) [Hu94] where the information of previous optimization steps is used to predict the appropriate way for the proceeding step. It should be mentioned that also the Car-Parrinello molecular dynamics method itself is successfully used today in order to minimize the Kohn Sham energy functional [Ca85].

4.4 *Ab Initio* Dynamics - Implementation in a Plane Wave Basis

The density functional theory - Car-Parrinello molecular dynamics approach has been implemented in a computer code named CPMD by Jürg Hutter and coworkers [Hu99].
This practical implementation employs a plane wave basis set that is the generic basis for periodic systems in solid state physics. Molecular dynamics making use (in many cases) of a periodically repeated simulation box highly appreciates the natural periodicity of these plane waves. A plane wave is given by

$$f_{\mathbf{G}}(\mathbf{r}) = \frac{1}{\sqrt{\Omega}}\, e^{i\mathbf{G}\mathbf{r}} \tag{4.53}$$

where the wave vector $\mathbf{G}$ is compatible with the periodic boundary condition of the cell of volume Ω. The plane waves constitute a complete and orthonormal basis. Hence any periodic function can be expanded in this basis:

$$\psi_i(\mathbf{r}) = \frac{1}{\sqrt{\Omega}} \sum_{\mathbf{G}} c_{i,\mathbf{G}}\, e^{i\mathbf{G}\mathbf{r}} \tag{4.54}$$

Apart from their natural periodicity, the plane waves have the advantage of being originless. This point is especially important regarding the appearance of Pulay terms as it was discussed in section 4.3.3. Furthermore they allow to switch very efficiently from real to momentum space by means of a fast Fourier transform (FFT). This implies the important correspondence between the wave functions $\psi(\mathbf{r})$ and the plane wave coefficients $c_{i,\mathbf{G}}$:

$$\text{real space} \qquad \psi_i(\mathbf{r}) \overset{\text{FFT}}{\longleftrightarrow} c_{i,\mathbf{G}} \qquad \text{reciprocal space} \tag{4.55}$$

For practical calculations the infinite sum over $\mathbf{G}$ vectors has to be truncated. Only G vectors with a kinetic energy lower than a given maximum are retained:

$$\frac{1}{2}|\mathbf{G}|^2 \leq E_{cut} \tag{4.56}$$

The number of involved plane waves N_{PW} can then be approximated by the assumption that, in reciprocal space, each plane wave state occupies the volume $(2\pi)^3/\Omega$ of a Fermi sphere of radius $\frac{4}{3}\pi|\mathbf{G}_{cut}|^3$. Therefore:

$$N_{PW} \approx \frac{1}{2\pi^2}\Omega E_{cut}^{3/2} \tag{4.57}$$

The Car-Parrinello Lagrangian and the equations of motion 4.40 and 4.41 have now to be written in terms of plane waves. In the plane wave representation the Car-Parrinello Lagrangian 4.39 reads

$$\begin{aligned}\mathcal{L}_{CP} &= \mu\sum_i\sum_{\mathbf{G}}|\dot{c}_i(\mathbf{G})|^2 + \frac{1}{2}\sum_I M_I\dot{\mathbf{R}}_I^2 - E^{KS}[\mathbf{G},\mathbf{R}_I] \\ &\quad + \sum_{i,j}\Lambda_{ij}\left(\sum_{\mathbf{G}}c_i^*(\mathbf{G})c_j(\mathbf{G}) - \delta_{ij}\right)\end{aligned} \tag{4.58}$$

The corresponding Euler-Lagrange equations are

$$\mu\ddot{c}_i(\mathbf{G}) = -\frac{\partial E^{KS}}{\partial c_i^*(\mathbf{G})} + \sum_j\Lambda_{ij}c_j(\mathbf{G}) \tag{4.59}$$

$$M_I\ddot{\mathbf{R}}_I = -\frac{\partial E^{KS}}{\partial \mathbf{R}_I} \tag{4.60}$$

4.4.1 Pseudopotentials

In order to avoid an all electron calculation which is computationally very demanding and chemically not necessary it is appropriate to introduce pseudopotentials for the core electrons of an atom. The pseudopotential has to reproduce atomic wavefunctions such that beyond a certain cut off radius r_c the pseudo wavefunction equals the total atomic wavefunction. In particular, the electronic charge distribution has to be correctly described at any point in space by the pseudopotential wave function, a requirement that leads to the so called property of *norm-conservation* [To74]. Inside the cutoff radius r_c the pseudo potential wavefunction $\Phi(r)$ should replace the real wavefunction in a very smooth way (of course with the constraint of norm-conservation). The smoother shape allows then to reduce the number of plane waves and hence to save computer time. The most common approach going back to Trouiller and Martins [Tr91] for such smooth wavefunction is to adapt a polynomial basis

$$\Phi(r) = c_o + c_2r^2 + c_4r^4 + c_6r^6 + c_8r^8 + c_{10}r^{10} + c_{12}r^{12} \tag{4.61}$$

Recently relaxations from the norm conservation have been proposed which lead to significant gains in computational time when dynamics is considered. The approach is called the Vanderbilt ultra-soft pseudopotential [Va90].

4.4.2 The Molecular Dynamics Algorithm

The flowchart for the Car-Parrinello molecular dynamics algorithm is shown in figure 4.5. At $t = 0$ the electronic wavefunction ψ_i of a particle is chosen according to the electronic structure at the given ionic configuration. For the first molecular dynamics time step the velocities are assigned to the atoms in order to follow a Maxwell Boltzmann distribution at

the desired temperature. This allows the total energy and the forces on the atoms, which are then given by the derivatives of the total energy with respect to the ionic positions $\{\mathbf{R}_I\}$ to be calculated. The integration of equations 4.59 and 4.60 is performed using a velocity-Verlet algorithm [Sw82, An83]. The two equations are coupled through the Kohn-Sham energy functional. The numerical integration procedure itself is optimized, however, regarding low computational cost and low storage capacity. In a first step the derivative with respect to the plane wave coefficient is expressed in terms of the Kohn-Sham Hamiltonian 4.51:

$$\frac{\delta E^{KS}}{\delta c_i^*(\mathbf{G})} = \mathcal{H}^{KS} c_i(\mathbf{G}) \tag{4.62}$$

Hence 4.59 reads without its orthogonality part:

$$\mu \ddot{c}_i(\mathbf{G}) = -\mathcal{H}^{KS} c_i(\mathbf{G}) \tag{4.63}$$

This avoids the need for a complete diagonalization and storage of the Hamiltonian matrix since the evaluation of $\mathcal{H}^{KS} c_i$ is sufficient in this algorithm. Compared to direct diagonalization techniques this can be considered as an tremendous advantage. Once $\mathcal{H}^{KS} c_i$ is known, 4.63 can be integrated in a velocity Verlet / rattle scheme [Sw82, An83]. Equation 4.63 does not yet contain the orthogonality forces that were taken out by definition. Therefore, an extra step is included in order to orthogonalize the electronic wavefunctions. Now the ionic equations 4.60 have to be integrated in an extra step, again using a velocity Verlet algorithm. Finally the time is increased and the current values for the electronic wavefunctions and the nuclear positions enter the following molecular dynamics step described in 4.59 and 4.60.
The complete details of the integration procedure have been described by Tuckerman and Parrinello in [Tu94].

4.4.3 Thermostats and chain Thermostats

An overview of appropriate molecular dynamics thermostating is given in [Tu00]. The thermodynamic ensemble considered in ordinary Newtonian molecular dynamics is the microcanonical or NVE (constant particles, volume and energy) ensemble where the particle number, the volume and the energy are the control variables. However, for practical applications it is desirable to establish a molecular dynamics that allows the temperature of the system to be controlled.
The following set of equations defines the so called Nosé-Hoover chain dynamics [Ma92]:

$$\dot{\mathbf{r}}_i = \frac{\mathbf{p}_i}{m_i} \tag{4.64}$$

$$\dot{\mathbf{p}}_i = \mathbf{F}_i - \mathbf{p}_i \frac{p_{\eta_1}}{Q_1} \tag{4.65}$$

$$\dot{\eta}_k = \frac{p_{\eta_k}}{Q_k} \qquad k = 1, ..., M \tag{4.66}$$

$$\dot{p}_{\eta_k} = G_k - \frac{p_{\eta_{k+1}}}{Q_{k+1}} p_{\eta_k} \qquad k = 1, ..., M-1 \tag{4.67}$$

$$\dot{p}_{\eta_M} = G_M \tag{4.68}$$

with the thermostat forces

$$G_1 = \sum_{i=1}^{N} \frac{\mathbf{p}_i^2}{m_i} - 3Nk_BT \tag{4.69}$$

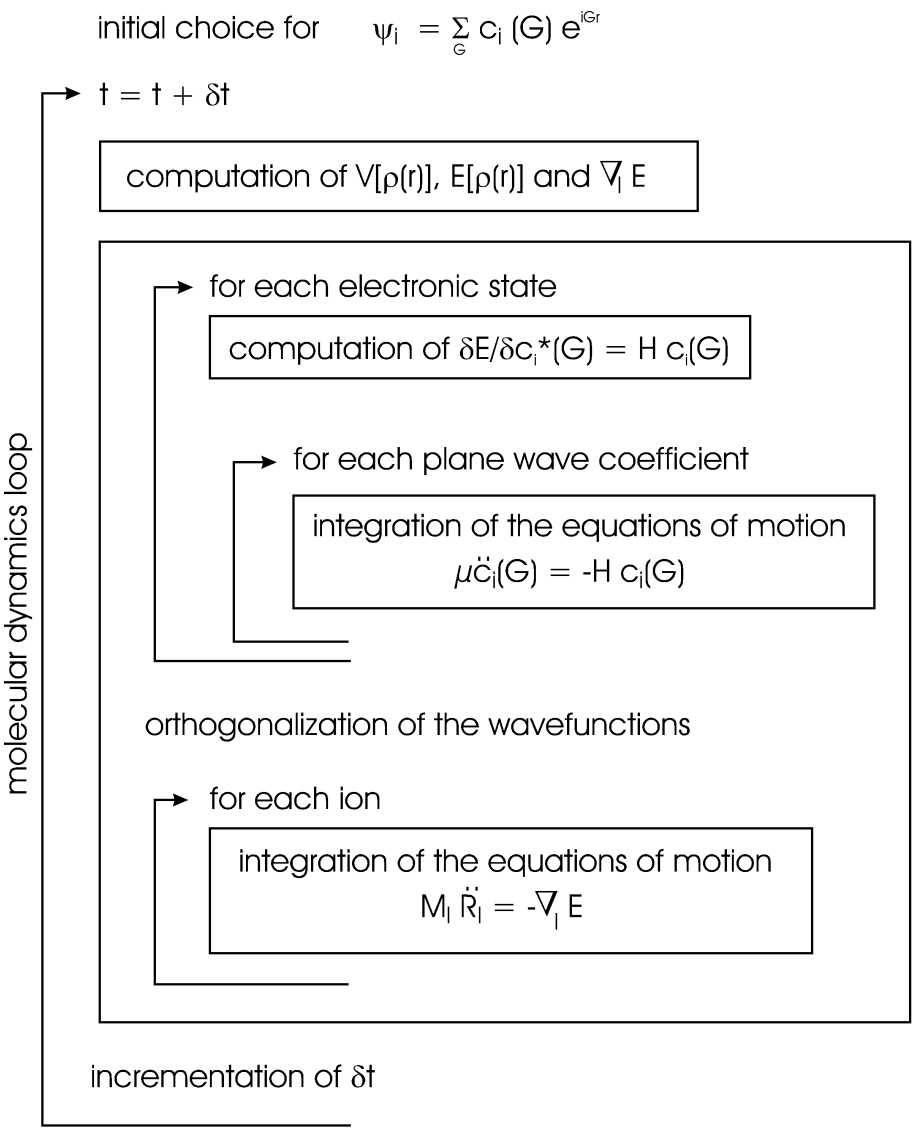

Figure 4.5: *The Car-Parrinello molecular dynamics cycle as implemented in the CPMD code.*

$$G_k = \frac{p_{\eta_{k-1}}^2}{Q_{k-1}} - k_B T \qquad k = 2, ..., M \tag{4.70}$$

Within this method, a heat bath is coupled to the system by M thermostat variables $\eta_1, ..., \eta_M$ and their conjugate momenta $p_{\eta_1}, ..., p_{\eta_M}$. The Q_k are the so called "masses" of the thermostat. They are given by $Q_1 = 3Nk_BT\tau^2$ and $Q_k = k_BT\tau^2$ and relate the time scale of a the thermostat motion via a single time scale τ to a characteristic time scale of the system which can e.g. be a vibrational frequency. The M thermostats, which successively thermostat each other, are coupled to the particles by equation 4.65 enabling a modulation/control of the kinetic energy of the particles.
The great advantage of Nosé-Hoover chains is that they generate the canonical distribution of the canonical NVT ensemble. In Newtonian dynamics, the Hamiltonian of an N-particle system is given by

$$H(\mathbf{p}, \mathbf{r}) = H(\mathbf{p}_1, ..., \mathbf{p}_N, \mathbf{r}_1, ..., \mathbf{r}_N) = \sum_{i=1}^{N} \frac{\mathbf{p}_i^2}{2m_i} + U(\mathbf{r}_1, ..., \mathbf{r}_N) \tag{4.71}$$

with a corresponding micro-canonical distribution function

$$f(\mathbf{p},\mathbf{r}) = \delta(H(\mathbf{p},\mathbf{r}) - E) \tag{4.72}$$

Hence, if Nosé-Hoover chains generate indeed the distribution of the canonical ensemble it has to be shown that

$$H' = H(\mathbf{p},\mathbf{r}) + \sum_{k=1}^{M} \frac{p_{\eta_k}^2}{2Q_k} + k_B T \left[3N\eta_1 + \sum_{k=2}^{M} \eta_k \right] \tag{4.73}$$

has a distribution

$$f(\mathbf{p},\mathbf{r},\mathbf{p}_\eta,\eta) \sim \exp\left[-\frac{1}{k_B T} \left(V(\mathbf{r}) + \sum_{i=1}^{N} \frac{p_i^2}{2m_i} + \sum_{k=1}^{M} \frac{p_{\eta_k}^2}{2Q_k} \right) \right] \tag{4.74}$$

In the general case this is true for $M \geq 2$. The special case $M = 1$ is usually referred to as (ordinary) Nosé-Hoover thermostating. In fact it turns out that for $M = 1$ the canonical distribution is not well reproduced for some cases. Figure 4.6 shows the exact position and momentum distributions for an one-dimensional harmonic oscillator in comparison to the Nosé-Hoover thermostated ($M = 1$) and Nosé-Hoover chain ($M = 2$) thermostated system. It becomes evident that for this system Nosé-Hoover thermostating is unacceptable if an invariant probability distribution is desired. An extreme case of Nosé-Hoover chain thermo-

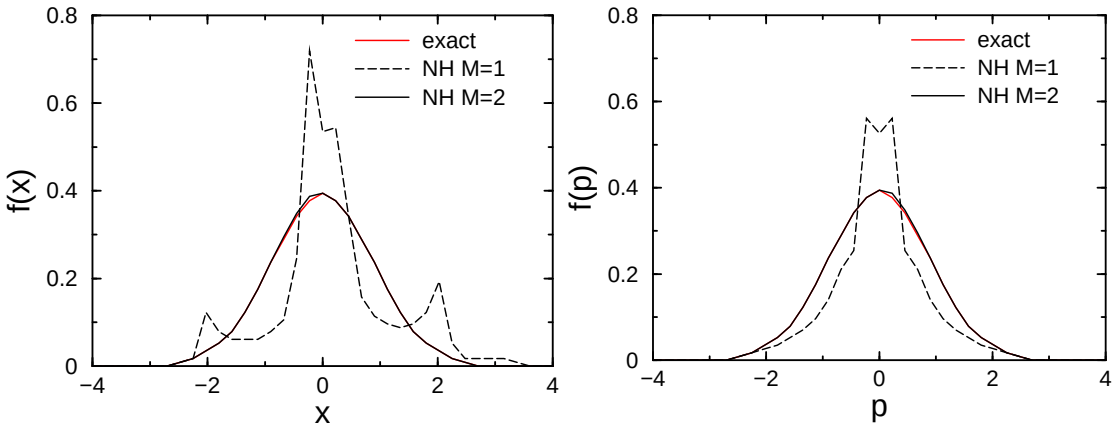

Figure 4.6: *Distribution functions of position (left panel) and momentum (right panel) for an harmonic oscillator with* $r(0) = 0$, $p(0) = 0$, $p_\eta(0) = 1$, $Q = 1$. *Exact distributions (red lines) and distributions as obtained by Nosé-Hoover thermostating* ($M = 1$, *dashed lines) and Nosé-Hoover chain thermostating* ($M = 2$, *solid lines). After [Ma92].*

stating is the so called "massive thermostating" where one separate Nosé-Hoover thermostat is coupled to each degree of freedom of the (nuclear) system [Ma96]. It was shown by Martyna *et al* [Ma96] that this way of thermostating leads to a very rapid equilibration of an atomic system.

To conclude the section on molecular dynamics, it should again be pointed out that the integration of the Car-Parrinello equations of motions according to figure 4.5 with an efficient thermostating of the electronic and the nuclear degrees of freedom are the kernel of Car-Parrinello computer simulations of silicates at high temperature. The complete implemented combined theory can be found in [Tu94].

Chapter 5

Theoretical and Experimental Setup

5.1 Conception and Hardware Performance

The concept of equilibration of a liquid in a molecular dynamics simulation is strongly related to the available computer power. The equilibration of a particular ensemble at a finite temperature takes a certain (real) time, depending on the size and the composition of the ensemble. Since the real equilibration time is strongly temperature dependent (that is a system equilibrates faster at higher temperatures) an equilibration on the computer is much less demanding at high temperatures. Indeed with present day's computers the times needed for an equilibration of a reasonably sized system of around 100 atoms at several thousands of Kelvin require a feasible amount of computer time. For a 100 atom system the today's accessible time window is several pico seconds in *ab initio* approaches.
The correspondence given in Eq. 4.55 allows the electron density and the contributions of the different terms to the Kohn-Sham energy of 4.47 to be expressed in the reciprocal space where they have a much more convenient form (that means where the numerical calculation is less demanding). The main work load for a computer is then to perform the fast Fourier transform from real space to momentum space (where the Kohn-Sham energy is easily accessible) and vice versa.
The question then is if the FFT to momentum space and back plus the energy determination in momentum space is more demanding than a direct minimization of E^{KS} (4.47). Several methods are feasible for a minimization in real space among which the direct inversion in iterative subspace [Hu94] is the fastest. Denoting the number of plane waves with M and the number of Kohn-Sham orbitals with N, this method scales with N^2M. On the other hand, the minimization in momentum space including the Fourier transforms scales with $NM\log M$ [An00] and is hence indeed much faster. An overview of the evolution of the benchmark for CPMD calculations in the 1990's is given in Table 5.1.

5.2 Implementation of the Simulations

In this section the setup of the hydrous silica system consisting of 30 SiO_2 units and 4 H_2O units is described. At important points, results are compared to a second system composed of 26 SiO_2 units and 8 H_2O units.
For the equilibration of hydrous silica systems a density functional (DFT) approach in a general gradient approximation with the PBE functional [Ko65, Pe96] was used. The core

Year	System (limit)	Type of calculation	Hardware	Type of algorithm
1992	One organic molecule	Dynamics;	RISC6000/580	Serial
	of roughly 50 atoms	electronic structure	(125 MFlops)	
1994	Liquid 100 atoms	Reaction dynamics	SP1-16 nodes	Parallel
	Organics water	free energy	(2 GFlops)	
1996	Biomolecules	Reaction dynamics;	SP2/66 MHz	Parallel
	200 atoms	electronic structure	16 nodes	
	in water		(4.2 GFlops)	
1998	Complex interfaces	All of the above	SP2/166 MHz	Parallel
	400 atoms. Water		32 nodes	
	oxide organic / metal		(20.5 GFlops)	

Table 5.1: *Benchmark evolution of CPMD calculations on the 1990's. After [An00].*

electrons were described with a Troullier-Martins type pseudopotential [Tr91]. A plane wave Γ point expansion with an energy cutoff of 50 Ry turned out to be sufficient for an appropriate description of the inter atomic forces. The 50 Ry cutoff with the PBE functional was first tested on the H_2O dimer and on α-quartz. The results of these tests are shown in Figure 5.1 for α-quartz and in Figure 5.2 for the H_2O dimer. From the left panel of Figure 5.1 one recognizes that the experimentally measured Si-O-Si angle of 144^o is at best approximated in the local density approximation (LDA). The angle found using generalized gradient approximations (GGA) with the PBE and BLYP [Be88, Le88] functionals are 140.5^o and 139^o, respectively which is in rather poor agreement with the experimental value of 144^o. However, for the PBE functional the value changes only very slightly if the cutoff is reduced from 70 Ry to 50 Ry. Also, for the generalized gradient approximation with the PBE functional, the two SiO distances of α-quartz are equal to 1.624 Å and to 1.628 Å independent on the energy cutoff between 50 Ry and 70 Ry as can be seen from the right panel of Figure 5.1. Again the experimental values of 1.608 Å and 1.611 Å are much better reproduced in a local density approximation and the use of the LDA seems to be preferable. On the other

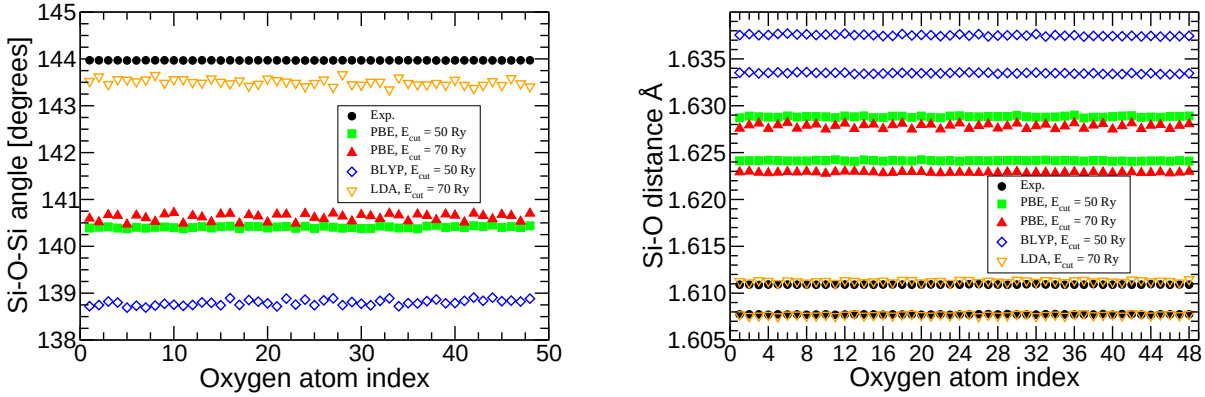

Figure 5.1: **Left**: *Si-O-Si angle for α- quartz. The experimental value is best represented in LDA followed by gradient approximations using the PBE and the BLYP functional.* **Right**: *The two Si-O interatomic distances in α-quartz. Again LDA approximates the experimental values at best, followed by gradient approximations with PBE and BLYP.*

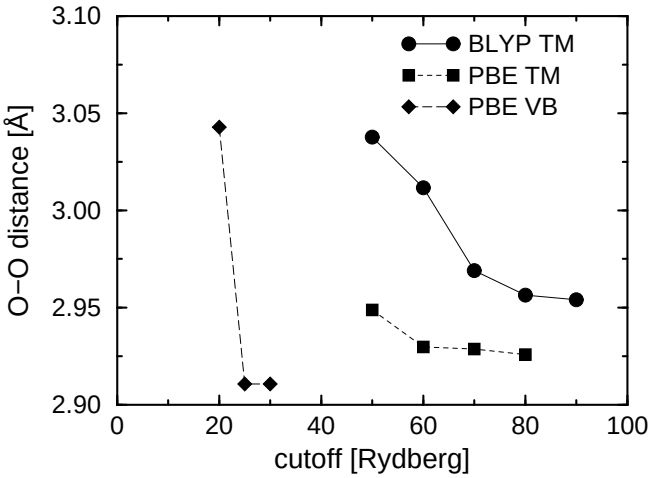

Figure 5.2: *Distance between the two oxygen atoms in a H_2O-dimer as a function of the cut-off parameter (i.e. the number of plane waves used). The three curves shown correspond to two different exchange functionals for the Troullier-Martins (TM) norm-conserving pseudopotential and the Vanderbilt (VB) ultra-soft pseudopotential.*

hand, it is known that LDA describes hydrogen very poorly. This becomes evident from figure 4.4 where the deviation of the calculated atomization energy from the experimental one is compared for several exchange correlations and for several small molecules. As already mentioned, the local density approximation is generally rather poor for systems containing hydrogen. Hence the use of the generalized gradient approximation using the PBE functional (which describes α-quartz next best after LDA) was tested on the H_2O dimer. For the H_2O dimer it was found that the O-O distance, the quantity which is the most sensitive to a change of the cutoff, shows, in GGA with the PBE functional, only a variation from 2.925 Å to 2.950 Å if the cutoff is decreased from 90 Ry to 50 Ry (Fig. 5.2) and the cohesive energy for the hydrogen bond in the water dimer was found to vary from 21.6466 kJ/mol at 80 Ry to 21.5883 kJ/mol at 50 Ry, both values being close to experiments (25.1 $\pm$ 3.2 kJ/mol) [Si92]. On the other hand, if the cutoff is varied in this range for the BLYP functional, the O-O interatomic distance changes considerably more.

It was also tested if the use of Vanderbilt ultra-soft pseudopotentials (USPP) [Va90] could be an alternative. Ultra-soft pseudopotentials would allow to reduce the cutoff to 25 Ry as can be seen from Figure 5.2. The 25 Ry energy cutoff compared to 50 Ry reduces the number of plane waves considerably which should speed up the calculations. To test this, two wavefunction optimizations, one with ordinary Troullier-Martins type pseudo potentials at a cutoff of 50 Ry and one with Vanderbilt pseudo potentials at a cutoff of 25 Ry were performed for the same atomic configuration on one processor on the Hitachi SR8000. The result was the following

pseudopotential	duration of an optimization step ($30SiO_2$+$4H_2O$)
50 Ry Troullier-Martins	42.6 s
25 Ry Vanderbilt	52.6 s

Obviously, the optimization with Troullier-Martins pseudo potentials is faster. This holds also for molecular dynamics runs. Also other systems like the water molecule, with and without periodically repeated box and several memory assignment like the BIGMEM keyword of CPMD were investigated. However, the runs with the Vanderbilt pseudo potentials have never been considerably faster than the ones with conventional Troullier-Martins pseudo potentials. The CPMD authors explained that this is most likely related to the fact that

CPMD runs on the Hitachi in vector mode. The USPP code has never been optimized for this type of machine and therefore they assume that some of the routines are very slow [Hu03a]. With the help of Jürg Hutter, CPMD version 3.8 was set up in which some subroutines were reprogrammed. Here it was possible to obtain a speedup of about 30 % using Vanderbilt pseudo potentials. However since this version of CPMD is not fully tested yet, the risk of using it for the present work was not taken.
According to the details presented above, it turned out that the use of Troullier-Martins norm-conserving pseudopotentials in a generalized gradient approximation with the PBE functional at a 50 Ry plane wave energy cutoff is the best compromise between an accurate description of SiO_2 on the one hand and hydrogen on the other hand. Also regarding computer time it did not become evident that the choice of Vanderbilt pseudopotentials at an energy cutoff of 25 Ry could speed up the calculations.
With the cutoff value of 50 Ry a series of tests on the Hitachi SR8000 machine have been performed in order to determine the speedup as a function of the number of processors used. The result of these tests are presented in Fig. 5.3 where the execution time for one step as a function of the number of processors is shown. Ideal scaling holds if this time is proportional to the 1/(number of processors) (see straight line in the figure). From the graph one recognizes that the program shows this ideal scaling up to 8 processors and that using 16 processors is also quite reasonable. Simulations are performed preferably at a density

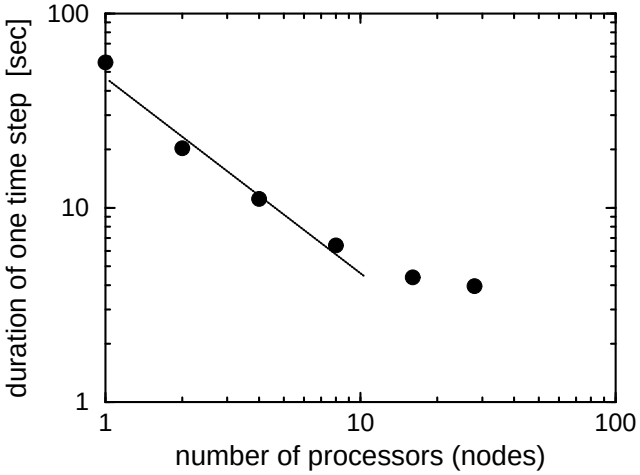

Figure 5.3: *Execution time per processor and CPMD time step as a function of number of processors used on the Hitachi SR8000-F1. The data shown was computed for the system $30SiO_2$-$4H_2O$ with a cutoff of 50 Ry. Results for the system $26SiO_2$-$8H_2O$ are quite similar. The straight line represents a slope of -1.*

that corresponds to a zero internal stress for the system. Since densities of water containing silicates, especially in the liquid state, are not known, these densities have to be found numerically with CPMD. The CPMD code allows the internal stress during a MD trajectory to be recorded. Results are shown here for the system of $26SiO_2$-$8H_2O$ where longer trajectories are available, but the procedure is similar for the system $30SiO_2$-$4H_2O$. The ensemble was equilibrated at 3000 K for several picoseconds with Car-Parrinello dynamics and the internal pressure was recorded for several hundred femtoseconds at three box lengths at 11.0 Å, 11.5 Å, and 12.0 Å in order to find the equilibrium density. These simulations were performed with a plane-wave energy cutoff of 80 Ry in order to obtain a good convergence of the stress. Note that the absolute value of the stress depends on the energy cutoff an the chosen GGA [Fr90]. Figure 5.4 shows the trace of the internal stress tensor along the molecular dynamics runs at 3000 K that have been carried out after a geometry optimization for each box size. From Fig. 5.4 one notes that the box length of 12.0 Å corresponds best to the requirement

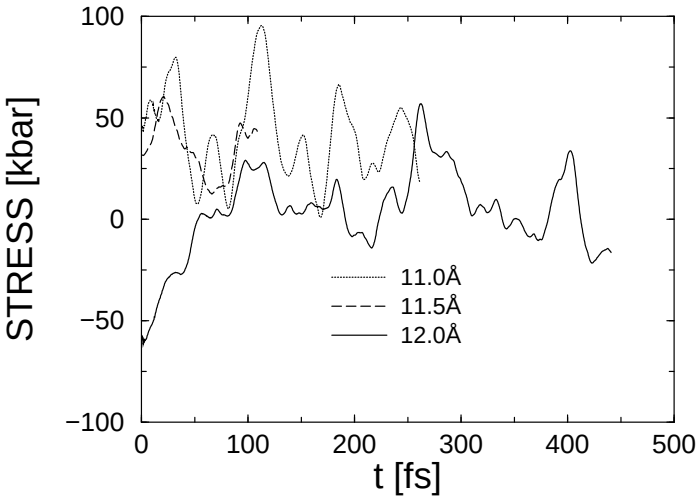

Figure 5.4: *Evolution of the trace of the internal stress tensor of the system $26SiO_2$-$8H_2O$ for three box lengths.*

of a low internal stress. However, the trace of the stress tensor fluctuates considerably. In particular it is not possible to distinguish between zero kbar and typical experimental pressures of 2-3 kbar. Figure 5.5 shows the resulting densities of the two equilibrated systems in comparison to the model established by Ochs and Lange [Oc97].

The model of Ochs and Lange is based on thermal expansion data of silicate melts of

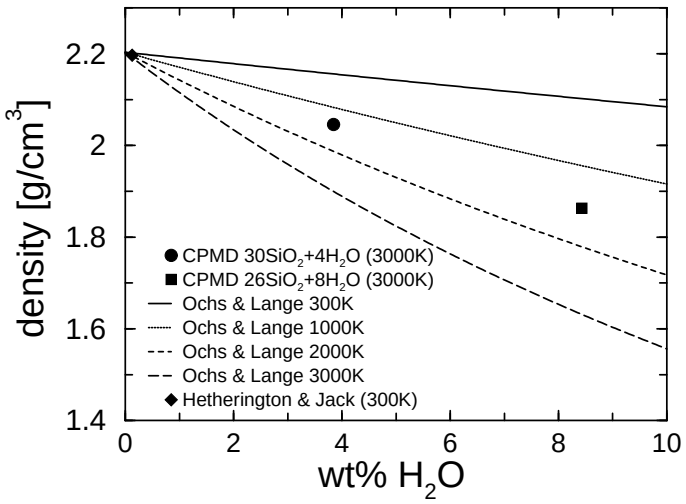

Figure 5.5: *Densities of hydrous silica systems as found by CPMD and after the model of Ochs and Lange [Oc97] and Hetherington and Jack [He62].*

various composition at various temperatures. As can be seen from figure 5.5, the effect of the thermal expansion is overestimated by the model compared to the Car-Parrinello simulations. Moreover, in the model of Ochs and Lange, the influence of the silicate temperature on the density is about one order of magnitude higher than the influence of the pressure. Accordingly a considerable alteration of the pressure would only require a very small adaption of the density and hence the simulation box size. Note that the temperature dependent behavior of the density of silicate melts is generally rather complex and hard to describe [La94].

The choice of the appropriate dynamics between Born-Oppenheimer (see section 4.3.1) and Car-Parrinello (see section 4.3.2) was made on the basis of short test trajectories. The following table gives the comparison of the execution time for a 100 fs trajectory of the system $30SiO_2$-$4H_2O$, using Born-Oppenheimer and Car-Parrinello dynamics:

method	CPUh for 100 fs of trajectory on the IBM SP3
Born-Oppenheimer	451
Car-Parrinello	55

Based on these results, Car-Parrinello dynamics was selected for the present work, also because of the stability against error accumulation (see the Car-Parrinello Credo in section 4.3.3). The next step in the setup was to find appropriate parameters for the Car-Parrinello electronic mass and the Nosé-Hoover thermostats. For the equilibration of $30SiO_2$-$4H_2O$, the masses of the ions were all set to 28 a.u. (the mass of a silicon atom). Note that a change of the ionic masses does not affect the structure of the liquid since at equilibrium all structural quantities are independent of the mass. On the other hand, the increase of the ionic masses (from 1 to 28 for hydrogen and from 16 to 28 for oxygen) allows an increase of the Car-Parrinello electronic mass and hence the use of a larger time step which thus leads to a faster equilibration. The equilibration of the system was performed at the two ionic temperatures of 3000 K and 3500 K employing Nosé-Hoover thermostats and an electronic mass of 600 a.u. (energy $\times$ time^2) at a time step of 4.5 a.u. (0.1088 fs). At high temperature, the electronic gap is too small compared to $k_{\mathrm{B}}T$ to ensure the decoupling of the ionic and the electronic degrees of freedom, which is needed to perform Car-Parrinello dynamics. The use of thermostats is therefore compulsory. To speed up the equilibration and to perform an efficient canonical sampling, one separate Nosé-Hoover thermostat chain for each ionic degree of freedom was used (known as "massive" thermostating [Ma96], see section 4.4.3). The ionic thermostat was coupled to the OH stretch vibrations at a frequency of 3000 cm^{-1}. As it was mentioned in section 4.4.3, such coupling is required in order to define a time scale for the thermostat motion. The electrons were controlled with one single thermostat chain [Ma92, Tu94]. Unfortunately, due to the use of thermostats the direct access to dynamical properties is no longer available. The complete input for the Car-Parrinello equilibration of the system is given in appendix E.

Having set up the system, it becomes immediately possible to make rough predictions about the dissolution of water. Starting from the model of section 2.1.1 one can predict the critical temperature for water exsolution with the ground state energies obtained in the calculations. Minima of the Gibbs free energy are found by a derivative of the free enthalpy of mixing (Eq. 2.7) [St89]

$$\frac{\partial \Delta G_m}{\partial \overline{x}} = \frac{\partial \Delta H}{\partial \overline{x}} - RT \ln\left(\frac{1-\overline{x}}{\overline{x}}\right) = 0 \tag{5.1}$$

Hence

$$T_c = \frac{1}{R}\frac{\Delta H_2 - \Delta H_1}{\overline{x}_2 - \overline{x}_1}\left[\ln\left(\frac{1-\overline{x}}{\overline{x}}\right)\right]^{-1} \tag{5.2}$$

The best way to approximate $\partial\Delta H = \Delta H_2 - \Delta H_1$ is to compare the two systems $30SiO_2$-$4H_2O$ and $26SiO_2$-$8H_2O$. $\partial\Delta H$ is roughly given by

$$\partial\Delta H = E^{KS}(30\mathrm{SiO_2}\text{-}4\mathrm{H_2O}) - E^{KS}(26\mathrm{SiO_2}\text{-}8\mathrm{H_2O}) + 4\,E^{KS}(\mathrm{H_2O}) - 4\,E^{KS}(\mathrm{SiO_2}) \tag{5.3}$$

Using the values of the optimization of the water dimer for $E^{KS}(4H_2O)$ and the one of the simulation of pure silica for $E^{KS}(4SiO_2)$ [Be04] one can extract ΔH =3.64 a.u.. With equation 5.2, a critical temperature of 2309 K is found. Note that this value is only a very rough approximation since, in particular, the pure SiO_2 system was simulated with different

parameters than the hydrous liquids. However, it was already mentioned that the application of the regular solution model itself is critical. Nevertheless, such approximations give a first hint that if the system will be equilibrated at higher temperatures it is stable and will not decompose into silica and water. Note that, if silicate systems demix thermodynamically this can be clearly seen in molecular dynamics simulations [Wi03].
The system $30SiO_2$-$4H_2O$ was equilibrated at two temperatures (3500 K and 3000 K) until in a log-log plot the averaged mean square displacements (MSD) of each particle type a

$$\langle \mathbf{R}_a^2(t) \rangle = \frac{1}{N_a} \sum_{I=1}^{N_a} \langle |\mathbf{R}_I(t) - \mathbf{R}_I(0)|^2 \rangle \tag{5.4}$$

showed at long times a slope close to unity according to equation 2.13. The thermal average was performed using the autocorrelated approximation

$$\langle \mathbf{R}_a^2(t) \rangle = \frac{1}{N_{steps} - t} \sum_{k=1}^{N_{steps}\Delta t - t} \left(\frac{1}{N_a} \sum_{I=1}^{N_a} |\mathbf{R}_I(t + k\Delta t) - \mathbf{R}_I(k\Delta t)|^2 \right) \tag{5.5}$$

Usually MSDs of viscous liquids are composed of three regions: The ballistic one in which

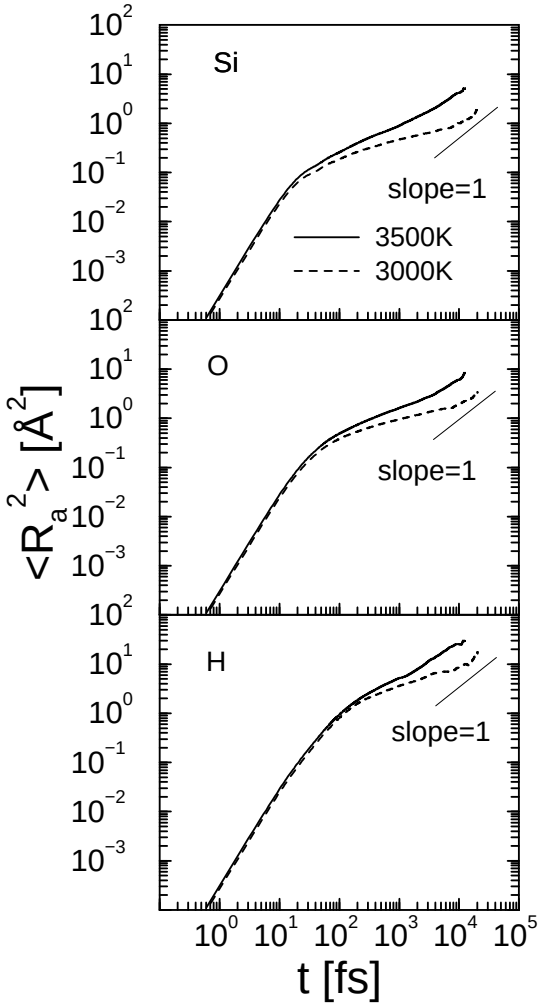

Figure 5.6: *Mean square displacements of the Si, O and H atoms at 3500 K (solid lines) and 3000 K (dashed lines).*

the atoms move without noticing their neighbors and hence a MSD that is proportional to t^2. This ballistic region is followed by a region where the atoms are temporarily confined in a cage made of their nearest neighbors (as already reported in section 2.2.2). In this regime, the atoms rattle around in the cage without significant displacement, leading to a MSD that

increases only slowly. Finally the atoms leave this cage and start to show a diffusion motion, i.e. a MSD that is proportional to t after equation 2.13. The choice of the masses and the thermostats affect also the MSD. However, the height of the plateau and the displacement at the onset of the diffusional regime should be independent of the thermostat. Hence, one can consider the system to be equilibrated once the diffusional regime is reached which was the case after 4.4 ps at 3500 K and 10.9 ps at 3000 K.
In order to check that the liquids were indeed well equilibrated and that there were no aging effects, the trajectories were cut into three equal parts. The averaged mean square displacements were then calculated for each part separately and compared to each other. Figure 5.7

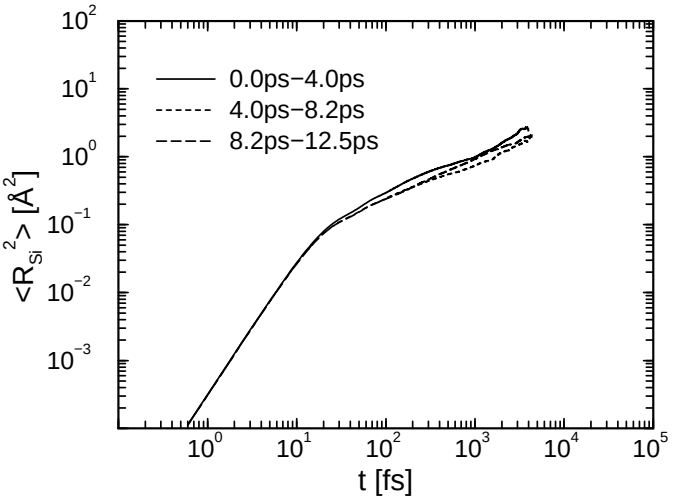

Figure 5.7: *Mean Square displacement of the Si atoms in the 3500 K trajectory at splitted into three parts.*

shows the msd of three parts of the trajectory at 3500 K. Since the three different averaged MSDs did not show any drift, aging effects can be excluded and equilibration was indeed obtained after the above mentioned times.
At temperatures of 3000 K and 3500 K the liquid reaches equilibrium after 10.9 ps and 4.4 ps, respectively. The total lengths of the recorded trajectories were 22.5 ps at 3000 K and 12.5 ps at 3500 K. With a time step of 4.5 a.u. (0.1088 fs), the numbers of computed time steps were 114900 at 3500 K and 206800 at 3000 K. Using a single processor, where one time step takes about 52 s on the Hitachi SR8000 (see Fig. 5.3), this corresponds to 1660 one processor CPU hours (13280 budget units) and 2990 one processor CPU hours (23920 budget units), respectively (the budget units are counted taking into account that CPMD runs on one processor per node, where one node has 8 processors).

5.3 Neutron Scattering at the ILL

5.3.1 Sample Preparation and Characterization

The samples were prepared at the laboratories of E13 at Munich Technical University and the facilities of the geological department of the Ludwig-Maximilians University Munich. The samples were prepared in platinum tubes of 5.0 mm diameter (0.1 mm wall thickness) and a length of 25 mm. In order to meet the temperature of 1200 K to 1700 K at several kbars of pressure, an internally heated autoclave was used. The samples were characterized

with optical microscopy, X-ray diffractometry, infra-red spectroscopy (FTIR), differential scanning calorimetry (DSC) and by simultaneous thermal analyzers (STA). It could clearly be shown that water is dissolved, partially to SiOH groups, partially in the form of physically dissolved water molecules. The details of the sample preparations were previously described by Müller [Mu04]. Unfortunately the preparation of deuterated samples was not successful in this work, due to exchange between normal and deuterated water in the autoclave.

5.3.2 Available Samples

The sodium and sodium alumino silicates were available as solid pieces as well as powders. The following samples were available for neutron scattering experiments. Note that NS3 refers to $Na_2O+3SiO_2=Na_2Si_3O_7$ and albite refers to $NaAlSi_3O_8$. In order to obtain the

silicate	X = 0.0	X = 1.8	X = 3.0	X = 3.4	X = 4.5
SiO_2 + X wt.% p	s	-	-	s	-
NS3 + X wt.% H_2O	p	p/s	p/s	-	-
albite + X wt.% H_2O	p	p/s	p/s	-	s

Table 5.2: *Samples provided by Axel Müller [Mu04]. Powder samples (p) and solid piece samples (s) were used for different types of experiments.*

physical properties of the samples it is necessary to switch from mass percentages to molar percentages. The following table gives the conversions to mol% of for the compositions of table 5.2. Since all physical the properties of the systems scale with the molar percentage of

silicate	X = 0.0	X = 1.8	X = 3.0	X = 3.4	X = 4.5
SiO_2 + X wt.% H_2O	0.0	-	-	10.5	-
NS3 + X wt.% H_2O	0.0	5.8	9.4	-	-
albite + X wt.% H_2O	0.0	5.8	9.4	-	13.7

Table 5.3: *Molar water percentages of the samples*

water, all concentrations are given in mol% in the following. Average molecular masses are, according to equations 4.16 and 4.17 needed in order to perform an incoherent approximation. The average atomic molecular masses of water (H_2O) and heavy water D_2O are 6 g/mol and 6.67 g/mol respectively. With these values and the molar percentages given in table 5.3 it is possible to compute the average atomic molar masses which are presented in table 5.4.

silicate	X = 0.0	X = 5.8	X = 9.4	X = 10.5	X = 13.7
SiO_2 + X mol% H_2O	20.0	-	-	18.5	-
NS3 + X mol% H_2O	20.2	19.4	18.8	-	-
albite + X mol% H_2O	20.2	19.3	18.8	-	18.2

Table 5.4: *Average atomic molar masses [g/mol] of the samples.*

The neutron scattering properties of the samples are given by their average scattering and absorption cross sections and the average number of scattering atoms in the beam. According to the compositions given in table 5.2 the average scattering cross sections for each sample can be calculated: This splits into coherent and incoherent contributions as follows The

silicate	X = 0.0	X = 5.8	X = 9.4	X = 10.5	X = 13.7
SiO_2 + X mol% H_2O	3.544	-	-	9.066	-
NS3 + X mol% H_2O	3.566	6.603	8.505	-	-
albite + X mol% H_2O	3.472	6.524	8.424	-	10.664

Table 5.5: *Scattering cross sections σ_s* [barn] *at of samples investigated in the present work.*

silicate	X = 0.0	X = 5.8	X = 9.4	X = 10.5	X = 13.7
SiO_2 + X mol% H_2O	3.542	-	-	3.434	-
NS3 + X mol% H_2O	3.285	3.244	3.225	-	-
albite + X mol% H_2O	3.346	3.301	3.274	-	3.240

Table 5.6: *Coherent scattering cross sections σ_{coh}* [barn] *at of samples investigated in the present work.*

silicate	X = 0.0	X = 5.8	X = 9.4	X = 10.5	X = 13.7
SiO_2 + X mol% H_2O	0.002	-	-	5.632	-
NS3 + X mol% H_2O	0.281	3.359	5.280	-	-
albite + X mol% H_2O	0.126	3.223	5.150	-	7.424

Table 5.7: *Incoherent scattering cross sections σ_{inc}* [barn] *at of samples investigated in the present work.*

absorption cross section are given in 5.8

5.3.3 Sample Environments

The first step in a successful experimental setup is the appropriate choice of the sample container. Unfortunately experiments are currently restricted to temperature below the glass transition temperature T_g. The desired environment for quasielastic experiment above T_g would be a pressure cell for elevated temperatures.
For the measurements below T_g, of course the ratio of neutron scattering from the sample container and the sample itself should be as small as possible and self-absorption and multiple scattering have to be suppressed. For this reason, a hollow cylinder is generally favorable. Solid piece sample were nevertheless put into full cylinders, in order not to destroy the pieces. The so called "cryoloop" was used for high and low temperature measurements. Here a flat slab, filled with powdered sample, is fixed inside a loop with heating and cooling (liquid nitrogen) facilities. The temperature can be kept stable with this apparatus within ± 0.5 K between 100 K and 500 K.

silicate	X = 0.0	X = 5.8	X = 9.4	X = 10.5	X = 13.7
SiO_2 + X mol% H_2O	0.057	-	-	0.074	-
NS3 + X mol% H_2O	0.131	0.136	0.140	-	-
albite + X mol% H_2O	0.098	0.105	0.110	-	0.115

Table 5.8: *Absorption cross sections σ_a [barn] at 2200 m/s of samples investigated in the present work.*

For the material of the container, a good compromise of intensity and multiple scattering / absorption has to be found. The material that is commonly used is aluminum, except for neutron diffraction. Since aluminum is a crystalline metal with a relatively high coherent scattering cross section of $\sigma_{coh} = 1.495$ barn , it would "contaminate" the amorphous diffraction pattern considerably. Therefore vanadium containers are preferred due to the high incoherent and a coherent scattering cross section of only 0.018 barn. On D20, the spectra were recorded, the solid sample pieces (as fabricated) put into full vanadium cylinders of 6 mm diameter and 0.1 mm thickness. For the time-of-flight measurements on IN6, the intensity of the samples respective to the aluminum can is sufficient in order to extract clean vibrational spectra (see figure 7.17). Also multiple scattering events seem to play no role. Unfortunately a really well defined geometry could only be realized with powder samples in full cylinders. The solid pieces have the natural disadvantage that they don't fill up the sample can completely. The same holds for powder samples in the flat slabs of the cryo-loop where the powder assembled in the bottom half of the vertically fixed slab. In the latter cases it is hence rather difficult to perform good self absorption and multiple scattering corrections.

5.3.4 Neutron Wave Lengths

For diffraction experiments the choice of the neutron wavelength λ is rather obvious since for elastic scattering the covered q-range is given by

$$q = \frac{4\pi}{\lambda} \sin(\Theta) \tag{5.6}$$

According to equation 5.6 lower wave lengths give access to higher q-ranges. Since the main interest in the case of hydrous silicates is the variation of the main structural peaks in the structure factor of pure silica, a wavelength of 0.95 Å on D20 is sufficient to record the structure factor from 0 $Å^{-1}$ to roughly 13 $Å^{-1}$.
In the case of inelastic scans on time-of-flight spectrometers, the choice of the appropriate wavelength follows in principle the same criteria. IN6 can be operated at only four wavelengths between 4.14 Å and 5.9 Å. The available neutron flux varies considerably between the four possible wavelengths. According to Eq. 4.3 the choice of the wavelength and hence k_i has also consequences for the inelastic part of the spectrum. Note that for elastic scattering Eq. 4.3 becomes Eq. 5.6. The full q-ω domain accessible on IN6 for a wavelength of 4.1 Å is shown in figure 5.8. For smaller wavelengths the accessible wave vector transfer range is higher for any energy transfer $\hbar\omega$. This property becomes particularly important if the inelastic spectrum has to be related to a vibrational density of states. It was pointed out in section 4.2 that in order to achieve a good cancellation of the interference terms

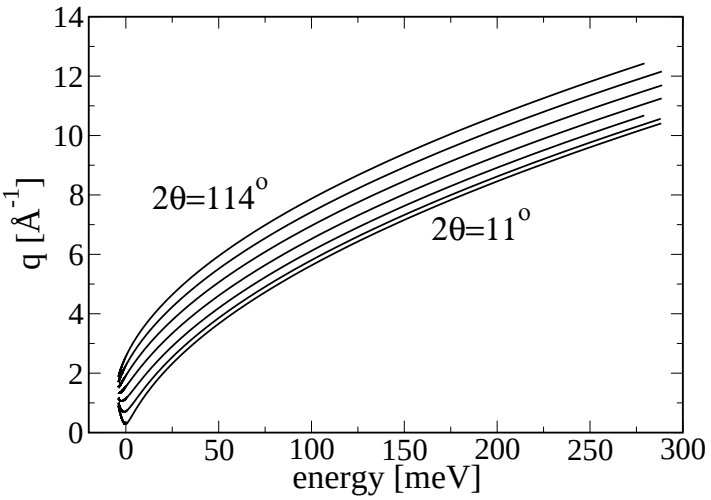

Figure 5.8: *q-ω domain of the ILL time-of-flight spectrometer IN6 at a wavelength of 4.1 Å.*

$\exp\{i\mathbf{q}(\mathbf{R}_J - \mathbf{R}_I)\}$ in equation 4.13, a high q-range in preferable. For that reason the wavelength of 4.1 Å was chosen on IN6 in order to record the vibrational properties of hydrous silicates. The chopper phases were mostly chosen such that all elastically scattered neutrons reach the detectors at the same time (*elastic focusing*). This corresponds to a chopper phase of one. Since the goal of the time of flight experiments on IN6 are to extract inelastic properties, a chopper focus on another energy could improve the instrument resolution. However, since time-of-flight focusing on inelastic parts of the spectrum would require a chopper phase of two which only allows half of the neutrons to be exploited, the option of inelastic focusing was not always chosen.
Further information on specific setups can be found in appendix D.

Chapter 6

Results of the Simulation

6.1 Structure of the Liquid

It should be mentioned at the beginning of this discussion that pure amorphous silica is a perfectly geometrically disordered network of SiO_4 tetrahedrons up to temperatures of several thousands of Kelvin. Apart from two membered SiOSiO rings that tend to form at elevated temperatures [Sa95a], no other significant structural changes occur at elevated temperatures. The following figure shows snapshots of pure and hydrous silica at a temperature of 3500 K. Apparently all hydrogen atoms are attached to the silica matrix in the form of

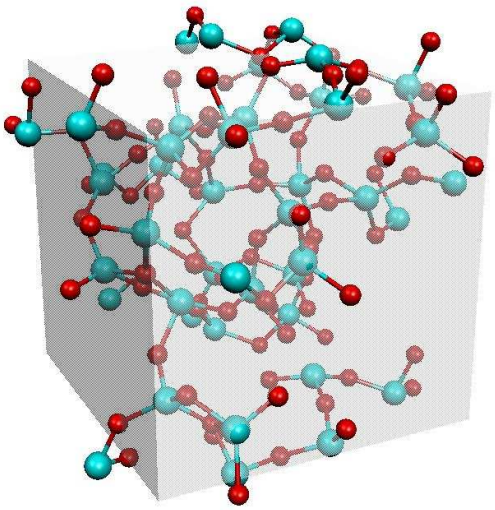

Figure 6.1: *Snapshot of SiO_2 at 3500K. Silicon atoms (green spheres) and oxygen atoms (red spheres) ordered in a tetrahedral network. Drawn from [Be00].*

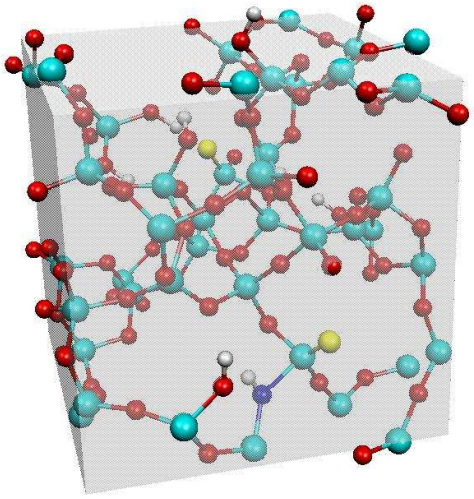

Figure 6.2: *Snapshot of SiO_2+11.8mol%H_2O at 3500K. Hydrogen (white spheres) and SiO dangling bonds (yellow spheres) and O tri-cluster (blue spheres).*

SiOH groups in the hydrous liquid. It can be seen that, apart from the presence of hydrogen atoms, the structure of the hydrous liquid exhibits also other states whose appearance is not a priori evident. In particular SiO dangling bonds highlighted in yellow and oxygen

tri-clusters highlighted in orange are present.
The aim of the present section is to specify quantitatively the occurrence of structural properties in the hydrous liquid compared to pure silica. The basis of the analysis is certainly not only the snapshot of figure 6.2 but an average over all configuration in the equilibrated part of the molecular dynamics trajectories at 3500K and 3000K. Commonly considered quantities like pair distribution functions, bond angle distributions, coordination numbers, Q-species distributions and bridging to non-bridging oxygen ratios will be discussed and, as far as possible, be compared to the data extracted from *ab initio* simulated silica and sodium silicate (NS4) melts [Is01, Be01]. In particular the comparison to a recently investigated sodium tetra-silicate melt [Is01] is highly interesting since the valence shell configuration of the sodium and the hydrogen atoms are equivalent.
In order to analyze the structure with particular attention to the formation and the rupture of the silica network, water molecules and hydroxyl groups, it turns out to be useful to distinguish several types of oxygen atoms:

O*	hydroxyl group oxygen Si-O-H (oxygen with one hydrogen and one silicon nearest neighbor)
wO	water molecule oxygen H-O-H (oxygen with at least two hydrogen atoms as nearest neighbors)
BO	bridging oxygen Si-O-Si (oxygen with two silicon atoms as nearest neighbors)
NBO	non-bridging oxygen Si-O(-?) (oxygen with less than two silicon nearest neighbors)
O3	tricluster oxygen (oxygen with three nearest neighbors)
O3H	hydrogen containing tricluster $\begin{matrix}\text{Si}\\\text{Si}\end{matrix}$>O-H (oxygen with two silicon and one hydrogen neighbor)

Note that, within these definitions, all the O* are also counted as NBO and that all the O3H are also counted as O3 as well as BO. The wO oxygen atoms can also have silicon neighbors, e.g. the oxygen atom in H_2OSi is considered as a wO.
The Si and H nearest neighbors of the oxygen atoms were determined as the Si and H atoms being located within a sphere the radius of which is given by the positions of the first minima in the Si-O and O-H pair distribution functions, respectively (see section 6.1.1).
Concerning the dynamical properties of the system, the restriction imposed by the thermostats should be recalled. Nevertheless it will be shown that also the structural analysis of the liquid is able to provide considerable information on the dynamics.

6.1.1 Radial Distribution Functions

In this subsection the short range correlations of the liquid are analyzed in terms of the radial distribution functions (RDF)

$$g_{ab}(r) = \frac{D_{ab}(r)}{4\pi r^2\, \rho_a A_b\, dr} \quad \text{with} \quad \rho_a = \frac{N_b}{V} \quad \text{and} \quad A_b = N_b - \delta_{ab} \tag{6.1}$$

where $D_{ab}(r)$ is the number of inter atomic distances between a and b atoms found between r and $r + dr$. N_i denotes the number of atoms of each kind and V is the volume of the

simulation box. The corresponding integrated coordination numbers (ICN) are

$$\mathrm{ICN}_{ab}(r) = \frac{1}{A_a}\int_0^r D_{ab}(r')\,dr' \quad \text{with} \quad A_a = N_a - \delta_{ab} \tag{6.2}$$

The RDF and ICN are presented in the left panel of Fig. 6.3 for the network forming atoms silicon and oxygen (a, b =Si,O) and in the right panel for the pairs involving H.

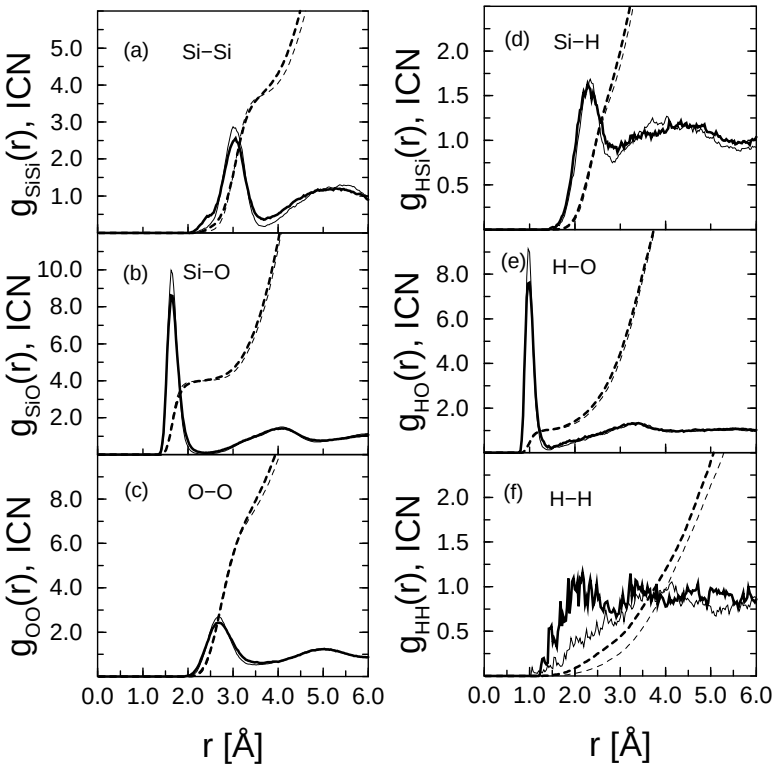

Figure 6.3: *Radial distribution function (solid lines) and integrated coordination numbers (dashed lines) of Si-Si (a), Si-O (b), O-O (c), Si-H (d), H-O (e), and H-H (f) for the SiO_2-H_2O liquids at 3500 K (bold lines) and 3000 K (thin lines).*

From this figure, one recognizes that the peaks of the distributions become broader as the temperature is increased. The RDFs involving the matrix atoms show a first peak followed by a well defined first minimum which becomes more pronounced if the temperature is decreased from 3500 K to 3000 K. In particular, the Si-O RDFs present, after the first peak, a very well defined minimum at 2.37 ± 0.05 Å for 3500 K and at 2.35 ± 0.05 Å for 3000 K. From the position of the Si-O first peak, one can deduce that the most probable Si-O distance is around 1.65 ± 0.02 Å for 3500 K and around 1.63 ± 0.02 Å for 3000 K.
The ICN for Si-O exhibits a plateau at a value of 4 which indicates that every silicon atom has on average four oxygen neighbors and hence that the principal units - the SiO_4 tetrahedron - are preserved also in the presence of water. Indeed only a small percentage of threefold and fivefold coordinated Si atoms are found in the liquids (7 % fivefold coordinated and 4 % threefold coordinated at 3500 K and 2 % fivefold coordinated and 1 % threefold coordinated at 3000 K). On the other hand, the ICN for Si-Si shows an inflection point at around 3.6, a value which is smaller than the one for a perfect tetrahedral network, 4.0, indicating that the tetrahedral network is partially broken.
Comparing the matrix distributions to those of the pure silica melt, one notes that the addition of water does not alter significantly the shapes of the Si-O, O-O and Si-Si RDFs

presented in [Be01], as it was already the case in the sodium silicate melt [Is01] upon the addition of sodium.

The RDFs for H-Si and H-O, right panel of Fig. 6.3, show somewhat better defined interatomic distances as the temperature is decreased, as was the case for the Si-O, Si-Si and O-O RDFs. On the other hand the H-H distribution seems to deviate from this behavior. Concerning the H-Si distribution, the first maximum is found around 2.3 Å. Since this value is much larger than the most probable Si-O distances (1.65 ± 0.02 Å and 1.63 ± 0.02 Å), the presence of stable molecular Si-H units is excluded. The height of the first peak in Si-H and the absence of a well-defined minimum reflect the presence of a broad distribution of these distances in the liquid. In contrast to this, the well-defined first peak in the H-O distribution functions, located at 0.99 ± 0.01 Å, followed by a well defined minimum at 1.48 ± 0.03 Å at 3500 K and at 1.43 ± 0.03 Å at 3000 K, reveals the O-H bond as the dominant stable configuration for the hydrogen atoms. Because of a lack of a well-defined first peak in the RDF for H-H, the existence of stable H_2 molecules can be excluded too. The striking point in the H-H distribution is the difference between the RDF at 3000 K and 3500 K between 1.5 Å and 3.0 Å. Whereas at 3000 K there are almost no H-H pairs with a distance around 2.0 Å a weak peak is found at this distance at 3500 K. This distance is very close to the H-H distance in a free water molecule and hence we have evidence that at this temperature water molecules do exist. Indeed, in a more detailed analysis of the coordination numbers as a function of time, it is found that oxygen atoms with two nearest neighbor hydrogens were stable over times of the order of 500 fs. The absence of this phenomenon at 3000 K is probably due to the considerably lower displacement of the hydrogen atoms (see Fig. 5.6) at this temperature which, because of a too small trajectory length, prevents two hydrogen atoms sufficiently close to each other to form a water molecule from being observed.

At this point it should be recalled that the configuration of the valence shell is the same for the hydrogen and the sodium atoms (although it is well known that the physical and chemical properties of compounds of equivalent stoichiometry involving these two atom types (such as H_2O and Na_2O) are rather different). This behavior motivates a comparison of the results of this study to those of the liquid sodium silicate [Is01]. In Fig. 6.4, the comparison of the above discussed hydrogen-containing RDFs with the corresponding Na-containing RDFs in the sodium tetra-silicate melt at 3500 K from Ref. [Is01] is presented. Two main properties seem to govern the character of the distributions: The size of the atoms and the ability of the two atom types to form either covalent or ionic bonds. In particular, the RDF for Si-X and X-X (X = Na, H) shown in Fig. 6.4 look quantitatively quite similar except that the peaks are shifted to larger distances in the case of Na. This behavior can be easily related to the atom size. In contrast to this, the O-X distribution function for X=H has a very different shape from the one for X=Na. As described above, for the O-H correlation, a sharp peak at an O-H distance of 0.99 Å $\pm$ 0.01 is followed by a well-defined minimum. In contrast to this, the first peak of the O-Na RDFs is much broader with a maximum at 2.32 ± 0.05 Å followed by a shallow minimum around 3.6 Å. These latter differences are the signature of the strong covalency of the OH bond and the ionicity of the Na-O bond.

To conclude the section on the radial distribution functions, it should be investigated how the different oxygen types defined above contribute to the RDF. In order to count the number of Si and H neighbors of a given oxygen atom, cutoff distances extracted from the first minima of the Si-O and H-O radial distribution functions, respectively (cutoff for SiO = 2.37

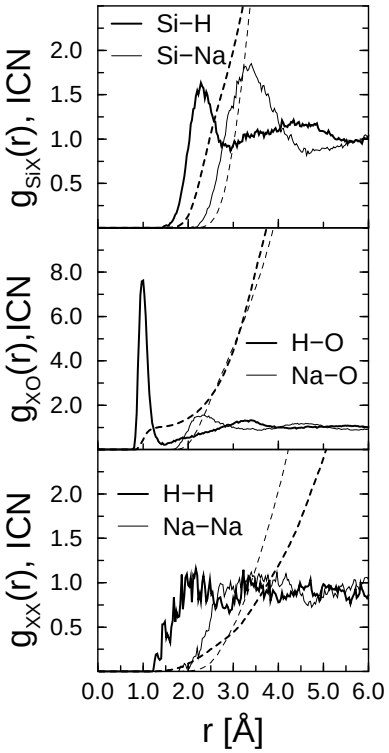

Figure 6.4: *Si-X, X-O, X-X (X=H,Na) radial distribution functions (solid lines) and integrated coordination numbers (dashed lines) for the hydrous silica (bold lines) and the NS4 melt from Ref. [Is01] (thin lines) at 3500 K.*

Å and 2.35 Å and cutoff for HO=1.48 Å and 1.42 Å for the higher and the lower temperature, respectively) were used. Figure 6.5 shows the H-O radial distribution functions for the different oxygen types (O*, NBO, BO) compared to the total H-O RDF at 3500 K. Results obtained for 3000 K are very similar and are therefore not shown here. The radial pair distributions for the different oxygen types were normalized on the corresponding number of the considered species at each time step (note that the number of each species can vary with time).

One notes that the RDFs for all the different oxygen types show a pronounced peak around 1.0 Å but that the height of this first peak depends strongly on the considered oxygen type. The H-O* RDF exhibits a first peak of height 65 which is much larger than the one for the total H-O which is around 8. In contrast to this, the RDF for H-BO has a first peak of height 1. The most striking point in Fig. 6.5 is that the peak for H-O* is significantly higher than the one for H-NBO. Since all O* atoms are also NBO atoms (remember that by definition the O* atoms have a hydrogen atom as second neighbor whereas for the NBO atoms this is not necessarily the case), the presence of a large number of Si-O dangling bonds becomes now evident. The existence and the temperature dependence of these dangling bonds will be discussed below. From the inset of Fig. 6.5, it can be concluded that the H-NBO contribution is dominant for distances between 1.5 Å - 2.5 Å. This means that the NBO atoms are also connected to hydrogen atoms via the so-called hydrogen bonds, the length of which is equal to 2.0 Å in the water dimer. The RDF for the other oxygen types also show a contribution in this range but it is less important. In Fig. 6.6, the contribution of the different oxygen types to the Si-O radial distribution function is presented. The height of the first peak of the Si-BO RDF is around 9.3 whereas the peak height of the total Si-O RDF is close to 8.7

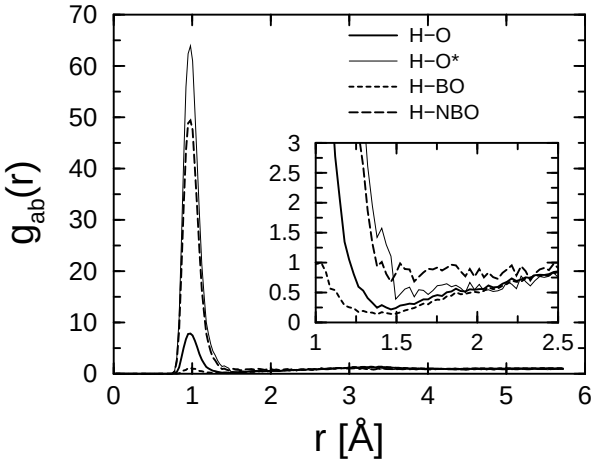

Figure 6.5: *Pair distribution functions at 3500 K for H-O (bold solid line), H-BO (dashed line), H-NBO (long dashed line) and H-O* (thin solid line). Inset: Zoom of the minima of the radial distribution functions after the first peaks.*

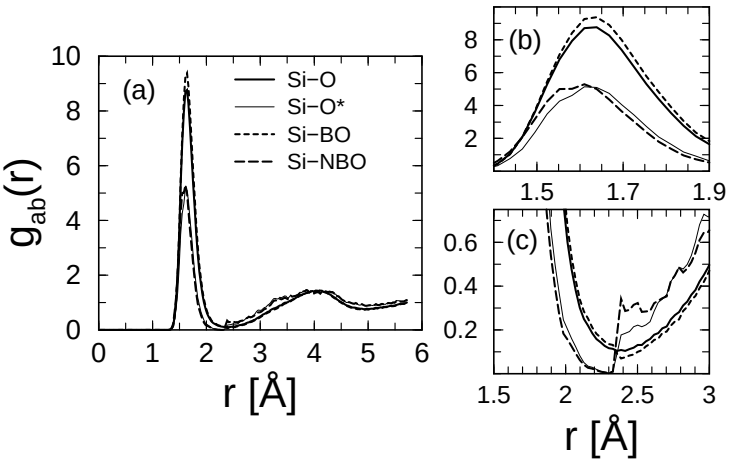

Figure 6.6: *Pair distribution functions at 3500 K for Si-O (bold solid line), Si-BO (dotted line), Si-NBO (dashed line), and Si-O* (thin solid line). (b) and (c) are magnifications of the first peaks and first minima, respectively.*

which indicates that the correlation of the bridging oxygen with silicon atoms is stronger than the total Si-O correlation (see Fig. 6.6b). The heights of the first peak in the Si-O* and Si-NBO RDFs are very close to each other at a value of ≈ 5.1. As shown in Fig. 6.6b, a slight shift of the peak positions can be observed: The Si-NBO and Si-O* peak positions are around 1.60 Å and 1.62 Å, respectively, whereas the Si-BO peak position is located at 1.63 Å. This result implies that the tetrahedron having one or more NBO atoms are distorted, as it has already been observed in other silicate systems (see Ref. [Is01] and references therein). Figure 6.6c shows the presence of a considerable jump in the RDFs for Si-O* and Si-NBO at the Si-O cutoff. Between 2.37 Å (the Si-O cutoff) and 4.0 Å, the Si-O* and Si-NBO RDFs are larger than the total one (Fig. 6.6c). This jump and the dominance of the Si-O* and Si-NBO can be associated to oxygens of the O* type or to NBOs that are connected to a second silicon atom by a weak Si-O bond. As soon as the distance to the second silicon atom becomes smaller than the cutoff (i.e. an O3H or BO is formed) the oxygen is considered as BO and therefore the Si-O* or Si-NBO distribution drops abruptly to zero at the cutoff distance. Thus this behavior gives insight into the formation and decay processes of the O3H

clusters and the Si-O dangling bonds, that will turn out to be one of the essential transition states for hydrogen diffusion.

6.1.2 Angular Distributions

Figure 6.7 presents the different angular distributions in the SiO_2-H_2O liquids at 3500 K and 3000 K and the comparison with NS4 at 3500 K. The angular distributions for the network formers (Si-O-Si) and (O-Si-O) are close to the ones of pure silica at 3500 K [Be01]. In

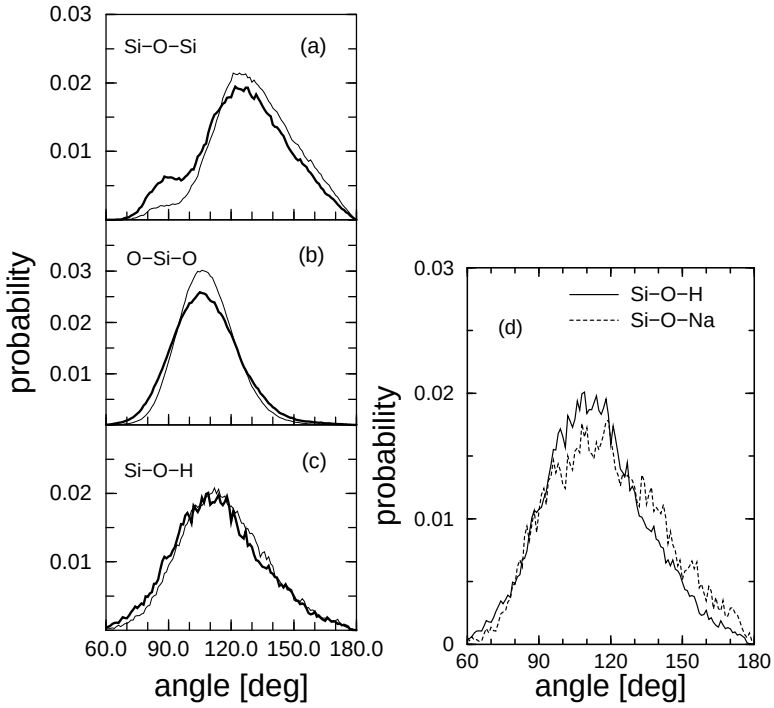

Figure 6.7: *(a)-(c) Angular distributions of the hydrous silica sample at 3500 K (bold lines) and 3000 K (thin lines); (d) comparison to NS4 at 3500K (dashed line).*

agreement with the behavior of the RDFs (Sec. 6.1.1), the angular distributions at the lower temperature are sharper and more peaked. The Si-O-Si distribution shows an additional hump at 90° that is also present in pure silica at 3500 K but much less pronounced. This hump is due to the two membered rings which are formed by two SiO_4 units connected by an edge and having two common oxygen atoms. As will be seen in Sec. 6.1.4, these units are related to intermediate states that are relevant for the diffusion process. From the Si-O-Si distribution in Fig. 6.7, one notes that the number of such rings increases with increasing temperature. The O-Si-O angular distributions present a well-defined maximum at $\approx 110°$ which corresponds to a typical intra-tetrahedral angular distribution (the ideal tetrahedral angle $\approx 109°$). Finally, one recognizes that the temperature dependence of the Si-O-H distribution seems to be significantly weaker than the one of the Si-O-Si and O-Si-O distributions. The Si-O-X (X= H, Na) angular distributions at 3500 K (Fig. 6.7d) present very similar shapes with a slight shift to larger angles for the sodium silicate liquid. In both cases a broad maximum can be seen at angles between 108° and 115°. A maximum in this range shows that, in both cases, the chemistry of a twofold coordinated oxygen with a lone pair is realized. The shift of the mean angle to a higher value for the sodium silicate is certainly

an effect of the larger size of the sodium atom since for larger atoms the repulsion of the electron shells of the two oxygen-ligand atoms becomes more important.

6.1.3 Structure Factors

The neutron scattering structure factor was calculated according to

$$S_n(q) = \frac{1}{N_{\mathrm{Si}} b_{\mathrm{Si}}^2 + N_{\mathrm{O}} b_{\mathrm{O}}^2 + N_{\mathrm{H}} b_{\mathrm{H}}^2} \sum_{k,l}^{N} b_k b_l \langle \exp[i\mathbf{q} \cdot (\mathbf{r}_k - \mathbf{r}_l)] \rangle \tag{6.3}$$

where b_k (k=Si,O,H) are the coherent neutron scattering lengths and $\langle \cdot \rangle$ is the thermal average. The scattering lengths were taken from Ref. [Ni95] where $b_{\mathrm{Si}} = 0.41491 \times 10^{-14}$ m, $b_{\mathrm{O}} = 0.5803 \times 10^{-14}$ m and $b_{\mathrm{H}} = -0.374 \times 10^{-14}$ m are reported. A very important feature for the experimental verification of the simulation is the replacement of hydrogen by its isotope deuterium. Since the coherent scattering length of deuterium ($b_{\mathrm{D}} = 0.671 \times 10^{-14}$ m) is quite different from that of hydrogen, the contribution of the hydrogen atoms to the total structure factor can be revealed. Figure 6.8a shows the neutron scattering structure

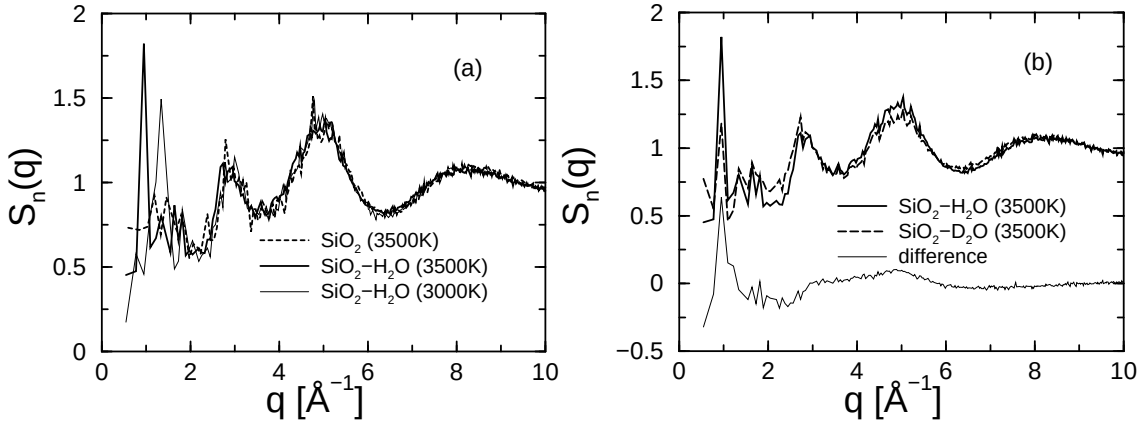

Figure 6.8: *(a) Total neutron scattering structure factor of the hydrous silica liquids at 3000 K (thin line) and at 3500 K (bold line) and of a pure silica liquid at 3500 K (dashed line); (b) Total neutron scattering structure factor for the hydrous silica liquid at 3500 K (bold solid line), the deuterated liquid (bold dashed line) and the difference (thin solid line).*

factor $S_n(q)$ for both simulated temperatures in comparison to the simulated dry silica liquid at 3500 K [Be01]. For $q > 2.0$ Å^{-1}, the three curves can be considered to be identical which is in agreement with the fact that we did not see any differences in the Si-Si, Si-O and O-O radial distribution functions for silica, the sodium silicate, and the hydrous silica liquids. In contrast to this, the $q \leq 2.0$ Å^{-1} region of $S_n(q)$ of the hydrous silica liquid exhibits a prepeak at 0.95 Å^{-1} at 3500 K and at 1.3 Å^{-1} at 3000 K which is not present in the pure silica melt. (It should be mentioned that the box size of the hydrous silica liquid is 11.5 Å, corresponding to a minimum value of q of 0.55 Å^{-1} and thus the prepeak found at 0.95 Å^{-1} can not be attributed to a size effect. Note also that the number of silicon and oxygen atoms was almost equivalent in the simulation of pure silica and hence the statistical accuracy is as well comparable.)

For the sodium silicate it turned out that the long range correlations ($q \leq 2.0$ Å^{-1}) contain important information on the diffusion mechanism as it was shown recently [Ho01, Ho02,

Me02, Me04]. It was found that in the liquid a network of channels is formed which enables the sodium atoms to move rapidly through the SiO-matrix. This channel structure is thus able to explain the relatively high diffusion constant of sodium atoms in sodium silicate melts. The characteristic distance between these channels is around 6 Å, i.e. two tetrahedron diameters, and gives rise to a prepeak in the structure factor at about 1 $Å^{-1}$, a structural feature which has indeed been found in recent neutron scattering experiments [Me02] (see also figure 1.5).

Fig. 6.8b shows the structure factor at 3500 K for the hydrated silica and deuterated silica liquids as well as their difference. Remarkable differences of the two signals are found at 0.95 $Å^{-1}$, around 2.0 $Å^{-1}$ and around 5.0 $Å^{-1}$. Since the most important contributions to the difference are located in the q-vector region of the prepeak (at 0.95 $Å^{-1}$), the prepeak can be directly attributed to the presence of the hydrogen atoms. For a deeper understanding of the prepeak origin in the hydrous melts, we analyzed the partial structure factors presented in Fig. 6.9.

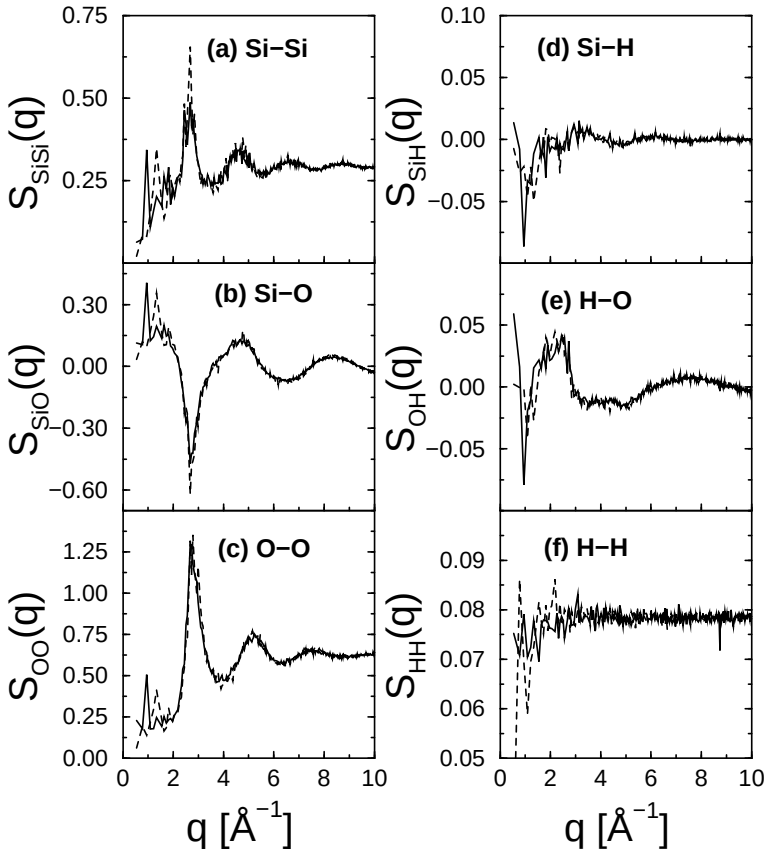

Figure 6.9: *Partial structure factors of the hydrous silica liquids at 3000 K (dashed line) and at 3500 K (bold line).*

The partial structure factors $S_{ab}(q)$ are related to the total $S_n(q)$ presented in Fig. 6.8 as follows:

$$S_n(q) = \frac{1}{\sum_a N_a b_a^2} \sum_{ab}^{N} b_a b_b S_{ab}(q) \tag{6.4}$$

where $S_{ab}(q)$ are given by

$$S_{ab}(q) = \frac{f_{ab}}{N} \sum_{k}^{N_a} \sum_{l}^{N_b} \langle \exp[i\mathbf{q} \cdot (\mathbf{r}_k - \mathbf{r}_l)] \rangle \tag{6.5}$$

and f_{ab} is equal to 0.5 for $a \neq b$ and equal to 1.0 for $a = b$. The partial structure factors in Fig. 6.9 can be separated in a group describing the silica matrix distributions (Si-Si, Si-O, O-O) and in a group involving distributions with H (Si-H, O-H, H-H) as it was done for the RDFs (see Sec. 6.1.1). For the matrix part, we find for $q > 2.0$ Å $^{-1}$ a nearly perfect agreement between the structure factors presented in Fig. 6.9 and the ones extracted from the NS4 liquid simulation from Ref. [Is01]. The only difference is the prepeak at 0.95 Å^{-1} for 3500 K and at 1.3 Å^{-1} for 3000 K. One recognizes therefore a modification of the matrix at a length scale between 4.8 Å and 6.6 Å which was not visible in the RDF representation. Since the prepeak is present not only in the partial structure factors involving hydrogen, but also in the O-O and Si-Si distributions, one notes that the network modification does not only concern the hydrogen atoms. This behavior can be understood by taking into account the strong and well defined bonding of the hydrogen atoms to the silica network (see the O-H radial distribution function in Fig. 6.3).

6.1.4 Distribution of Nearest Neighbors

In this section the nearest neighbor coordination numbers are discussed. The nearest neighbors of an atom were again determined as the atoms that are located within a sphere with a radius that is given by the positions of the first minima in the corresponding radial distribution function. Whereas the average coordination number has already been extracted from the RDFs themselves (Fig. 6.3), the distributions are presented now. The discussion is limited to the coordinations of the network forming atoms. The errors for the results presented in this section are related to the number of independent configurations in the liquid. A configuration is assumed to be independent of a previous one if they are separated by the time it takes for the atoms to show a diffusive motion. From Fig. 5.6 it can be recognized that for T=3000 K and T=3500 K one has two and three independent configurations, respectively. Thus the relative errors are $1/\sqrt{2} = 0.71$ at 3000 K and $1/\sqrt{3} = 0.58$ at 3500 K which are then divided by the square root of the average quantities in question. The resulting absolute errors will be given in the text.

As for the other quantities described above, we begin with the temperature dependence of the distributions in the hydrous liquid and extend the study of the comparison of these distributions with the ones found in the sodium silicate liquid.

Figures 6.10a and b present the Si-O and O-Si distributions for the two temperatures of the hydrous silica liquid. Both coordination probabilities confirm the picture drawn from the analysis of the previous quantities: The silica network is still present in the hydrous silica liquid since one finds a maximum of the Si-O distribution at a coordination of four and a maximum of the O-Si distribution at a coordination of two.

In agreement with the temperature dependence of the RDFs and of the angle distributions, the coordination distributions become broader as the temperature is increased. For the higher temperature, the Si-O distribution shows significant contributions at coordination numbers of three and five and the O-Si distribution shows contributions at a coordination of one.

In addition, the O-Si coordination reveals the speciation of the water molecules, since one does not find a significant contribution at a coordination number of zero. Therefore the existence of free water molecules can be excluded (a free water molecule has zero silicon

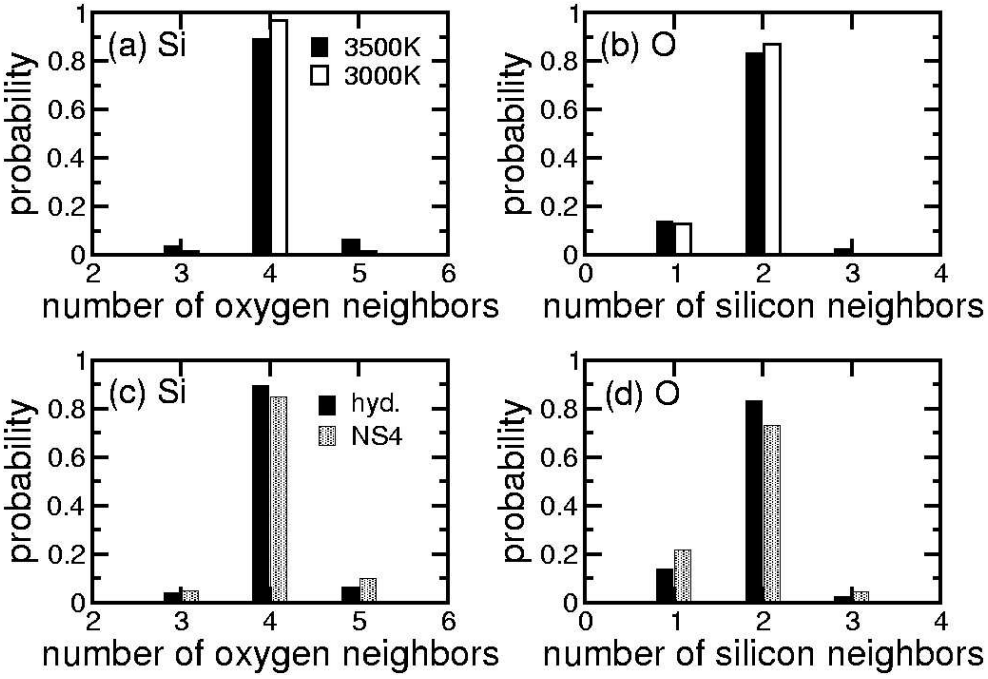

Figure 6.10: *Si-O (a) and O-Si (b) coordination distributions for the hydrous silica liquids at 3500 K (black bar) and 3000 K (white bar) and Si-O (c) and O-Si (d) for the sodium tetra-silicate at 3500 K (gray bar) [Is01]. The black bars in (c) and (d) are identical to the ones in (a) and (b) and represent the hydrous liquid at 3500 K.*

neighbor). Note that in reality the numerical value is non-zero (but too small to be visible in the figure) because of the presence of *transient* water molecules in the liquid at 3500 K. In contrast, the contribution at a coordination of one is roughly $\frac{1}{8}$ at both temperatures, corresponding to the fraction of the non-bridging oxygens in the system that compensates the charges of the eight hydrogen atoms in the form of O-H groups.

Since the dissolution product of water in silica is almost exclusively made of Si-OH units, the dissolution mechanism is similar to that of disodium oxide in the NS4 liquid. To compare these two mechanisms, the Si-O and O-Si coordination numbers of the hydrous silica liquid and of the sodium tetra-silicate liquid at 3500 K are presented in Figs. 6.10c and d [Is01]. When comparing these two systems, the concentration of sodium atoms of 13.3 mol % in the NS4 melt and the concentration of hydrogen atoms of 7.8 mol % in the hydrous silica melt should be taken into account. The Si-O coordination distribution has basically the same shape for both systems with a clear maximum at a coordination number of 4 even though the distribution for NS4 is, somewhat broader. The O-Si coordination probability presents stronger differences. Both distributions have their maximum at 2 (indicating that in both cases the silica network is still present) but the absolute values are quite different. In both cases the O-Si probability for having one silicon neighbor deviates significantly from zero. This indicates the formation of O* in the hydrous melt and equivalent oxygen types in the NS4 melt (hereafter denoted by NaO*). If the dissolution product was exclusively given by O* and NaO*, the coordination probability would correspond to the N_H/N_O ratio or to the N_{Na}/N_O ratio, respectively, where N_H, N_O and N_{Na} are the number of hydrogen, oxygen or sodium atoms in the different systems. These ratios are equal to $\frac{12}{54} = 0.222$ for the sodium silicate liquid and to $\frac{8}{64} = 0.125$ in the hydrous silica one. Figure 6.10d shows a contribution

of 0.139 ± 0.027 for the hydrous silica sample and of 0.218 ± 0.037 for the NS4 sample which is in agreement with the simple theoretical prediction. In the hydrous case, one notes again the important presence of Si-O dangling bonds at 3500 K compared to the NS4 liquid at the same temperature.

A quantity closely related to the O-Si and Si-O coordinations is the distribution of the Q^n species, where n denotes the number of bridging oxygens attached to a silicon atom. For the simulated systems, one notes that for a perfect dissolution of the water into OH groups, one expects a probability for Q^3 equal to $\frac{8}{30} = 0.267$, the ratio between the number of hydrogen and silicon atoms, if all OH groups are attached to different silicon atoms. Indeed Fig. 6.11

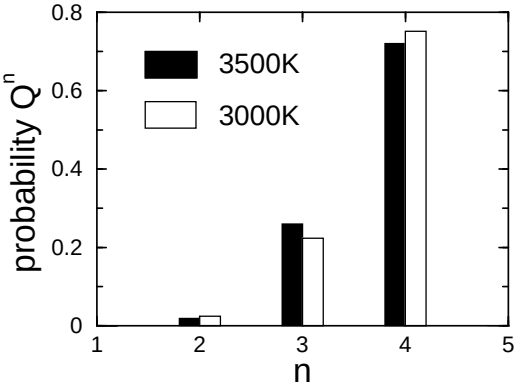

Figure 6.11: *Probability to have a Q^n speciation for the hydrous sample at 3500 K (black bars) and 3000 K (white bars).*

exhibits a probability of Q^3 sites of 0.229 ± 0.062 at 3000 K and of 0.269 ± 0.055 at 3500 K, respectively. The contributions at $n = 2$ of 0.029 ± 0.022 at 3000 K and of 0.023 ± 0.016 at 3500 K are relatively small. In particular, these contributions are smaller than $\frac{8}{30}\frac{7}{30} = 0.062$, the probability that two H among the eight of the system are found on the same Si tetrahedron, which indicates that the Si-O-H groups tend to avoid each other. Due to the absence of contributions at $n = 1$ and $n = 0$, one can exclude the possibility for a clustering of O-H groups on specific silicon atoms. Consequently a relatively homogeneous distribution of the O-H groups over the silicon atoms is observed. Besides, note that one Q^2 site in the system would give a probability of $\frac{1}{30} = 0.033$ which is larger than the probabilities for Q^2 presented in Fig. 6.11. This indicates that the Q^2 sites do not exist throughout the trajectories.

The Q^n species distribution is experimentally accessible with NMR spectroscopy. Farnan *et al.* [Fa87] have determined these quantities for hydrous silica glasses from ^{29}Si NMR spectroscopy. Their samples contained 7.9 and 24.1 mol % H_2O and the measured Q^3 probabilities were 0.086 ± 0.008 and 0.235 ± 0.025, respectively, e.g. values that are significantly lower than the Q^3 probabilities found in the present study. This might be due to the fact that in the samples of Ref. [Fa87] only half or less of the water molecules were dissolved into OH groups. For the 7.9 mol % H_2O sample, the authors found a ratio of OH over H_2O of 1/1 and an even lower value in the 24.1 mol % H_2O sample. Since the samples were prepared at only 1550°C, these difference in the concentration of the Q^3 species might be due to the difference between the experimental temperature and the present simulation temperatures. The probabilities to find oxygen atoms of different types during the trajectories at 3000 K and 3500 K were also evaluated. In particular the appearance of intermediate states like Si-O dangling bonds and O3H triclusters as well as water oxygens (wO) can have consequences for the hydrogen diffusion in the melt. Figure 6.12 shows the probability of finding O* and

O3H cluster units in the trajectories at 3000 K and 3500 K.

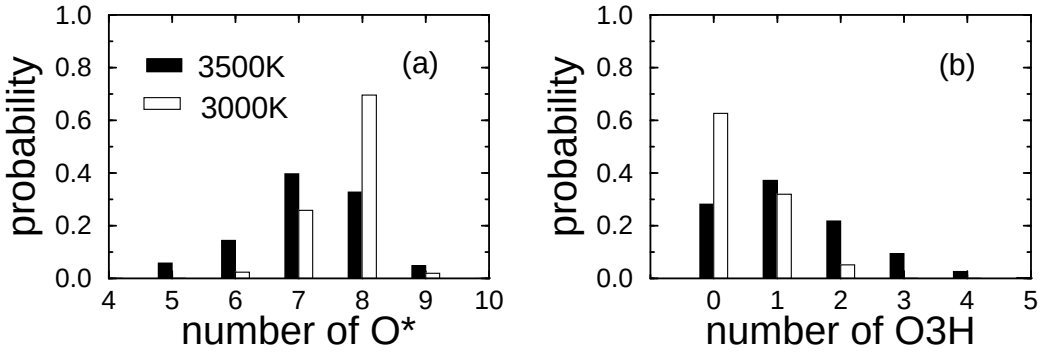

Figure 6.12: *Probability to find O* (a) and O3H cluster (b) in the hydrous silica liquid at 3500 K (black bar) and 3000 K (white bar).*

It should be recalled that a dissolution of all hydrogen atoms into O-H groups would give an exact number of eight O* (the number of H atoms). As it can be seen in Fig. 6.12a, the probability distribution is shifted towards values smaller than eight and that at 3500 K the maximum is not even at eight. In contrast, the number of O3H cluster increases with increasing temperature (Fig. 6.12b). Since the number of free O-H groups and free water molecules is negligible, one concludes that the decrease in concentration of O* at high temperature is due to a direct conversion into O3H clusters. The important re-decay of O3H clusters into O*, which will be presented in Sec. 6.2, seems to confirm this hypothesis. From Fig. 6.10 and the simulation of pure silica at 3500 K [Be01], it is known that three silicon coordinated oxygen atoms are hardly present. The tricluster site formation is hence facilitated by the presence of hydrogen atoms. Obviously the O-H groups constitute "dead-end-pieces" and a higher angular mobility for an O* oxygen than for a BO one can be expected. This higher angular mobility enables the approach of the O* to another silicon atom and hence the formation of a tricluster. The lower mobility of BO atoms seems to suppress this process in pure silica. The relation of the O3H cluster and the two membered rings was also studied and significant correlation was found since more than half of the O3H clusters is part of two membered rings. The existence of Si-O dangling bonds has been demonstrated in Fig. 6.5. In Fig. 6.13 the temperature dependence of the probability of finding a given number of these oxygen types in the hydrous silica liquid is presented. Whereas at 3000 K the maximum of

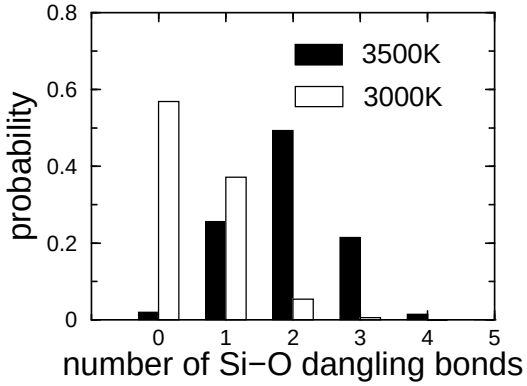

Figure 6.13: *Probability distribution of the Si-O dangling bonds for the hydrous silica liquid at 3500 K (black bars) and 3000 K (white bars).*

the distribution is at zero, it shifts to a value of two at 3500 K and the probability to find

zero dangling bonds at this temperature is small. Hence, the formation of these species is an effect of the elevated temperature. Since this structural feature is not found in a pure silica liquid, the question of its origin emerges. The existence of these dangling bonds might be directly linked to the formation of the O3H cluster. Since these tricluster units increase the coordination of the oxygen atom from two to three, the system attempts to compensate this stoichiometry violation. Since the coordination of the hydrogen and silicon atoms are rarely violated, the appearance of the Si-O dangling bonds (where O has only one neighbor) is certainly associated to the appearance of the O3H clusters.
Now that the existence of the Si-O dangling bonds is evident, the question of their contribution to an eventual fast hydrogen diffusion emerges. Do these dangling bonds serve as acceptor and donor states for hydrogen ? From Figs. 6.5 and 6.6, one knows that Si-O dangling bonds exist both with a weak bond to a silicon atom and with a weak bond to a hydrogen atom. But the analysis of the recombination of these sites shows that only about 17 % of the dangling bonds recombine to a O* site and 83 % recombine to a BO site (see Sec. 6.2). The last oxygen species to be presented here is the water oxygen (wO). As already discussed in the introduction, these units are supposed to play a decisive role for the proton transport. One also knows from the H-H RDF first peak at 3500 K (Fig. 6.3) that such units exist at this temperature. Figure 6.14 shows the probability of finding such water units. Indeed at the higher temperature, one water unit is present with a probability of roughly 10

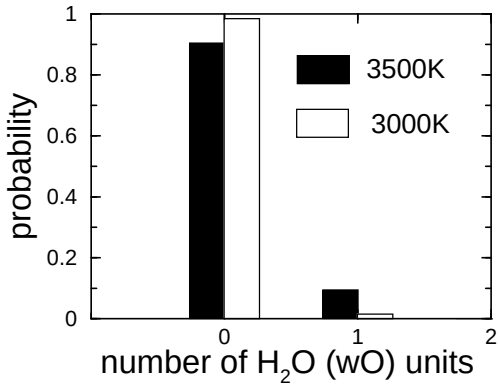

Figure 6.14: *Probability for H_2O units at 3500K (black bars) and 3000K (white bars).*

% along the trajectory. At 3000 K this probability is only 2 %. The corresponding water concentrations are 0.30 mol % and 0.06 mol %, respectively. Note that the concentration of 0.30 mol % at 3500 K should give rise to a probability of 0.003 for the zero O-Si coordination in Fig. 6.10 if the water molecules were free. Since the contribution at zero is two orders of magnitude lower, one should underline the important point that those water units are not free. A detailed analysis reveals an O3 coordination with two hydrogen neighbors and one silicon neighbor. As already mentioned above, the water unit concentrations are far remote from experimentally measured water concentrations. Considering again the data of Farnan *et al.* [Fa87] where a ratio of OH over H_2O of 1/1 (50 mol % H_2O) at a total water content of 8.9 mol % is found, one would expect important contributions around two in Fig. 6.14. Again these differences in the concentration of molecular water probably arise from the difference between the experimental temperature and the present simulation ones.

The section on the structural properties shall be concluded with a brief summary of the figures that showed evidence of the existence of the different intermediate states and that

quantify their probability of occurrence in the liquid:

structural unit	relevant figures
SiOH groups	6.3e (evidence), 6.12a (quantification)
Si-O dangling bonds	6.5 (evidence), 6.6 (evidence), 6.13 (quantification)
O3H triclusters	6.6c (evidence), 6.12b (quantification)
water molecules	6.3f (evidence), 6.14 (quantification)

Table 6.1: *Figures that show evidence for the existence of the transition states and that quantify their probability of occurrence.*

6.2 Dynamics in the Liquid

In this section the possible mechanisms for hydrogen diffusion are discussed. It should be emphasized again that, due to the presence of thermostats, dynamical quantities like the diffusion constants cannot be extracted reliably. Nevertheless, the structural characteristics of the melt should allow it to obtain at least some insight into its dynamical properties. The aim is therefore to determine whether the structural units we discussed in Sec. 6.1.4, such as the O3H clusters or the Si-O dangling bonds, can serve as intermediate states for hydrogen diffusion processes in SiO_2-H_2O liquids.
This discussion is started by making a list of the possible hydrogen diffusion mechanisms in liquid silica, eliminating the free water molecules or stable O-H groups as possible free hydrogen carriers since, as discussed above, they are absent in the simulation data. As the hydrogen atoms are attached to the silica matrix in the form of Si-O-H groups, three possible mechanisms come into play:

1. motion of the hydrogen in the form O-H- - -O $\longrightarrow$ O- - -H-O

2. motion of the oxygen in the form H-O- - -H $\longrightarrow$ H- - -O-H

3. motion of the O-H group in the form Si-(OH)- - -Si $\longrightarrow$ Si- - -(OH)-Si.

The first two mechanisms require the rupture of an O-H bond whereas the third one requires the rupture of a Si-O bond. In the following, it will be shown that among processes **1.** and **2.**, the first one dominates with $\approx$ 90 % and that the third process is indeed present in the liquid. A typical reaction involving the two first processes are shown in Figs. 6.15 and 6.16.

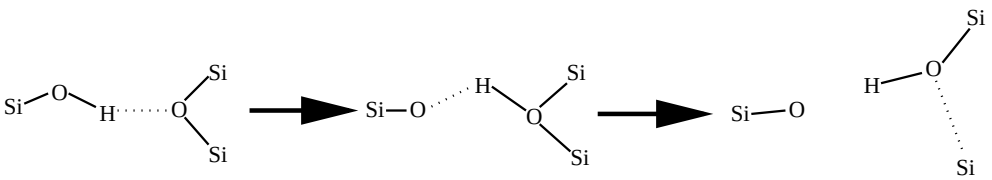

Figure 6.15: *Typical hydrogen diffusion reaction of process* **1.**. *A hydrogen is released from an Si-O-H (O*) to a bridging oxygen (BO) forming subsequently another O*. A Si-O dangling bond and an unsaturated silicon atom are the resulting products.*

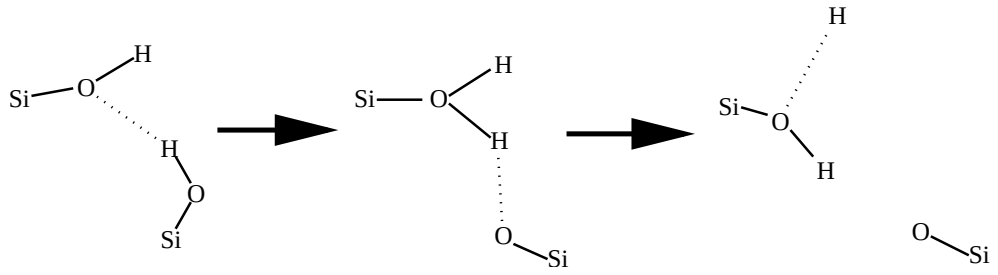

Figure 6.16: *Typical hydrogen diffusion reaction of process* **2.**. *A hydrogen is released from an Si-O-H (O*) to another Si-O-H group (O*) forming a water like structure. An Si-O dangling bond and an released hydrogen atom are the resulting products.*

In the simulated trajectories, one can easily count the number of O-H ruptures in order to find out whether the first two mechanisms exist in the liquid. However, it is possible to distinguish the two processes only by looking at the reactants and the decay products associated with each O-H rupture. The possible reactants (resp. decay products) for the formation (resp. rupture) of an O-H group are given in Tab. 6.2 where the O* refers to an oxygen in a Si-O-H group, wO to an oxygen atom in a water molecule, BO to an oxygen atom in a Si-O-Si group and O3H to an oxygen atom in a Si-(OH)-Si group (see the definitions in the introduction of Sec. 6.1). Note that the formation or rupture of an O-H bond associated with a wO $\longrightarrow$ O* requires the water molecule to be close to a silicon atom which is indeed the case since it was deduced from Fig. 6.10 that no free water molecules exist in the liquid. The average number of O-H bonds in the SiO_2-H_2O melts is found to be equal to 8.4 at 3500

O-H formation		O-H rupture	
reactant	final state	initial state	decay product
Si-O dangling	O*	O*	Si-O dangling
O*	wO	wO	O*
BO	O3H	O3H	BO

Table 6.2: *List of possible reactants for the O-H formation and of possible decay products for the O-H rupture. The notations refer to the definition of the different oxygen types given in the introduction of Sec. 6.1. The final (resp. initial) state gives the type of the oxygen atom in the formed (resp. destroyed) O-H unit.*

K and to 8.1 at 3000 K and is therefore larger than the total number of hydrogen atoms in the system. Hence one concludes that intermediate states with two oxygen atoms close to a single hydrogen exist and that they must serve as intermediate states for hydrogen exchange reactions (process number **1.**).

By counting the number of O-H ruptures along the trajectories and the type of reactants/decay products associated with these ruptures, it is possible to show the existence of hydrogen diffusion processes of types **1.** and **2.**. For the following it is assumed that an O-H bond was formed if the O-H interatomic distance was larger than the O-H cutoff at step t and smaller than the O-H cutoff at step $t + \Delta t$ (Δt being the length of a time step of 0.1088 fs). The nature of the reactant is found by counting, at time t, all silicon and hydrogen neighbors (again in terms of the nearest neighbor cutoff) of the later O-H oxygen. A rupture of an O-H bond was assumed to have happened if one H and one O atom had an

interatomic distance smaller than the O-H cutoff at time t and if their interatomic distance became larger than the O-H cutoff at step $t + \Delta t$, irrespective of whether subsequently the same bond was formed again or not. The decay product of an O-H rupture is the H donor unit (without the H atom) and is found by counting, at step $t + \Delta t$, all silicon and hydrogen neighbors (again in terms of the nearest neighbor cutoff) of the former O-H oxygen.

At 3500 K the total number of O-H formations and ruptures was 97 and 94 respectively, during the equilibrated part of the trajectory (8.1 ps). At 3000 K the number of 68 O-H formations and 69 ruptures was found during the equilibrated part of the trajectory (11.6 ps). However, in order to take into account the O-H formations and ruptures that serve for hydrogen diffusion, one also has to distinguish between the formations and ruptures that give rise to *hydrogen transfers* or *recombinations*. In order to perform this separation between transfers and recombinations it is necessary to relate each decay of an OH bond to a formation of an OH bond. A hydrogen transfer requires the rupture of one O-H bond and the formation of a *different* one, whereas a recombination implies only one bond. Note that the rupture of the first bond will occur before the formation of the new bond if a transient free hydrogen is formed, or, as in almost every case, after the formation of a new bond which implies the formation of the intermediate state. Making this distinction between transfers and recombinations, one finds 28 transfers at 3500 K (corresponding to a ratio of $\frac{28}{94} = 28.8$ % transfers and 71.2 % recombinations) and 8 transfers at 3000 K (corresponding to a ratio of $\frac{8}{68} = 11.8$ % transfers and 88.2 % recombinations). The ratio between the number of ruptures involved in a transfer and the total number of ruptures gives the recombination rate.

Figs. 6.17a and b give the percentage of the reactants and decay products for the O-H formations and ruptures including recombinations and Figs. 6.17c and d the related transfer reactions (i.e. without recombinations). For the transfers, due to the small numbers, the error bars are quite large. At both temperatures, the contributions of the Si-O dangling bonds are higher for the transfer related ruptures than for the overall ruptures, i.e. transfers and recombinations. Furthermore it can be recognized from Figs. 6.17c and d that the Si-O dangling bonds and the BOs are the main acceptors and rupture products, with almost equal probability.

Concerning transfers, the Si-O dangling bonds react with a probability of 40 % at 3500 K and 60 % at 3000 K into an SiOH group and the SiOH group (O*) decays with a probability of 40 % at 3500 K and 50 % at 3000 K into a Si-O dangling bond. However the corresponding probability that includes recombinations is for both the formation and the decay around 30 %. This result indicates that the Si-O dangling bonds are more involved in the formation and rupture of the O-H bonds when the transfers are considered and the recombinations are taken out. Furthermore it also demonstrates the existence of large vibrations of the H atoms around the O atoms of the Si-O dangling bonds and hence the existence of the "weak" hydrogen bonds described in Sec. 6.1.1.

The BOs serve, with a probability of 50 % at 3500 K and of 40 % at 3000 K, as reactants for a hydrogen transfer leading to a new O-H group (60 % including recombinations at both temperatures). On the other side, the BOs serve as products of a hydrogen transfer with a probability of about 50 %, and therefore the participation of the BOs to the formation and rupture of the O-H bonds is slightly decreased when transfers are compared to the reactions including recombinations.

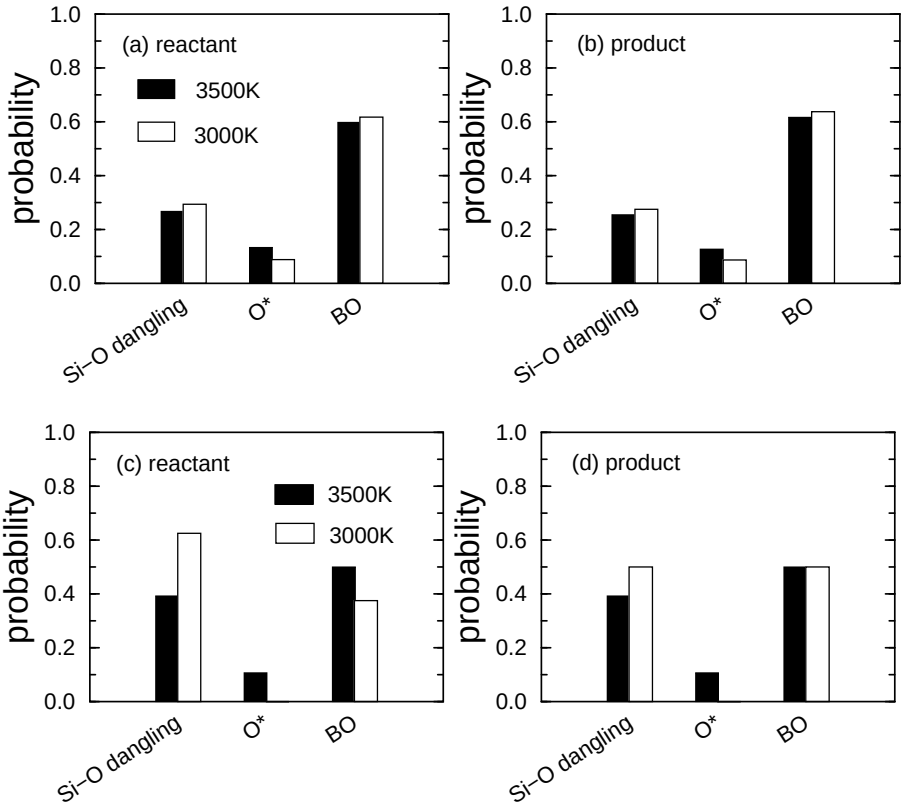

Figure 6.17: *Probabilities of O-H group formation and decay including recombinations, (a) and (b), and without recombinations, (c) and (d), associated to Si-O dangling bonds, O* and BO. Black and white bars correspond to 3500 K and 3000 K, respectively.*

Finally, the O* contribute much less to the O-H group formation and decay than the other species, with a probability of about 10 % (12 % including recombinations) at 3500 K and 0 % (8 % including recombinations) at 3000 K.
From Fig. 6.17, one can deduce that hydrogen transfers involving Si-O dangling bonds or BOs as reactants as well as decay products dominate with $\approx$ 90 %. Since these units are associated to O* or O3H as initial or final states, they correspond to the hydrogen diffusion process number **1.** which means that among the processes **1.** and **2.**, the former dominates with $\approx$ 90 %.
Finally the third hydrogen diffusion mechanism shall be considered. It is associated with the motion of a O-H unit as a whole (without any O-H rupture) which can be obtained via the formation and decay of an O3H cluster as sketched in Fig. 6.18. Note that this process

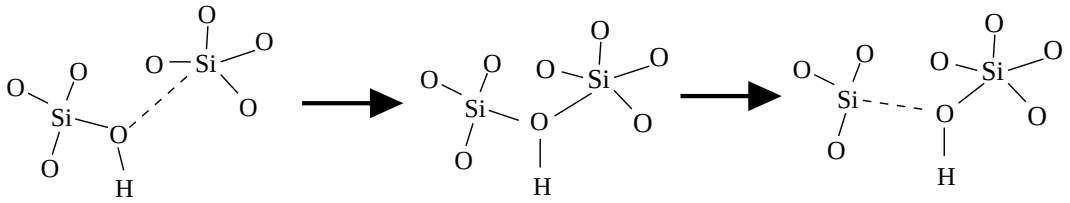

Figure 6.18: *Typical hydrogen diffusion reaction of process three involving a O3H. A O-H group is released from an Si-O-H (O*) to a O3H cluster decaying subsequently in another O*. An oversaturated and an unsaturated silicon atoms are subsequent products.*

requires the presence of "weak" Si-O bonds, the existence of which was inferred from Fig. 6.6 and leads to the formation of threefold and fivefold coordinated silicon atoms. As for the

O-H bonds, the probabilities to find the different reactants and decay products for the O3H cluster formation and rupture were analyzed. Along the equilibrated part of the trajectories, one finds 142 formations and 139 ruptures at 3500 K and 104 formations and 103 ruptures at 3000 K. In the case of O3H clusters, the possible reactants and decay products are the oxygen atoms involved in a Si-O-H unit (O*) or a bridging oxygen (BO). The latter case involves an O-H rupture event whereas the first case does not. This is the reason why a distinction between *recombinations* and *transfers* is not easily feasible for these species since the transfered object can either be a hydrogen atom (as in Tab. 6.2) or an entire O-H group (as in Fig. 6.18). Therefore only the distribution for O3H formations and ruptures including recombinations is displayed in Fig. 6.19. There are only very small differences between

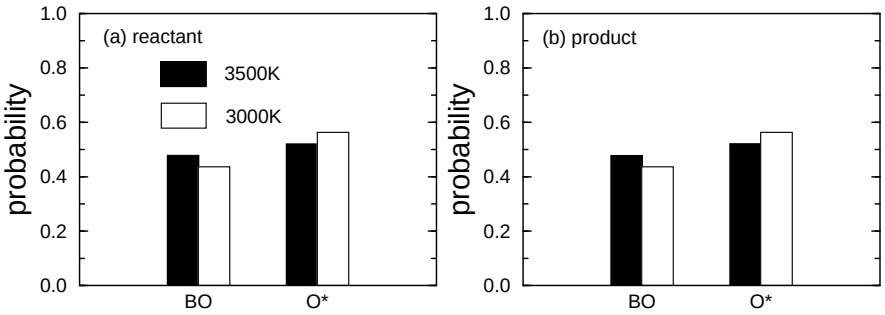

Figure 6.19: *O3H group formation (left) and decay (right) products at 3500 K (black bars) and 3000 K (white bars) including recombinations.*

formation and decay. At both temperatures, the O3H clusters form and decay from and into BO and O*, with almost the same probabilities. However at 3000 K, the probability from and into O* is slightly preferred with a value of 56 % for O* vs. 44 % for BO. This indicates that the hydrogen diffusion process involving the motion of a O-H group without any O-H bond rupture (process number **3.**) occurs in the liquids as well.

To conclude this section on the diffusion process, the activation energy for a hydrogen transfer corresponding to the rupture of an O-H bond (without recombination) is analyzed. One can calculate the activation energy for a hydrogen transfer reaction assuming an Arrhenius behavior

$$R(T) = A \exp\left\{-\frac{E_A}{k_B T}\right\} \ , \tag{6.6}$$

where the reaction rate $R(T)$ is given by a constant A and the activation energy E_A. Using the two numbers of O-H ruptures leading to transfers of 28 for 3500 K and 8 for 3000 K one obtains 280 kJ/mol (2.91 eV) for the activation energy (the different lengths of the equilibrated trajectories already taken into account). Unfortunately the constant A depends explicitly on the transfers per time and can hence not be determined due to the above mentioned problem of the thermostats. The activation energies for the generation and dissociation of various $Si_xO_yH_z$ molecules in the gas phase have been determined by Zachariah *et al* [Za95] with the GAUSSIAN *ab initio* package [Ga90]. Zachariah *et al* found a value for the activation energy of the formation of OSiOH from SiO_2 and H of 254 kJ/mol which compares very well to the above value of 280 kJ/mol for a hydrogen transfer. Also Bakos *et al.* [Ba02] estimated a diffusion reaction barrier of more than 2 eV (193 kJ/mol) for water molecules in small rings. Note that if the activation energy of an OH rupture was much smaller than the reaction barrier of water molecules, molecular water would form.

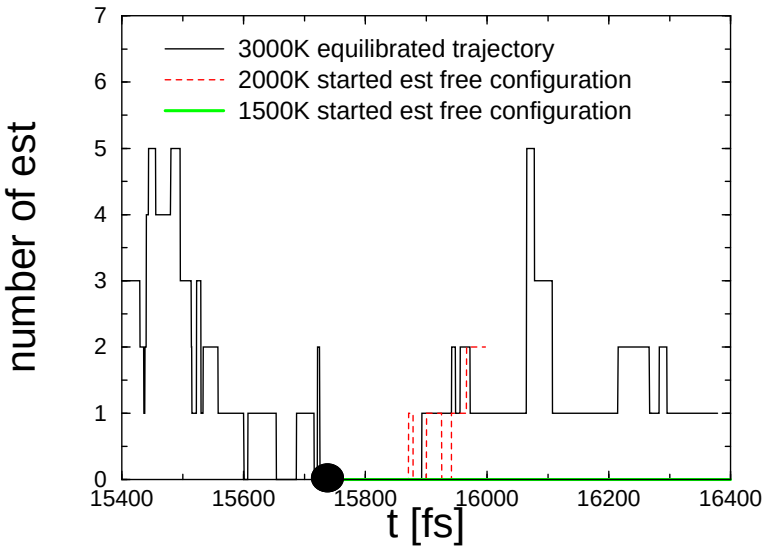

Figure 6.20: *Evolution of the edge-sharing tetrahedrons as a function of time in the equilibrated trajectory at 3000 K and in the selected configurations that were driven to 2000 K and 1500 K. The big dot on the x-axis indicates the configuration from where the 2000 K and 1500 K runs are started. The selected configuration is the initial one for sample 3.*

6.3 The Quench

6.3.1 General Features

Experimental quenches of liquids usually reach cooling rates of 0.1 K/s to 10 K/s [Vo96]. Due to finite computer time, the lowest computationally accessible quench rates are of the order 10^{12} K/s [Vo96]. This discrepancy hinders the simulated system to perform relaxations of intermediate states that decay at a natural quench rate. Hence it becomes mandatory to select carefully initial configurations for the quench. In particular, these initial configurations must have a low number of these intermediate states (like oxygen tri-clusters, edge-sharing tetrahedrons or dangling bonds). In pure silica, the number of edge-sharing tetrahedrons (est) is roughly zero and in hydrous silicates, only little is known about the presence of other intermediate states at ambient temperature. Therefore we selected initial configurations for the quench having a low number of edge-sharing tetrahedrons. The selection of appropriate configurations of the liquid is demonstrated in Fig. 6.20.

These configurations were subsequently quenched to 2000 K and then to 1500 K. Figure 6.20 shows the evolution of the est at the two temperatures started from the selected point with zero est. Since the est form again at 2000 K nearly similar to the trajectory at 3000 K and no reformation occurs at 1500 K, the relaxation time of the system seems to show a significant alteration between 2000 K and 1500 K. One can therefore roughly estimate the glass transition temperature of the system between 2000 K and 1500 K. Once the critical temperature for the change of the dynamical properties is roughly fixed, it is not clear which is the most natural way to simulate crossing of the glass transition temperature. However, since the glass transition is a transition of dynamical properties rather than of structural ones, the way of quenching can be supposed to have little influence on the structure of the glass. Note again, that unfortunately due to the use of thermostats, the access to dynamical properties in the liquid state of the system is lost. Figure 6.21 shows the three different types of quenches that were used in the present study. The initial configuration for quenches 1.

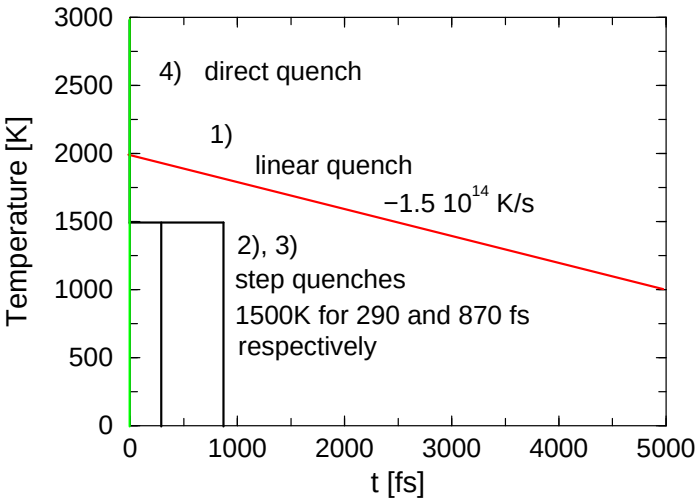

Figure 6.21: *Different quenching curves in the simulation: 1) linear quench at a rate of 1.5 10^{14} K/s, 2), 3) step quenches, 4) direct quench.*

and 2. was identical. It was picked from the trajectory at 3000 K at a time of 19.37 ps. The initial configuration for quench 3. was picked from the 3000 K trajectory at 15.73 ps and the configuration for quench 4 was picked from the 3500 K trajectory at 4.40 ps. According to Vollmayer *et al* [Vo96], within the computationally accessible rates, the actual speed has only little importance for the final structure. The most "natural" way of quenching is probably the linear quench, but it is of course questionable what are the final structural differences compared to a direct quench or a step quench of the same initial configuration.
Having considered the different ways of quenching for the present system it turns out that indeed different structures are obtained. In particular it is observed that in direct and step quenches, with a length of the step of several hundred ps below T_g, we are able to freeze the structural transition states that occur numerously in the liquid as discussed in the previous section. The structural transition states like SiO dangling bonds and O3H clusters mostly decompose if linear quenches at rates of 10^{14} K/s are used. Since such transition states are absent in pure silica, the type of quench had a minor importance in the studies of Vollmayer *et al* [Vo96]. The use of different quenching techniques is hence in the present study a nice tool in order to systematically create and investigate structural intermediate states in hydrous silica glasses.

6.3.2 Implementation of a Linear Quench in CPMD

Quenches are not implemented in the standard CPMD code. Therefore the following modifications had to be applied. The variable `TFIRST` is the initial temperature (which is fixed), `QUENCHR` is the quench rate in K/a.u., `NFI` is the MD step number, `DELT_IONS` is the timestep value in a.u. and `TEMPP` is the real temperature of the system at MD step `NFI`. The velocities are multiplied by a factor `ALFAP` (see below) which is obtained by the value of `ANNERI`. Usually, one enters directly `ANNERI` in the input file of CPMD, but if the same factor `ALFAP` is used at each time step, an exponential quench would be obtained. If a linear quench is desired, one has to recompute the `ALFAP` factor at each MD step and CPMD has to be modified:

```
ANNERI=(TFIRST-QUENCHR*NFI*DELT_IONS)/TEMPP
ALFAP=ANNERI**(0.25)
    DO IS=1,NSP
```

```
    DO IA=1,NA(IS)
        VELP(1,IA,IS)=ALFAP*VELP(1,IA,IS)
        VELP(2,IA,IS)=ALFAP*VELP(2,IA,IS)
        VELP(3,IA,IS)=ALFAP*VELP(3,IA,IS)
    ENDDO
ENDDO
```

The 0.25 power comes from the fact that the `ALFAP` factor is applied twice to the velocities at each MD step.

For the linear quench, 125 000 MD steps at the quench rate of 1.5 10^{14} K/s (=0.0036 K/a.u.), correspond to a final temperature of 650 K if the quench is started from a 2000 K initial temperature with a timestep of 3.5 a.u. Each MD step costs roughly 9 seconds (real time) on 16 processors on the IDRIS platform, which makes 9x16=144 sec CPU. So with 125 000 MD steps, 5000 CPU hours were used.

6.3.3 Available Samples

According to the three different quenches presented in figure 6.21, different ambient temperature glass samples were obtained. At 300 K the glass samples were equilibrated for some hundred femto seconds. During the equilibration the defects were stable. In order to discuss their properties it is useful to note the structural anomalies the samples exhibit. The following table gives an overview: As already mentioned above, it can be seen that structural

sample	quench	NBO	O*	SiO dangling	O3H	SiO_3	SiO_5	Si_3O
1	linear from 2000 K	8	8	0	0	0	0	0
2	step from 3000 K	9	7	2	1	0	0	1
3	step from 3000 K	8	7	1	1	0	0	0
4	instantaneous f. 3500 K	9	8	1	0	1	1	1

Table 6.3: *Overview over available glass samples, the nature of their quench and the structural anomalies. Samples 1 and 2 were obtained starting from the same initial configuration.*

defects of the liquid can be conserved or decompose depending on the quench rate. Note that the fact that the most natural, linear quench shows the least anomalies does not mean that defects will be absent in a natural glass. If the simulation comprised more atoms it is well believed that also in natural linear quenches some structural anomalies can be preserved during the quench. Therefore the investigation of the defects in the following chapter is not without relevance for natural glasses. The investigation will focus on the analysis of the electronic and vibrational properties of the four samples with particular attention to the influence of the structural anomalies presented in table 6.3.

6.4 Electronic Structure

6.4.1 The Electronic Structure of Pure and Hydrous Silica

The electronic structure of amorphous silica is close to the one of crystalline forms of SiO_2 such as tridymite or cristobalite [Pa76]. Historically the electronic structure of the amorphous material was therefore deduced from the crystalline structure. A simple linear-combination-of-atomic-orbitals (LCAO) approach [Ro51] can monitor the main electronic features. The starting point for this kind of model is a construction of four tetrahedrally directed sp^3 hybrid orbitals for a silicon atom. The main structural unit to be considered in order to obtain the electronic structure of amorphous silica is then the Si-O-Si unit as displayed in figure 6.22. Two Si hybrids, $|h_1\rangle$ and $|h_2\rangle$ point in the direction of the oxygen atom. The atomic basis set is then composed of the three p-orbitals of the oxygen atom ($|p_x\rangle$, $|p_y\rangle$, and $|p_z\rangle$) and the silicon hybrid orbitals $|h_1\rangle$ and $|h_2\rangle$. If the orbitals are allowed to interact, the symmetry of the bond allows mixing between $|p_x\rangle$ and $|h_1\rangle$ and $|h_2\rangle$ as well as $|p_z\rangle$ and $|h_1\rangle$ and $|h_2\rangle$. According to the LCAO Ansatz [Ro51] the following orbitals can be formed:

$$|B_z\rangle = \beta_{p_z}|p_z\rangle + \beta_{h_z}\left(|h_1\rangle + |h_2\rangle\right) = \beta_{p_z}|p_z\rangle + \beta_{h_z}|a\rangle \tag{6.7}$$

$$|B_x\rangle = \beta_{p_x}|p_x\rangle + \beta_{h_x}\left(|h_1\rangle - |h_2\rangle\right) = \beta_{p_z}|p_z\rangle + \beta_{h_x}|b\rangle \tag{6.8}$$

$$|B_z^*\rangle = \beta_{p_z}|p_z\rangle - \beta_{h_z}\left(|h_1\rangle + |h_2\rangle\right) = \beta_{p_z}|p_z\rangle - \beta_{h_z}|a\rangle \tag{6.9}$$

$$|B_x^*\rangle = \beta_{p_x}|p_x\rangle - \beta_{h_x}\left(|h_1\rangle - |h_2\rangle\right) = \beta_{p_z}|p_z\rangle - \beta_{h_x}|b\rangle \tag{6.10}$$

with the so called "bonding" orbitals $|B\rangle$ and the "anti-bonding" orbitals $|B^*\rangle$. The numerical coefficients β depend on the overlap integrals $\langle\psi_i|\psi_j\rangle$ (where ψ_k is one of the five orbitals of the atomic basis set) and the bond angle Θ as introduced in figure 6.22. The orbitals $|p_y\rangle$ are "non-bonding" in the chosen geometry. The band gap of roughly 9 eV emerges then between the non-bonding and the anti-bonding orbitals as demonstrated in figure 6.22. The

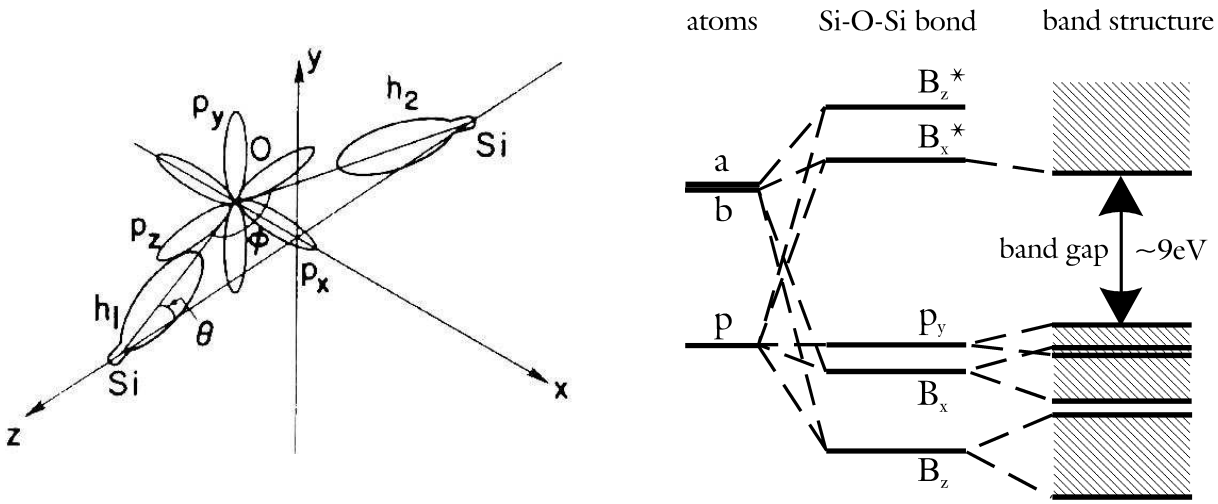

Figure 6.22: **Left**: *Atomic p-orbitals of oxygen and their interaction with the Si hybrids* $|h\rangle$*. The y-direction is not affected by the interaction with the Si atoms. The positive and negative linear combination of the Si hybrids is usually referred to* $|a\rangle$ *and* $|b\rangle$*, respectively.* **Right**: *Resulting electronic band structure in amorphous silica. The band gap arises between the bonding orbitals* $|B\rangle$ *and anti-bonding orbitals* $|B^*\rangle$*. After [Pa76].*

real electronic structure related to the schematic idea obtained in Figure 6.22 is obtained

from the Kohn-Sham orbitals in the simulation. In order to understand the influence of water on the electronic structure of silica, it is useful to study quantities like the electronic density of states (edos).

For the extraction of the Kohn-Sham energies from the samples at 300 K, the diagonalization method of Lanczos is employed [Fi01]. The differences between the electronic density of states of pure silica and two samples of hydrous silica are shown in figure 6.23. According to

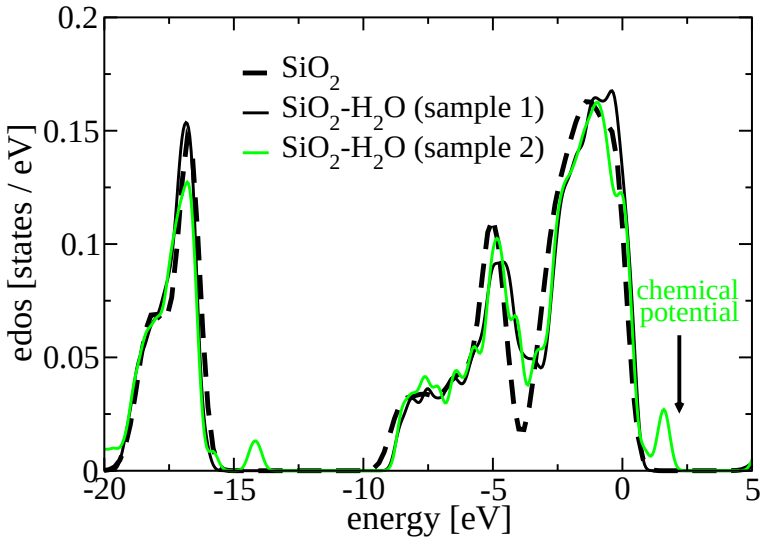

Figure 6.23: *The electronic structure of pure and hydrous silica at 300 K. According to table 6.3, the two hydrous samples were quenched from the same initial configuration. Only the rapidly quenched hydrous sample shows electronic states in the band gap of silica.*

the idea developed in figure 6.22, the states from -10 eV to -4 eV correspond to the bonding orbitals formed by the sp^3 hybrids and the O $2p$ orbitals. The O 2p nonbonding orbitals form the states between -4 eV and the highest occupied orbital. Finally, the states between -20 eV and -15 eV arise from the oxygen $2s$ orbitals. The insulating properties of bulk silica are due to its band gap of $\approx$ 9 eV (not fully shown in figure 6.23). We note that a large underestimation of the band gap is usual in DFT [Go88]. Nevertheless it is recognized in the literature that the relative order of the electronic states is well represented in pure silica [Be00].

Note that according to table 6.3, the two hydrous samples were quenched starting from the same initial configuration. It can be seen that both edos have rather similar shape, however, only the rapidly quenched hydrous sample seems to show states in the electronic band gap of pure amorphous silica. It is well known that hydrogen (atomic or molecular) and molecular water and also SiOH groups do not possess electronic states in the SiO_2 band gap [Ro88, Hu03b]. Hence the states in the band gap have to be due to the intermediate states like the dangling bonds or O3H clusters present in sample 2. It is therefore interesting to investigate the influence of these structural anomalies on the electronic structure of the material with particular attention to the band gap. It has already been proposed in figure 3.1 that the SiO dangling bond created by the reactions presented in Figures 6.15 and 6.16 produces a gap state at around 1 eV. In the following it will be shown that the present model is indeed able to confirm some of the predictions of the molecular orbital calculations of the 1970's and 1980's. The only difference is that the molecular structure is not arbitrarily chosen as in the old models but obtained from a molecular dynamics run that really confirms

predictions on the hydrogen diffusion and the creation of defects. However, the molecular dynamics run in the present study is performed at an extremely high temperature at a subsequent extremely rapid quench. Therefore it should be pointed out that the investigation of properties of semiconductor devices with molecular dynamics simulations at very high temperature followed by a very rapid quench is established in literature [Pa98]. In order to relate structural defects in the electronic density of states, it becomes necessary to localize the Kohn-Sham orbitals.

6.4.2 Orbital Localization

Such localization is a rather sophisticated task using origin-less plane waves as basis function like in the CPMD code. The non-localized basis set was highly appreciated for the molecular dynamics runs since Pulay forces are suppressed (see section 4.3.3) but now, trying to localize the orbitals, the bill has to be payed. Fortunately methods have been developed to obtain maximally localized functions, for periodic and amorphous systems.
Here the maximally localized Wannier functions are used. This method has been developed by Marzari and Silvestrelli [Ma97, Si98] and is fully implemented in the CPMD code. In periodic systems electronic wave functions are described by Bloch functions $\Psi_{n,\mathbf{k}}(\mathbf{r})$, according to their localization in the Brillouin zone $\mathbf{k}$ and the band n. Since Bloch functions are periodic in reciprocal space a Fourier expansion can be given as $\Psi_{n,\mathbf{k}}(\mathbf{r}) = \sum_{\mathbf{R}} w_n(\mathbf{r},\mathbf{R})\, e^{i\mathbf{kr}}$ with the Fourier coefficients $w_n(\mathbf{r},\mathbf{R})$. In periodic systems they depend only on the difference $\mathbf{r}-\mathbf{R}$. Hence the *Wannier* functions $w_n(\mathbf{r}-\mathbf{R})$ [Wa37] are given by

$$w_n(\mathbf{r}-\mathbf{R}) = \frac{V}{(2\pi)^3}\int d^3k\, e^{i\mathbf{kR}}\Psi_{n,\mathbf{k}}(\mathbf{r}) \tag{6.11}$$

Unfortunately, these Wannier functions are not unique since the Bloch orbitals $\Psi_{n,\mathbf{k}}(\mathbf{r})$ have a phase indeterminacy $e^{i\Phi_n(\mathbf{k})}$. This indeterminacy can be resolved by the criterion that the sum Ξ of the second moments of the expectation value of the position operator

$$\Xi = \sum_n \left(\langle r^2\rangle_n - \langle\mathbf{r}\rangle_n^2\right) \tag{6.12}$$

is minimized. The expectation value $\langle....\rangle_n$ refers to the n-th Wannier function $w_n(\mathbf{r}-\mathbf{R})$. For finite systems (systems without periodicity) an equivalent criterion has already been given much earlier by Boys which is today known as Boys' localization [Bo66].
For the consideration of amorphous systems, the investigation can be restricted to a Γ-point only sampling. In the limit of a single k-point (the Γ point), the distinction between Bloch and Wannier functions becomes irrelevant. The problem reduces to finding the unitary matrix that rotates the Kohn-Sham ground state into the maximally-localized representation. In a cubic simulation supercell of length L the spread criterion of equation 6.12 can, after [Si98], be reduced to the problem of maximizing $\Xi = \sum_n \left(|X_{nn}|^2 + |Y_{nn}|^2 + |Z_{nn}|^2\right)$ where $X_{mn} = \langle w_m|e^{-i\frac{2\pi}{L}x}|w_n\rangle$ with analogue definitions for Y_{mn} and Z_{mn}. The maximization can then be performed using numerical methods making use of the above defined matrices and the KS orbitals.
The x coordinate x_n of the n-th Wannier(-function) center is computed as

$$x_n = -\frac{L}{2\pi}\mathsf{Im}\ln\langle w_n|e^{-i\frac{2\pi}{L}x}|w_n\rangle \tag{6.13}$$

where, again, equivalent formulas hold for y_n and z_n.
As was already indicated above, the Wannier formalism constitutes a description of the electronic charge distribution in terms of well defined localized functions. In particular it becomes possible to localize features of the electronic density of states in real space. This can be achieved by the definition of the "projected density of states"

$$N_n(E) = \sum_m |\langle w_n|\psi_m\rangle|^2 \, \delta(E - E_m) \tag{6.14}$$

where ψ_m and E_m are the Kohn Sham eigenvectors and eigenvalues, respectively. Unfortunately CPMD does not currently allow such quantities to be extracted. Thus the convolution cannot be performed. However, other quantities, that reveal even more details about the electronic structure are available.
Once the electronic ground states have been decomposed in well-localized Wannier orbitals, it becomes possible to study the spatial distribution and the distribution of the Wannier centers. Figure 6.24 shows the atomic positions and figure 6.25 the overlay of the Wannier centers and the atomic positions (right panel) of a frozen configuration at 300 K.
The Wannier centers are clearly located at the oxygen atoms, and approximately tetra-

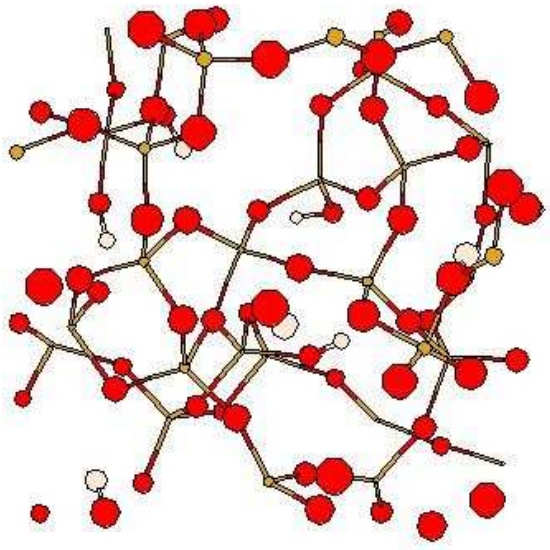

Figure 6.24: *A given structure (sample 2), silicon is yellow, oxygen is red, and hydrogen is white.*

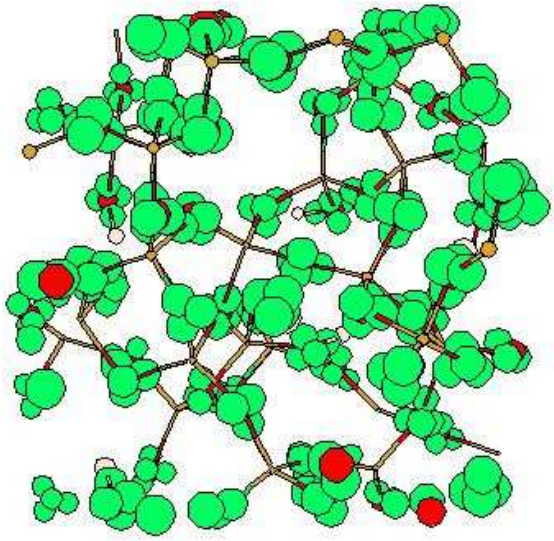

Figure 6.25: *Overlay with Wannier centers (green). The Wannier centers cluster around the oxygen atoms.*

hedrally disposed. Their localization on the oxygen atoms is a logic consequence of the high electronegativity of the oxygen atom. In order to analyze the electronic properties of an (amorphous) solid the whole charge distribution does not have to to be studies. The knowledge of the positions of the Wannier centers and their spread can reveal most of the chemistry of a system. In particular anomalies in the electronic properties that are related to structural properties can be captured just with the knowledge of the position of the Wannier centers. The Wannier centers are treated as an additional class of particles. The solid can then be considered as an assembly of ion-particles and Wannier-center-particles.
If the Wannier centers are treated as an additional type of particles, it becomes possible to consider quantities like pair or angle distributions and coordination numbers in order

to characterize the electronic properties. According to the discussion of the liquid state presented in section 6.1, the radial pair distribution of the oxygen atoms and the Wannier centers, g_{OWC} is presented in Figures 6.26, 6.27 and 6.28 for the step and instantaneous quenches. The main contributions for all samples are between 0.2 and 0.5 Å. This reflects the fact that all Wannier centers are located near the oxygen atoms as was already proposed by figure 6.25. A common feature of all distribution functions seems to be the two well separated peaks at roughly 0.3 Å and 0.4 Å. Taking into account the angle of the Si-O-Si and Si-O-H bonds this behavior can be rationalized. Note that negative electronic charge centers on an oxygen atom will order according to the geometry imposed by the bonds to other atoms. However, relative heights of the peaks at 0.3 Å and 0.4 Å seem to depend on the oxygen type. In particular, comparing to BO oxygens, the peak at 0.4 Å seems to be less pronounced for NBO oxygens and more pronounced for SiO dangling oxygens. Only sample 4 seems to deviate from the rule for the case of the SiO dangling bonds. The distribution of the BO Wannier centers is close to the corresponding quantity of pure silica. This reflects another time the similarity of the electronic density of states of pure and hydrous silica as it was already discussed in figure 6.23. If the power of such distributions can certainly be seen in the fact that they are able to provide a statistical picture of differences between the electronic structure of different oxygen types, their explicative power is limited.
In the following the anomalies of the Wannier functions and Wannier centers associated with the structural defects like SiO dangling bonds and O3H clusters are analyzed. The discussion is started by the visualization of two isosurfaces of the density distributions for typical Wannier functions of a regular OH bond and a SiO dangling oxygen in figure 6.29. As can be seen in a comparison of the left and the right panels of figure 6.29, the density distributions of Wannier functions located at SiO dangling bonds are deformed to a "mushroom" like isosurface. Such deformation is a first indication for electronic anomalies.
A further quantity of interest is the spread Ξ of the Wannier functions as defined in equation 6.12. Figure 6.30 shows this distribution for three different samples. One notes from figure 6.30 that all three configurations have rather similar distributions of the spread of the Wannier functions. Interestingly differences seem to occur between the samples at the high spread end of the distributions. A detailed analysis reveals indeed that these contributions arise from Wannier centers located near SiO dangling bonds.

6.4.3 Charge Density Deformations

For the chemist (with experience) it is sufficient to have a close look to the structure of a molecular system in order to distinguish electron-rich and electron-poor regions. The concept of electronegativity may stand here as an example. Evidently these concepts have to fail if a finite temperature is considered and transition states come into play.
Many theoretical measures of atomic charges have been proposed [Mu55, Hi77]. The main idea of such atomic charge concepts is to divide the molecule into atomic fragments and to investigate how their charges differ from those of the free atom. Simple it sounds, it becomes delicate in practice when the atomic fragments have to be defined and their charge has finally to add up to the one of the molecule. Since the quantity "atomic charge" is not an experimental observable, the theoretical descriptions cannot be classified into true or false.
Perhaps the most efficient way to compute a measure for atomic charges is the method

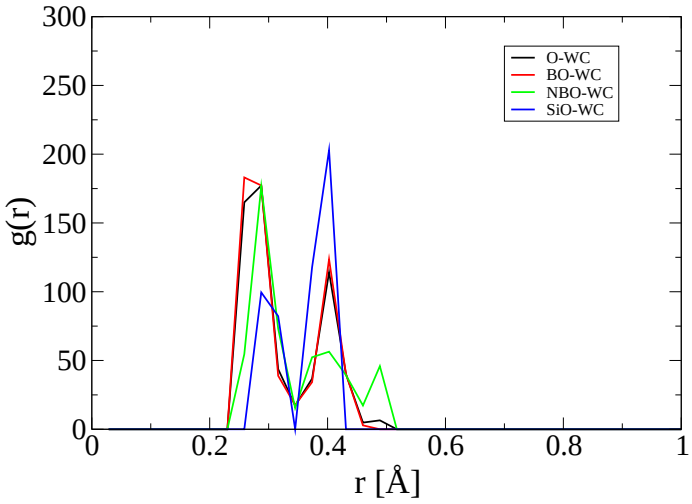

Figure 6.26: *Radial pair distribution g_{OWC} for sample 2.*

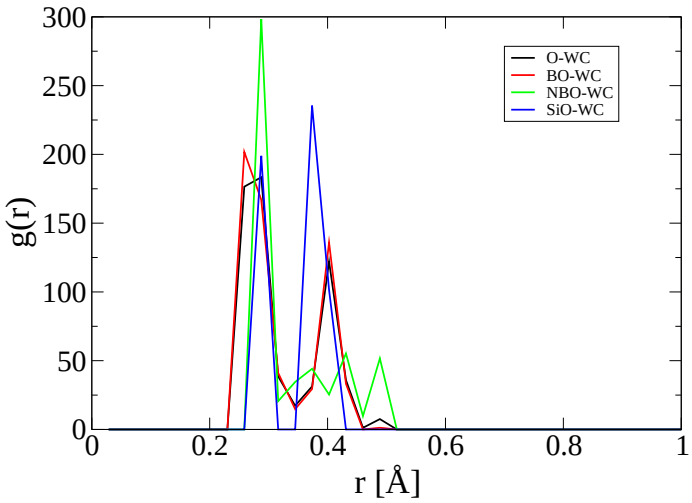

Figure 6.27: *Radial pair distribution g_{OWC} for sample 3.*

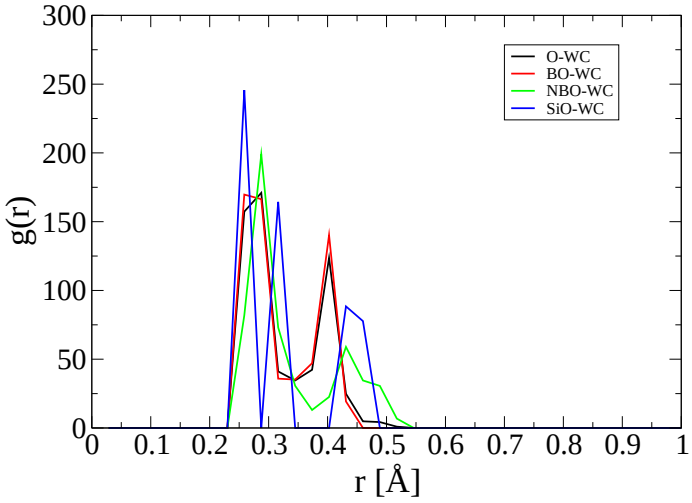

Figure 6.28: *Radial pair distribution g_{OWC} for sample 4.*

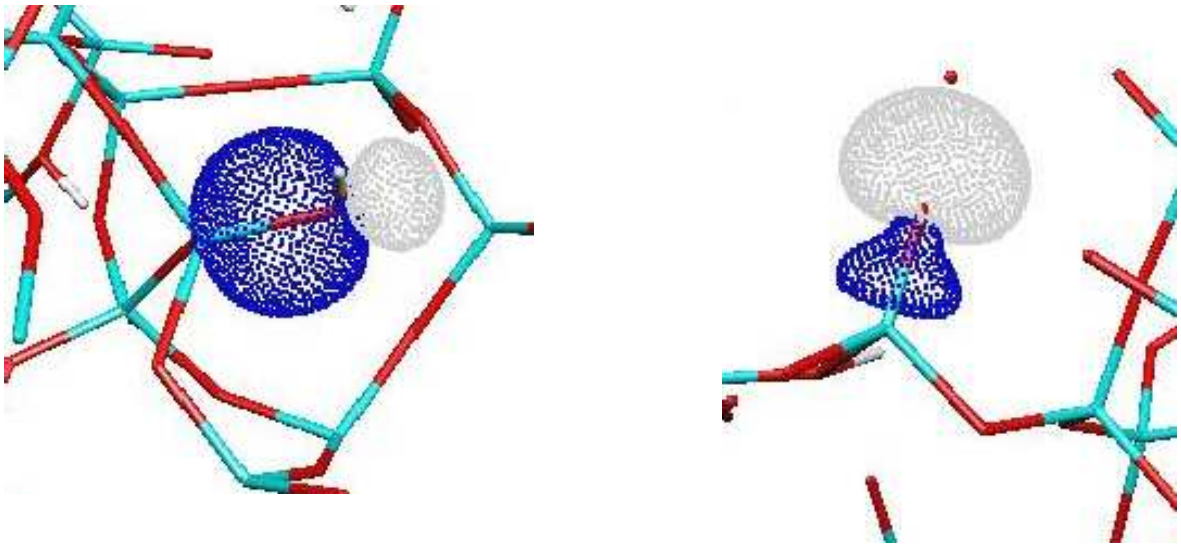

Figure 6.29: *Isosurface of 0.05 corresponding to a Wannier function of a regular OH bond (left panel) and isosurface of 0.05 corresponding to a deformed Wannier function of an SiO dangling bond.*

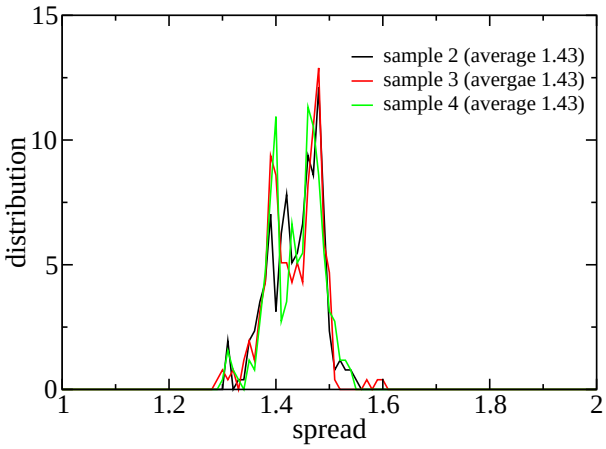

Figure 6.30: *Spread of the Wannier centers for three samples.*

proposed by Hirshfeld [Hi77]. In this approach, the molecular electron density for a virtually constructed pro-molecule $\rho^{pro}(\mathbf{r})$ at a certain position $\mathbf{r}$ is constructed from the sum of atomic densities ρ_I^{at} of the free atoms. To achieve that separation of the total electron density, the actual molecular density $\rho^{mol}(\mathbf{r})$ has to be split among the atoms in proportion to their respective contributions to the molecular density. Mathematically this can be expressed as follows. The molecular density $\rho^{pro}(\mathbf{r})$ is given by a sum of atomic densities

$$\rho^{pro}(\mathbf{r}) = \sum_I \rho_I^{at}(\mathbf{r}) \tag{6.15}$$

with the ground state atomic densities $\rho_I^{at}(\mathbf{r})$. A charge sharing function $w_I(\mathbf{r})$ for every atom is then given by

$$w_I(\mathbf{r}) = \rho_I^{at}(\mathbf{r})/\rho^{pro}(\mathbf{r}) \tag{6.16}$$

which assigns the charge fragment

$$\rho_I^{b.a.}(\mathbf{r}) = w_I(\mathbf{r})\rho^{mol}(\mathbf{r}) \tag{6.17}$$

to each bonded atom (b.a.). Subtracting the density $\rho_I^{at}(\mathbf{r})$ of the free atom from the one of the bonded atom $\rho_I^{b.a.}(\mathbf{r})$ yields the *atomic charge deformation density*:

$$\delta\rho_I(\mathbf{r}) = \rho_I^{b.a.}(\mathbf{r}) - \rho_I^{at}(\mathbf{r}) \tag{6.18}$$

The quantity $\delta\rho_I(\mathbf{r})$ gives the perturbation of the electronic density of the isolated atom due to the presence of other atoms and the bonds. It is a way to find the difference between the "total" charge of the free atom and the actual charge of the bonded atom. This difference is usually referred to as the *net charge deformation density*. By convention of negatively charged electrons, the total charge for the bonded and free atom are obtained by

$$Q_I = -\int d^3r\ \rho_I^{b.a.}(\mathbf{r}) \quad \text{and} \quad Z_I = -\int d^3r\ \rho_I^{at}(\mathbf{r}) \tag{6.19}$$

with the nuclear charge $-Z_I$. The net atomic charge q_I is then obtained as the sum of the electronic charge Q_I and the nuclear charge $-Z_I$:

$$q_I = Q_I - Z_I \tag{6.20}$$

The net atomic charges for the investigated quenched configuration is given in table 6.4 in comparison to the values for pure silica computed by Benoit *et al* [Be00]. Table 6.4 shows

species	$q_I(SiO_2\text{-}H_2O)$	$q_I(SiO_2)$	$q_I(SiO_2\text{-}4Na_2O)$
Si	$+0.220 \pm 0.031$	$+0.218 \pm 0.010$	$+0.240 \pm 0.041$
BO oxygen	-0.101 ± 0.026	-0.109 ± 0.007	-0.089 ± 0.009
SiOX (X=H,Na)	-0.116 ± 0.021	-	-0.249 ± 0.015
SiO dangling	-0.277 ± 0.046	-	-
O3H	$+0.023 \pm 0.000$	-	-
X	$+0.038 \pm 0.030$	-	$+0.082 \pm 0.34$

Table 6.4: *Average Hirshfeld atomic net charges (average ± sigma) for sample 2, pure silica [Be00] as well as sodium tetra-silicate [Is01] (X=Na). Other samples show similar features.*

that the atomic net charges for the silicon and bridging oxygen atoms in the hydrous sample are very similar to those of pure silica. The charges of the different oxygen species in the hydrous sample differ considerably. In particular the SiO dangling bonds exhibit a negative charge that is higher than the average BO Hirshfeld net charge. In contrast, the O3H cluster is undersaturated with electrons and exhibits a positive charge. The analysis of all available hydrous samples shows that the net charges of the SiO dangling bonds varies considerably. Interestingly the net charges seem to be correlated to the position of the associated electronic states in the band gap of amorphous silica. Table 6.5 gives an overview of this correlation.

6.4.4 Electron Localization

A well established tool in order to describe the localization of electrons in a molecular structure is the so called Electron Localization Function (ELF) [CPFS02]. The definition of the ELF goes mainly back to Becke and Edgecombe [BE90]. They associated the localization of an electron with the probability density to find a second electron of the same spin near

the reference electron. The Pauli repulsion between two electrons of the same spin is taken as a measure of the electron localization. The ELF itself is only a relative measure of the electron localization and a reference-localization is required. Becke and Edgecombe [BE90] took the localization of the uniform electron gas as reference-localization. In the definition of Becke and Edgecombe, ELF values are bound between 0 and 1, *high ELF* at a certain position exhibits a higher localization than in the uniform electron gas and *low ELF* refers to low electron localization.
A term used in topological analysis is that of a f-localization domain. It is a region in space bounded by the isosurface $ELF(\mathbf{r}) = f$. Figure 6.31 shows the isosurface of the ELF to an isovalue of $f = 0.886$ for a 300 K sample of hydrous silica. It can be seen that regions of high electron localization are situated around the hydrogen atoms and that also the lone pair electrons at O^* are well localized. They seem to have a similar electronic localization compared to oxygen atoms in molecular water [Ma04]. In contrast, electrons on BO do not seem to exhibit high electronic localization. Decreasing the f-localization boundary value shows indeed that localized electrons sit also on BO oxygens as it was proposed by the investigation of silica polymorph structures [Gi03]. Interestingly, the SiO dangling bonds with energetically elevated states in the band gap exhibit a lower localization than BO and SiO dangling bonds without electronic contributions in the band gap. Note that such a behavior is consistent with the picture obtained from the spread of the Wannier functions (see figure 6.30). Figure 6.32 shows the two SiO dangling bonds of sample 2. It can be seen that only one of the SiO dangling bonds, the one producing the band gap state, carries delocalized electrons.

From the above discussion it becomes indeed evident that the SiO dangling bonds constitute electrical active centers that can serve as charge traps in silicon oxide (note the high negative charge of some dangling bonds) and hence degrade the electronically insulating properties of the material. But not all of the dangling bonds produce electronic states in the band gap of pure silica. In order to relate the Kohn-Sham energies (that constitute the edos) to the physical structure of the silicate, it is useful to visualize the Kohn-Sham orbitals. Even if the Kohn-Sham orbitals are not localized by definition, the associated charge densities are centered at certain parts of the structure. Analyzing the spatial localization of the Kohn-Sham orbitals it becomes possible to get to know which Wannier functions contribute to a Kohn-Sham state, and vice versa. Clearly that means, that it becomes possible to relate the electronic localization (expressed in terms of the Wannier-spread) to the Kohn-Sham states and their energies. For a relation of the Wannier spread to the orbital energies, it is useful to look at table 6.5. The average of the spread was performed over the four Wannier centers located at the SiO dangling bond. A comparison to figure 6.30 shows, that indeed the electrons on the SiO dangling bonds exhibit an average spread at the upper end of the distribution of the individual spreads.
The chemical potential of pure silica is around 0.5 eV. Therefore, the Kohn-Sham states of the third and fourth case listed in table 6.5 are clearly located in the electronic band gap. Generally, higher average spread of the Wannier centers on the SiO dangling bond seems to be responsible for an energy increase of the electronic state. Obviously, also higher net charges on the SiO dangling bonds lead to higher electronic energies. Such behavior was already empirically found by O'Reilly *et al* [Re83]. The dependency of the energy on the

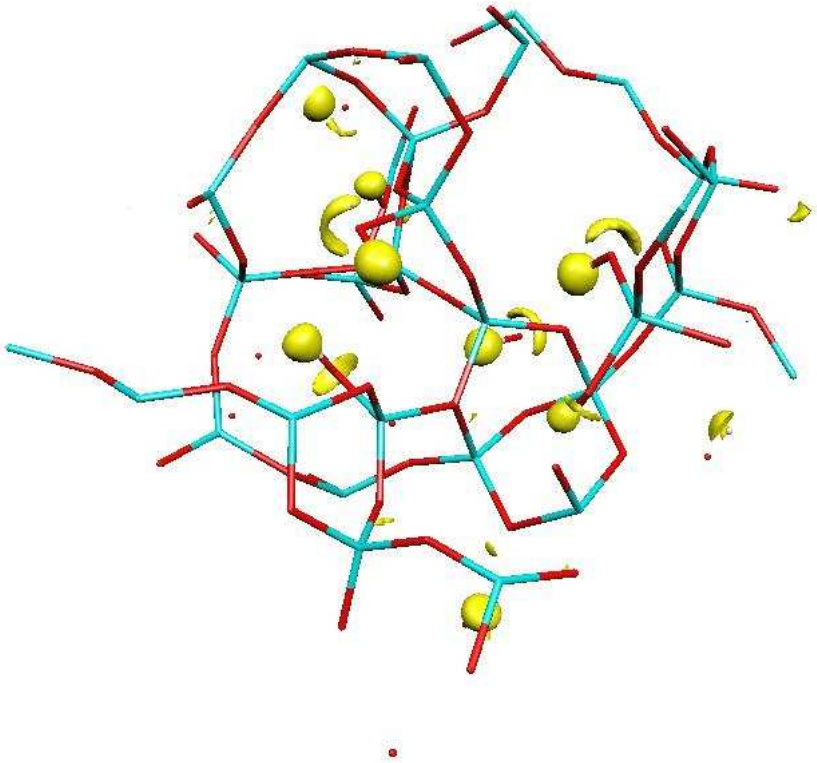

Figure 6.31: *Electron Localization Function (ELF) corresponding to an isosurface value of 0.886 (yellow surfaces). It can be seen that localized electrons can preferably be found at hydrogen atoms and NBO oxygens and in particular not at BO oxygens.*

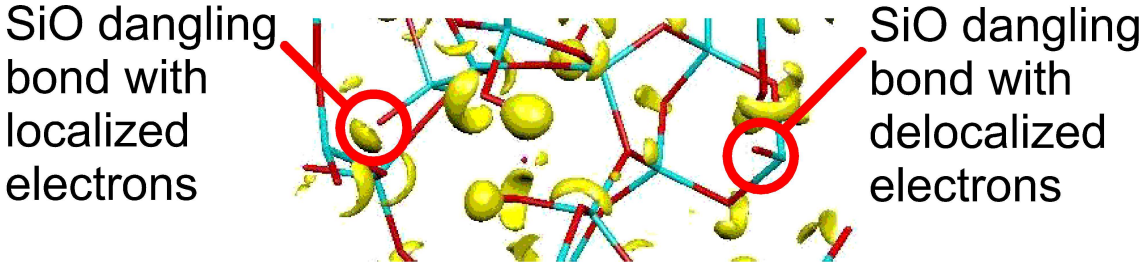

Figure 6.32: *Electron Localization Function at the two SiO dangling bonds of sample 2 at an isovalue of $f = 0.87$. Only if the electrons are delocalized, the SiO dangling bonds exhibit an electronic band gap state.*

average WC spread	net charge	energy of related Kohn Sham state	length of weak H bond
1.508	-0.323	0.155 eV	2.873 Å
1.523	-0.166	0.192 eV	1.758 Å
1.531	-0.231	1.746 eV	1.522 Å
1.564	-0.338	2.427 eV	2.203 Å

Table 6.5: *Electronic Kohn-Sham energy versus average electronic Wannier-spread and net charge of SiO dangling bonds. The combination of high charge and high spread increases the energy and can push the electronic states into the band gap (above 0.5 eV).*

net charge carried by the dangling bond comes from charge transfer effects that raise the self-energies of the dangling oxygen orbitals. Only the first case listed in table 6.5 seems to deviate from this rule. A particular inspection of this situation shows that the concerned dangling bond is situated close to an O3H cluster. Hence it might be possible that the close presence of another structural (and electronic) anomaly leads to a very particular behavior. It was also investigated if the energy of the KS-states depends on the distance of the associated weak hydrogen bond. Although the charge seems to scale somehow with the distance in table 6.5, a clear relation between the bond length and the energy of the Kohn-Sahm state cannot be fixed.

Therefore, according to the four studied cases, it seems to be the combination of high electronic charge and electronic delocalization that pushes the states into the band gap. Electronic delocalization can be achieved, if the dangling bond is stabilized by a weak hydrogen bond or, generally interaction with another atom. In this picture the band gap states are a result of a *push and pull* in the structure; the electrons are pushed by repulsion with the charge of another electron on the dangling bond and pulled by any kind of interaction with remote atoms.

As was explained in section 1.2.2 the dangerous situation for semiconductor devices is the semi-occupied SiO· state in the band gap since it can serve as negative charge trap. In the present case, in particular the electronic SiO dangling bonds in the band gap are two-fold occupied, as can be deduced from the high negative charge. This corresponds to the picture *the charge has already been trapped*, which is somehow the proof that, indeed, the SiO dangling bonds serve as electrically active centers in the oxide. It was also examined if the two-fold occupation is not the result of a spin polarized state. Computing the Kohn-Sham energies with spin functionals (LSDA), this possibility could be excluded.

Within the present study it became, for the first time, possible to get insight into this concern of the semiconductor industry from a molecular dynamics point of view. The predictions and assumptions made for such defects in the 1970's and 1980's could be confirmed. Moreover, the present results confirm also experimental findings (see [Gr03] and references cited therein). It was pointed out by Gritsenko [Gr03] that in particular a charged dangling bond is likely to form at photon illumination. As already mentioned in section 1.2.2, the SiO defect density in fused industrial oxides is about $5{\cdot}10^{16}$ cm^{-3}. Hence, note that the number of 102 in the present study atoms would be totally insufficient to obtain a picture of the defects. Only the rapid quenches employed enabled us to provide a model.

6.5 Structural and Vibrational Properties of the Glass

6.5.1 Structure Factors

At ambient temperature, it is however the main interest to look at properties that are experimentally accessible.
Figure 6.33 shows a comparison between the structure factor at ambient temperature and the same quantity in the liquid state at 3000 K and 3500 K. The structure factor is averaged over all samples that were available at 300 K. According to less intense atomic displacements

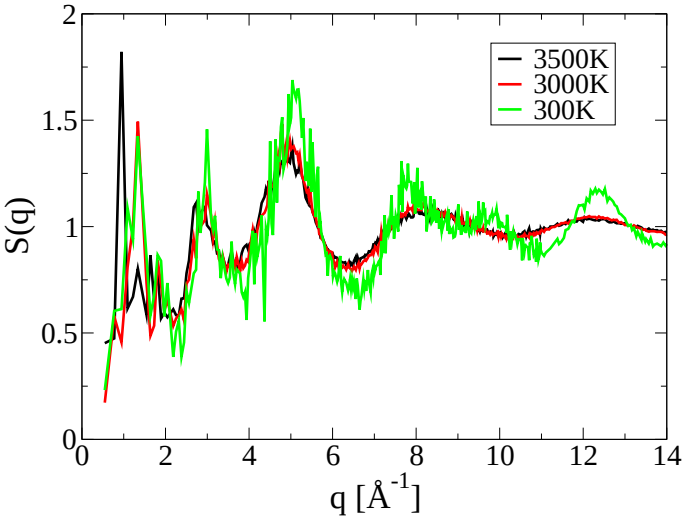

Figure 6.33: *Neutron scattering structure factor of hydrous silica in the glassy state at 300 K compared to the liquid state at 3000 K and 3500 K.*

at ambient temperature, the network is more ordered and the amplitude of the structure factor increases. However, the main humps characterizing the structure at 1.7 Å^{-1}, 3.0 Å^{-1} and 5.2 Å^{-1} are within the statistics at the same positions as in the liquid state. The latter behavior indicates that important structural changes do not occur during the quench. This is rather unexpected due to the ultra-fast quench rates. Note that at low quench rates, a quenched structure is much closer to the equilibrium structure than at high quench rates. At low quench rates the structure has, in a certain temperature range, much more time to equilibrate and is hence closer to equilibrium.

The comparison to the structure factor of pure silica [Be02] is presented in figure 6.34. Both structure factors are almost identical. A small difference can be assumed in the range of the first sharp diffraction peak at roughly 1.7 Å^{-1} and minor deviations are also seen at wave vector transfers larger than 11 Å^{-1}. The differences at 1.7 Å^{-1} are interesting since this region of the structure factor contains information on the relative arrangement of the tetrahedrons with respect to each other. Unfortunately due to the bad statistics it is not possible to reveal details. Remember that the structure factor of hydrous silica was already very close to the one of pure silica in the liquid state (see figure 6.8).

6.5.2 Vibrational Density of States

The vibrational density of states of the glasses was calculated according to the method of finite displacements which allows to obtain the dynamical matrix [UG97]. The diagonalization of this matrix was performed according to section 3.3.
The vibrational spectrum of hydrous silica is compared to the one of pure silica in figure

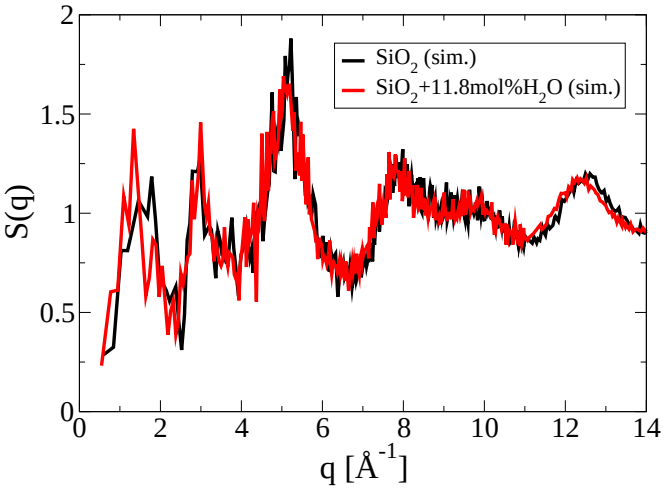

Figure 6.34: *Neutron scattering structure factor of hydrous silica at 300 K compared to the one of pure silica at 300 K.*

6.35. The main frame shows the complete vdos in units of inverse centimeters, whereas the inset is a zoom on the region of the vibrations of pure silica in units of meV. The use of different energy units is very common in literature. The region of the vibrations of the silica matrix is usually investigated with neutrons where meV is the established energy unit. All vibrations with frequencies higher than 160 meV are the domain of light scattering, a discipline in which cm^{-1} is the traditional energy unit. Note that the conversion factor between these units is 8.0655. The differences of the densities of states of the differently obtained hydrous glasses are tiny. But, the differences with the vibrational density of states of dry silica are statistically significant. Performing an average over all three hydrous samples is hence suitable. The averaged curve is shown in figure 6.38. The little differences are also the reason why the relatively costly optimization was not applied to sample three.

As is predicted by Raman spectroscopy, the contributions of the OH-stretch vibrations are situated at 370 meV to 470 meV (3000-3800 cm^{-1}) [My86]. Contributions in the range between 1400 cm^{-1} and 3000 cm^{-1} are only present for sample 2. In a detailed analysis these effects could be related to the O3H anomaly in this sample.

Since only little structural information can be obtained from the OH stretch vibrations, the discussion is limited to the region between 0 meV and 160 meV (0 cm^{-1} and 1300 cm^{-1}). It can be seen that the main shape of the vibrational density of SiO_2 is only slightly altered. In particular it can be said that the difference between the vdos of hydrous silica compared to pure silica is much weaker than the difference between the vdos of sodium silicate and pure silica [Is03]. This result can be expected according to the investigations of the liquid structure where it became evident that sodium oxide has much more influence on the short range order of the structure than water. Perhaps the most striking difference between the vibrational spectrum of pure and hydrous silica in the 0 - 160 meV region is that the experimentally and theoretically observed double peak structure between 120 meV and 160 meV vanishes. The question of the origin of the double peak structure leads to the contributions of the partial vibrational densities of states (as defined in equation 3.15) to the total vdos 3.14. Figure 6.36 shows partial vibrational densities of states (pvdos) for Si, BO, NBO and H atoms in the sample. The Si and BO pvdos are compared to the ones of pure silica.

For the latter ones one notes that the spectra are rather equivalent for pure and hydrous

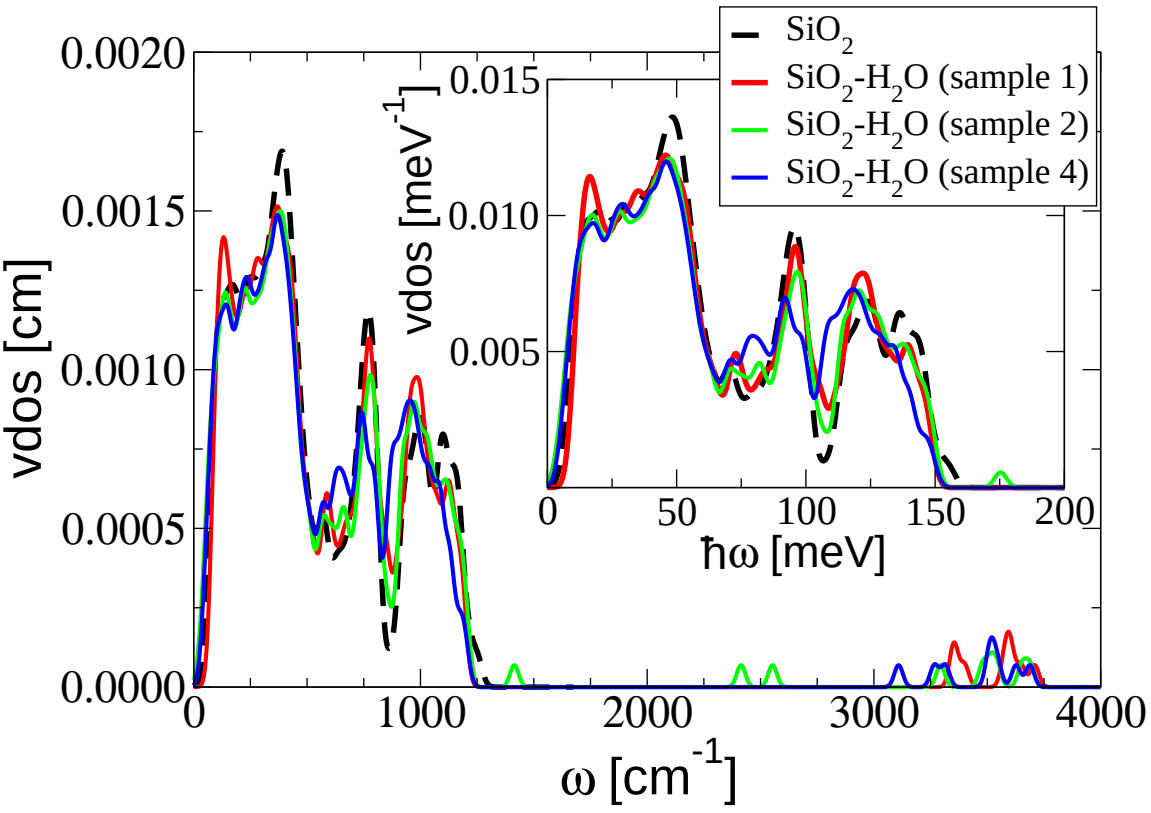

Figure 6.35: *The vibrational density of states of pure silica (dashed line) [Be02], and the vibrational density of states of three configurations (solid lines). The spectra are convoluted with a Gaussian function.*

silica. The silicon pvdos is governed by a peak at roughly 100 meV which is also visible in the total vdos in figure 6.35. The BO pvdos reassembles very much the total vdos. The highest intensity is situated between 15 meV and 60 meV and between 120 meV and 140 meV. The latter region corresponds to the stretch vibrations of the SiO_4 tetrahedrons [Sa97, Ol99, Ta97a]. However, the double peak structure seems to be somehow deformed in the BO pvdos of hydrous silica. The NBO pvdos is characterized by two sharp peaks at 15 meV and 120 meV. Little intensity is present between 60 meV and 100 meV and between 125 to 150 meV. It is now interesting that the double peak structure is totally lost in the case of the pvdos of NBO atoms. Generally the shape of the NBO pvdos seems to have little to do with the one of the BO pvdos. Indeed this seems to be a very common feature in glasses [Is03]. The pvdos of hydrogen shows contributions over the whole range of the vibrational spectrum from 0 to 150 meV. Obviously hydrogen participates in nearly all vibrations. Such behavior is certainly related to the very low mass of the hydrogen atom compared to the other atoms. The statistics for the hydrogen pvdos is rather bad due to the low number of only 8 hydrogen atoms in the sample.

Since the pvdos for Si and BO for the hydrous sample are very close to those of pure silica, the differences in the total vdos emerge from the influence of the NBO and H contributions. Therefore it is interesting to understand why the NBO-vdos differs so much from the BO-vdos and in particular why the second one of the double peaks at 140 meV is totally

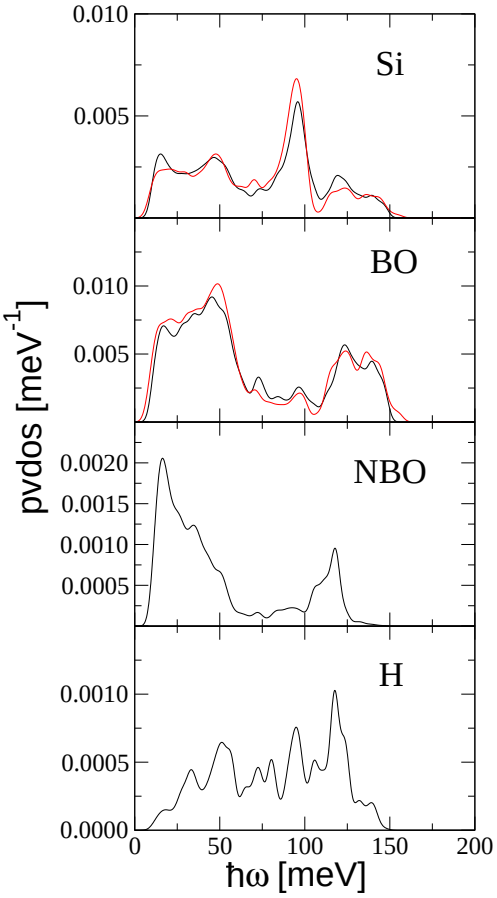

Figure 6.36: *Partial vibrational densities of states of the linear quenched sample (black lines). The Si and BO spectra are compared to corresponding quantities of pure silica (red lines). The spectra are convoluted with a Gaussian function.*

suppressed in hydrous silica. The origin of the double peaked structure at the high energy end of the vdos in amorphous SiO_2 has recently been understood [Sa97, Ol99, Ta97a]. It was found that the two peaks arise from two different SiO stretching modes in the SiO_4 tetrahedrons. The character table of the group T_d of the SiO_4 tetrahedron is given in table 6.6. The vibrations of the one dimensional irreducible representation A_1 and the three di-

T_d	E	$8C_3$	$3C_2$	$6\sigma_d$	$6S_4$
A_1	1	1	1	1	1
A_2	1	1	1	-1	-1
E	2	-1	2	0	0
T_1	3	0	-1	-1	1
T_2	3	0	-1	1	-1

Table 6.6: *Character table for the point group T_d.*

mensional irreducible representation T_2 are responsible for the double peak structure in the vdos of pure silica. A_1 corresponds to an in phase motion of all oxygen atoms towards the central silicon atom, where as T_2 is threefold degenerate and corresponds to a displacement of two oxygen atoms towards the silicon atoms and two oxygen atoms away from the silicon atom. It turns out that the peak at 98 meV and at 120 meV are strongly related to the vibrations with T_2 symmetry, whereas the energetically higher one of the double peaks at

140 meV emerges from vibrations with A_1 symmetry.

It is now a question why only the peak arising from A_1 symmetry vibrations is suppressed

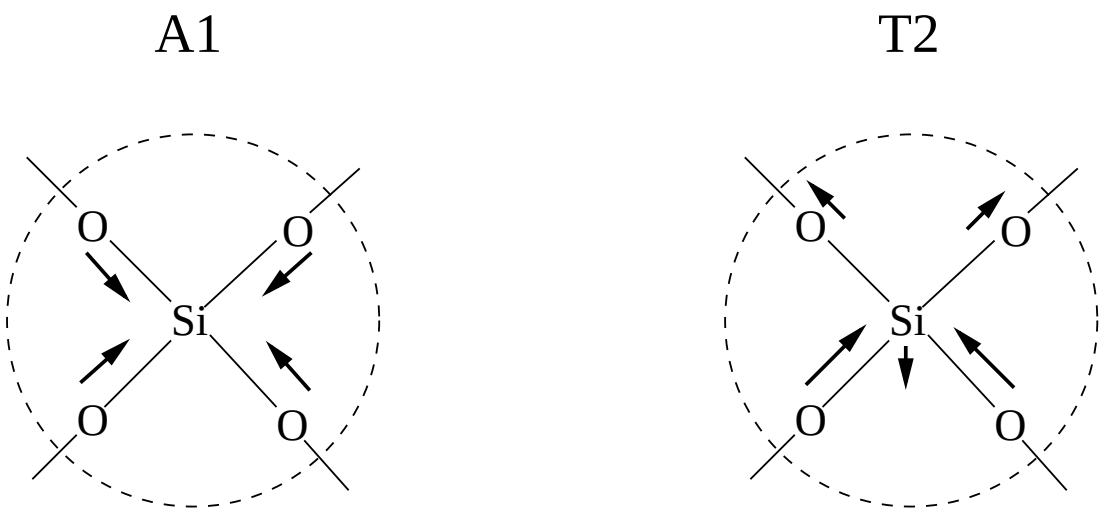

Figure 6.37: *Two dimensional visualization of the A1 and T2 vibrational modes of pure silica. If only the atoms shown inside the circle are considered for vibrational analysis, the replacement of one SiOSi by an SiOH unit should not affect the vibrational properties. In fact, the different charge on an O* compared to an BO suppresses A1.*

by the addition of water, whereas the vibrations having T_2 symmetry are even more pronounced. It should be pointed out that the considered subunit, the SiO_4 tetrahedron, is not changed if water is introduced. In other words, the replacement of one BO by an NBO does not modify the underlying SiO_4 stoichiometry of the silicon atom (interior of the circles in figure 6.37). The A_1 contributions to the total vdos are very sensitive to the electronic structure and hence the interatomic potential. This behavior was already recognized many years ago in α-quartz by Schober [Sc88]. He investigated the vibrational properties of quartz with several potentials. He came to the conclusion that only in models that describe very well the atomic charges, the double peak structure appears. If the charges are badly described, the double peak structure merges to a one peak structure in a way that the peak with the higher energy moves onto the one with lower energy. From this point of view the attached hydrogen changes the charge of an oxygen atom and one should hence observe the same effect. Despite of the conserved stoichiometry of the silicon atom, the underlying symmetry (of a coordination four equivalent oxygen atoms) is then broken in the tetrahedron and the vibrational frequencies change. The condition of four equivalent oxygen atoms is naturally not required for T2 vibrations.

The last point to be discussed in the section on the vibrational density of states is the corresponding neutron vibrational density of states (ndos). As it was shown in section 4.2 the ndos can be obtained with the knowledge of the pvdos via Eq. 4.29. The ndos for the hydrous silica is shown in figure 6.38. In order to have the best available statistics for hydrogen, the pvdos were averaged over all three hydrous samples.

According to the low mass of the hydrogen atom and its high neutron scattering length, the ndos is dominated by the pvdos of hydrogen. However, this is the worst case since the statistics of hydrogen vdos is based on only 8 hydrogen atoms in each of the three samples. The ndos is therefore not very reliable. What can be said from figure 6.38 is that the ndos is characterized by a shoulder at 50 meV and a dominating peak at 120 meV due to a strong

hydrogen contribution at this frequency.

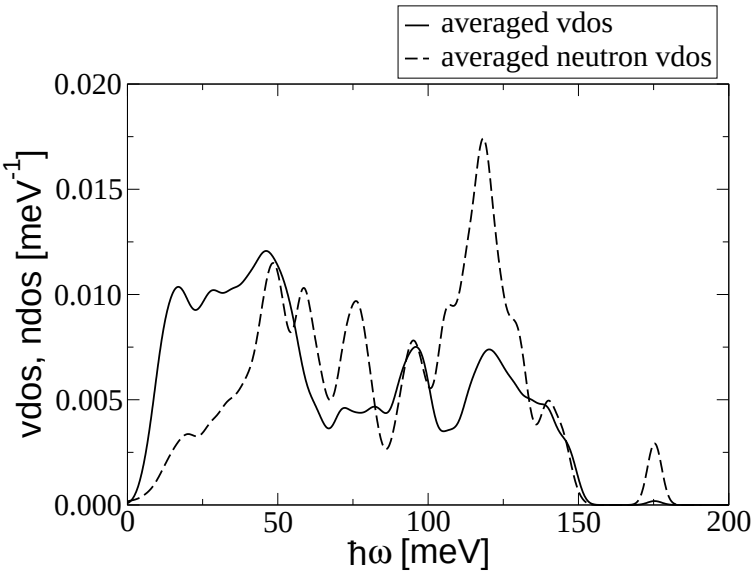

Figure 6.38: *Vibrational density of states, vdos (bold line) and effective neutron vibrational density of states, ndos (dashed line). The spectra are convoluted with a Gaussian function.*

Chapter 7

Results of the Experiments

Since it is already known that water is released from the samples if the temperature exceeds the glass transition temperature and no pressure is applied, neutron scattering experiments are currently restricted to measure the time and space correlations of the samples below the glass transition temperature. Except for some cases (where it is explicitly mentioned) all the following results were obtained at ambient temperature (300 K). It was already pointed out by Müller [Mu04] that, at these temperatures, the water diffusion is too slow to be quantitatively recorded by neutron scattering techniques.

7.1 Diffraction

7.1.1 Data Reduction and Correction

Self-Absorption Corrections A simple subtraction of the container signal from the sample (plus container) signal is not feasible since such simple treatment would not take into account screening due to absorption. Note that two effects occur: Screening of the container on the sample and screening of the sample on the container. It was Paalman and Pings in 1962 [Pa62] who first gave the integrals to be evaluated for a proper self absorption correction. The correct value $I(\mathbf{q},\omega)$ of the scattering from the sample corrected for absorption in the sample S and the container C is given as:

$$I_S(\mathbf{q},\omega) = \frac{1}{A_{S,SC}(\mathbf{q},\omega)} I_{S+C}(\mathbf{q},\omega) - \frac{A_{C,SC}(\mathbf{q},\omega)}{A_{S,SC}(\mathbf{q},\omega) A_{C,C}(\mathbf{q},\omega)} I_C(\mathbf{q},\omega) \tag{7.1}$$

where I_{S+C} is the scattering from the sample and the container and I_C is the container only scattering and

$A_{C,C}(\mathbf{q},\omega)$	is the absorption factor for scattering and self-absorption in the container
$A_{C,SC}(\mathbf{q},\omega)$	is the absorption factor for scattering in container and absorption in both sample and container
$A_{S,SC}(\mathbf{q},\omega)$	is the absorption factor for scattering in sample and absorption for both sample and container.

The fraction $A_{C,SC}/A_{C,C}$ that occurs only in front of the container contribution is usually grouped to a coefficient called A_{rel}.

Multiple Scattering A major concern in the treatment of neutron scattering data is to separate primary scattering of neutrons from the higher orders. Multiple scattering can, if not taken into account properly, represent a substantial portion of the measured intensity. It is obvious that such corrections have especially to be applied to samples with high diameter, i.e. full cylinder and flat slab scattering geometries. The case of full cylinders was treated by Blech and Averbach [Bl65] and the case of flat slabs was treated by Agrawal [Ag71]. Blech and Averbach evaluated the secondary scattering numerically as a function of the absorption coefficient μ, the cylinder radius R and its height h, and the ratio σ_s/σ_{tot} of the scattering cross section and the total cross section as shown in Fig. 7.1. The primary scattering takes place after the paths length L_I in the volume element dV. The secondary scattered intensity is calculated from a *primary* scattering at a volume element dV' after the path L. The

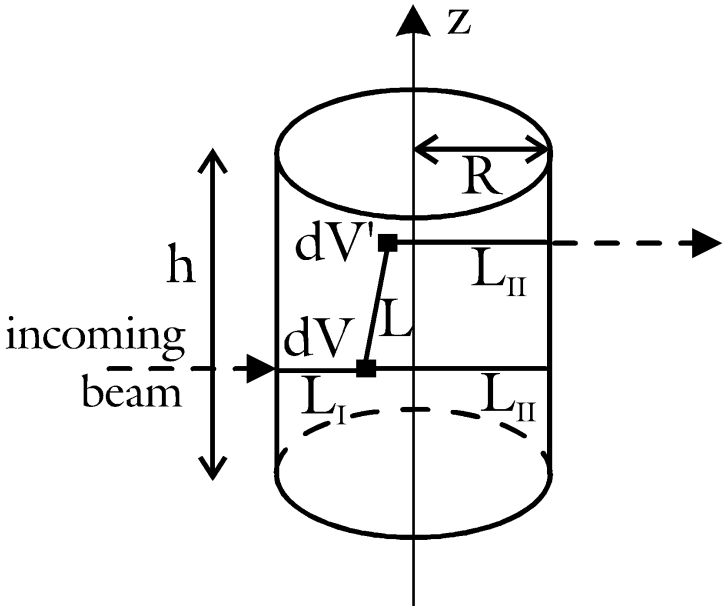

Figure 7.1: *Primary and secondary scattering in a full cylinder.*

intensity of multiple scattering I^M can then be calculated from the isotropic total intensity $\langle I \rangle$

$$I^M = \langle I \rangle \frac{\sigma_{tot} - \sigma_a}{\sigma_{tot}} \delta \tag{7.2}$$

where the ratio δ is obtained by an integration of the Lambert law over the cylinder volume [Bl65]:

$$\delta = \frac{\mu}{A(\Theta)} \left(\frac{2}{4\pi^2 R^2 h} \right) \int_{r=0}^{R} dr \int_{r'=0}^{R} dr' \int_{\Theta=0}^{2\pi} d\Theta \int_{\Theta'=0}^{2\pi} d\Theta' \int_{z=0}^{h} dz \int_{z'=0}^{h-z} dz' \, \frac{e^{-\mu L}}{L^2} r r' e^{-\mu(L_I + L_{II})} \tag{7.3}$$

The ratio δ is tabulated as a function of R/h and μR in ref. [Bl65] and visualized in Figure 7.2. Of course, it is questionable how to evaluate the isotropic total intensity $\langle I \rangle$. Is it preferable to average over all scattering angles, or, should only angles be taken into account where inelasticity effects are relatively small, i.e. small angles ? In fact, it was shown by Bertagnolli [Be76] that for hydrogenous (organic) liquids -taking the average over small angles only- measured signals could be verified at best.

The sample NS3+5.8mol%H_2O was measured in three different scattering geometries. The following table provides the ratios μR and R/h for this sample, that govern the multiple scattering according to Blech and Averbach. For the values of table 7.1 one reads off from

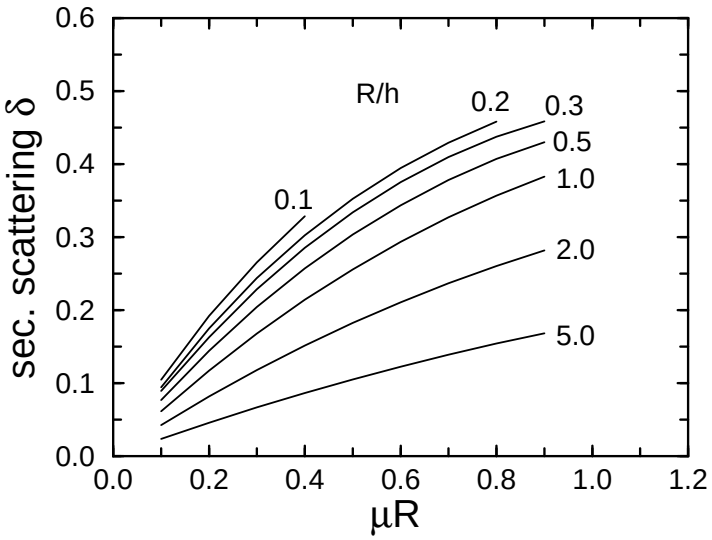

Figure 7.2: *Coefficient δ for secondary scattering dependent on the scattering coefficient μ and the geometry R/h of a cylinder; after [Bl65].*

geometry	R/h	μd	$\exp[-\xi\mu d]$
hollow cylinder (sept. 2001)	0.019	0.019	0.943
flat slab (aug. 2002)	-	0.032	0.964
full cylinder (oct. 2003)	0.0833	0.047	0.863

Table 7.1: *Quantities for multiple scattering of NS3+5.8mol%H_2O for the different geometries in use. $I/I_o \sim \exp[-\xi\mu d]$ gives roughly the ratio of unscattered neutrons behind of the sample. The thickness d corresponds to the distance between the cylinders in the hollow cylinder geometry, to the cylinder radius R in the full cylinder geometry and to the slab thickness in the flat slab geometry. The geometry factor ξ equals π in the case of cylinders and scales with $\sec\phi$ in the case of the flat slab, where ϕ is the angle between the slab plane and the incoming beam (60^o in the considered experiment) [Ag71].*

figure 7.2 that the coefficient δ for multiple scattering is smaller than 0.1 for the cylinder geometries. Generally the effect of multiple scattering dependent on the scattering geometry is easy to investigate directly from the experiment. Figure 7.3 shows the q-averaged and normalized time-of-flight signal (see eq. 7.18) for a NS3+5.8mol%H_2O sample in three different scattering geometries: Hollow cylinder, flat slab, and full cylinder. As it is predicted by the calculations of Blech and Averbach, the multiple scattering has minor importance in all the used geometries. Within the statistics obtained in the experiments, the effect of multiple scattering vanishes.

Placzek Correction Once the empty can contribution is subtracted and the signal is corrected for multiple scattering events, the scattered intensity can be normalized and related to a sample only scattering cross section. In a diffraction experiment the effective differential scattering cross section $d\sigma/d\Omega$ is measured where, according to Eq. 4.4

$$I^{norm} = \int_0^\infty f(E')\frac{d^2\sigma}{d\Omega dE'}dE' \approx N f_o \left(\frac{d\sigma}{d\Omega}\right)^{norm} \tag{7.4}$$

with the energy dependent detector efficiency $f(E')$. The detectors thus carry out the integration with respect to the final energy. In order to extract the static structure factor 4.12

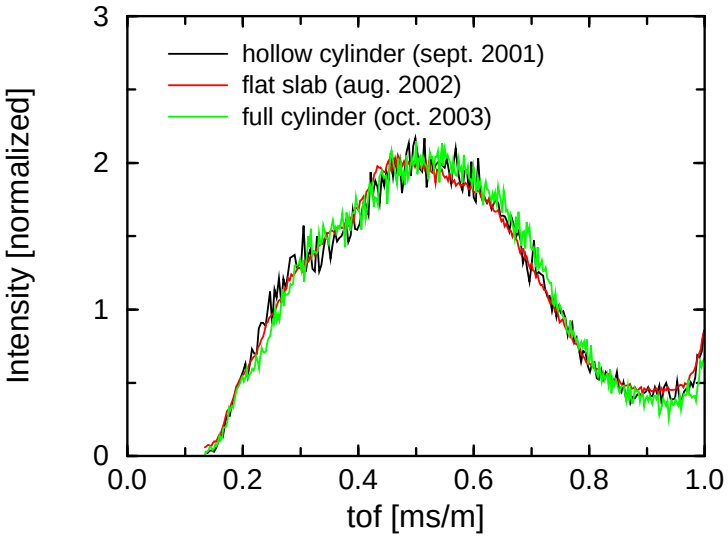

Figure 7.3: *Normalized time-of-flight signals summed over q for NS3+5.8mol%H_2O samples in three different scattering geometries. Within the statistics differences are not seen, showing that self absorption and multiple scattering events are little important.*

it becomes necessary to correct for inelasticity and incoherent contributions. The approximation in equation 7.4 takes into account the detector efficiency in the factor f_o for elastic scattering only.

Placzek suggested in 1952 a method of calculating the corrections to the static approximation if the mean energies $E - E' = \hbar\omega$ obtained by inelastic scattering are small compared to the incident energy E' [Pl52]. Hence it is appropriate to expand the scattering law 4.6 in orders of $(E - E')/E$. The corrected intensity can be expressed with the self $(I = J)$ and distinct $(I \neq J)$ part of the structure factor. The self part comprises naturally some coherent and all incoherent contributions $((d\sigma/d\Omega)^{self} = (d\sigma/d\Omega)_{coh}^{I=J} + (d\sigma/d\Omega)_{inc})$ and the distinct part comprises coherent terms only $((d\sigma/d\Omega)^{dis} = (d\sigma/d\Omega)_{coh}^{I\neq J})$. In this expansion 7.4 reads:

$$I^{norm} = N f_o \left[\left(\frac{d\sigma}{d\Omega}\right)^{dis} + \left(\frac{d\sigma}{d\Omega}\right)^{self} \left\{ 1 + P\left(\frac{m_n \mathbf{q}^2}{\overline{M} k^2}\right) + O\left(\frac{m_n^2 \mathbf{q}^4}{\overline{M}^2 k^4}\right) \right\} \right] \tag{7.5}$$

with the second order polynomial

$$P\left(\frac{m\mathbf{q}^2}{Mk^2}\right) = \frac{m_n}{\overline{M}} \left\{ \frac{\bar{K}}{3E} - \frac{\mathbf{q}^2}{2k^2}\left(1 + \frac{\bar{K}}{3E}\right) \right\} \tag{7.6}$$

where m_n is the neutron mass and $\overline{M}$ is the average mass of a nucleus in the liquid. $\bar{K}$ is the mean kinetic energy of a nucleus equal to $\frac{3}{2}k_BT$ in the classical limit. Equation 7.5 exhibits an expansion of the scattering law $S(\mathbf{q},\omega)$ in orders of the square of the scattering vector $(\mathbf{q}^2/k^2)$ and the mass ratio $(m_n/\overline{M})$. The latter one increases the quality of the approximation for heavy nuclei and high incident energies. Accordingly the corrections are significant for systems involving hydrogen where the mass ratio reaches unity. Hence the Placzek corrections have definitely to be taken into account for hydrous silicates.

The normalization factor f_o is obtained from a vanadium run. Since vanadium is a purely incoherent scatterer, equation 7.5 yields for vanadium in first order in q^2

$$f_o = \frac{I_V^{norm}(q)}{N_V b_{inc,V}^2 \left[1 + P_V\left(\frac{m_n \mathbf{q}^2}{\overline{M} k^2}\right)\right]} \tag{7.7}$$

with $(d\sigma/d\Omega)^{dis} = 0$ and $(d\sigma/d\Omega)^{self} = b^2_{inc,V}$. Inserting 7.7 into 7.4 leads then to an expression where the normalization factor is expressed in the numbers of atoms in the sample and the vanadium can:

$$\left(\frac{d\sigma}{d\Omega}\right)^{norm} = \frac{I^{norm}}{I^{norm}_V}\frac{N_V}{N}b^2_{inc,V}P_V\left(\frac{m_n\mathbf{q}^2}{\overline{M}k^2}\right) \tag{7.8}$$

If higher orders are neglected, the coherent contribution of the scattered intensity can be extracted from 7.5 as

$$\left(\frac{d\sigma}{d\Omega}\right)^{dis}_{coh} = \left(\frac{d\sigma}{d\Omega}\right)^{norm} - \left(\frac{d\sigma}{d\Omega}\right)^{self}\left\{1 + P\left(\frac{m_n\mathbf{q}^2}{\overline{M}k^2}\right)\right\} \tag{7.9}$$

The factor in $(d\sigma/d\Omega)^{self}$ in 7.9 can be easily determined since

$$\left(\frac{d\sigma}{d\Omega}\right)^{self} = \left(\frac{d\sigma}{d\Omega}\right)^{self}_{coh} + \left(\frac{d\sigma}{d\Omega}\right)_{inc} = \langle b_I\rangle^2 + b^2_{I,inc} = \langle\overline{b^2_I}\rangle = \frac{\sigma_s}{4\pi} \tag{7.10}$$

From equation 4.5 it is evident that the coherent scattering law 7.9 can be easily related to the static structure factor 4.12. From equation 4.12 one splits the coherent part of the static structure factor in a self and a distinct part according to

$$S(\mathbf{q}) = \frac{1}{N\langle\overline{b^2_{I,coh}}\rangle}\left[N\langle\overline{b^2_{I,coh}}\rangle + \sum_{I\neq J}\overline{b}_{I,coh}\overline{b}_{J,coh}\langle e^{i\mathbf{q}(\mathbf{R}_I-\mathbf{R}_J)}\rangle\right] \tag{7.11}$$

where the second contribution on the parenthesis can directly be identified with the distinct contribution of the coherent scattering cross section 7.9. Hence

$$S(\mathbf{q}) = 1 + \frac{1}{\langle\overline{b^2_{I,coh}}\rangle}\left(\frac{d\sigma}{d\Omega}\right)^{dis}_{coh} \tag{7.12}$$

Equation 7.12 allows the neutron scattering structure factor from the Placzek-corrected normalized scattering signal 7.9 to be extracted.

7.1.2 Normalized Curves

The first step in order to come to a structure factor from the output of the detectors is to apply the corrections for self absorption and multiple scattering and to normalize on the vanadium run. The self absorption coefficients were calculated according to the definitions given by Paalman and Pings [Pa62] with the *IDA* program package [Wu01]. Due to the cylinder symmetric geometry and the thickness of only 0.1 mm in the diffraction experiment, the absorption by the screening of the metallic can is rather low. The crucial variable for the self absorption of the sample is the number density of scatterers (number of scatterers / cell volume). The number of scatterers is accessible from the mass of the sample and its (known) composition. The following table gives the number of scatterers for the samples as they were in use for the diffraction experiment on D20. The density is then obtained dividing by the container volume. For the diffraction experiment on D20, the illuminated beam height was 3.6 cm. With an inner container radius of 0.3 cm, the volume of the illuminated part of the container is equal to 1.018 cm^3. It should just be mentioned that the sample sizes

silicate	X = 0.0	X = 5.8	X = 9.4	X = 10.5	X = 13.7
SiO_2 + X mol% H_2O	2.791	-	-	2.938	-
NS3 + X mol% H_2O	2.717	2.439	3.146	-	-
albite + X mol% H_2O	2.860	2.800	2.740	-	1.555
vanadium	0.496	-	-	-	-

Table 7.2: *Number of scatterers in units of* $[10^{22} particles]$ *in the samples investigated in the present work as derived from the sample mass and the volume of the sample holder.*

were much smaller than could actually be accommodated in the beam, but the complicated and extremely costly fabrication process did not allow us to fabricate more material. For most of the samples the filling height was around 3.0 cm. Unfortunately the sample pieces had no cylindrical geometry so that the volume was also not completely filled with sample material. In order to calculate self absorption coefficients, the sample was assumed to be distributed homogeneously in the cylinder volume of 1.018 cm^3. Note that other treatments would lead to ill-defined screening contributions in the case of very small occupied volumes. Figure 7.4 and 7.5 show the correction factor A_{rel} for scattering and self absorption for the sodium silicate samples, energy dependent and energy averaged, dependent on the scattering angle. The self absorption correction factors are shown for the vanadium container for the

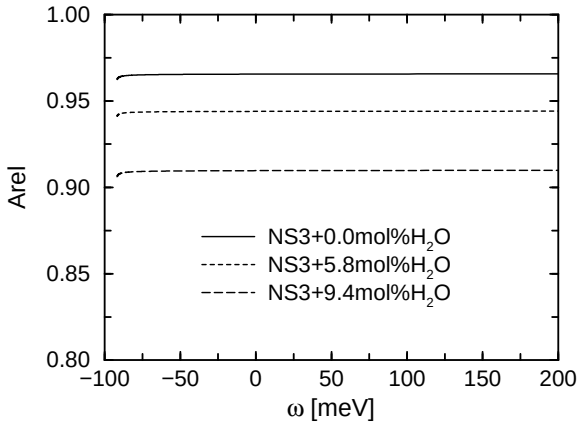

Figure 7.4: A_{rel} *summed over* q

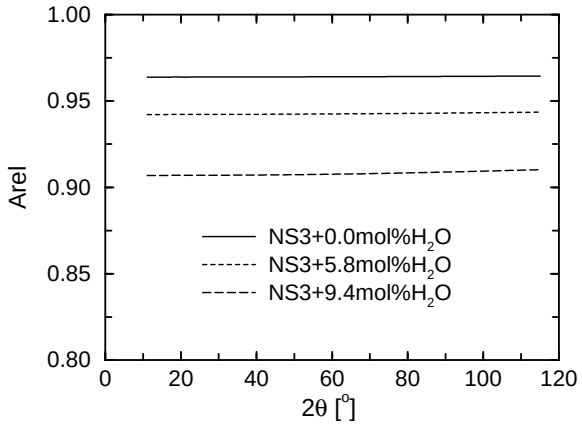

Figure 7.5: A_{rel} *averaged over* ω

diffraction experiments at a neutron energy of 92.58 meV. It can be seen that the curves are rather flat, in the energy dependent representation as well as in the plot over the scattering angle. Results for the lower neutron energy for the time-of-flight experiments are similar. Generally, the coefficient A_{rel} decreases with increasing water content due to the high scattering cross section of water.

The flat character is a general feature of the self absorption coefficients for the considered geometries and materials. It is therefore appropriate to approximate the coefficients with a constant. The following tables summarize the (constant) self absorption coefficients A_{SSC} and A_{rel}.

The corrections for multiple scattering are governed by the scattering cross section and become more important for higher scattering cross sections and therefore higher water content. For the present geometry these contributions are all below $\delta = 0.1$. It turns out that, since also the self absorption coefficient A_{SSC} is water concentration dependent but in the inverse

silicate	X = 0.0	X = 5.8	X = 9.4	X = 10.5	X = 13.7
SiO_2 + X mol% H_2O	0.94	-	-	0.87	-
NS3 + X mol% H_2O	0.94	0.92	0.87	-	-
albite + X mol% H_2O	0.95	0.91	0.88	-	0.92

Table 7.3: *Constant coefficients A_{SSC} for scattering and self absorption in the used samples.*

silicate	X = 0.0	X = 5.8	X = 9.4	X = 10.5	X = 13.7
SiO_2 + X mol% H_2O	0.97	-	-	0.91	-
NS3 + X mol% H_2O	0.96	0.94	0.91	-	-
albite + X mol% H_2O	0.96	0.94	0.92	-	0.95

Table 7.4: *Constant coefficients A_{rel} for scattering and self absorption in the used samples.*

sense of δ, the product $A_{SSC}^{-1}(1-\delta) \sim 1$ equals unity taking the number density of scatterers into account. Once the sample container is subtracted, a normalized intensity according to 7.8 can be obtained for the samples. This requires the number of scattering atoms of the vanadium cylinder. If it is assumed that the container bottom is not in the beam, the following number is obtained from the density and the thickness of the cylinder according to

$$N_V = \frac{\rho_V V_V}{M_V} = \frac{\rho_V}{M_V} \pi h (r_{outer}^2 - r_{inner}^2) \tag{7.13}$$

where $h = 3.6$ cm is the illuminated height of the cylinder, $M_V = 50.94$ g/mol is the atomic mass of vanadium and $r_{outer} = 0.31$ cm and $r_{inner} = 0.30$ cm are the outer and inner radius of the can, respectively. The resulting value for the number of vanadium atoms is 4.962 10^{21}. With this value and the scattering length of vanadium of 6.35 10^{-15} m, the normalized intensity arising from the sample is given after equation 7.8

$$\left(\frac{d\sigma}{d\Omega}\right)^{norm} = \frac{I_S}{I_V}\frac{1}{N_S} \cdot 2.00 \cdot 10^{-7} m^2 P_V \left(\frac{m_n \mathbf{q}^2}{\overline{M} k^2}\right) \tag{7.14}$$

where N_S is the number of scatterers obtained form table 7.2.
The normalized intensity for the albite samples is shown in figure 7.6. The normalized intensity of vanadium, as completely incoherent scatterer, given by the average scattering lengths as shown in 7.10 which was fixed in figure 7.6. All other intensities are shown relative to the intensity of the vanadium can. Also for albite samples the self contribution is according to equation 7.10 given by the square of their scattering lengths. These values can be easily obtained from table 5.5. For the dry and the three hydrous albite samples they are given as $27.63 \cdot 10^{-30}$ m^2, $51.92 \cdot 10^{-30}$ m^2, $67.04 \cdot 10^{-30}$ m^2, and $84.86 \cdot 10^{-30}$ m^2, respectively. A comparison of these values to the small-q end of the curves of figure 7.6 (where the Placzek polynomial has little influence) shows quickly that the average intensities as normalized to vanadium are lower than the expected averages according to equation 7.10. This can be explained with the fact that the bottom of the vanadium container was not completely out off the beam. Also the ratios between the albite curves themselves seem to deviate little from the expected values. This is most likely due to over or underestimated effects of multiple scattering and self absorption as well as uncertainties in the water content. Since the

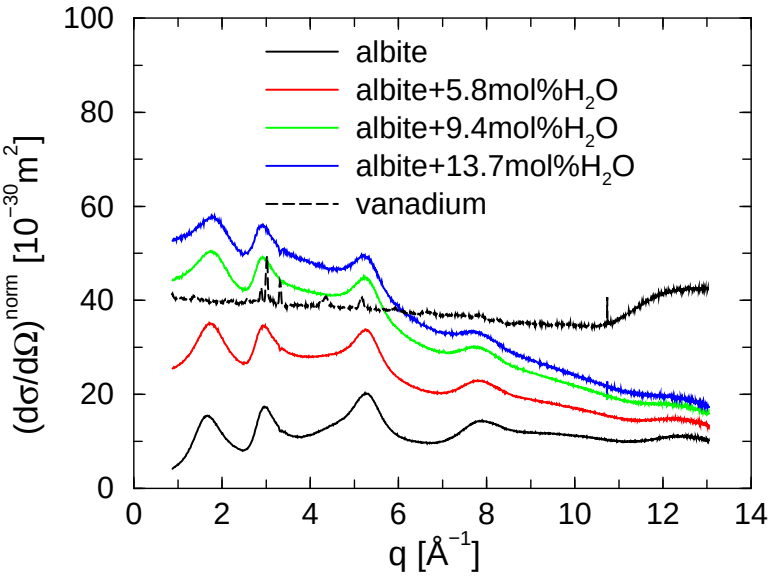

Figure 7.6: *Normalized intensities for the albite samples.*

wrong normalization on vanadium affects also the "amplitudes" in the final structure factors, the error will be corrected by a comparison to data found in literature. In particular, the structure factor of pure SiO_2 has been measured many times on different instruments [Si80, Pr87, Su91]. Comparisons with these studies show that in the present case the intensity of the scattering is underestimated by a factor of 1.9. This is in rather fair agreement with the deviations of the expected total structure factors and the self contributions found in figure 7.6.

As can be seen from figure 7.6 the absolute intensities are strongly affected by the incoherent and inelastic contributions of hydrogen in the hydrous samples. In order to obtain a coherent structure factor the curves have to be appropriately corrected for these contributions according to the Placzek formalism presented in section 7.1.1. The relatively short q range available on D20 allows only fits of a Placzek polynomial of quadratic order. Higher orders fitted to the small q range lead to unphysical inflection points in the polynomial. The quadratic Placzek correction for the sample albite + 5.8mol%H_2O is shown in figure 7.7. It has to be pointed out that, despite of the quadratic order the quality of the fit is rather bad and it is known that fits including higher q values than those available on D20 lead to rather different correction polynomials. In fact it turns out that the corrected curves show features that are clearly related to insufficient accuracy of the Placzek fit. This becomes evident if the differences between the corrected curves for different water concentrations are considered. The differences between the curves are themselves nearly quadratic functions, except for distinct q values that can be supposed to contain the physical effects associated to the different water concentrations. In order to reveal these interesting q-values and to remove the errors caused by the insufficiency of the polynomial, the differences of each hydrous sample to the corresponding dry composition were quadratically fitted again and subtracted from the signal. Note that choosing again a quadratic fit function allows for a correction of the Placzek correction within the space spanned by the entity of the quadratic fit functions. Effects that exhibit a more complex behavior than quadratic are naturally untreated by such a second order correction.

In order to take care of errors that arise from the rather small q-range on D20, comparison to the curves recorded on the spectrometer D4 were made. On D4, q-ranges up to 35 $Å^{-1}$ are

and the secondary correction of the dry sample with respect to the more reliable curve obtained on D4. In order to obtain reliable data also for wave vectors below 2 $Å^{-1}$, all samples were remeasured on D20 with a wavelength of 2.41 Å . These additional spectra were also corrected with a Placzek polynomial and for the difference to the D4 data and then matched to the distinct spectra obtained at a wavelength of 0.95 $Å^{-1}$. The final normalization is performed according to equation 7.12. The average coherent squared scattering lengths are the values of table 5.6 divided by 4π.

7.1.3 Results of the Data Analysis

Fig. 7.9 shows the structure factors of the dry silicates. The main peaks at 1.7 $Å^{-1}$, 3.0 $Å^{-1}$

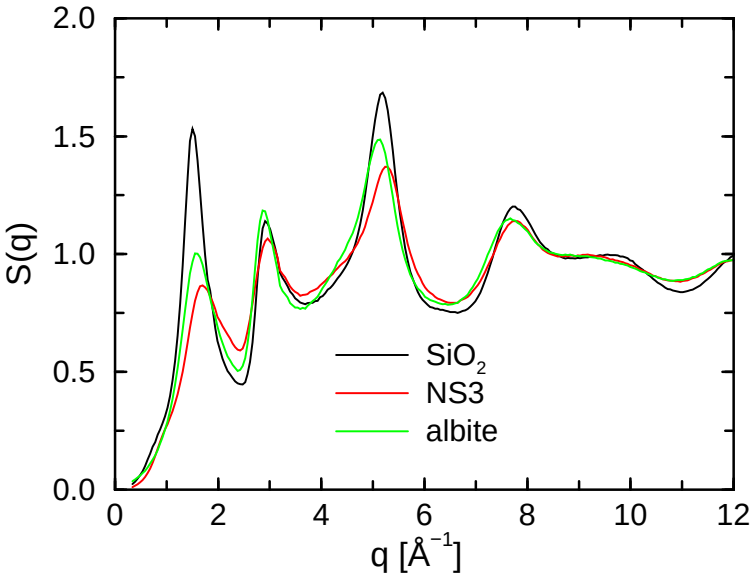

Figure 7.9: *Structure factor of dry amorphous SiO_2, dry NS3, and dry albite. Peak heights seem to follow the rule (from low to high) NS3, albite, SiO_2.*

and 5.2 $Å^{-1}$ are due to typical distances in the tetrahedral network of the silicate. Their position seems to vary only slightly when the network modifiers are added. In contrast, their heights are well affected by the modifier addition. In particular, the heights seem to follow the rule (from low to high) NS3, albite, SiO_2. We associate this behavior to the extent that the perfect tetrahedral network is destroyed by the addition of the modifiers. According to this, the SiO_2 network has naturally the highest order, followed by albite and NS3.

It seems strange to find a higher order in the sodium alumino silicate than in the sodium silicate. This behavior can be understood taking into account the structural properties of the two compounds. It was found that sodium silicates show a prepeak effect in the structure factor at roughly 1.0 $Å^{-1}$ [Me02, Ho01]. This prepeak was associated by molecular dynamics studies to channels that maintain sodium diffusion in the silicate [Me04, Ho02]. These sodium rich channels disrupt the network. The disturbance results obviously in smoother network related peaks at 1.7 $Å^{-1}$, 3.0 $Å^{-1}$ and 5.2 $Å^{-1}$ in the structure factor and on the other hand in the channel related prepeak at roughly 1.0 $Å^{-1}$ (see figure 1.5). It was also found that the channel system is redestroyed by the addition of aluminum [Ka04a]. This destruction may explain the more intense peaks in the albite S(q).

Figures 7.10, 7.11 and 7.12 show the structure factors for the hydrous samples as obtained after all corrections. It can be seen that for one silicate composition, the structure factors are very close for different water contents. The main differences regarding the water content

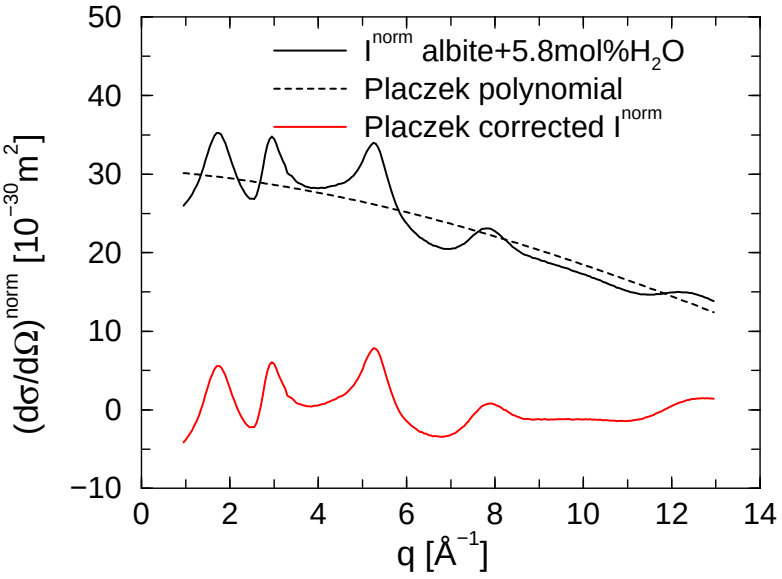

Figure 7.7: *Placzek correction for the sample albite + 5.8mol%H_2O.*

available. Indeed it turns out that for a dry SiO_2 sample the corrected spectrum obtained from D4 differs from the one on D20. Due to the higher q-ranges covered on D4, the data obtained there can be supposed to be much more reliable. Starting again from the same argument as above, that secondary corrections within the space spanned by the primary corrections should not touch relevant physical effects, the same procedure can be applied again on the difference between the signals of D4 and D20. Note that such secondary treatment practically corresponds to the normalization on a different detector efficiency (vanadium). Figure 7.8 shows the distinct scattering cross sections for SiO_2 as obtained on the spectrometers D20 and D4 after the Placzek correction. It can be seen that the D20 data have

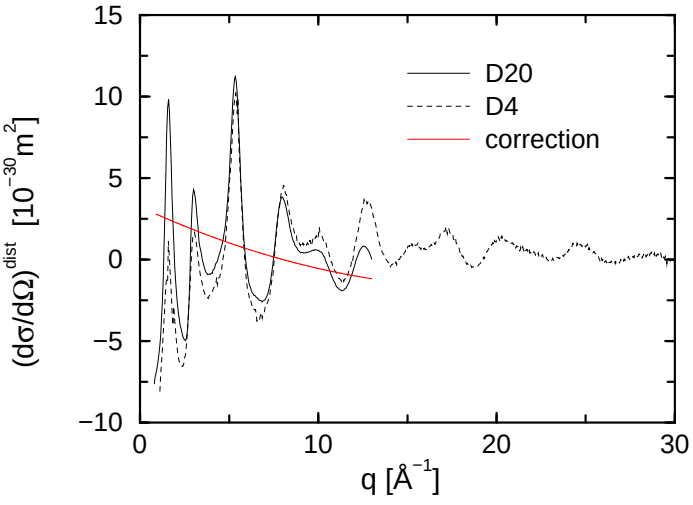

Figure 7.8: *Distinct scattering cross sections as obtained on the spectrometers D20 and D4 for SiO_2 after Placzek corrections with a second order polynomial.*

generally an equivalent shape compared to the D4 data. The D4 data is little reliable below 3 $Å^{-1}$ due to an instrument specific high background. However, due to the Placzek fit of lower quality performed on the D20 data, the D20 curve shows higher intensities below 7 $Å^{-1}$ compared to the D4 data and smaller values above 7 $Å^{-1}$. Since the Placzek fit on the D4 data is more reliable, the D20 data was corrected by the difference to the D4 data.
The above discussion of the correction of the data obtained on D20 can be summarized in two steps: The secondary correction of the hydrous samples with respect to the dry sample

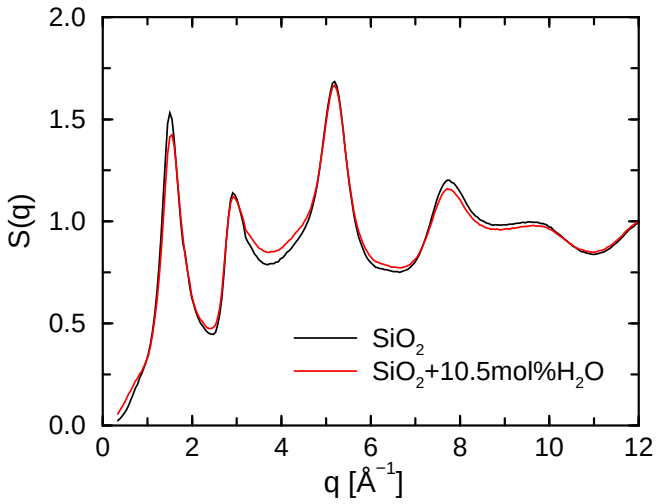

Figure 7.10: *Structure factors of pure and hydrous silica.*

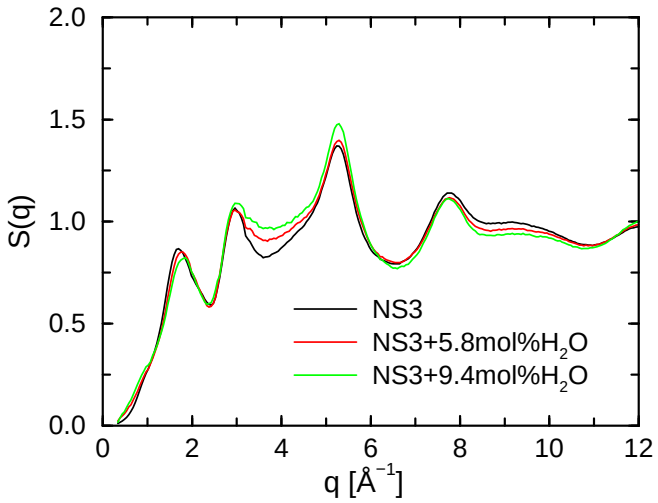

Figure 7.11: *Structure factors of pure and hydrous NS3.*

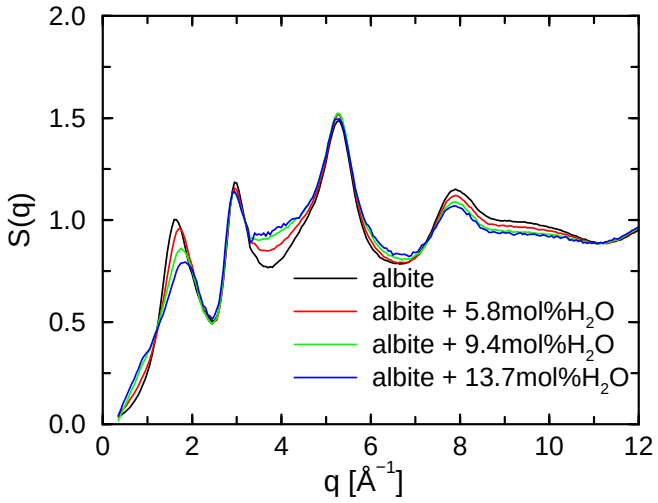

Figure 7.12: *Structure factors of pure and hydrous albite.*

for one silicate composition occur at q-vectors of about 4 $Å^{-1}$. Also, in the case of hydrous silica and hydrous albite, the height of the first sharp diffraction peak seems to be slightly decreased with increasing water content. The q-vector of 4 $Å^{-1}$ corresponds to a real space distance of roughly 1.6 Å. Note that this value is rather close to the H-H interatomic distance in the water molecule of 1.51 Å. Since the partial contributions of the structure factors are currently not known, the origin of the enhancement in the structure factors at 4 $Å^{-1}$ cannot be unequivocally assigned. However, the characteristic distance and the scaling with the water content are strong evidence for water molecules in the sample. The results for the hydrous samples can be compared to those of Zotov *et al.* [Zo96] for deuterated samples which are shown in figure 7.13. Whereas in the case of hydrous samples the coherent scattering is dominated by oxygen, in the deuterated material the coherent scattering arises from deuterium ($\sigma_{coh,D} = 5.592$ barn $> \sigma_{coh,O} = 4.232$ barn $> \sigma_{coh,H} = 1.757$ barn).

Obviously for deuterated samples, the differences between the dry and deuterated curves

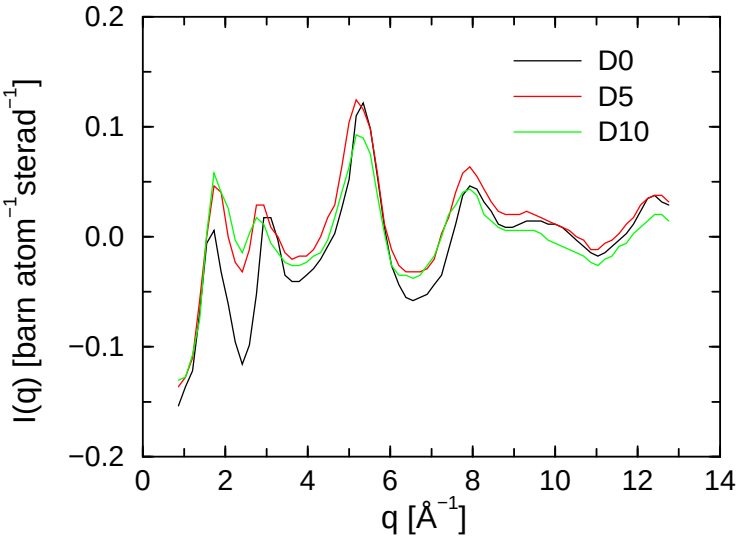

Figure 7.13: *Normalized coherent structure factor of deuterated NS2, after Zotov et al [Zo96]. D0, D5 and D10 refer to NS2+0.0 mol %D_2O, NS2+15.1 mol % (5.0 wt.%) D_2O, NS2+27.2 mol % (10 wt.%) D_2O*

occur, in contrast to hydrous samples, in the region around 2.5 $Å^{-1}$. Note that such difference is in agreement with the simulated structure factor in figure 6.8, where in the region around 2.5 $Å^{-1}$ the structure factor of the deuterated sample lies above the one of the hydrated sample. A similar picture is obtained from the structure factors of hydrous and deuterated liquid water which are shown in figure 7.14. It can be seen that indeed the substitution of hydrogen by deuterium leads to a shift of the first sharp diffraction peak (FSDP) in the structure factor of water from 3.1 $Å^{-1}$ to 2 $Å^{-1}$. At elevated temperature or pressures the FSDP can be shifted to higher wave vectors.

Last but not least it should be mentioned that the prepeak at 1 $Å^{-1}$ is not visible in the structure factor of hydrous silica. Note that a prepeak was neither seen in dry sodium silicate. Hence, as in the case of sodium silicate it is from the current ambient temperature measurements not evident that a characteristic length scale of 6 Å is present in the glass. Therefore, experiments at elevated temperature are required in order to validate the results on the prepeak presented in section 6.1.3.

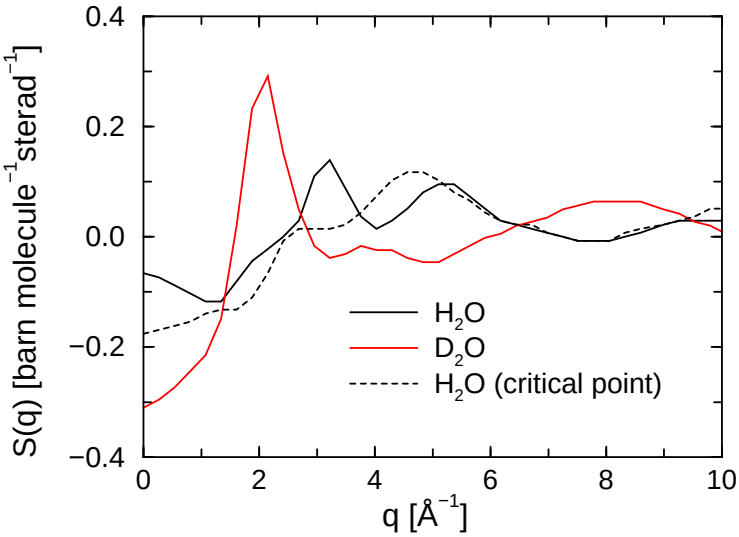

Figure 7.14: *Structure factor of hydrous and deuterated liquid water and hydrous water at the critical point (646 K / 221 bar). Redrawn from [So97].*

7.2 Inelastic Spectra

Inelastic neutron scattering gives information about the vibrational density of states as was demonstrated in section 4.2. Such conversion of the inelastic spectra to a vdos is certainly subject to the incoherent approximation, in particular for coherent scatterers. The large incoherent scattering length of hydrogen improves the quality of the approximations as will be demonstrated in figure 7.21.
Remember for the following discussion that the abbreviations vdos, ndos, and pvdos refer to the vibrational density of states (equation 3.14), the neutron vibrational density of states (equation 4.29), and the partial vibrational density of states (equation 3.15), respectively.

7.2.1 Ndos of Dry Silicates and Amorphous Ice

Before the discussion of the vibrational properties of hydrous silicates it is useful to summarize the main features of vibrational properties of the dry silicates and molecular water.
The vibrational density of states of SiO_2 has been extensively investigated with neutron scattering [CP85] and several computer simulations [Be02, Sa97, Ol99, Ta97a]. Its main features were already presented in section 3.3. The vibrational density of states of sodium silicates was recently theoretically investigated by Ispas *et al* [Is03] and Zotov *et al* [Zo01a]. For dry albite, simulations are not yet completed. Figure 7.15 shows the vibrational densities of states for dry silica as found by Carpenter *et al.* [CP85] and dry NS3 and dry albite as recorded at the ILL-spectrometer IN6. Note that the incoherent approximation (eq. 4.16) works poorly for dry silicates due to their relatively high coherent scattering length and the limited q-range available on IN6. Very generally it can be said, that all densities of states exhibit high intensities in the range from 0 to 60 meV and lower intensities above 60 meV. However, details are only accessible with computer simulations as mentioned above.
For water, in order to get some insight into the physical background of an experimentally measured vibrational spectrum it is useful to estimate the different contributions of translational and rotational motions. If the sample contains water molecules, rotational librations can be expected to occur (see section 3.3). An approach for the separation of translational and rotational motions in a neutron frequency spectrum was proposed by Prask and Boutin

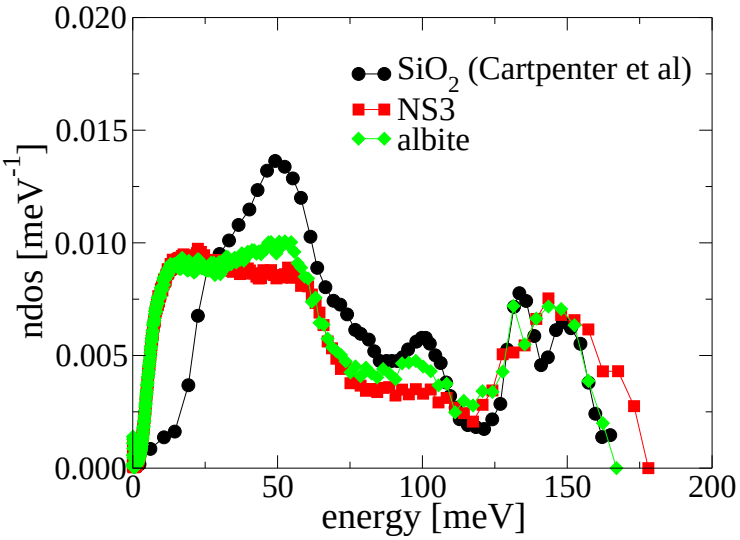

Figure 7.15: *Neutron vibrational densities of states (ndos) of the dry silica (from Carpenter and Price [CP85]) and dry NS3 and albite as obtained on IN6.*

[Pr68]. Their approach starts off by a decomposition of the atomic displacement in 4.6 in displacements of the center of mass $\mathbf{R}_{cm}(t)$ and molecular internal positions $\mathbf{b}_I(t)$:

$$\mathbf{R}_I(t) = \mathbf{R}_{cm}(t) + \mathbf{b}_I(t) \tag{7.15}$$

It is then possible to show that variations of $\mathbf{R}_{cm}(t)$ and $\mathbf{b}_I(t)$ lead - according to eq. 4.15 - each to a separate vibrational density of states, $g_T(\omega)$ of translations and $g_R(\omega)$ of rotations. Both parts of the ndos are additive to the total ndos 4.23

$$g_{eff}(\omega) = g_T(\omega) + \frac{M_T}{M_R} g_R(\omega) \tag{7.16}$$

if the (rather bad) assumption of no translation-rotation coupling is made. For the model case of a molecule whose N strongly scattering nuclei of mass M_{IR} are placed on a sphere of radius $b_I = |\mathbf{b}_I|$ the effective mass for rotations M_R is given by $M_R = N \cdot M_{IR}$. The mass M_T for the translation of the center of mass of a molecular unit is identical with the total molecular mass. For a water molecule performing librational motions the mass ratio is given by

$$\frac{M_T}{M_R} = \frac{18}{2} = 9 \tag{7.17}$$

This means that a neutron scattering experiment is roughly a factor of ten more sensitive to librations than to translations of a water like molecular unit. Therefore, if we had free water molecules in the samples, one should see this also in the inelastic spectrum due to the discussed sensitivity on librations. It will be shown later that librations occur indeed in a rejected water bubble containing sample that showed also quasielastic behavior. It can be anticipated that for the other samples we have neither experimental evidence from NMR spectroscopy for inclusions of liquid water [Hi04].

7.2.2 Quasielastic Behavior

Quasielastic behavior is clearly not seen in the considered samples. This fact clearly rules out the existence of liquid water pockets in the solids. However, the fabrication of some of the samples failed (samples were rejected if they were not transparent [Mu04]). In these

cases it turned out with optical microscopy that the samples contain bubbles. We also investigated one of these samples with time-of-flight spectrometry. The time-of-flight spectra from detectors at different angles can be summed according to

$$I^{tof} = \frac{1}{C_N} \int_{\Theta_{min}}^{\Theta_{max}} \left(\frac{d^2\sigma}{d\Omega dtof} \right) \sin\Theta d\Theta \tag{7.18}$$

(with the normalization $C_N \sim (\theta_{max} - \theta_{min})$) and optionally be transformed into a summed scattering law $S(2\theta, \omega)$ according to equations 4.2 and 4.5. Figure 7.16 shows the elastic lines of the summed scattering law $S(2\theta, \omega)$ of the bubble containing sample of the composition SiO_2+13.7mol%H_2O and the one of the regular sample of the composition SiO_2+10.5mol%H_2O. It can be seen that in the sample with 13.7 mol%H_2O it comes indeed to a quasielastic broadening of the elastic line as it would be observed in liquid water. This behavior proves with neutron that the sample contains highly mobile units carrying hydrogen that are most likely free water molecules.

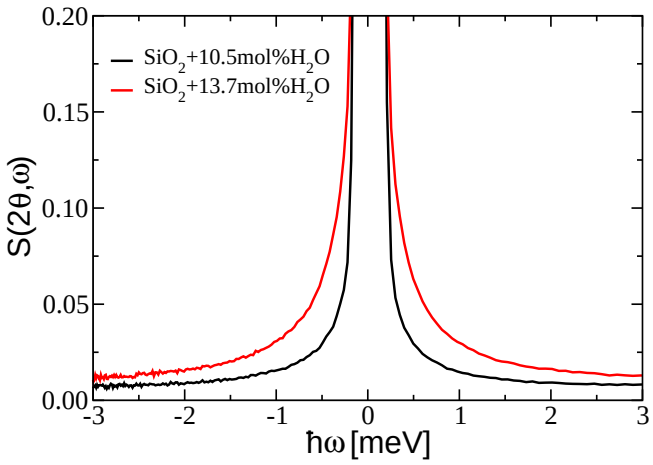

Figure 7.16: *Summed quasi- elastic signal of SiO_2+10.5mol%H_2O (black line) and SiO_2+13.7mol%H_2O (red line). It can be seen that the sample SiO_2+13.7mol%H_2O shows quasielastic broadening at the flanks of the elastic line of SiO_2+10.5mol%H_2O.*

7.2.3 Vibrational Excitations of Hydrous Silicates

The discussion is started off with the consideration of the time-of-flight spectra of the hydrous silicates. It is important to note that the sample spectra are not perturbed by noise of the background or the empty can. Figure 7.17 shows the logarithmic plot of the I^{tof} spectra of the empty instrument, the empty can and the sample. It can be seen that the signal of the sample is roughly one order of magnitude higher than the one of the empty can and even two orders of magnitude higher than the signal of the empty instrument.
Figure 7.18 shows the summed time-of-flight spectra of the compositions SiO_2+10.5mol%H_2O, NS3+9.4mol%H_2O and albite+9.4mol%H_2O. The elastic peak corresponding to a neutron wave length of 4.14 Å is situated at a flight time of 1.05 ms / m. Shorter flight times correspond to neutrons that gained energy from the sample due to interactions with phonons. The time-of-flight spectra of all hydrous silicates show two faint peaks left of the elastic line. In the case of hydrous silica, the first peak is situated at 0.7 ms/m, for hydrous NS3 and hydrous albite the first peak is shifted to 0.5 ms/m. In contrast to the first peak, the second peak has a similar location in hydrous silica and hydrous NS3 at 0.35 ms/m, whereas hydrous albite seems to deviate with a peak position of only 0.3 ms/m. The equivalent peak

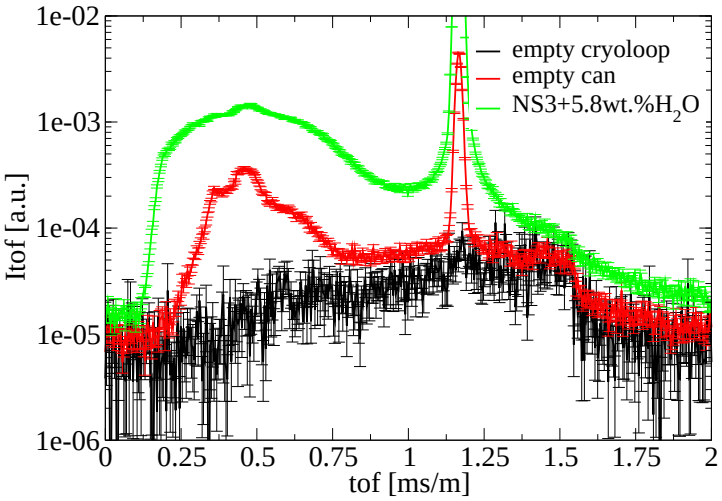

Figure 7.17: *Summed intensities of the sample, the empty can and the empty instrument with the cryoloop (with error bars).*

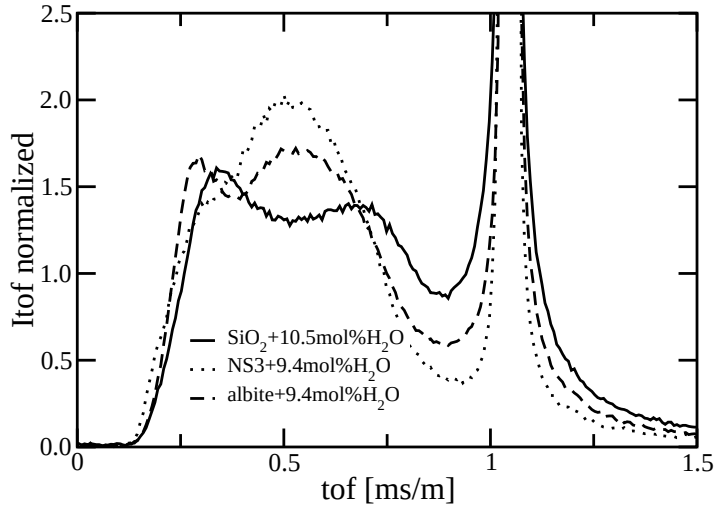

Figure 7.18: *Summed time-of-flight spectra of the silica+10.5mol%H_2O, NS3+9.4mol%H_2O and albite +9.4mol%H_2O (normalized on area under of the up-scattering intensity).*

positions in the time-of-flight spectrum give a first indication that some features of the vibrational spectrum are retained from SiO_2 to albite. Some other properties may change with the composition of the matrix if peak positions are shifted. For flight times shorter than 0.17 ms/m the time-of-flight spectrum approaches again zero. No more phonon excitations occur. Since a flight time of 0.17 ms/m corresponds to an energy of 180 meV, the estimations of section 3.4.2 for the energy range of the vibrational excitations in hydrous silicates seem to be confirmed.

In the above discussion, spectra of hydrous silicates at roughly the same water content were compared for different matrices. For the matrices where samples with different water content are available (NS3 and albite), the influence of the water content on the time-of-flight spectra is discussed in the following.

Figure 7.19 shows the time-of-flight spectra for different albite-water mixtures. It is interesting to note that the relative intensities with respect to the dry sample can be easily predicted. Starting from eq. 4.29 it can be shown that the differential cross section 4.5 is proportional

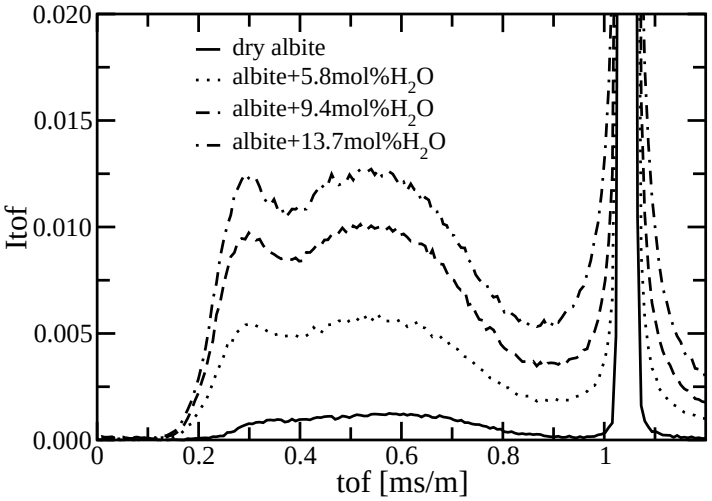

Figure 7.19: *Summed time-of-flight spectra of the hydrous albites. The figure shows absolute intensities normalized to the same vanadium and corrected for the weight.*

to the water concentration

$$I^{tof} \sim \left[\frac{\sigma_{H_2O}}{\overline{M}_{H_2O}} C_{H_2O} + \frac{\sigma_{albite}}{\overline{M}_{albite}} C_{albite} \right] \tag{7.19}$$

The cross sections σ_{H_2O} and σ_{albite} are 81.67 barn and 3.74 barn, the molar concentrations are the ones of table 5.3 and the average atomic masses can be found in table 5.4. With these values of the tables one finds that according to equation 7.19 the inelastic scattering intensities of the samples have the ratio:
$I_{alb+0.0mol\%H_2O}/I_{alb+5.8mol\%H_2O}/I_{alb+9.4mol\%H_2O}/I_{alb+13.7mol\%H_2O} = 1.0/4.1/6.0/8.3$ which corresponds rather well to figure 7.19. This shows that the water contents obtained from light scattering were correct within 10%.
In order to obtain a neutron vibrational density of states, the time-of-flight spectrum has now to be brought onto a neutron energy gain based scale. This conversion is performed according to equation 4.2. Since the recorded spectrum naturally contains multi-phonon processes, an appropriate multi-phonon treatment is mandatory. The determination of multi-phonons in the vibrational spectrum is a rather sophisticated task. The algorithm proposed by Reichart [Re84] (as demonstrated in section 4.2) was employed in order to find the approximate neutron one phonon density of states. Figure 7.20 shows the ndos obtained for the sum 4.21 truncated after 2,3,4,5 and 6 terms. It can be seen that indeed the increment between two terms decreases as the order increases. However, it is difficult to obtain a good convergence for the present form of the non-corrected spectrum. Other algorithms [Wu93] struggled also with the computation of the multi-phonons at high energies.
In order to test if the incoherent approximation 4.16 works well, it can be tested if the vibrational density of states generated on the basis of spectra corresponding to different values of momentum transfer lead to the same results. Figure 7.21 shows the ndos for hydrous silica obtained if the total number of detectors is split in three groups - low q's, intermediate q's and high q's - each group comprising the same number of detectors. It can be seen that within statistical limitations and the convergence of the algorithm, differences between the ndos arising from different q-vectors do not occur.
Apart from the neutron vibrational density of states, another interesting quantity to look at is the signal of the protons. The contributions of the protons to the vibrational spectrum cannot be directly extracted experimentally. However, a certain approximate idea of this

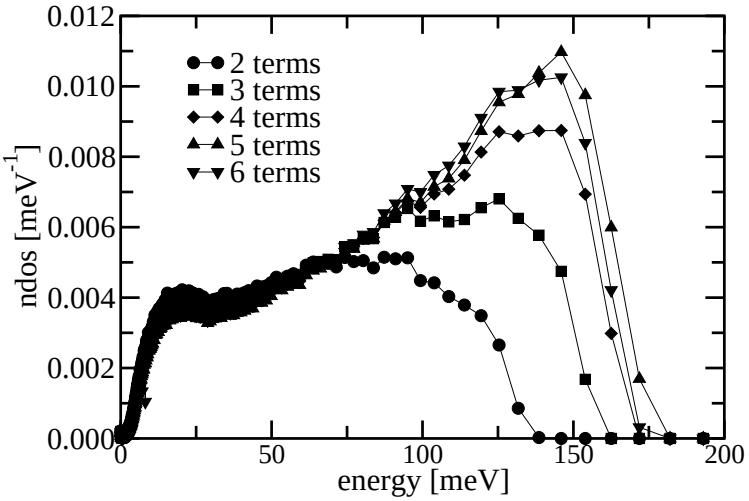

Figure 7.20: *Multi-phonon expansion with 2, 3, 4 and 5 multi-phonon terms. Only the curve corresponding to 6 terms is normalized.*

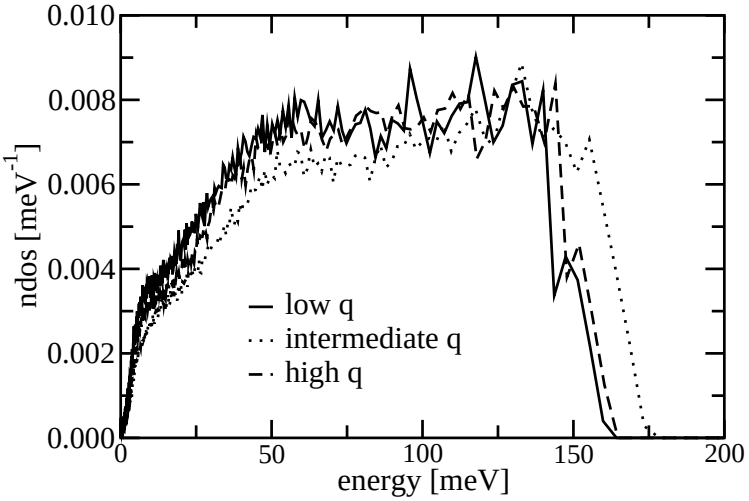

Figure 7.21: *ndos based on detectors at low, intermediate and high angles. The deviation of the curve corresponding to the intermediate q's arises from a bad normalization due to a different high energy cutoff.*

quantity van be obtained from the difference of the hydrous and the dry samples. Performing such differences in the time-of-flight-angle space

$$I^{tof}_{proton} = I^{tof}_{hydrous} - I^{tof}_{dry} \tag{7.20}$$

opens -in principle- the possibility of obtaining a density of states free from incoherent approximations since protons are extremely close to incoherent only scatterers. In addition, the incoherent contribution of (water-)oxygen ($\sigma_{inc} = 0.0008$ barn) is tiny compared to hydrogen ($\sigma_{inc} = 80.25$ barn). Note that such an approximation of course neglects the influence of the oxygen atoms of the water molecules and the influence of water on the dry vibrational spectrum (the "cross terms"). A further restriction of this approximation emerges from the failure of the multi-phonon expansion 4.9 in the case of very light scatterers such as protons (remember that $(\hbar q^2/2\overline{M}\omega) < 1$ was the condition for the multi phonon expansion 4.9).
In the following, the proton densities of states of the considered samples will be discussed using the average masses of table 5.4.

Hydrous Silica Figure 7.22 shows the ndos of a sample of SiO_2+10.5mol%H_2O in comparison to a water bubble containing sample of SiO_2+13.7mol%H_2O. The ndos of SiO_2+10.5

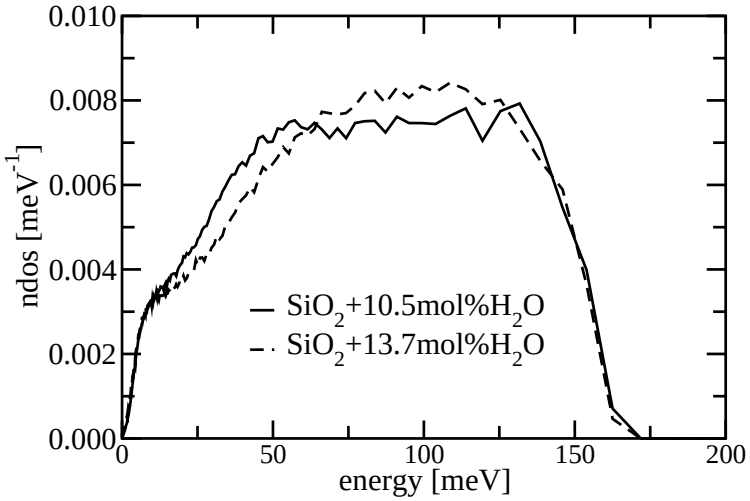

Figure 7.22: *Neutron vibrational density of SiO_2+10.5mol%H_2O (dashed line) and the water bubble containing sample of SiO_2+13.7mol%H_2O (solid line).*

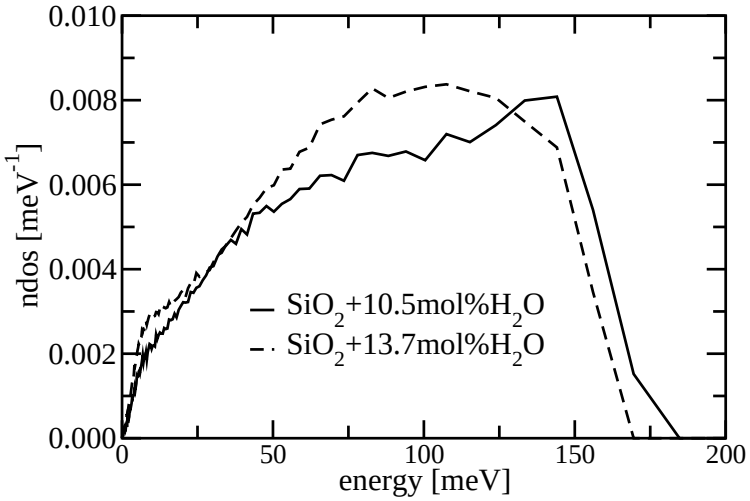

Figure 7.23: *Corresponding proton contribution.*

mol%H_2O is characterized by a very flat shape between 50 meV and 140 meV. In the region between 0 meV and 50 meV a certain emerging peak at roughly 12 meV can be recognized. For energies greater than 140 meV, the ndos drops abruptly to zero. This high energy cut off at roughly 150 meV was already expected according to the discussion in section 3.4.2.
Due to the absence of property-characterizing peaks in the vibrational spectrum of SiO_2+10.5-mol%H_2O, the comparisons to deuterated samples and other water concentrations would be of particular importance. Unfortunately deuterated samples are not available. The only spectrum to compare is the one of the sample of SiO_2+13.7wt%H_2O that was rejected since it turned out during the sample preparations that the sample contains bubbles and shows therefore quasielastic behavior (see figure 7.16).
Figure 7.22 shows that the vibrational spectrum of the bubble containing SiO_2+13.7mol%H_2O spectrum has a rather similar shape compared to the one of the SiO_2+10.5mol%H_2O sample. However, important differences can be recognized: The shoulder at roughly 50 meV is less pronounced in the vibrational spectrum of SiO_2+13.7mol%H_2O and some intensity seems to be shifted to the region between 60 meV and 120 meV. Since one knows from figure 3.4 and the discussion of section 7.2.1 that librational vibrations of water molecules are energetically located in this region, the intensity enhancement between 60 meV and 120 meV in the vibrational spectrum of the SiO_2+13.7mol%H_2O can most likely be attributed to the presence of

free water molecules. The loss of intensity compared to the SiO_2+10.5mol%H_2O spectrum between 10 meV and 50 meV suggests a less important influence of the water molecules in the bubbles in this region. Hence the interesting point in the comparison between the two spectra is indeed that a clear picture of the energetic location of contributions of free water molecules and water dissolved water can be obtained. This is also important for the discussion of the other silicate compositions where it will be shown that scaling of the intensity around 60 meV is absent.
It is also interesting to compare the vibrational spectrum of SiO_2+10.5mol%H_2O to the one of opal (a crystalline form of silica with water) as obtained by Susnowska *et al.* [Su97]. The spectrum of Susnowska *et al.* for the density of states of hydrous opal exhibits a strong peak at roughly 8 meV. This corresponds exactly to the region where phonon excitations of ice are located (see figure 3.4) . Since, in the present study such excitations in this region are not seen, it must be concluded that water is dissolved in a different way than in opal.

Hydrous Sodium Tri-Silicate Figure 7.24 shows the comparison of the vibrational spectra of NS3+5.8mol%H_2O and NS3+9.4mol%H_2O. The shape of the two spectra deviates considerably from the one of silica-water system but spectra for sodium silicate with the two water contents are rather close to each other. The spectrum of hydrous sodium silicate is characterized by the shoulder at 20 meV and the dominating peak at 140 meV. Information

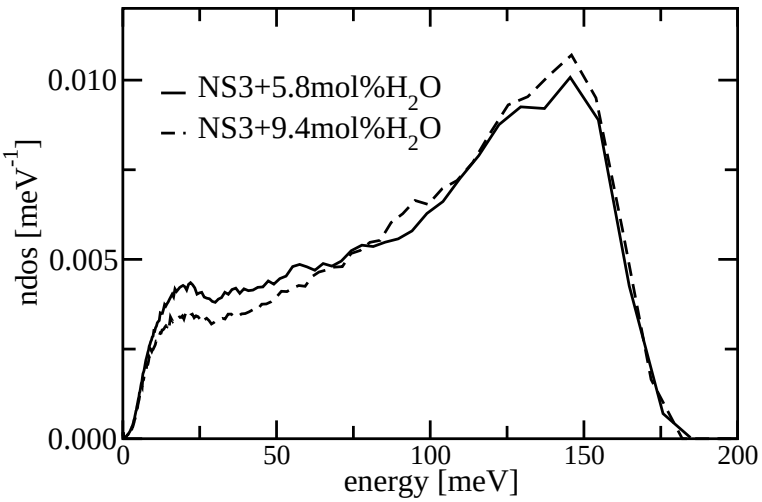

Figure 7.24: *Neutron vibrational density of NS3+5.8mol%H_2O (solid line) and NS3+9.4mol%H_2O (dashed line).*

on the contributions of water to the vibrational spectrum of sodium silicates can be obtained if water is heated off at temperatures above the glass transition temperature of the system. Figure 7.26 shows the comparison of the ndos between a sample of NS3+5.8mol%H_2O before and after it was kept at 600 K for roughly 60 minutes. From the weight loss of the sample it was estimated that roughly 30% of the total water content were lost during storage at 600 K. The loss of intensity can be recognized over the total vibrational spectrum but the intensity loss is higher at energies higher than 50 meV. Note that it became already evident that this is the range where water contributes most to the vibrational spectrum (see figure 7.23). If a reconversion of SiOH groups to water molecules takes place at such temperature where the sample is not in thermal equilibrium cannot unfortunately be addressed.
Concerning the general shape of the vibrational spectrum of hydrous sodium silicate, it would be interesting to understand the origin of the strong peak at 140 meV. Unfortunately

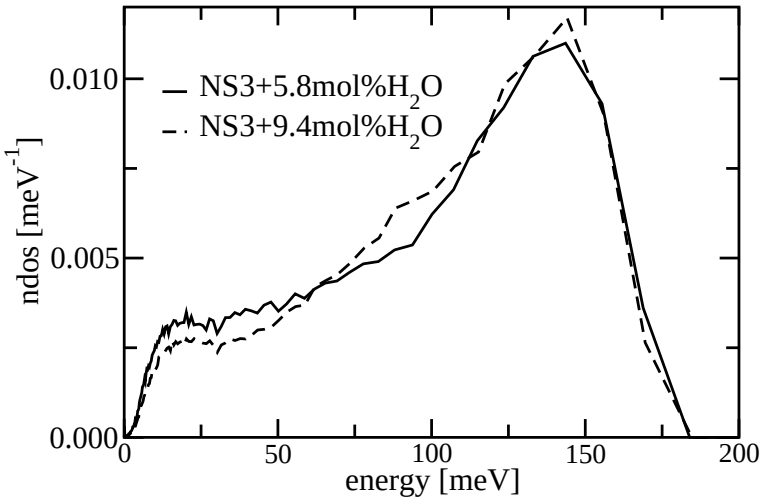

Figure 7.25: *Corresponding proton contribution*

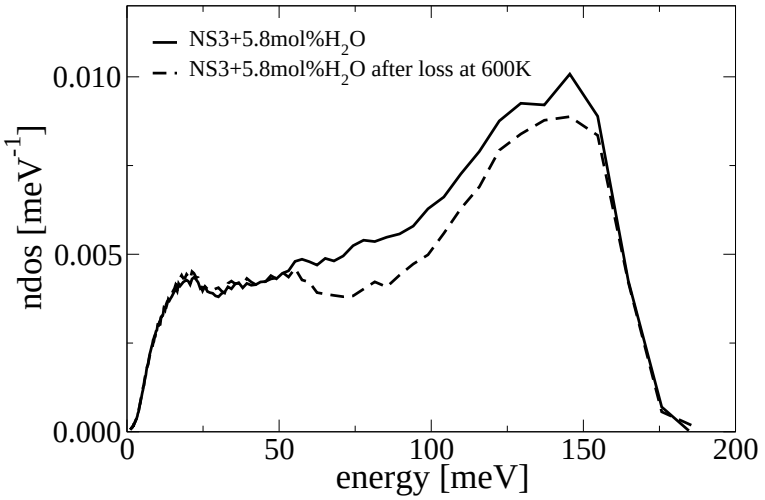

Figure 7.26: *Neutron vibrational density of NS3+5.8mol%H_2O and NS3+5.8mol%H_2O after weight loss at 600 K. The intensity for the latter sample is scaled on the first one in the range between 0 and 50 meV.*

the experiment alone is not able to provide much explanation. One knows from the vibrational spectrum of dry sodium silicate that it is mainly the stretch vibrations of non bridging oxygens that contribute to a peak at 120 meV [Is03]. Since it was suggested by the present computer simulations that also NBO of the form SiOH have significant contributions at 120 meV (see figure 6.36), the large peak in the spectrum may be the result of an addition of the contributions of NBO of the form SiOH and SiONa. Last but not least, it should be mentioned that also the shoulder at 25 meV is known to have its origin in the presence of NBO.

Hydrous Albite The vibrational spectrum of hydrous albite with 5.8mol%H_2O, 9.4mol%H_2O and 13.7mol%H_2O is presented in figure 7.27. The spectra are characterized by a shoulder at 15 meV and another one at 70 meV. It is striking that the vibrational spectrum seems to be much closer to the one of hydrous silica than the one of hydrous sodium silicate. In particular they seem to be close to the spectrum of the hydrous silica sample that contains liquid water in bubbles. In fact, it is known that protons show a much higher mobility in hydrous albite than in other silicate compositions [Zo01b]. But from the vibrational density of states alone it is difficult to draw conclusions since also the altered dry matrix may change the vibrational spectrum of the hydrous silicate. Indeed, the comparison

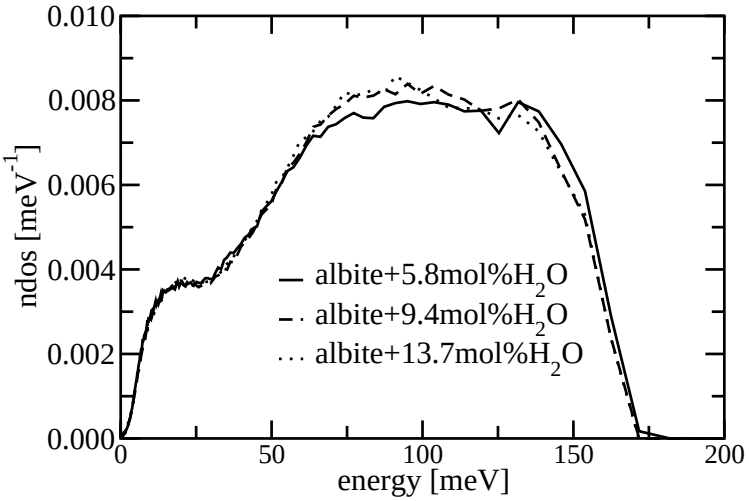

Figure 7.27: *Neutron vibrational density of states of albite+5.8mol%H_2O (solid line), albite+9.4mol%H_2O (dashed line) and albite+13.7mol%H_2O (dotted line). Systematic dependencies on the water content cannot be seen (deviations are within the error bars).*

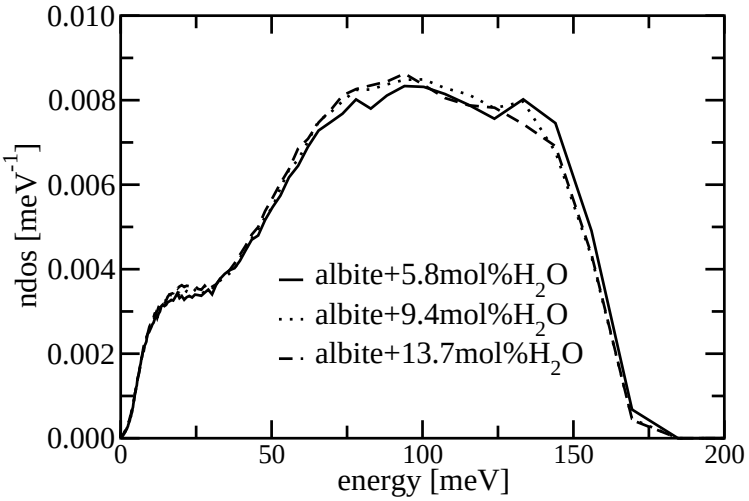

Figure 7.28: *Corresponding proton contribution.*

to the vibrational density of states of dry albite shows that also dry albite has a shoulder in the region of 70 meV. Evidence for similar structure of alumino-silicates and silica comes also from the fact that the addition of Al_2O_3 to sodium silicate seems to rearrange the tetrahedral network of the silicate in the dry states [Ka04a].

Regarding the spectra of hydrous albites of different water concentration, it can be recognized that, with growing water content the form of the spectrum does not change. It can be excluded that such effect can be due to (inappropriate) multi-phonon corrections. The time-of-flight spectra (figure 7.19) were also scaled onto each other. Deviations did neither occur between the curves corresponding to different water concentrations. Remember that in figure 7.19 it was well shown that the samples contain different amounts of water. Remember also that already the vibrational spectrum for the sodium silicate showed a similar inertion regarding the alteration of the water content.

The lack of changes with increased water content can be interpreted in a way that the hydrogen atoms are attached very strongly to to the silicate network. Due to their small mass and the strong attachment they mainly sample the vibrations of the matrix. Since the matrix itself is only little altered by the presence of water, the vibrational properties neither change. This is also seen by the computer simulation (see figure 6.35). Note that the light scattering experiments are highly sensitive to stretch vibrations of OH bonds at more than 300 meV. In

this region the peaks of the OH and H_2O vibrations are not "contaminated" by the matrix.

Temperature Dependence For the case of hydrous sodium silicate, temperature dependent ndos are available. Figure 7.29 shows the neutron vibrational density of states for NS3+5.8mol%H_2O at temperatures of 200 K, 300 K, 400 K, and 500 K. Obviously no important structural changes that are associated to changes of the vibrational spectrum take place in this considerable temperature range. Note that usually the vibrational density of states of a substance can be regarded as a very sensitive probe of structural changes.

At 500 K the ndos deviates slightly from the curves corresponding to the other tempera-

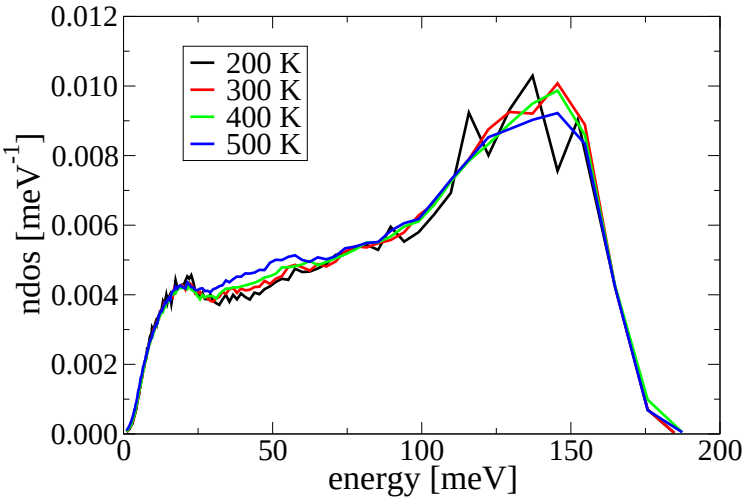

Figure 7.29: *Temperature dependent neutron vibrational density of NS3+5.8mol%H_2O.*

tures. This might indeed be related to an anharmonic effect but in that case it shows that the ndos is not very sensitive to anharmonic effects.

The second remarkable point regarding the temperature independence of the vibrational spectrum is that obviously no physical effects emerge at the freezing point (273 K) and boiling point (373 K) of liquid water. Such behavior suggests again that inclusions of liquid water are absent and water is strongly bound to the silicate matrix in any dissolution state. Since even at 373 K no water speciation change occurs one can even say that water is bound with much higher forces to the silicate matrix than the inter-molecular forces in liquid water (the hydrogen bonds) that are broken if water is vaporized at its boiling point.

Also a speciation change of water at or above the glass transition temperature (at roughly 420 K [Mu04]) cannot be observed for the present sample. This is in contradiction with other studies [Sh95], but it cannot be excluded that such mechanism depends on the composition on the silicate matrix.

Chapter 8

Comparisons and General Conclusions

8.1 Comparisons of Simulation and Experiment

8.1.1 The Structure Factor

First of all it should be pointed out that the structure factor -in contradiction to its name- is rather **in**sensitive to structural details in disordered matter as liquids and glasses. This restriction is certainly evident if it is taken into account that a three dimensional structure is mapped in a function depending only on one (the radial) direction. This causes of course information loss. For example the differences between the structure factors of the dry silicates are already rather small (see figure 7.9). In the following it will be shown that the insensitivity on structural details holds in particular upon water addition.

Figure 8.1 shows the simulated and experimental neutron scattering structure factor for

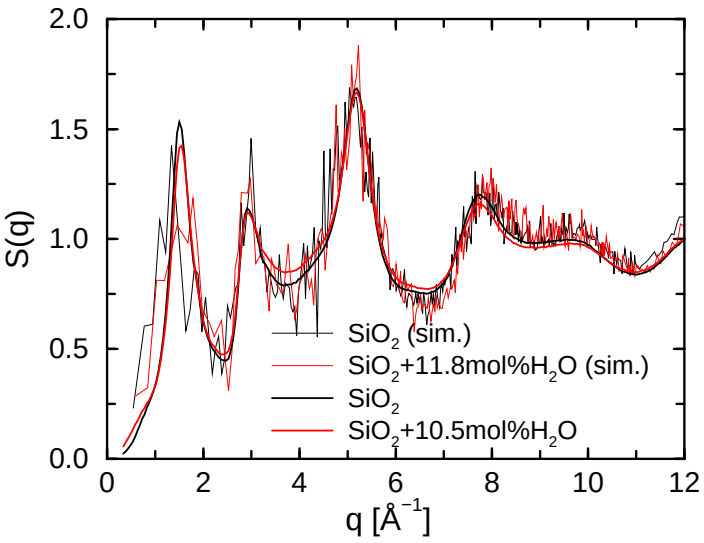

Figure 8.1: *Neutron scattering structure factor of hydrous silica at 300 K as obtained from the experiment with a sample of SiO_2+10.5mol%H_2O and the simulation with a system of SiO_2+11.8mol%H_2O.*

dry and hydrous silica. Generally the experimental and simulated curves are in relatively good agreement. Deviations occur only for very low q and between 9 Å^{-1} and 12 Å^{-1}. At low q the deviations from the simulation to the experiment can be ascribed to the finite box size in the simulation and the rapid quench. The deviations between 9 Å^{-1} and 12 Å^{-1} arise most likely from uncertainties in the data treatment (see section 7.1.2) . However, it should be recognized that -for a first main outcome- from the experimental and from the simulation

side there are no indications that water affects the structure factor of silica considerably. Note that, on the other hand it was shown in figure 6.2 that a silica network is broken by the addition of water and viscosity changes by orders of magnitude [Ba86].

8.1.2 The Partial Vibrational Density of States

The vibrational density of states is known to be much more sensitive to structural details than the neutron scattering structure factor. The reason for this is that the density of states is not only sensitive to interatomic distances but also to the direct environment of the atoms ("the potential"). Unfortunately, as it was already discussed, the neutron vibrational density of states is rather difficult to compute since in the simulation the hydrogen atom which dominates the spectrum due to its high scattering length is the species with the worst statistics. On the experimental side the most reliable quantity is the proton signal where uncertainties due to the incoherent approximation can be excluded. Figure 8.2 shows the

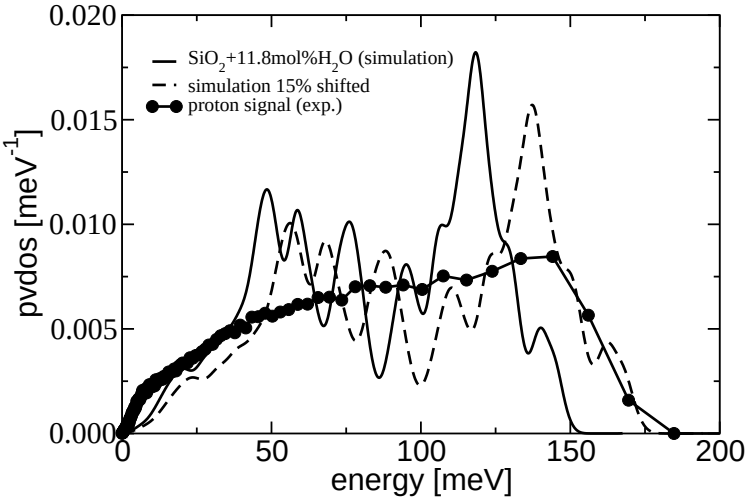

Figure 8.2: *Proton signal as obtained from the experiment with a sample of SiO_2+10.5mol%H_2O and the partial vibrational density of states for hydrogen as extracted from the simulation with a system of SiO_2+11.8mol%H_2O.*

comparison of the computed partial vibrational density of states for hydrogen and the experimentally measured proton signal. It is well known that vibrational spectra are considerably influenced by the exchange correlation functional. Remember the influence of the exchange correlation functional on the interatomic distances and the angle is crystalline silica (figure 5.1). Therefore, the dashed line in figure 8.2 indicates an arbitrary multiplication of the simulated data by a factor of 1.15. This is the range of the error we ascribe to the change of the exchange correlation functional. The main differences occur between 0 and 50 meV and between 120 and 150 meV where the simulation shows an intense peak. In this energy range the resolution of the neutron spectrometer is already poor, making an appropriate comparison even more difficult. Of course one can also compare the ndos as obtained from the simulation (figure 6.38) and the experiment (figure 7.22), but the agreement is of the same quality.

8.2 General Conclusions

In order to conclude the discussion, the general framework of the present investigations should be pointed out again:

- *Experiments were in principle limited to the glassy state.* Since no pressure equipment is currently available for inelastic neutron scattering instruments at high temperatures, experimental data could only be obtained up to temperatures where water is released from the silicate. This was the case above the glass transition temperature of the mixtures at several hundred Kelvin. (Note that more than 1000 K at several kbar are required in order to bring the mixtures to equilibrium.)

- *Simulations were in principle limited to the liquid state.* Today's available computer power puts clear limits to the *ab initio* equilibration of viscous liquids. For the system size of about hundred atoms, the time limit is at some tens of pico-seconds. The lowest temperature at which equilibration could be achieved was 3000 K. Information on the glass could only be obtained from samples based on ultra-rapid quenches.

The main results will now be summarized according to this "technical" separation.

8.2.1 The Liquid State

The main point of the present study is certainly that it provided the first real space picture ever for a structure of a hydrous silicate and the hydrogen diffusion at finite temperature. However, due to the thermostats, diffusion constants and diffusion velocities are not accessible.
Nevertheless, a liquid of silica containing 11.8mol% H_2O at 3500 K and 3000 K was equilibrated using first-principles molecular-dynamics simulations. It is observed that the water is mostly attached to the silica network in the form of Si-OH groups. Water molecules or free O-H groups occur only at the highest temperature but are not stable and decay rapidly. The SiO_4 tetrahedrons are still the basic network forming units, as in pure silica. The short range correlation (i.e. the radial distribution functions) suggest that the structure of the matrix is as much changed by the addition of water as by the addition of the same amount of sodium oxide to the liquid. However, characteristic first neighbor distances are smaller in hydrous silica due to the smaller size of the hydrogen atom. In contrast to this, the way the modifier cation itself is attached to the matrix seems to be quite different. The sodium atoms tend to form bonds of ionic character with oxygen, whereas the hydrogen atoms are attached by covalent bonds. This difference in the bonding character of O-H and O-Na could be the reason for the slower diffusion of the hydrogen atoms in liquid silica compared to that of sodium atoms.
The simulated neutron scattering structure factor shows a pronounced prepeak at a wave vector of about 1Å^{-1}, i.e. there is evidence for the presence of long range correlations. The prepeak is even more intense than that for the sodium silicate at the same wave vector transfer. The origin of this feature in the hydrous liquid seems to be different from that of the sodium silicate, since the partial structure factor for H-H contributes only little. Furthermore, in the hydrous case, the silica matrix itself seems to be modified since the prepeak occurs as well in the partial structure factors for the matrix. The data show a shift to higher q-vectors and a decrease of the intensity at the lowest temperature. At ambient temperature the prepeak and the first sharp diffraction peak merge.
The other experimentally accessible quantity, the Q^n distribution, shows clearly that the O-H groups try to avoid each other. Silicon atoms with two and more Si-O dangling bonds or O^* (Q^n sites with $n \leq 2$) are rarely found. Despite the strong covalent character of the O-H

bond, the O-H units have a high radial mobility and oxygen triclusters $HO < \begin{matrix}Si\\Si\end{matrix}$ (bridging hydroxyl groups) have a high tendency to form. These oxygen triclusters violate the oxygen stoichiometry and the system compensates this violation by the formation of Si-O dangling bonds. The dangling bonds and the triclusters constitute mainly the intermediate states for the diffusion mechanism of the hydrogen atoms in the melt.
On the one hand, it turned out that the O-H groups are very stable species and it requires a certain stoichiometry violation to weaken the O-H bonds (note that in O-H-O transition units the stoichiometry of the H atom is also violated). On the other hand these bond weakening intermediate states occur in sufficiently high quantity to assure the hydrogen diffusion. Analyzing the nearest neighbor environments of the oxygen atom of the initial OH bond and of the oxygen atom of the formed OH bond, the following equilibria were found:

Exchange of hydrogen between a SiOH group and a bridging oxygen

$$\mathrm{SiOH} \;+\; \mathrm{O} < \begin{matrix}\mathrm{Si}\\\mathrm{Si}\end{matrix} \;\longleftrightarrow\; \mathrm{SiO} \;+\; \mathrm{HO} < \begin{matrix}\mathrm{Si}\\\mathrm{Si}\end{matrix} \tag{8.1}$$

Exchange of hydrogen between two bridging oxygens (bridging hydroxyl groups)

$$\begin{matrix}\mathrm{Si}\\\mathrm{Si}\end{matrix} > \mathrm{OH} \;+\; \mathrm{O} < \begin{matrix}\mathrm{Si}\\\mathrm{Si}\end{matrix} \;\longleftrightarrow\; \begin{matrix}\mathrm{Si}\\\mathrm{Si}\end{matrix} > \mathrm{O} \;+\; \mathrm{HO} < \begin{matrix}\mathrm{Si}\\\mathrm{Si}\end{matrix} \tag{8.2}$$

Exchange of hydrogen between two SiOH (formation of water)

$$\mathrm{SiOH} \;+\; \mathrm{HOSi} \;\longleftrightarrow\; \mathrm{SiO} \;+\; \begin{matrix}\mathrm{H}\\\mathrm{H}\end{matrix} > \mathrm{OSi} \tag{8.3}$$

Redecay of water

$$\mathrm{SiO} < \begin{matrix}\mathrm{H}\\\mathrm{H}\end{matrix} \;+\; \mathrm{O} < \begin{matrix}\mathrm{Si}\\\mathrm{Si}\end{matrix} \;\longleftrightarrow\; \mathrm{SiOH} \;+\; \mathrm{HO} < \begin{matrix}\mathrm{Si}\\\mathrm{Si}\end{matrix} \tag{8.4}$$

Apart from the hydrogen diffusion reactions associated to OH ruptures (eq. 8.1 to 8.4), there is also evidence for the transport of OH units. These hydroxyl units can be transfered from one silicon atom to another involving again a bridging hydroxyl group as intermediate state. The corresponding equation reads as follows:

$$\mathrm{SiOH} \;+\; \mathrm{Si} \;\longleftrightarrow\; \begin{matrix}\mathrm{Si}\\\mathrm{Si}\end{matrix} > \mathrm{OH} \;\longleftrightarrow\; \mathrm{Si} \;+\; \mathrm{HOSi} \tag{8.5}$$

Whatever the influence of pressure and temperature on such system may be, it is likely that the encountered mechanisms will still be covered by equations 8.1 to 8.5, but with different reaction constants.
A clustering of hydrogen and the formation of stable water molecules do not take place, especially at the lower temperature. If the formation of clusters occurred, one would expect a higher signal in the H-H radial distribution function at typical H-H distances found in liquid water (2-3 Å) and perhaps a signal in the Q^n distribution for $n \leq 2$. Hence there is no evidence for water clustering at the considered temperatures. In this context the present study should also be compared to previous *ab initio* approaches to the subject. Bakos *et al* [Ba02] pointed out that in an equilibrated structure of silica and water, SiOH should be the dominating dissolution species. Therefore, from this study it seems to be confirmed that

from the quantum chemical point of view, the dissolution of water to SiOH groups is the energetically favorable mechanism in the equilibrated regime. One should recognize that the sudden alteration of temperature and pressure conditions can bring the system out of thermal equilibrium and may lead to cluster formation. Also the composition of the silicate on the water speciation (especially the addition of Al_2O_3) has not been investigated yet and further work of the present kind will be mandatory.

8.2.2 The Glass

In the glassy state it is possible to compare statistical quantities like the neutron scattering structure factor and the vibrational densities of states that can be extracted from the experiment as well as the simulation.

Two main outcomes of the neutron scattering experiments are evident: The small change of the neutron scattering structure factor and the vibrational density of states with increased water content and the dependence of the neutron scattering structure factor and the vibrational density of states on the silicate matrix (at equivalent water concentration). Note that the little structural alteration was already ascribed to the small size of the hydrogen atom (see section 6.1.1). The chemical analogy of hydrous silica and sodium silicates should be recalled another time at this place. As it can be seen from figure 7.9 and figure 7.10, the influence of sodium oxide on the structure factor of silica is much larger than the influence of water. In contrast to sodium, due to their low mass and the strong attachment to the silicate, the hydrogen atoms sample mostly the vibrations of the matrix. Therefore, it becomes understandable that also the ndos changes as little as the matrix changes with increasing water content. Note again that the bend and stretch vibrations of water and SiOH groups are energetically located outside the region of the matrix vibrations from 0 to 200 meV (0 to 1600 cm^{-1}) where neutrons are sensitive. This is the reason that despite of the change of the ratio of SiOH to H_2O with increasing total water content (as seen by with Raman and infrared spectroscopy), neutrons are able to show that the silicate matrix is not affected by this change. Since the matrix constitutes the viscosity of the silicate one further concludes that neither the viscosity (as most important quantity for volcanism) is related to the $SiOH/H_2O$ ratio.

A prepeak at 0.9 $Å^{-1}$ in the neutron scattering structure factor of hydrous silica is not seen in the glassy state as it was already the case for sodium silicate. Since there are indications from the simulation for a prepeak in the molten state also for hydrous silica, experiments at high temperature (and high pressure) will be mandatory in order to calibrate the simulation. On the other hand, note also that the q-dependence of the prepeak was recently investigated in various silicates by Kargl *et al* [Ka04b]. It was found that in the series of $(1\text{-}x)SiO_2+xK_2O$, $(1\text{-}x)SiO_2+xNa_2O$, and $(1\text{-}x)SiO_2+xLi_2O$, the prepeak is shifted into the first sharp diffraction peak at 1.7 $Å^{-1}$. It can be assumed that the following member of the chain which is $(1\text{-}x)SiO_2+xH_2O$, will have a prepeak which is indistinguishable from the first sharp diffraction peak at 1.7 $Å^{-1}$.

As already mentioned above, the comparison to the CPMD simulation is always subject of the validity of the ultrafast numerical quench. However, the direct comparison of the experimental and the simulated neutron scattering structure factor showed generally good agreement. This confirms the picture of a small alteration of the matrix due to the small size of the hydrogen atom also from the theoretical point of view. Note that it was also seen from

the simulations that the vibrational density of states is only little affected by the addition of water (see section 6.5.2). Almost only the high incoherent scattering length of hydrogen is responsible for the difference of the simulated neutron densities of states of pure and hydrous silica. A further common result from the experimental and the theoretical side is that hydrogen participated in vibrational modes at all frequencies. This is another proof for the strong coupling of the hydrogen to the matrix. Exactly this fact makes it experimentally difficult to draw conclusions from the vibrational density of states. It is questionable if deuterated samples could improve the situation. Since stretch vibrations are far out off the domain of neutron scattering, direct shifts of characteristic frequencies will not be observable.
A side-outcome of the computer simulation are the results on the electronic structure. Together with the information on the hydrogen diffusion in the liquid (at high temperature), the results obtained were able to confirm predictions on defects in silica used as dielectric material in semiconductor devices. In this context the SiO dangling bond as negative charge trap is of outstanding importance because it provides acceptor states in the electronic band gap (see figure 3.1). It could be shown that this site can be systematically created at high temperatures followed by an ultrarapid quench. The analysis of the Hirshfeld charge density deformations and the electron localization function showed that electronic delocalization (due to neighbor atoms) pushes the energy of the electronic state in the band gap. Moreover the present study is the first dynamical approach ever that leads to these results.

8.2.3 Outlook

Last but not least, possible further steps have to be discussed. On the simulation side the computer power will certainly not increase that much in the forthcoming years so that considerable lower equilibration temperatures and natural quench rates will become accessible. That means that from the conceptional point of view progress cannot be expected. This is a relative dramatic restriction since the conditions for the experimental procedure for the sample preparation cannot be simulated and comparisons to experiments are hence much more difficult. In particular this might have consequences for the experimentally and theoretically found H_2O/SiOH ratios. However, as already said above, it is believed that all possible chemical transformations (at any temperature) in hydrous silica are already covered by reactions 8.1 to 8.5. This is also important concerning an possible increase of the number of atoms at the same stoichiometry which might then only improve statistics.
On the other hand, what can be done on the simulation side is the consequent variation of the composition of the silicate. In particular the equilibration of water richer systems than the present one could give hints on the existence of stable water molecules. From the point of view of the questions associated to explosive volcanism, the work should certainly be extended over hydrous sodium silicates to hydrous albite (the simplest natural lava). The ultimate goal would be to adapt an interatomic potential to such data (according to figure 3.2). This would allow to perform longer runs and to extract diffusion constants for hydrogen since the use of thermostats is no longer compulsory. For that kind of work, it should be pointed out that the measured structure factors and densities of states can be used in order to calibrate any new simulation. For *ab initio* approaches, a certain calibration with existing experimental data can also be obtained from the generation of the Raman and infrared spectra according to equation 3.3.
On the experimental side the construction of a pressure cell for the use in neutron spectrom-

eters is under way. The availability of the new TUM neutron source FRMII will definitely provide more beam time to the subject. If reliable data in the liquid state could be obtained, an extraction of hydrogen diffusion constants could be envisaged. Moreover it might be considered to employ also inelastic X-ray methods in order to get information on the water dynamics via the sound velocities extracted from dispersion curves. Probably the employment of recently developed numerical methods like the Reverse Monte Carlo (RMC) method [Ke90] could shed more light on the water speciation issue.

Appendix A

Acknowledgments

A.1 Globally

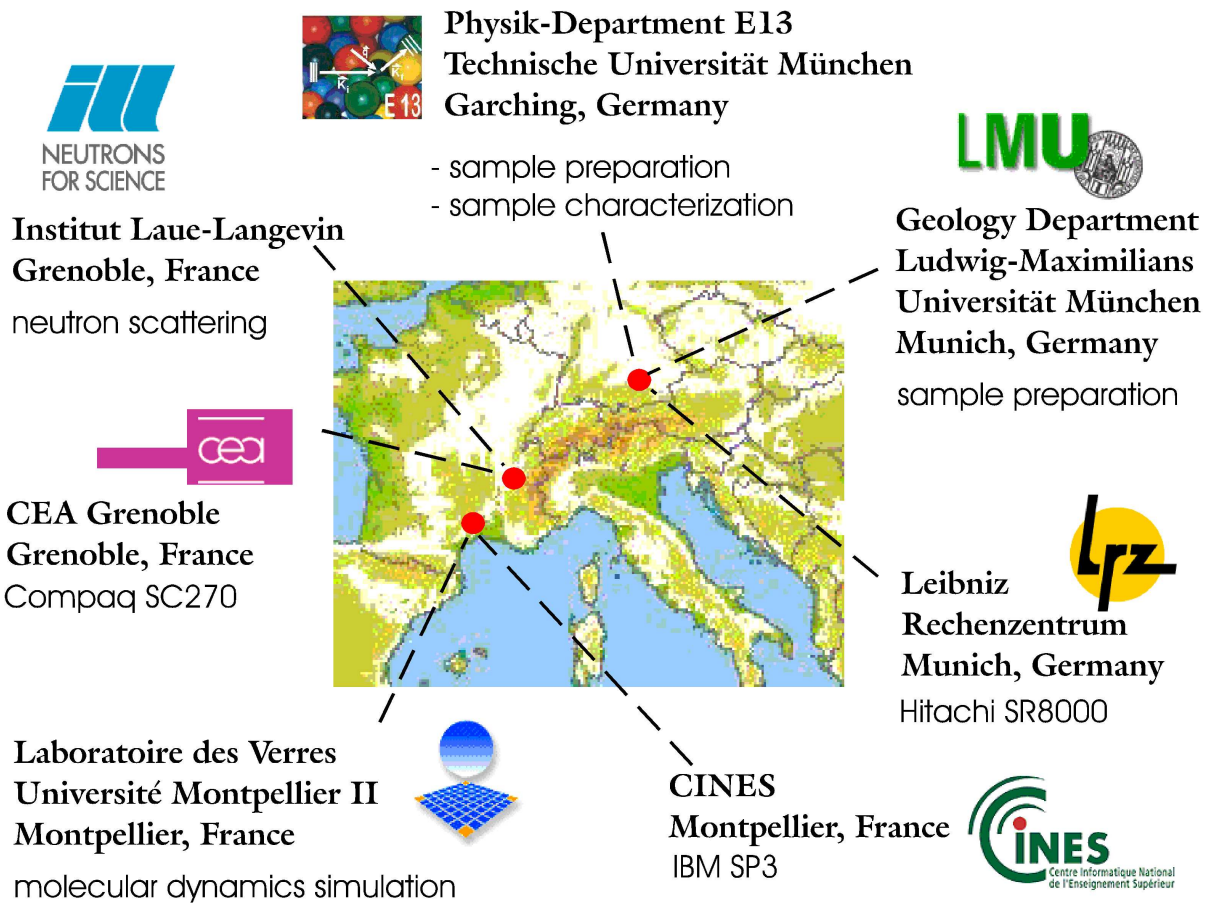

Generally I acknowledge all the above institutions for the fruitful atmosphere they provided for the present work. Concerning financial support, I would like to thank the Bund der Freunde der Technischen Universität München for a thesis grant and the Institut Laue-Langevin for a contrat de formation par la recherche (CFR). Travel allowance for trips from Munich to Montpellier was provided by the French Science Ministry.

A.2 Particularly

In the first place thanks should certainly be addressed to my supervising community which assured a collaborative and fruitful environment over the whole period of the work. In particular I would like to thank Andreas Meyer and Walter Kob for the idea of this two leg based thesis, their excellent scientific advice and their willingness to overcome the many associated administrative hurdles. Apart from these people, most thanks go clearly to Magali Benoit who did really most of the work with me and who introduced me to the Car-Parrinello-DFT framework, who was always there when I needed support and who was always open to new ideas. Helmut Schober should be acknowledged for having invited me to conduct the thesis-research in his group at the ILL, his help with the experiments and the data treatment and the introduction to many neutron associated hardwares and softwares. Last but not least I would like to thank Mark Johnson who supported me always with software from his group and gave me excellent introductions. Very special thanks go also to him for correcting the English of the present manuscript.

Apart from direct supervisors I owe thanks to many people in Montpellier, at the ILL and Munich. In particular I would like to address thanks to Simona Ispas for many of her programs I could use and the data of the sodium silicate liquid. At the ILL many thanks go to Michael Marek Koza for local-contacting many experiments on IN6, the many unofficial days he accorded me and his explanations on the physics of ices. Also the contributions of Gabriel Cuello should be acknowledged. He provided me with introductions to neutron diffraction and programs for diffraction data treatment as well as unofficial beam time on D4. Further courtesy beam time was provided by John Stride on IN4. Thomas Hansen should be acknowledged for hosting the D20 experiment and his help with the data treatment in LAMP. In Munich I would like to address special thanks to Axel Müller for the difficult sample preparation and to Florian Kargl for his help and programming of IDA and his introduction to sample preparation.

Apart from scientific contributions I have to acknowledge non-scientific (which is, for a continuous proceeding at least as important) help from many people. Here I would like to mention Caroline Soudan and Marie-Elisabeth Duplan who always provided me with a room in Montpellier. Also I would like to address thanks to many administrative people who had a lot of work with me: Elke Fehsenfeld and Conny Simon at E13, Tina Rabeharivelo at the LDV as well as Allison Mader and Inga Volino at the ILL, and Marlene Bartenstein from the central administration of the TUM who coordinated the cotutelle contract.

Appendix B

Alphabetic List of Quantities and Abbreviations

a	typical hopping distance	$\overline{a}$	chemical activity
$A_{X,X}$	Paalmann-Pings coefficients	α	polarizability tensor
b_I	scattering length of nucleus I	B	constant in miscibility model
C	concentration	c	heat capacity
c_i	vector of plane wave coefficient	D	diffusion constant
$D_{\alpha\beta}$	number of interatomic distances in Ω	δ	coefficient for secondary scattering
e	electronic charge	$\mathbf{e}_I^k$	k-th eigenvector component on atom I
E^{KS}	(Kohn-Sham) energy	E_a	activation energy
η	viscosity	ϵ_o,ϵ	(vacuum) dielectric constant
ϵ_{xc}	exchange correlation density	$\mathbf{E}$	electric field
$\mathbf{F}$	force	f	detector efficiency
F_k	dynamical structure factor	g	vibrational density of states
g_{ab}	radial pair distribution	G_m	free enthalpy of mixing
$\mathbf{G}$	vector of reciprocal lattice	G_∞	elastic shear modulus
γ	activity coefficient	H_m	enthalpy of mixing
$\mathcal{H}$	Hamiltonians	I	intensity
$\mathbf{J}$	rate transfer (flux)	K	chemical equilibrium constant
$\mathbf{k}_i$	initial wave vector	$\mathbf{k}_f$	final wave vector
k_B	Boltzmann's constant	K_H	Henry's constant
κ	thermal conductivity	L	length of simulation box
$\mathcal{L}$	Lagrangian	Λ	Lagrangian multiplier
λ	wavelength	$\mathbf{m}$	dipole moment
m_e	electronic mass	m_n	neutron mass
M_I	mass of nucleus I	$\overline{M}$	average mass of nuclei in a system
μ	Car-Parrinello electronic mass	N	number of atoms
n	refraction index	$\langle n_k \rangle$	Bose-Einstein distribution

n_c	channel number	N_1	number of water sites in Flory-Meyer model
N_2	number of SiO_2 sites in Flory-Meyer model	$N_n(\omega)$	projected vibrational density of states
ω	(vibrational) frequency	R	gas constant
Ω	simulation cell volume	P	Placzek polynomial
$\mathbf{p}$	momentum	p	pressure
ϕ	latitude	Φ	all particle wave function electrostatic potential
Ψ	all electron wavefunction	ψ_i	wavefunction of electron i
$\mathbf{q}$	wave vector transfer	q_i	charge of atom i
Q	heat, thermostat variables	R	gas constant
r	radial variable in R^3	$\overline{r}$	fraction of oxygen sharing SiO_2 units in Flory-Meyer model
$\mathbf{r}_i$	position of electron i	$\mathbf{R}_I$	position of nucleus I
ρ	liquid or solid density	ρ^{pro}	Hirshfeld pro molecule charge density
ρ^{at}	charge density of atom i	$\mathbf{s}$	displacement
S_m	entropy of mixing	$S(\mathbf{q},\omega)$	scattering law
σ	surface tension	σ_I	scattering cross section of nucleus I
σ_s, σ_a	scattering absorption cross section	t	time
T	kinetic energy absolute temperature	T_g	glass transition temperature
T_n	multiphonon term of order n	τ	stress tensor
2Θ	scattering angle	$\mathbf{u}$	displacement
$\mathbf{v}$	velocity	V	potential energy
V_c	container solid volume	w_n	Wannier function
W	Debye-Waller factor	x	x-direction in R^3
$\overline{x}$	molar fraction of total water	x_n	x value of n-th Wannier center
Ξ_n	spread (second moment) of n-th Wannier function	y	y-direction in R^3
y_n	y value of n-th Wannier center	z	z-direction in R^3
Z_I	charge of nucleus I	z_n	z value of n-th Wannier center

Note that indices are not listed and may be multiply used.

Appendix C

Accessibility of Natural Rocks

The goal to understand natural lavas with a certain amount of volatiles is to go from systems of relatively simple chemical composition to more and more complex systems. Starting from SiO_2-H_2O, the way to the simplest natural rock -albite ($NaAlSi_3O_8$)- goes over hydrous sodium silicates. For computer simulations, systems become more and more difficult the more atom types involved. On the experimental side, restrictions emerge with high pressures and temperatures, that are required in order to make hydrous SiO_2. Figure C.1 shows a classification of the systems by their theoretical and experimental accessibility. Typical compositions of other types of lava such as rhyolite, dacite, andesite and basalt are given in the figure C.2.

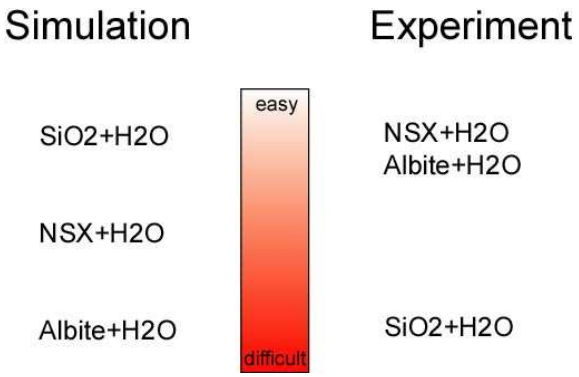

Figure C.1: *Experimental and simulational accessibility of hydrous SiO_2, hydrous sodium silicates, and hydrous albite.*

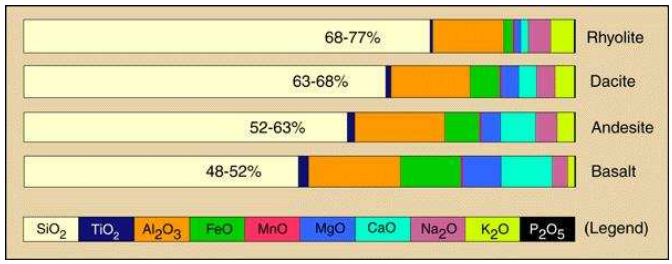

Figure C.2: *Compositions of naturally found lavas. From [US00].*

Appendix D

List of ILL Experiments

IN6 September 2001

$\lambda = 4.1$Å
elastic peak 343/1024
channel width 9.625 μs
empty instrument
niobium hollow cylinder
inelastic focussing

substance	temperature [K]	time [min]
dry NS3	300	113
NS3 9.4 mol% H_2O	300	34
NS3 9.4 mol% "D_2O"	300	304
NS3 9.4 mol% H_2O	300	21
NS3 9.4 mol% "D_2O"	300	248
dry albite	300	258
albite 9.4 mol% H_2O	300	180
albite 9.4 mol% "D_2O"	300	42

cryo-loop, Al-can
$\lambda = 5.1$Å

substance	temperature [K]	time [min]
NS3 9.4 mol% H_2O	375	10
NS3 9.4 mol% H_2O	450	10
NS3 9.4 mol% H_2O	500	10
NS3 9.4 mol% H_2O	550	10
NS3 9.4 mol% H_2O	600	10

IN6 May 2002

$\lambda = 4.62$Å
elastic peak 280/512
channel width 10.875 μs
cryoloop, aluminum flat slab
elastic focussing

substance	temperature [K]	time [min]
NS3 5.8 mol% H_2O	300	60
NS3 5.8 mol% H_2O	360	60
NS3 5.8 mol% H_2O	420	60
dry NS3	360	60
NS3 9.4 mol% H_2O	310	60
NS3 9.4 mol% H_2O	420	60

IN6 August 2002

$\lambda = 4.1$Å
elastic peak 400/512
channel width 10.875 μs
cryoloop
aluminum flat slab
inelastic focussing

substance	temperature [K]	time [min]
NS3 5.8 mol% H_2O	200	120
NS3 5.8 mol% H_2O	260	90
NS3 5.8 mol% H_2O	300	240
NS3 5.8 mol% H_2O	350	200
NS3 5.8 mol% H_2O	400	200
NS3 5.8 mol% H_2O	500	120
NS3 5.8 mol% H_2O	600	20
NS3 remaining water	300	240
NS3 remaining water	400	240

IN4 December 2002

$\lambda = 2.2$Å
elastic peak 262/512
channel width 5.8 μs
5.719μs effective
cryostat, no sample can,
sample fixed in Cd frame
elastic focussing

substance	temperature [K]	time [min]
dry NS2	300	450

D20 October 2003

$\lambda = 0.94$Å
no cryostat
Vanadium sample can
6mm diameter

substance	temperature [K]	time [min]
dry SiO_2	300	60
SiO_2 10.5 mol% H_2O	300	60
SiO_2 10.5 mol% "D_2O"	300	90
dry NS3	300	60
NS3 5.8 mol% H_2O	300	60
NS3 5.8 mol% "D_2O"	300	60
NS3 9.4 mol% H_2O	300	60
dry albite	300	60
albite 5.8 mol% H_2O	300	60
albite 5.8 mol% "D_2O"	300	60
albite 9.4 mol% H_2O	300	60
albite 9.4 mol% "D_2O"	300	60
albite 13.7 mol% H_2O	300	20

$\lambda = 2.4$Å
no cryostat
Vanadium sample can
6mm diameter

substance	temperature [K]	time [min]
dry SiO_2	300	90
SiO_2 10.5 mol% H_2O	300	60
SiO_2 13.7 mol% H_2O	300	60
dry NS3	300	60
NS3 5.8 mol% H_2O	300	60
NS3 5.8 mol% "D_2O"	300	60
NS3 9.4 mol% H_2O	300	60
dry albite	300	60
albite 5.8 mol% H_2O	300	60
albite 5.8 mol% "D_2O"	300	60
albite 9.4 mol% H_2O	300	60
albite 9.4 mol% "D_2O"	300	60
albite 13.7 mol% H_2O	300	20

IN6 October 2003

$\lambda = 4.1$Å
elastic peak 805/1024
channel width 5.857 μs
empty instrument
aluminum can
elastic focussing

substance	temperature [K]	time [min]
dry SiO_2	300	100
SiO_2 10.5 mol% H_2O	300	100
SiO_2 10.5 mol% "D_2O"	300	100
dry NS3	300	100
NS3 5.8 mol% H_2O	300	130
NS3 5.8 mol% "D_2O"	300	100
dry albite	300	100
albite 5.8 mol% H_2O	300	100
albite 5.8 mol% "D_2O"	300	100
albite 9.4 mol% H_2O	300	80
albite 9.4 mol% "D_2O"	300	100
albite 13.7 mol% H_2O	300	100

D4 March 2004

$\lambda = 0.35$Å
cryostat
Vanadium sample can
6mm diameter

substance	temperature [K]	time [min]
dry SiO_2	300	1200

IN6 April 2004
$\lambda = 4.1$Å
elastic peak 693/1024
channel width 5.857 μs
empty instrument
aluminum can
elastic focussing

substance	temperature [K]	time [min]
SiO_2 10.5 mol% H_2O	300	400
SiO_2 13.7 mol% H_2O	300	315
NS3 9.4 mol% H_2O	300	270
albite 9.4 mol% H_2O	300	240
albite 13.7 mol% H_2O	300	420

IN6 June 2004
$\lambda = 4.1$Å
elastic peak 693/1024
channel width 5.857 μs
empty instrument
aluminum can
elastic focussing

substance	temperature [K]	time [min]
albite 5.8 mol% H_2O	300	270
albite 5.8 mol% H_2O	300	275
albite 9.4 mol% H_2O	300	313
albite 13.7 mol% H_2O	300	95

IN6 August 2004
$\lambda = 4.1$Å
elastic peak 400/512
channel width 6.75 μs
cryostat
aluminum bonbon
inelastic focussing

substance	temperature [K]	time [min]
dry albite	300	420
dry NS3	300	480

Appendix E

CPMD 3.4.3 Inputs for Molecular Dynamics

```
&CPMD
   MOLECULAR DYNAMICS
   RESTART WAVEFUNCTIONS
   RESTART COORDINATE
   RESTART VELOCITIES
   RESTART NOSEE
   RESTART NOSEP
   SPLINE POINTS
     5000
   NOSE IONS MASSIVE
     3500.0 3000
   NOSE ELECTRONS
     0.12 10000    NOSE PARAMETERS
     4 4 4 6 15 7
   MAXSTEP
     10000
   STORE
     500
   PRINT FORCES COORDINATES
     500
   TRAJECTORY SAMPLE
     5
   TIMESTEP
     4.5
   EMASS
     600.0
   CONVERGENCE
     1.e-6 5.e-3
&END
&SYSTEM
   SYMMETRY
```

```
     1
   ANGSTROMS    CELL
     11.50 1.0 1.0 0.0 0.0 0.0
   CUTOFF
     50.
&END
&ATOMS
SI.OUT1 KLEINMAN-BYLANDER RAGGIO=1.d0
   LMAX=D LOC=D
   30
     6.224504 6.543059 13.001739
     ...  ...  ...

O.OUT1.harder KLEINMAN-BYLANDER RAGGIO=1.0
   LMAX=P LOC=P
   64
     9.211886 10.064283 5.274018
     ...  ...  ...

H.OUT1 KLEINMAN-BYLANDER RAGGIO=1.0
   LMAX=S
   8
     -7.602708 3.151306 -2.172956
     ...  ...  ...

   ISOTOPE
     28
     28
     28

&END
&DFT
   FUNCTIONAL PBE
&END
```

Bibliography

[Ag71] A. K. Agrawal. *Multiple sacttering of neutrons in gaseous liquid methane.* Phys. Rev. A **4**, 1560 (1971)

[An82] C. A. Angell, P. A. Cheeseman, and S. Tamaddon. *Computer simulation studies of migration mechanisms in ionic glasses and liquids.* J. Phys. **43**, C9-831 (1982)

[An83] H.C. Andersen, and C. Rattle. *A velocity version of the Shake algorithm for molecular dynamics calculations.* J. Comp. Phys. **52**, 24 (1983)

[An00] W. Andreoni and A. Curioni. *New advances in chemistry and materials science with CPMD and parallel computing.* Parallel Computing **26**, 819 (2000)

[Ar59] G. W. Arnold and W. D. Compton. *Radiation effects in silica at low temperatures.* Phys. Rev. **116**, 802 (1959)

[Ar03] W. Arden. *Future Roadblocks and solutions in silicon technology as outlined by the ITRS roadmap.* Mat. Sci. Semicond. Proc. **5**, 313 (2003)

[As76] N. W. Ashcroft and N. D. Mermin. *Solid state physics.* Holt-Sounders International Editions Japan LTD, Tokyo (1976)

[Ba86] N. P. Bansal and R. H. Doremus. *Handbook of glass properties.* Academic Press, Inc. Orlando, San Diego, New York, Austin, London, Montreal, Sydney, Tokyo, Toronto (1986)

[Ba02] T. Bakos, S. N. Rashkeev, and S.T. Pantelides. *Reactions and diffusion of water and oxygen molecules in amorphous SiO_2.* Phys. Rev. Lett. **88**, 0555081 (2002)

[Ba03] T. Bakos, S. N. Rashkeev, and S. T. Pantelides. *H_2O and O_2 molecules in amorphous SiO_2: Defect formation and annihilation mechanisms.* Phys. Rev. B **69**, 195206 (2004)

[Ba04] T. Bakos, S. N. Rashkeev, and S.T. Pantelides. *Role of electronic versus atomic relaxations in Stokes shifts at defects in solids.* Phys. Rev. Lett. **91** 226401 (2004)

[Be71] A. J. Bennett and L. M. Roth. *Electronic structure of defect centers in SiO_2.* J. Phys. Chem. Solids **32**, 1251 (1971)

[BP76] B. J. Berne and R. Pecora. *Dynamic light scattering with applications to chemistry, biology and physics.* John Wiley & Sons Inc. New York, London, Sydney, Toronto (1976)

[Be76] H. Bertagnolli, P. Chieux, and M. D. Zeidler. *A neutron-diffraction study of liquid acetonitrile I. $CD_3C^{14}N$.* Mol. Phys. **32**, 759 (1976)

[Be88] A. D. Becke. *Density-functional exchange-energy approximation with correct asymptotic behavior.* Phys. Rev. A **38**, 3098 (1988)

[Be90] B.W.H. van Beest, G.J. Kramer, and R.A. van Santen. *Force fields for silicas and aluminophosphates based on ab initio calculations.* Phys. Rev. Lett. **64**, 1955 (1990)

[BE90] A. D. Becke and K. E. Edgecombe. *A simple measure of electron localization in atomic and molecular systems.* J. Chem. Phys. **92**, 5397 (1990)

[Be93] A. Becke. *Density-functional thermochemistry. III. The role of exact exchange.* J. Chem. Phys. **98**, 5648 (1993)

[Be96] H. Behrens, C. Romano, M. Nowak, F. Holtz, and D. B. Dingwell. *Near-infrared spectroscopic determination of water species in glasses of the system $MAlSi_3O_8$ (M=Li,Na,K): an inter-laboratory study.* Chem. Geol. **128**, 41 (1996)

[Be00] M. Benoit, S. Ispas, P. Jund, R. Jullien. *Model of silica glass from combined classical and ab initio molecular dynamics simulations.* Eur. Phys. J. B **13**, 631 (2000)

[Be01] M. Benoit, S. Isapas, and M. E. Tuckerman. Structural properties of molten silicates from *ab initio* molecular-dynamics simulation: Comparison between CaO-Al_2O_3-SiO_2 and SiO_2. Phys. Rev. B **64**, 224205 (2001)

[Be02] M. Benoit and W. Kob. *The vibrational dynamics of vitreous silica: Classical force field vs. first-principles.* Europhys. Lett. **60**, 269 (2002)

[Be03] H. Behrens and M. Nowak. *Quantification of H_2O Speciation in Silicate Glasses and Melts by IR Spectroscopy - in situ versus Quench Techniques.* Phase Transitions **76**, 45 (2003)

[Be04] M. Benoit and P. Ganster. Personal communication.

[Bl65] I. A. Blech and B. L. Averbach. *Multiple scattering of neutrons in vanadium and copper.* Phys. Rev. **137**, A1113 (1965)

[Bo27] M. Born and R. Oppenheimer. *Zur Quantentheorie der Molekeln.* Ann. Phys. **84**, 457 (1927)

[Bo28] N. L. Bowen. *The evolution of igneous rocks.* Princeton University Press, Princeton N.J. (1928)

[Bo66] S. F. Boys. Localized orbitals and localized adjustment functions. *Quantum theory of atoms, molecules, and the solid state.* P. O. Löwdin (ed.). Academic Press, New York, 1966

[Bo98] F. A. Bornemann and C. Schütte. *A mathematical investigation of the Car-Parrinello method.* Num. Math. **78**, 359 (1998)

[Bo99] F. A. Bornemann and C. Schütte. *Adaptive accuracy control for Car-Parrinello simulations.* Numer. Math. **83**, 179 (1999)

[Br64] R. Brückner. *Charakteristische physikalische Eigenschaften der oxydischen Hauptglasbildner und ihre Beziehung zur Struktur der Gläser. Teil 2: Mechanische und optische Eigenschaften als Funktion der thermischen Vorgeschichte.* Glastechn. Ber. **37**, 459 (1964)

[Bu71] C. W. Burnham and N. Davis. *The role of H_2O in silicate melts I. P-V-T relations in the system $NaAlSi_3O_8 - H_2O$ to $10 kilobars$ and 1000^oC.* Am. J. Sci. **270**, 54 (1971)

[Bu79] C. W. Burnham. The importance of volatile constituents. *The evolution of igneous rocks: Fiftieth Anniversary Perspectives.* H. S. Yoder (ed.). Princeton University Press, Princeton (1979)

[Bu94] C. W. Burnham. *Development of the Burnham model for prediction of H_2O solubility in magmas.* Rev. Mineral. **30**, 123 (1994)

[Ca85] R. Car and M. Parrinello. *Unified approach to molecular dynamics and density functional theory.* Phys. Rev. Lett. **55**, 2471 (1985)

[CP85] J. M. Carpenter and D. L. Price. *Correlated motions in glasses studied by coherent inelastic neutron scattering.* Phys. Rev. Lett. **54**, 441 (1985)

[Cr75] J. Crank. *Mathematics of Diffusion.* 2nd. ed. Oxford Press, London (1975)

[CPFS02] Web site of the Max-Planck-Institut für Chemische Physik fester Stoffe. http://www.cpfs.mpg.de/ELF/

[Da96a] K. M. Davis, A. Agrawal, M. Tomozawa, K. Hirao. *Quantitative infrared spectroscopic measurement of hydroxyl concentrations in silica glass.* J. Non-Cryst. Solids **203**, 27 (1996)

[Da96b] K. M. Davis and M. Tomozawa. *An infrared spectroscopic study of water-related species in silica glasses.* J. Non-Cryst. Solids **201**, 177 (1996)

[De65] B. E. Deal and A. S. Grove. *General relationship for the thermal oxidation of silicon.* J. Appl. Phys. **36**, 3770 (1965)

[Di90] D. B. Dingwell, S. L. Webb. *Relaxation in silicate melts.* Eur. J. Mineral. **12**, 427 (1990)

[Di95] D. B. Dingwell. *Relaxation is silicate melts: Some applications.* Rev. Mineral. **32**, 21 (1995)

[Di96a] D. B. Dingwell. *Volcanic Dilemma.* Science **273**, 1054 (1996)

[Di96b] D. B. Dingwell, C. Romano, and K. U. Hess. *The effect of water on the viscosity of a haplogranitic melt under P-T-X conditions relevant to silicic volcanism.* Contrib. Mineral. Petrol. **124**, 19 (1996)

[Do69] R. H. Doremus, in *Reactivity of Solids*, edited by J. N. Mitchell, R. C. Devris, R. W. Roberts, and P. Cannon. p. 66. John Wiley, New York, (1969)

[Do95] R. H. Doremeus. *Diffusion of water in silica glass.* J. Mater. Res. **10**, 2379 (1995)

[ESS02] The web page of the European Spallation Source. www.ess-europe.de

[Fa87] I. Farnan, S. C. Kohn, and R. Dupree. *A study of the role of water in hydrous silica glass using cross-polarization magic angle spinning NMR.* Geochim. Cosmochim. Acta **51**, 2869 (1987)

[Fe39] R. P. Feynman. *Forces in molecules.* Phys. Rev. **56**, 340 (1939)

[Fe89] B. P. Feusten and S. H. Garofalini. *Empirical three-body potential for vitreous silica.* J. Chem. Phys. **89**, 5818 (1988)

[Fe90] B. P. Feusten and S. H. Garofalini. *Oligomerization in silica sols.* J. Phys. Chem. **94**, 5351 (1990)

[Fi98] M. Filatov and W. Thiel. *Exchange-correlation density functional beyond the gradient approximation.* Phys. Rev. A **57**, 189 (1998)

[Fi01] F. Filippone and M. Parrinello. *Vibrational analysis from linear response theory.* Chem. Phys. Lett. **345**, 197 (2001)

[Fl42] P. Flory. *The thermodynamics of high polymers.* J. Chem. Phys **10**, 51 (1942)

[Fr86] E. J. Friebele and D. L. Griscom. *Color centers in glass optical fiber waveguides.* Mat. Res. Soc. Symp. Proc. **61**, 319 (1996)

[Fr90] G. P. Francis and M. C. Payne. *Finite basis set corrections to total energy pseudopotential calculations.* J. Phys. Condens. Matter **2**, 4395 (1990)

[Ga90] M. J. Frish, M. Head-Gordon, G. W. Trucks, J. B. Foresman, H. B. Schlegel, K. Rakhavachari, M. A. Robb, J. S. Binkley, C. Gonzales, D. J. DeFrees, D. J. Fox, R. A. Whiteside, R. Seeger, C. F. Melius, J. Baker, L. R. Martin, L. R. Kahn, J. Stewart, S. Topiol, and J. A. Pople. *Gaussian 90*; Gaussian Inc. Pittsburgh, PA 1990

[Gi03] G. V. Gibbs, D. F. Cox, M. B. Boisen, R. T. Downs, and N. L. Ross. *The electron localization function: a tool for locating favorable proton docking sites in silica polymorphs.* Phys. Chem. Minerals **30**, 305 (2003)

[Go31] R. W. Goranson. *The solubility of water in granite magmas.* Am. J. Sci. **22**, 481 (1931)

[Go88] R. W. Godby, M. Schlüter, and L.J. Sham. *Self-energy operators and exchange-correlation potentials in semiconductors.* Phys. Rev. B **37**, 10159 (1988)

[Go92] W. Götze and L. Sjogren. *Relaxation processes in supercooled liquids.* Rep. Prog. Phys. **55**, 241 (1992)

[Gr85] G. N. Greaves. *EXAFS and the structure of glass.* J. Non-Cryst. Solids **71**, 203 (1985)

[Gr03] V. A. Gritsenko, A. V. Shaposhnokov, Y. N. Novikov, A. P. Baraban, H. Wong, G. M. Zhidomirov, and M. Roger. *Onefold coordinated oxygen atom: an electron trap in the silicon oxide.* Microel. Reliability **43**, 665 (2003)

[Ha99] B. Hammer, L. B. Hansen, and J. K. Norskov. *Improved adsorption energetics within density-functional theory using revised Perdew-Burke-Ernzerhof functionals.* Phys. Rev. B **59**, 7413 (1999)

[Ha98] F. A. Hamprecht, A. J. Cohen, D. J. Tozer, and N. C. Handy. *Development and assessment of new exchange-correlation functionals.* J. Chem. Phys. **109**, 6264 (1998)

[He33] H. Hellmann. *Zur Rolle der kinetischen Elektronenenergie für die zwischenatomaren Kräfte.* Z. Phys. **85**, 180 (1933)

[He62] G. Hetherington and K. H. Jack. *Water in vitreous silica, part 1: Influence of water content on the properties of vitreous silica.* Phys. Chem. Glasses **3**, 129 (1964)

[He94] C. R. Helms and E. H. Poindexter. *The silicon-silicon-dioxide system: Its microstructure and imperfections.* Rep. Prog. Phys. **57**, 791 (1994)

[Hi16] J. H. Hildebrand. *Solubility.* J. Am. Chem. Soc. **38**, 1452 (1916)

[Hi77] F. L. Hirshfeld. *Bonded-atom fragments for describing molecular charge densities.* Theor. Chim. Acta **44**, 129 (1977)

[Hi85] B. Himmel, T. Gerber, and H.-G. Neumann. *X-Ray diffraction investigations of differently prepared amorphous silicas.* Phys. stat. sol. (a) **88**, K127 (1985)

[Hi94] J.-R. Hill and J. Sauer. *Molecular mechanics potential for silica and zeolite catalysis based on ab-initio calculations. 1. Dense and microporous silica.* J. Phys. Chem. **98**, 1238 (1994)

[Hi04] Gerald Hinze, University of Mainz, personal communication

[Ho96] F. Holtz, J.-M. Beny, B. O. Mysen, and M. Pichavent. *High-temperature Raman spectroscopy of silicate and aluminosilicate hydrous glasses: Implications for water speciation.* Chem. Geol. **128**, 25 (1996)

[Ho01] J. Horbach, W. Kob, and K. Binder. *Structural and dynamical properties of sodium silicate melts: An investigation by molecular dynamics computer simulation.* Chem. Geol. **174**, 87 (2001)

[Ho02] J. Horbach, W. Kob, and K. Binder. *The dynamics of sodium in sodium disilicate melts: Channel relaxation and sodium diffusion.* Phys. Rev. Lett. **88**, 125502 (2002)

[Hu31] E. Hückel. *Quantentheoretische Beiträge zum Benzolproblem.* Z. Phys. **70**, 204 (1931)

[Hu94] J. Hutter, H. P. Lüthi, and M. Parrinello. *Electronic structure optimization in plane-wave-based density functional calculations by direct inversion in the iterative subspace.* Comput. Mat. Sci. **2**, 244 (1994)

[Hu99] CPMD Version 3.3. J. Hutter, A. Alavi, T. Deutsch, M. Bernasconi, S. Goedecker, D. Marx, M. Tuckerman, M. Parrinello, MPI für Festkörperforschung and IBM Zürich Research Laboratory (1995-99)

[Hu03a] J. Hutter 2003. Personal communication

[Hu03b] P. Hunt, M. Sprik, and R. Vuilleumier. *Thermal versus electronic broadening in the density of states of liquid water.* Chem. Phys. Lett. **376**, 68 (2003)

[Is01] S. Ispas, M. Benoit, P. Jund, and R. Jullien. *Structural and electronic properties of the sodium tetrasilicate glass $Na_2Si_4O_9$ from classical and ab initio molecular dynamics simulations.* Phys. Rev. B **64**, 214206 (2001)

[Is03] S. Ispas, N. Zotov, S. De Wispelaere, and W. Kob. *Vibrational properties of a sodium tetrasilicate glass: Ab initio versus classical force fields.* J. Non-Cryst. Solids (in press)

[Jo51] J. R. Johnson, R. H. Bristow, and H. H. Blau. *Diffusion of ions in some simple glasses.* J. Am. Ceram. Soc. **34**, 165 (1951)

[Ka04a] F. Kargl, A. Meyer. *Inelastic neutron scattering on sodium aluminosilicate melts: Sodium diffusion and intermediate range order.* Chem. Geol. **213**, 165 (2004)

[Ka04b] F. Kargl, A. Meyer, H. Schober, and M. Koza. *Alkali silicate melts: Formation of channels for fast ion diffusion.* Submitted to Phys. Rev. B.

[Ke62] G. C. Kennedy, G. J. Wasserburg, H. C. Heard, and R. C. Newton. *The upper three phase region in the system $SiO_2 - H_2O$.* Am. J. Sci. **260**, 501 (1962)

[Ke90] D. A. Keen, R. L. McGreevy. *Structural modeling of glasses using reverse Monte Carlo simulation.* Nature **344**, 423 (1990)

[Kn94] R. Knoche, D. B. Dingwell, F. A. Seifert, and S. L. Webb. *Non-linear properties of supercooled liquids in the system Na_2O-SiO_2.* Chem. Geol. **116**, 1 (1994)

[Ko65] W. Kohn and L. Sham. Self-consistent equations including exchange and correlation effects. Phys. Rev. **140**, 1133 (1965)

[Ko89] S. C. Kohn, R. Dupree, and M. E. Smith. *Proton environments and hydrogen bonding in hydrous silicate glasses from proton NMR.* Nature **337**, 539 (1989)

[Ko99] W. Kob. *Computer simulations of supercooled liquids and glasses.* J. Phys. Cond. Matter. **11**, R85 (1999)

[Ko00] S. C. Kohn. *The dissolution mechanisms of water in silicate melts; a synthesis of recent data.* Mineralogical Magazine **64**, 389 (2000)

[Ko01] M. Koza. *Studium der statischen und dynamischen Eigenschaften amorpher und kristalliner Wasserphasen und ihrer Phasenumwandlungskinetik.* Dissertation, Technische Universität Darmstadt (2001)

[Kr91] G. J. Kramer, A. J. M. deMan, and R. A. van Santen. *Zeolites versus aluminosilicate clusters: The validity of a local description.* J. Am. Chem. Soc. **64**, 6435 (1991)

[Ku92] J. Kümmerlen, L. H. Merwin, A. Sebald, and H. Keppler. *Structural role of H_2O in sodium silicate glasses: Results from ^{27}Si and ^{1}H NMR spectroscopy.* J. Phys. Chem. **96**, 6405 (1992)

[Ku99] S. Kurth, J. P. Perdew, and P. Blaha. *Molecular and solid-state tests of density functional approximations: LSD, GGAs and Meta-GGAs.* Int. J. Quantum Chem. **75**, 889 (1999)

[La94] R. A. Lange. *The effect oh H_2O, CO_2 and F on the density and viscosity of silicate melts.* Rev. Mineral. **30**, 331 (1994)

[Le88] C. Lee, W. Yang, and R. G. Parr. *Development of the Colle-Salvetti correlation-energy formula into a functional of the electron density.* Phys. Rev. B **37**, 785 (1988)

[Ma90] J. R. Maple, T. S. Thatcher, U. Dinur, A. T. Hagler. *Biosym force field research results in new techniques for the extraction of inter- and intramolecular forces.* Chemical Design Automation News 5 **9**, 5 (1990)

[Ma92] G. J. Martyna, M. E. Tuckerman, and M. L. Klein. *Noé-Hoover chains: The canonical ensemble via continuous dynamics.* J. Chem. Phys. **97**, 2635 (1996)

[Ma96] G. J. Martyna, M. E. Tuckerman, D. J. Tobias and M. L. Klein. *Explicit reversible integrators for extended system dynamics.* Mol. Phys. **87**, 1117 (1996)

[Ma97] N. Mazari and D. Vanderbilt. *Maximally localized Wannier functions for composite energy bands.* Phys. Rev. B. **56**, 12847 (1997)

[Ma98] H. Maekawa, T. Saito, and T. Yokokawa. *Water in silicate glasses: ^{17}O NMR of hydrous silica, albite and $Na_2Si_4O_9$ glasses.* J. Phys. Chem. B **102**, 523 (1998)

[Ma04] D. Marx. *Wasser, Eis und Protonen.* Physik Journal **3**, 33 (2004)

[Me35] K. H. Meyer and R. Luhdemann. *Über das Verhalten höherer molekularer Verbindungen in Lösung.* Helvet. Chim. Acta **18**, 307 (1935)

[Me02] A. Meyer, H. Schober, and D. B. Dingwell. *Structure, structural relaxation and ion diffusion in sodium disilicate melts.* Europhys. Lett. **59**, 708 (2002)

[Me04] A. Meyer, J. Horbach, W. Kob, F. Kargl, and H. Schober. *Channel formation and intermediate range order in sodium silicate melts and glasses.* Phys. Rev. Lett. **93**, 027801 (2004)

[Mi84] P. F. McMillan. *Structural studies of silicate glasses and melts - applications and limitations of Raman spectroscopy.* Am. Mineral. **69**, 622 (1984)

[Mi86] P. F. McMillan and R. L. Remmele. *Hydroxyl sites in SiO_2 glass: A note on infrared and Raman spectra.* Am. Mineral. **71**, 772 (1986)

[Mi94] P. F. McMillan. *Water solubility and speciation models.* Rev. Mineral. **30**, 131 (1994)

[Mi02] S. Mikhailenko, D. Desplantier-Giscard, C. Danumah, and S. Kaliaguine. *Solid electrolyte properties of sulfonic acid functionalized mesostructured porous silica.* Micropor. Mesopor. Mat. **52**, 29 (2002)

[Mu55] R. S. Mulliken. *Electronic population analysis on LCAO-MO [linear combination of atomic orbital-molecular orbital] molecular wave functions. I.* J. Chem. Phys. **23**, 1833 (1955)

[Mu04] A. R. Müller. *Struktur und Dynamik wasserhaltiger Silikatgläser untersucht mit Neutronenstreuung.* Diploma Thesis, Munich Technical University E13, Feb. 2004.

[My86] B. O. Mysen and D. Virgo. *Volatiles in silicate melts at high pressure and temperature. 1. Interaction between OH groups and Si^{4+}, Al^{3+}, Ca^{2+}, Na^{+}, and H^{+}.* Chem. Geol. **57**, 303 (1986)

[Na98] O. Navon, A. Chekhmir, and V. Lyakhovsky. *Bubble growth in highly viscous melt: theory, experiments and autoexplosivity of dome lavas.* Earth and Plan. Sci. Lett. **160**, 763 (1998)

[Ni93] H. Nishikawa, R. Nakamura, and Y. Ohki. *Correlation of preexisting diamagnetic defect centers with induced paramagnetic defect centers by ultraviolet or vacuum-ultraviolet photons in high-purity silica glasses.* Phys. Rev. B **48**, 15584 (1993)

[Ni95] www.ncnr.nist.gov/resources/n-lengths/elements/

[Ni03] www.ncnr.nist.gov/chemistry web book

[No97] M. Nogami and Y. Abe. *Evidence for water-cooperative proton conduction in silica glasses.* Phys. Rev. B **55**, 12108 (1997)

[No99] T. Norby. *Solid-state protonic conductors: principles, properties, progress and prospects.* Solid State Ionics **125**, 1 (1999)

[Oc97] F. A. Ochs and R. A. Lange. *The partial molar volume, thermal expansivity and compressibility of H_2O in $NaAlSi_3O_8$ liquid: new measurements and an internally consistent model.* Contrib. Mineral. Petrol. **129**, 155 (1997)

[Ol99] C. Oligschleger. *Dynamics of SiO_2 glasses.* Phys. Rev. B **60**, 3182 (1999)

[Pa62] H. H. Paalman and C. J. Pings. *Numerical evaluation of X-ray absorption factors for cylindrical samples and annular samples.* J. Appl. Phys. **33**, 2635 (1962)

[Pa76] S. Pantelides and W. Harrison. *Electronic structure, spectra, and properties of 4:2-coordinated materials. I. Crystalline and amorphous SiO_2 and GeO_2.* Phys. Rev. B **13**, 2667 (1976)

[Pa91] G. Pastore, E. Smargiassi, and F. Buda. *Theory of ab-initio molecular dynamics calculations.* Phys. Rev. A **44**, 6334 (1991)

[Pa97] A. Pasquarello and R. Car. *Dynamical Charge Tensors and Infrared Spectrum of Amorphous SiO_2.* Phys. Rev. Lett. **79**, 1766 (1997)

[Pa98] A. Pasquarello, M. S. Hybertsen, and R. Car. *Interface structure between silicon and its oxide by first-principles molecular dynamics.* Nature **396**, 58 (1998)

[Pa01] A. Pasquarello. *First-principles simulations of vitreous systems.* Curr. Op. Sol. State Mat. Sci. **5**, 503 (2001)

[Pe96] J. P. Perdew, K. Burke, and M. Ernzerhof. *Generalized gradient approximation made simple.* Phys. Rev. Lett. **77**, 3865 (1996)

[Pe97] A. G. Pelmenschikov, G. Morosi, and A. Gamba. *Adsorption of water and Methanol on silica hydroxyls: Ab initio energy and frequency calculations.* J. Phys. Chem. A **101**, 1178 (1997)

[Pe99] J. P. Perdew, S. Kurth, A. Zupan, and P. Blaha. *Accurate density functional with correct formal properties: A step beyond the generalized gradient approximation.* Phys. Rev. Lett. **82**, 2544 (1999)

[Pf81] R. Pfeffer and M. Ohring. *Network oxygen exchange during water diffusion in SiO_2.* J. Appl. Phys. **52**, 777 (1981)

[Pl52] G. Placzek. *The scattering of neutrons by systems of heavy nuclei.* Phys. Rev. **86**, 377 (1952)

[Po95] E. H. Poindexter. *Physical chemistry of hydrogenous species in the Si-SiO_2 system.* Z. Naturforsch. **50a**, 653 (1995)

[Po99] P. H. Poole, P. F. McMillan, and G. H. Wolf. *Computer simulations of silicate melts.* Rev. Mineralogy **32**, 563 (1999)

[Pr68] H. Prask and H. Boutin. *Frequency spectrum of hydrogenous molecular solids by inelastic neutron scattering. Hexagonal H_2O ice.* J. Chem. Phys. **48**, 3367 (1968)

[Pr86] D. L. Price and K. Sköld, in: *Neutron Scattering*, Part A, eds. K. Sköld and D. L. Price (Academic Press, Orlando 1986) p.1

[Pr87] D. L. Price and J. M. Carpenter. Scattering function of vitreous silica. J. Non-Cryst. Solids **92**, 153 (1987)

[Pr89] W. H. Press, B.P. Flannery, S. A. Teukolsky, W. T. Vetterling. *Numerical recipes, the art of scientific computing.* Cambridge University Press, Cambridge, New York, Port Chester, Melbourne, Sydney (1989)

[Pr98] A. A. Proussevitch, D. L. Sahagian. Dynamics and energetics of bubble growth in magmas: Analytical formulation and numerical modeling. J. Geophys. Res. **103** B8, 18223 (1998)

[Pu69] P. Pulay. *Ab initio calculation of force constants and equilibrium geometries in polyatomic molecules. I. Theory.* Molec. Phys. **17**, 197 (1969)

[Re68] R. H. Redwine and M. B. Field. *The effect of microstructure on the physical properties of glasses in the sodium silicate system.* J. Meter. Sci. **3**, 380 (1968)

[Re83] E. P. O'Reilly and J. Robertson. *Theory of defects in vitreous silicon dioxide.* Phys. Rev. B. **27**, 3780 (1983)

[Re84] W. Reichardt. Bericht des Forschungszentrums Karlsruhe (1984)

[Ri96] P. Richet, A.-M. Lejeune, F. Holtz, and J. Roux. *Water and the viscosity of andesite melts.* Chem. Geol. **128**, 185 (1996)

[Ro51] C. Roothaan. *New developments in molecular orbital theory.* Rev. Mod. Phys. **23**, 69 (1951)

[Ro88] J. Robertson. Electronic structure of defects in amorphous SiO_2. *The physics and technology of amorphous SiO_2.* R. Devine (Ed.). Plenum Press, New York (1988)

[Sa95a] J. Sarnthein, A. Pasquarello, and R. Car. *Structural end electronic properties of liquid and amorphous SiO_2: An ab initio molecular dynamics study.* Phys. Rev. Lett. **74**, 4682 (1995)

[Sa95b] J. Sarnthein, A. Pasquarello, and R. Car. *Model of vitreous SiO_2 generated by ab initio molecular-dynamics quench from the melt.* Phys. Rev. B **52**, 12690 (1995)

[Sa97] J. Sarnthein, A. Pasquarello, and R. Car. *Origin of the high-frequency doublett in the vibrational spectrum of vitreous SiO_2.* Science **275**, 1925 (1997)

[Sa99] D. Sahagian. *Magma fragmentation in eruptions.* Nature **402**, 589 (1999)

[Sc59] H. Scholze, H. Franz and L. Merker. *Der Einbau des Wassers in Gläsern. VI. Der Einfluss des Wassers auf einige Glaseigenschaften, insbesondere auf Dichte und Lichtbrechung.* Glastechn. Ber. **32**, 421 (1959)

[Sc88] H. Schober. *Ladungen in der Gitterdynamik.* Diloma thesis, University of Regensburg (1988)

[Sc96] F. Schulze, H. Behrens, F. Holtz, J. Roux, and W. Johannes. *The influence of H_2O on the viscosity of a haplogranitic melt.* Am. Mineral. **81**, 1155 (1996)

[Sc02] H. Schober. *Spectroscopie neutronique: Un outil idéal pour le scientifique des matériaux.*

[Sh64] H. Shaw. *Theoretical solubility of H_2O in silicate melts. Quasi-crystalline models.* J. Geology **72**, 601 (1964)

[Sh95] A. Shen and H. Keppler. *Infrared-spectroscopy of hydrous silicate melts to 1000°C and 10kbar - direct observation of H_2O speciation in a diamond-anvil cell.* Amer. Mineral. **80**, 1335 (1995)

[Sh96] D. W. Shin and M. Tomozawa. *Effects of fictive temperature and water content on electrical conductivity of silica glasses.* J. Non-Cryst. Solids **203**, 262 (1996)

[Si80] R. N. Sinclair, J. A. Desa, G. Etherington, P. A. V. Johnson, and A. C. Wright. *Neutron diffraction studies of amorphous solids.* J. Non-Cryst. Solids **42**, 107 (1980)

[Si89] L. Silver and E. Stolper. *Water in albitic glasses.* J. Petrol. **30**, 667 (1989)

[Si92] F. Sim, A. St-Amant, I. Papai, and D. R. Salahub. *Gaussian density functional calculations on hydrogen-bonded systems.* J. Am. Chem. Soc. **114**, 4391 (1992)

[Si98] P. L. Silvestrelli, N. Marzari, D. Vanderbilt, and M. Parrinello. *Maximally localized Wannier functions for disordered systems: Application to amorphous silicon.* Sol. Stat. Commun. **107**, 7 (1998)

[SIA01] http://public.itrs.net/

[So97] A. K, Soper, F. Bruni, and M. A. Ricci. *Site-site pair correlation functions of water from 25 to 400 °C: Revised analysis of new and old diffraction data.* J. Chem. Phys. **106**, 247 (1997)

[St76] R. H. Stolen and G. E. Walrafen. *Water and its relation to broken bond defects in fused silica.* J. Chem. Phys. **64**, 2623 (1976)

[St78] F. H. Stillinger and A. Rahman. *Revised central force potentials for water.* J. Chem. Phys. **68**, 666 (1978)

[St82] E. M. Stolper. *Water in glasses: An infrared spectroscopic study.* Contrib. Mineral. Petrol. **81**, 1 (1982)

[St89] H. P. Stadler. *Chemical Thermodynamics, Revision and worked examples.* The Royal Society of Chemistry, Cambridge (1989)

[Su91] S. Susman, K. J. Volin, D. L. Price, M. Grimsditch, J. P. Rino, R. K. Kalia, P. Vashishta, G. Gwanmesia, Y. Wang, and R. C. Liebermann. *Intermediate-range order in permanently densified vitreous SiO_2: A neutron-diffraction and molecular-dynamics study.* Phys. Rev. B **43**, 1194 (1991)

[Su97] I. Susnowska, U. Buchenau, G. Reichenauer, H. Graetsch, K. Ibel, and B. Frick. *Structure and dynamics of the opal silica-water system.* Physica B **234-236**, 455 (1997)

[Sw82] W. C. Swope, H. C. Anderson, P. H. Berens, and K. R. Wilson. *A computer simulation method for the calculation of equilibrium constants for the formation of physical clusters of molecules: Application to small water clusters.* J. Chem. Phys. **76**, 637 (1982)

[Ta97a] S. N. Taraskin and S. R. Elliott. *Nature of vibrational excitations in vitreous silica.* Phys. Rev. B **56**, 8605 (1997)

[Ta97b] S. N. Taraskin and S. R. Elliott. *Connection between the true vibrational density of states and that derived from inelastic neutron scattering.* Phys. Rev. B. **55**, 117 (1997)

[To74] W. Topp and J. Hopfield. *Chemically motivated pseudopotential for sodium.* Phys. Rev. B **7**, 1295 (1974)

[Tr91] N. Troullier and J. L. Martins. *Efficient pseudopotentials for plane-wave calculations.* Phys. Rev. B **43**, 1993 (1991)

[Tu48] O. F. Tuttle and I. I. Friedman. *Liquid immiscibility in the system $H_2O - Na_2O - SiO_2$.* J. Am. Chem. Soc. **70**, 919 (1948)

[Tu94] M. E. Tuckerman and M. Parrinello. *Integrating the Car-Parrinello equations. I. Basis Integration techniques.* J. Chem. Phys. **101**, 1302 (1994)

[Tu00] M. E. Tuckerman and G. Martyna. *Understanding modern molecular dynamics: Techniques and applications.* J. Phys. Chem. **104**, 159 (2000)

[UG97] web site of the Center for Computational Chemistry of the University of Georgia: http://zopyros.ccqc.uga.edu/lec_top/irint/node11.html

[US00] web site of the U.S. Geological Survey: http://volcanoes/usgs/gov/

[Va90] D. Vanderbilt. *Soft self-consistent pseudopotentials in a generalized eigenvalue formalism.* Phys. Rev. B **41**, 7892 (1990)

[Vo96] K. Vollmayr, W. Kob, and K. Binder. *Cooling rate effects in amorphous silica: A computer simulation study.* Phys. Rev. B **54**, 15808 (1996)

[Wa37] G. H. Wannier. *The structure of electronic excitation levels in insulating crystals.* Phys. Rev. **52**, 191 (1937)

[Wa38] B. E. Warren and J. Biscoe. *Fourier analysis of X-ray patterns of soda lime-silica glass.* J. Am. Chem. Soc. **21**, 259 (1938)

[Wa57] G. J. Wasserburg. *The effect of H_2O in silicate systems.* J. Geology **65**, 15 (1957)

[Wa64] F. E. Wagstaff, S. D. Brown and I. B. Cutler. *The influence of H_2O and O_2 atmospheres on the crystallization rate of vitreous silica.* Phys. Chem. Glasses **5**, 76 (1964)

[We64] R. A. Weeks and E. Lell. *Relation Between E Centers and Hydroxyl Bonds in Silica.* J. Appl. Phys. **35**, 1932 (1964)

[We76] R. C. Weast. *Handbook of Chemistry and Physics.* CRC Press, Boca Raton, Fla (1976)

[We94] S. Wen and H. Nevaskil. *Ideal associated solutions: Applications for the system albite-quartz-H_2O.* Am. Mineral **79**, 316 (1994)

[Wi03] A. Winkler, J. Horbach, W. Kob, and K. Binder. *Structure and diffusion in amorphous aluminium silicate. A molecular dynamics computer simulation.* J. Chem. Phys. **120**, 384 (2003)

[Wu93] J. Wuttke, M. Kiebel, E. Bartsch, F. Fujara, W. Petry, and H. Sillescu. *Relaxation and phonons in viscous and glassy orthoterphenyl by neutron scattering.* Z. Phys. B: Condensed Matter **91**, 357 (1993)

[Wu01] J. Wuttke. *IDA: A package for ingenious data analysis.* http://www.e13.ph.tum.de/Wuttke/Ida.html (2001)

[Za95] M. R. Zachariah and W. Tsang. *Theoretical Calculation of Thermochemistry, Energetics, and Kinetics of High-Temperature SixHyOz Reactions.* J. Phys. Chem. **99**, 5308 (1995)

[Ze96] Q. Zeng and H. Nekvasil. *An associated solution model for albite-water melts.* Geochim. Cosmochim. Acta **60**, 59 (1996)

[Zh97] Y. Zhang, R. Belcher, P. D. Ihinger, L. Wang, Z. Xu, and S. Newman. *New calibration of infrared measurement of dissolved water in rhyolic glasses.* Geochim. Cosmochim. Acta **61**, 3089 (1997)

[Za02] G. Zandt. *The slippery slope.* Nature **417**, 497 (2002).

[Zo92] N. Zotov, Y. Yanev, M. Epelbaum, and L. Konstantinov. *Effect of water on the structure of rhyolite glasses -X-ray diffraction and Raman spectroscopy studies.* J. Non-Cryst. Solids **142**, 234 (1992)

[Zo96] N. Zotov, H. Keppler, A. C. Hannon, and A. K. Soper. *The effect of water on the structure of silicate glasses. A neutron diffraction study.* J. Non-Cryst. Solids **202**, 153 (1996)

[Zo01a] N. Zotov. *Effects of composition on the vibrational properties of sodium silicate glasses.* J. Non-Cryst. Solids **287**, 231 (2001)

[Zo01b] R. Zorn, H. Behrens, P. Heitjans, and S. Indris. *Dynamics of water in aluminosilicate glasses.* Experimental report No 6-05-496, Institut Laue-Langevin (2001)

Own Publications

Thanks to the kind approval of the Fakultät für Physik and the Laboratoire des Verres, the following articles could already be published on the subject:

1. M. Pöhlmann, M. Benoit, and W. Kob. *First-principles molecular-dynamics simulations of a hydrous silica melt: Structural properties and hydrogen diffusion mechanism.* Phys. Rev. B, **70**, 184209 (2004)

2. M. Pöhlmann, A. Meyer, M. Benoit, and W. Kob. *Ab initio molecular dynamics simulations of hydrous silicate systems.* High Performance Computing in Science and Engineering, Munich 2004. Transactions of the Second Joint HLRB and KONWIHR Result and Reviewing Workshop, March 2nd and 3rd, 2004, Technical University of Munich. Springer-Verlag, Berlin, Heidelberg, New York, p 199 (2004)

3. M. Pöhlmann, H. Schober, M. Benoit, and W. Kob. *First-Principles Molecular-Dynamics Simulations of a Hydrous Silica Melt: Hydrogen Diffusion Mechanisms and Electronic Properties.* Technical Proceedings of the 2004 NSTI Nanotechnology Conference and Trade Show, Boston (Ma), USA, Volume III, p 73. The Nano Science and Technology Institute, Cambridge (2004)

In preparation:

4. M. Pöhlmann, A. Meyer, A. Müller, H. Schober, and T. Hansen. *Structural and dynamical properties of hydrous amorphous silicates as seen by neutron scattering.* In submission to Phys. Rev. B.

5. M. Benoit, M. Pöhlmann and W. Kob. *Electronic structure of point defects in a hydrous silica glass.*